

Heterogeneity and its effects on simple chemical events in molten multi-component systems

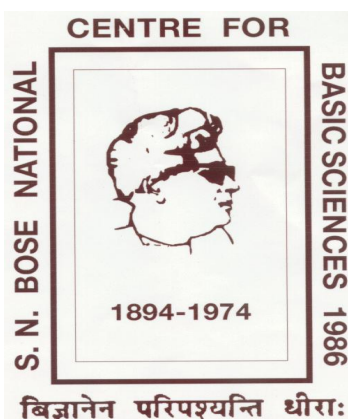
**Thesis Submitted for the Degree of
Doctor of Philosophy (Science)**

of

Jadavpur University

By

Suman Das



Department of Chemical, Biological and Macromolecular Sciences

S. N. Bose National Centre for Basic Sciences

Block-JD, Sector-III, Salt Lake City

Kolkata-700106, India

July 2016

सत्येन्द्र नाथ बसु राष्ट्रीय मौलिक विज्ञान केन्द्र
SATYENDRA NATH BOSE NATIONAL
CENTRE FOR BASIC SCIENCES
সত্যেন্দ্র নাথ বসু জাতীয় মৌল বিজ্ঞান কেন্দ্র

CERTIFICATE FROM THE SUPERVISOR(S)

This is to certify that the thesis entitled “Heterogeneity and its effects on simple chemical events in molten multi-component systems”, submitted by Sri Suman Das (Index no. 28/13/Chem./22), who got his name registered on 14/03/13 for the award of Ph.D. (Science) degree of Jadavpur University, is absolutely based upon his own work under the supervision of Prof. Ranjit Biswas and that neither this thesis nor any part of it has been submitted for either any degree/diploma or any other academic award anywhere before.

Ranjit Biswas
20/07/16
Dr Ranjit Biswas

Professor,

Department of Chemical, Biological and Macromolecular Sciences

S. N. Bose National Centre for Basic Sciences

Block-JD, Sector-III, Salt Lake, Kolkata-700106, West Bengal, India

DR. RANJIT BISWAS

Professor

Dept. of Chemical, Biological & Macromolecular Sciences
S. N. Bose National Centre for Basic Sciences
Block - JD, Sector - III, Salt Lake, Kolkata - 700 098, India

Dedicated
To
My Family...

Acknowledgement

It is my pleasure to express my earnest thanks and deepest gratitude to my research guide Prof. Ranjit Biswas for being a wonderful supervisor and giving me the freedom to work independently. His guidance, constant encouragement and illuminating discussions have made this research work a memorable journey towards academic enrichment. His kind and affectionate attitude is worth cherishing for entire life. I have been extremely fortunate to have an advisor like him.

I cannot express in words my gratitude to my research collaborator Dr. Biswaroop Mukherjee for teaching me patiently the complex yet beautiful aspect of molecular dynamics simulation method. His untiring help, immense support and enthusiasm have helped me to learn the ways of dealing scientific problems intelligently. I convey my deepest thanks to him for sharing his vast knowledge during the research period. He has been truly my unofficial co-supervisor for my Thesis.

My sincere thank to all the members of my Thesis committee Prof. Sanjoy Bandyopadhyay (IIT Kharagpur), Prof. Manoranjan Kumar, Prof. Punyabrata Pradhan for devoting their valuable time for me.

I am grateful to all the faculty members, research scholars and non-teaching staffs for their kind help and co-operation. My sincere thank to the staff-members of the academic section of the institute. I wish to thank every individual associated with the computational facility of the Centre. I have been immensely benefitted from TUE-CMS computational facility.

I wish to thank all my present lab-mates, Sandipa di, Kallol, Ejaj, Juriti, Kausik, Kajal, Sommonita and Atanu for proving me a wonderful environment of research. I convey my thank to all of my past lab members, Dr. Tuhin Pradhan, Dr. Hemant Kumar Kashyap, Dr. Harun Al. Rashid Gazi, Dr. Biswajit Guchhait, Dr. Snehasis Daschakraborty, Dr. Tamisra Pal , Dr. Anuradha Das and Dr. Mainak Sadhukhan for their help, suggestions and companionship.

I express my sincere regards to Dr. Parijat Das for her extreme caring attitude. I'll always cherish the sweet moments I've spent with Rwitoban and Arshaman.

I heartily thank all of my friends here at the centre. I would also like to thank my friends Alapon, Chiranjib, Mrinmoy, Arindam for their help whenever required. I am especially thankful to Dr. Pritam Ganguly and Dr. Anirban Samanta for many helpful discussions.

Financial assistance from CSIR and the centre is gratefully acknowledged.

I would like to convey my gratitude to my father Bimal Kumar Das and mother Chandrabati Das for their love, blessings and encouragement. I am grateful to my Family-in-Law - Tapan Kumar Sarkar and Gita Sarkar for their immense support. I thank my sister Epa, brothers Sourav and Sumit for their warmth uplifting of my spirit. My heartfelt thanks are due to all my relatives for their blessings. I would like to add a special note of thanks for my wife Dr. Ivy Das Sarkar for her immense support and encouragement.

I am thankful to my school (Singur Mahamaya High School) teachers, college (Ramakrishna Mission Vidyamandira, Belur) professors, faculty members of Department of Chemistry, IIT Guwahati for their guidance in the voyage of academic excellence. I express my sincere gratitude to Prof. Sandip Paul, IIT Guwahati for introducing me to this wonderful world of molecular dynamics during my M.Sc. days.

Finally, I would like to thank all those people, who have directly or indirectly helped me at various stages of my research work.

“The function of education is to teach one to think intensively and to think critically. Intelligence plus character – that is the goal of true education”

- **Martin Luther King, Jr.**

Abstract

Understanding the structure and dynamics of solvents for better utilization is one of the principal concerns of chemical science. Deep eutectic solvents (DESs) and ionic liquids (ILs) are solvents with diverse range of application potential in technologies and industries. DESs are multi-component mixtures which can acquire liquid phase near room temperature although individual melting temperatures of the mixture constituents can be much higher than the room temperature. Extensive interspecies hydrogen bonding and the entropic gain in liquid state favor accessing the liquid phase. DESs can be of both ionic and non-ionic in nature. In contrast, ILs consist entirely of ions and remain in liquid below 373 K. Heterogeneity (both spatial and dynamical) plays a major role on determining structural and dynamical properties of these solvents. This Thesis is mainly focused on studying the effects of heterogeneity on interaction and dynamics of deep eutectic solvents (DESs) and ionic liquids (ILs). We have performed molecular dynamics simulations with all-atom potential to investigate the structure and dynamics of these systems with particular emphasis on spatio-temporal heterogeneity in DESs. The systems considered are DESs comprised of amide and various electrolytes, and the IL, 1-butyl-3-methylimidazolium hexafluorophosphate.

The medium heterogeneity has been monitored following protocols used earlier to study deeply supercooled liquids. The heterogeneity aspect has been manifested in terms of various two and multi-point correlations which offer a qualitative estimate of correlated domain size and timescale. The spatial heterogeneity has been observed in terms of various cluster size and lifetime distributions. We have also investigated the ion and temperature dependence of both spatial (static) and temporal (dynamic) heterogeneities. Extensive analysis has been carried out to explore the existence of angular jumps in molten acetamide and acetamide/electrolyte deep eutectics. Simulated jump characteristics such as jump and waiting time distributions of acetamide/electrolyte DESs depict a power law at long time, suggesting presence of temporal heterogeneity in these multi-component molten mixtures around room temperature. Hydrogen bond relaxations and orientational dynamics of these DESs also reflect the presence of

heterogeneity in the solution via distributed kinetics (stretched exponential relaxation). For a better understanding of microscopic dynamics we have separated out the individual contributions of the averaged-out total relaxation. Finally, we have investigated the orientational jumps in 1-butyl-3-methylimidazolium hexafluorophosphate IL where we have separately analyzed the dynamics of cation and anion. Our study of these complex liquids has generated an overall microscopic understanding which will be useful for engineering solvent systems for tailoring reactions.

Chapter 1 of the Thesis presents an introduction of the present work with a brief review of relevant literature. Chapter 2 describes the orientational dynamics of molten acetamide and connects it to hydrogen bond relaxation. Chapter 3 provides orientational jump of acetamide in presence of various electrolytes. Chapter 4 contains the collective dynamic dipole moment fluctuations and cooperative hydrogen bond relaxations of acetamide in ionic deep eutectics. Chapter 5 discusses the structural aspect of these deep eutectics via simulating various cluster size and lifetime distributions. Chapter 6 describes the dynamic heterogeneity aspect of acetamide/electrolyte DESs. Chapter 7 presents the orientational jump dynamics of 1-butyl-3-methylimidazolium hexafluorophosphate IL. Chapter 8 ends the Thesis with a concluding remark and provides some interesting problems which can be performed in near future. In summary, the work on DESs reported in the present Thesis reveals substantial glassy behavior for systems at temperatures that are ~ 200 K above the respective glass transition temperatures. The work on IL then explores commonality in reorientational mechanism between these two (IL and DES) exotic solvent systems.

List of Publications

1. “Fast fluctuations in deep eutectic melts: Multi-probe fluorescence measurements and all-atom molecular dynamics simulation study” by Anuradha Das, **Suman Das** and Ranjit Biswas, *Chem. Phys. Lett.* **581**, 47 (2013).
2. “Interaction and dynamics of (alkylamide + electrolyte) deep eutectics: Dependence on alkyl chain-length, temperature, and anion identity” by Biswajit Guchhait, **Suman Das**, Snehasis Daschakraborty, and Ranjit Biswas, *J. Chem. Phys.* **140**, 104514 (2014).
3. “Reorientational Jump Dynamics and Its Connections to Hydrogen Bond Relaxation in Molten Acetamide: An All-Atom Molecular Dynamics Simulation Study” by **Suman Das**, Ranjit Biswas and Biswaroop Mukherjee, *J. Phys. Chem. B* **119**, 274 (2015).
4. * “Density relaxation and particle motion characteristics in a non-ionic deep eutectic solvent (acetamide + urea): Time-resolved fluorescence measurements and all-atom molecular dynamics simulations” by Anuradha Das, **Suman Das**, and Ranjit Biswas, *J. Chem. Phys.* **142**, 034505 (2015).
5. “Orientational Jumps in (Acetamide + Electrolyte) Deep Eutectics: Anion Dependence” by **Suman Das**, Ranjit Biswas, and Biswaroop Mukherjee, *J. Phys. Chem. B* **119**, 11157 (2015).
6. “Collective Dynamic Dipole Moment Fluctuations, Cooperative Hydrogen Bond Relaxations and Their Connections to Dielectric Relaxation in Ionic Acetamide Deep Eutectics: Microscopic Insight from Simulations” by **Suman Das**, Ranjit Biswas, and Biswaroop Mukherjee, *J. Chem. Phys.* (**under minor review**).
7. “Structural Aspects of Amide Deep Eutectics: A Molecular Dynamics Investigation” by **Suman Das**, Biswaroop Mukherjee, and Ranjit Biswas, *J. Phys. Chem. B* (to be submitted).
8. “Dynamic Heterogeneity in Acetamide /Electrolyte Deep Eutectic Solvents: Dependence on Temperature and Anion Identity” by **Suman Das**, Biswaroop Mukherjee, and Ranjit Biswas, *J. Chem. Phys.* (to be submitted).

9. “Reorientational Dynamics in 1-butyl-3-methylimidazolium hexafluorophosphate ([BMIM][PF₆]) Ionic Liquid: Are Angular Jumps Predominant?” by **Suman Das**, Biswaroop Mukherjee, and Ranjit Biswas, *J. Phys. Chem. B* (to be submitted).
10. “Temperature Dependent Dielectric Relaxation of molten Urea, and Acetamide/Urea Deep Eutectics: Polarity and the Possible Origin of the Relaxation Timescales” by Kallol Mukherjee, **Suman Das**, Anjan Barman, and Ranjit Biswas, *J. Phys. Chem. B* (to be submitted).
11. “Urea-Induced Homogenization of Ionic Deep Eutectics: Signatures from Time-Resolved Fluorescence Measurements and All-atom Simulations” by Anuradha Das, **Suman Das**, and Ranjit Biswas, *J. Phys. Chem. B* (to be submitted).
12. “Decoupling of Viscosity from Diffusive Dynamics in (Acetamide+Electrolyte) Deep Eutectics: Effect of Cation and Anion” by Biswajit Guchhait, **Suman Das**, and Ranjit Biswas, (Manuscript in preparation).

* not included in this Thesis

Contents

Chapter 1: Introduction.....	1
Chapter 2: Reorientational Jump Dynamics and Its Connections to Hydrogen Bond Relaxation in Molten Acetamide: An All-Atom Molecular Dynamics Simulation Study....	16
2.1. Introduction.....	16
2.2. Simulation Details.....	17
2.3. Analysis Protocol.....	18
2.4. Results and Discussion.....	28
2.5. Conclusions.....	43
Chapter 3: Orientational Jumps in (Acetamide + Electrolyte) Deep Eutectics: Anion Dependence.....	49
3.1. Introduction.....	49
3.2. Simulation Details.....	51
3.3. Analysis Protocol.....	52
3.4. Results and Discussion.....	64
3.5. Concluding Remarks.....	77
Chapter 4: Collective Dynamic Dipole Moment Fluctuations, Cooperative Hydrogen Bond Relaxations and Their Connections to Dielectric Relaxation in Ionic Acetamide Deep Eutectics: Microscopic Insight from Simulations.....	84
4.1. Introduction.....	84

4.2. Simulation Details.....	87
4.3. Analysis Protocol.....	89
4.4. Results and Discussion.....	95
4.4.1. Reorientational correlation relaxation: effects of electrolyte and anion dependence.....	95
4.4.2. Microscopic origin of the slow long-time relaxation: Role of ion-acetamide interaction.....	101
4.4.3. Orientation jump and waiting time distributions: Anion dependence of the characteristic timescales.....	111
4.4.4. Hydrogen bond correlation functions, $S_{HB}(t)$ and $C_{HB}(t)$: Connection to orientational relaxations.....	115
4.4.5. Separation of $S_{HB}(t)$ and $C_{HB}(t)$ relaxations into acetamide-acetamide and acetamide-anion components: Effects of Li^+ and origin of slowing down.....	122
4.5. Conclusions.....	126
Chapter 5: Structural Aspects of Amide Deep Eutectics: A Molecular Dynamics Investigation.....	133
5.1. Introduction.....	133
5.2. Simulation Details.....	135
5.3. Results and Discussion.....	136
5.3.1. Radial Distribution Function.....	136
5.3.2. Cluster Size and Lifetime Analysis.....	145
5.4. Conclusions.....	156

Chapter 6: Dynamic Heterogeneity in Acetamide/Electrolyte Deep Eutectic Solvents: Dependence on Temperature and Anion Identity.....163

6.1. Introduction.....163

6.2. Simulation Details.....165

6.3. Results and Discussion.....166

 6.3.1. Mean Square Displacement (MSD).....166

 6.3.2. Non-Gaussian ($\alpha_2(t)$) and new Non-Gaussian ($\gamma(t)$) Parameter.....169

 6.3.3. Self and distinct parts of acetamide dynamic structure factor.....172

 6.3.4. Temporal Heterogeneity and Anion Dependence of acetamide dynamic structure factor.....174

 6.3.5. Self-part of van-Hove Function ($G_S(r,t)$).....179

 6.3.6. Probability distributions of single particle displacements ($P(\log_{10}(\delta r);t)$).....181

 6.3.7. Four-point dynamic susceptibility, overlap function and correlation length.....183

6.4. Concluding Remarks.....191

Chapter 7: Reorientational Dynamics in 1-butyl-3-methylimidazolium hexafluorophosphate ([BMIM][PF₆]) Ionic Liquid: Are Angular Jumps Predominant?..201

7.1. Introduction.....201

7.2. Simulation Details.....203

7.3. Analysis Protocol.....205

7.4. Results and Discussion.....215

7.5. Conclusions.....231

Chapter 8: Concluding Remarks and Future Problems.....	236
8.1 Concluding Remarks.....	236
8.2. Future Problems.....	237
8.2.1. Alkyl chain length dependence of spatial and temporal heterogeneity in amide/electrolyte deep eutectics.....	237
8.2.2. Dielectric relaxation and solvation dynamics in amide/electrolyte deep eutectics.....	237
8.2.3. Microsecond simulation Study of DESs close to glass transition temperature.....	238
8.2.4. Effect of medium heterogeneity on the interaction and dynamics of choline chloride/urea deep eutectics.....	239
8.2.5. Effect of non-polar solvents on medium heterogeneity in IL/solvent binary mixtures.....	239
8.2.6 Effect of heterogeneity on the transport properties of polymer ILs.....	240
8.2.7 Transport in ionic deep eutectics: Validity of the Hole Theory.....	240
Appendix A.....	244
Appendix B.....	247
Appendix C.....	261
Appendix D.....	263
Appendix E.....	267
Appendix F.....	271
Addendum I.....	281
Addendum II.....	293
Addendum III.....	308

Chapter 1

Introduction

Heterogeneity refers to the presence of diverse spatial and dynamical local features in liquids. When a liquid is cooled down quickly near its glass-transition temperature (T_g), medium dynamics slows down dramatically, imparting heterogeneity in solution/solvent structure and dynamics.¹⁻¹⁰ Structural or spatial heterogeneity refers to different local arrangements/configurations of molecules that survive long enough for measurements. Temporal heterogeneity, on the other hand, means spatially varying rates for the molecules that are forming local microscopic domains. Keeping the relaxation rates in mind, solvent/solution particles are sometimes divided as ‘mobile’ and ‘immobile’ particles. Transport properties of liquids at very low temperatures are then understood in terms of this classification. It is known that viscosity (η) of super-cooled liquids near glass transition is $\sim 10^{13}$ P, irrespective of variation in molecular-level interactions. This remarkable slowdown in momentum transfer is then linked to structural relaxation time (τ).¹¹⁻¹² Also, the dynamics of a particular region in such liquids can differ substantially relative to that in the nearby region. The density correlation functions calculated to characterize medium dynamics may become stretched exponential in nature with the exponent (β) assuming a value much less than unity.¹³⁻¹⁶ Note observation of distributed kinetics (stretched exponential relaxation) is considered as evidence for molecules that are relaxing at different rates in the different regions within a given liquid. In a heterogeneous system, the particle displacements also deviate from the Gaussian distribution typical for hot homogeneous liquids.¹⁷ Surprisingly, the static structure of liquids is affected very little as observed from X-ray and neutron scattering experiments.¹ This peculiar behavior has triggered immense interest in detailed characterization of the heterogeneity aspect of metastable liquids.¹⁸⁻
20

Advanced experimental techniques, such as, nuclear magnetic resonance (NMR),²¹⁻²³ fluorescence spectroscopy,²⁴⁻²⁵ confocal microscopy,²⁶⁻²⁸ X-ray and neutron scattering,²⁹ X-ray

photon correlation spectroscopy,³⁰ and dielectric relaxation³¹⁻³² have been applied to understand dynamics of glass former liquids. After the seminal simulation studies on Lennard-Jones binary mixtures³³⁻³⁵, a large number of simulations attempted characterizing the heterogeneity aspect.³⁶⁻⁴⁶ These simulation studies have particularly reported the presence of particles with varying motion⁴⁷: mobile particles which undergo large displacements and immobile particles that execute small displacements. These large and small displacements are relative to the displacements predicted from the Gaussian distribution for homogeneous system. Apart from the inevitable fundamental scientific interest, the presence of domains with mobile and immobile particles has significant application in synthesizing nano pores.⁴⁷ It has been suggested that in such systems there exists more than one spatial length-scales connected to local dynamics. Characterization of these length scales can be carried out via following multi-point correlation which essentially tracks the variance of the fluctuations in the dynamic structure factor.⁴⁸⁻⁵¹ However, several conceptual difficulties arise when one tries to compare the growing length scale and time scales of medium dynamics as a function of decreasing temperature.^{11,20} Interconnection between this length- and time-scales has remained a challenging problem. In spite of the recent advancement in the computation facility, extensive simulation studies of glass former liquids are still restricted to the Lennard-Jones binary mixtures³³⁻⁴⁷ which are devoid of complex chemical interactions. The reasons for such a scenario are multiple, some of them being quite non-trivial to overcome. For example, it is very difficult to consider Avogadro number (10^{23}) of particles in a simulation. Incorporation of specific interactions, such as, H-bond interactions further compounds the problem. Interestingly, deep eutectic solvents⁵²⁻⁶² (DESs) and room temperature ionic liquids⁶³⁻⁸⁴ (RTILs) show several heterogeneity features at ambient conditions, although their glass transition temperatures are around 190 K.⁵³ Thus, they offer a great opportunity to investigate heterogeneity at or around room temperature where viscosity has not reached a value of 10^{13} P.

Engineering reaction media for large scale applications in chemical industry is a priority area. Decades of hard work, understanding of fundamental scientific aspects and constant demand from the industry have motivated the discovery of environment-friendly solvents, namely,

DESs⁸⁵⁻⁹² and ILs.⁹³⁻⁹⁸ DESs are the mixtures of various inorganic or organic compounds that form stable liquid phase and remain so at temperatures much lower than the melting temperatures of the individual mixture components. It is believed that the extensive inter-species hydrogen bonding (H-bonding) coupled with the enhanced entropy in the liquid state brings down the melting point. This may be considered as metastability for these systems as crystallization is avoided via both enthalpic and entropic factors. Several DESs can be considered as “green solvents”, a much desired alternative to the traditional organic solvents because of biodegradability of some the constituents.⁸⁶ The easy preparation procedure along with cost-effectiveness, easy handling, moisture resistance property and recyclability have triggered promising applications in pharmaceutical industry, biomass treatment, biocatalysis, electrodeposition, media for synthesizing functional materials, removal of glycerols from biodiesel, processing of metal oxides, synthesis of cellulose derivatives etc.⁸⁵⁻⁹² DESs can be of both ionic and non-ionic in nature. If one of the components is electrolyte then the mixture can be termed as ionic DES; otherwise, the mixture may be designated as non-ionic DES. Typical examples of ionic DESs are amide+lithium bromide/nitrate/perchlorate/tetrafluoroborate ($RCONH_2 + LiBr / NO_3 / ClO_4 / BF_4$) mixtures, amide+sodium perchlorate/thiocyanate ($RCONH_2 + NaClO_4 / SCN$) mixtures, amide+potassium thiocyanate ($RCONH_2 + KSCN$) mixtures. On the other hand, amide+urea ($RCONH_2 + CO(NH_2)_2$) and amide+ethylene glycol ($RCONH_2 + C_2H_6O_2$) systems are representatives of non-ionic DESs. DESs have some advantages over traditional ILs in terms of ease of preparation/transportation, low production cost and, in some cases, relatively lower toxicity. Tuning of physico-chemical properties (for example, viscosity, polarity, surface tension etc.) by suitably choosing the mixture components and thereby tailoring the rate of a chemical reaction⁹⁹⁻¹⁰¹ provides further motivation to employ these molten mixtures as reaction media.

Here, we have considered acetamide (CH_3CONH_2) as the amide for the DESs studied because of its unique solvating power which arises due to the presence of several functional groups, high dipole moment ($3.7 D$) and large static dielectric constant ($\epsilon_0 \approx 60$)¹⁰² in molten state. Presence

of microheterogeneity in acetamide/electrolyte DESs have been investigated by viscoelastic,¹⁰³⁻¹⁰⁴ ultrasonic,¹⁰⁵⁻¹⁰⁶ nuclear magnetic resonance,¹⁰⁷ fluorescence anisotropy measurements^{52-53,56-60} and dielectric relaxation spectroscopy.^{105,108-109} However, the experimental tools used here have certain limitations to fully characterize the microscopic dynamics. For example, the dielectric relaxation set up, limited in the frequency range $0.2 \leq \nu/\text{GHz} \leq 50$ cannot detect the much slower timescale present in these systems.¹⁰⁹ Also, the experimentally obtained time scale is an average over all the species present in such a mixture. This prevents to assign one particular timescale to a specific type of interaction and thus unable to provide molecular insight. However, molecular simulations can track individual relaxation dynamics and thus separate out the contributing interactions. We have carried out extensive simulation studies with molten acetamide and acetamide/electrolyte DESs to understand the collective response measured in experiments in terms of microscopic mechanism. Several dynamical aspects, such as, orientational correlation functions, H-bond fluctuations, multi-point density relaxations, jump and waiting time distributions have been monitored, and spatial features including cluster size and lifetime distributions examined. All these observations then integrated to unravel the heterogeneity aspect of these exotic chemical systems.

In Chapter 2, we report results from our molecular dynamics simulations on orientational relaxation and H-bond dynamics of molten acetamide¹¹⁰. Signatures for orientational jumps have been detected with jump barrier estimated to be $\sim 0.7 k_B T$. Simulated orientational relaxations indicate deviations from hydrodynamics and this deviation has been ascribed to the detected orientational jumps. Simulated free energy surfaces obtained at various distances between the rotating acetamide and its initial and final H-bond acceptors have been found to be symmetric double-well in nature at the transition state. H-bond relaxation times obtained from our simulations corroborate well with the timescales associated with the jump and waiting time distributions, suggesting an interrelationship between jump dynamics and H-bond fluctuations. Jump angle distributions are asymmetric and depict long tails extending to large angles.

In Chapter 3, all-atom molecular dynamics simulations carried out to investigate orientation jumps of acetamide molecules in three different ionic deep eutectics made of acetamide (CH_3CONH_2) and lithium salts of bromide (Br^-), nitrate (NO_3^-) and perchlorate (ClO_4^-) at approximately 80:20 mole ratio and 303 K.¹¹¹ Orientational jumps have been dissected into acetamide-acetamide and acetamide-ion categories. Simulated jump characteristics have been found to register a considerable dependence on the anion identity. For example, large angle jumps are relatively less frequent in presence of NO_3^- than in presence of other two anions. Distribution of jump angles for rotation of acetamide molecules H-bonded to anions has been found to be bimodal in presence of Br^- , and is qualitatively different from the other two cases. Estimated energy barrier for orientation jumps of these acetamide molecules (H-bonded to anions) differ by a factor of ~ 2 between NO_3^- and ClO_4^- , the barrier height for the latter being lower and $\sim 0.5 k_B T$. Relative radial and angular displacements during jumps describe the sequence $ClO_4^- > NO_3^- > Br^-$ and follow a reverse viscosity trend. Jump barrier for acetamide-acetamide pairs reflects weak dependence on anion identity, and remains closer to the magnitude ($\sim 0.7 k_B T$) found for orientation jumps in molten acetamide. Jump time distributions exhibit a power law dependence of the type, $P(t_{\text{jump}}) \propto A(t_{\text{jump}}/\tau)^{-\beta}$, with both β and τ showing substantial anion dependence. The latter suggests presence of dynamic heterogeneity in these systems and supports earlier conclusions from time-resolved fluorescence measurements.⁵²⁻⁵³

In Chapter 4, we report a detailed simulation study on collective dipole moment relaxation, cooperative H-bond fluctuations and their connections to dielectric relaxation (DR) in deep eutectic solvents made of acetamide (CH_3CONH_2) and three uni-univalent electrolytes, lithium nitrate ($LiNO_3$), lithium bromide ($LiBr$) and lithium perchlorate ($LiClO_4$).¹¹² Because cooperative H-bond fluctuations and ion migration complicate the straightforward interpretation of the measured DR timescales in terms of molecular dipolar rotations for these solutions which are conducting and support extensive intra- and inter-species H-bonding, one needs to separate out the individual relaxation components that constitute the over-all relaxation and examine the microscopic origin of various timescales. Our study does so and finds that reorientation of

acetamide molecules that are interacting with the ions can generate relaxation timescales in the sub-nanosecond to nanosecond range. This explains in molecular terms the nanosecond timescales reported by recent giga-Hertz DR measurements. Interestingly, the simulated survival timescale for the acetamide- Li^+ complex has been found to be in a few tens of nanosecond, suggesting such a cation-complexed species may give rise to a similar timescale reported by mega-Hertz DR measurements for acetamide/potassium thiocyanate deep eutectics near room temperature.¹¹³ The issue of collective versus single particle relaxation is discussed and jump waiting time distributions determined. Dependence on anion-identity in each of the cases has been examined. In short, the present study demonstrates that assumption of formation of nano-sized domains is not required to explain the DR detected nanosecond and longer timescales in these media.

In Chapter 5, we have demonstrated simulation results performed with acetamide (CH_3CONH_2) and three electrolytes, lithium nitrate (LiNO_3), lithium bromide (LiBr) and lithium perchlorate (LiClO_4) at 303 K and 350 K to investigate the microstructures formed due to inter-species interactions. Extensive analyses have been carried out to understand the structural properties. First we have compared the structures of acetamide in presence and absence of the added electrolytes to investigate the effects of electrolyte. Next, we address the structural properties resulting from various ionic and H-bond interactions and their dependence on anion identity. Several radial distribution functions have been analyzed and spatial arrangements visualized in order to gain knowledge about the local structures. The results reveal that amide-amide H-bond interaction decreases significantly on addition of electrolytes. Also, the interaction of Li^+ with anions and acetamide creates heterogeneous environments in the solution mixture which agrees qualitatively with the existing time-resolved fluorescence measurements.⁵²⁻⁵³ Further, we have calculated the cluster size and lifetime distributions in order to understand the size of local microstructures and their stability. Both the distributions have been separated into individual contributions arising from (a) $\text{CH}_3\text{CONH}_2 - \text{CH}_3\text{CONH}_2$, (b) $\text{Li}^+ - \text{CH}_3\text{CONH}_2$ and (c) $\text{Li}^+ - \text{X}^- (\text{Br}^-, \text{NO}_3^-, \text{ClO}_4^-)$ interactions separately. Both size and lifetime distributions display heterogeneous dynamics and also show pronounced anion dependence.

In Chapter 6, we report an extensive and systematic analysis of various two point and four-point correlation functions to reveal dynamic heterogeneity (DH) of acetamide/electrolyte deep eutectic solvents. All-atom molecular dynamic simulations have been performed with acetamide (CH_3CONH_2) and lithium (Li^+) salts of bromide (Br^-), perchlorate (ClO_4^-) and nitrate (NO_3^-) at 303 K and 350 K. Our main aim here is to quantify the length scale and time scale associated with DH and to analyze its ion and temperature dependence. Mean square displacement plots show evidence of “caging” of acetamide, a typical signature of DH. DH timescales have been obtained from non-Gaussian parameter ($\alpha_2(t)$), new non-Gaussian parameter ($\gamma(t)$), four-point dynamic susceptibility ($\chi_4(k,t)$) and overlap function ($Q(t)$). Note, the timescale obtained from the new non-Gaussian parameters remarkably differ from the corresponding non-Gaussian parameters depending on the ion identity. Simulated self-part of the van Hove Correlation ($G_s(r,t)$) also deviates from Gaussian distribution showing substantial presence of DH. Single particle displacement distribution function ($P(\log_{10}(\delta r);t)$) exhibit pronounced deviation from Gaussian peak height even at 350 K. However, it does not show any bimodality in the timescale of structural relaxation. The average jump length detected for acetamide corresponds to ~ 2 times of its diameter. Finally, we quantify the dynamic correlation length ($\xi(t)$) from fitting of four point correlation function ($S_4(k,t)$) which spans ~ 2 times of acetamide diameter. Interestingly it does not show any ion and temperature dependence.

In Chapter 7, we have studied the reorientational dynamics of 1-butyl-3-methylimidazolium hexafluorophosphate ($BMIM + PF_6$) IL. Non-diffusive reorientation motion via large amplitude angular jump appears to be a generic feature for all H-bonded liquids. Though there are some experimental evidences of the presence of large amplitude angular jumps for ionic liquids,¹¹⁴ there are hardly any detailed study available. The present study attempts to investigate reorientational dynamics of ($BMIM + PF_6$) IL employing all-atom molecular dynamics simulations. Simulated orientational correlation functions of different ranks of both the ions suggest the presence of non-diffusive motions. Both the cation and anion are found to undergo large amplitude angular jumps. However, jumps are less frequent for the cation than for the

anion. The translational displacement during microscopic jump is found to be similar for both the ions depending on atom type identity while the rotational displacement is greater for the anion by more than a factor of two. Jump and waiting time distributions follow power law dependence for both the ions suggesting the presence of dynamic heterogeneity. Mean jump time calculated for the anion is found to be higher than the mean waiting time; this is opposite to the general trend observed for various systems already studied. Jump angle distributions for the cation are found to be narrower than those of the anion. Simulated H-bond correlation functions obtained from our simulations matched well with the various timescales associated with microscopic jumps.

Chapter 8 ends the Thesis with a brief concluding remark and present some relevant future problems. These representative problems are only showing a small glimpse of the vast research that involves DESs and ILs.

References:

1. M. D. Ediger, *Annu. Rev. Phys. Chem.* **51**, 99 (2000).
2. M. D. Ediger, C. A. Angell, and S. R. Nagel, *J. Phys. Chem. B* **100**, 13200 (1996).
3. R. Richert, *J. Non-Cryst. Solids* **172-174**, 209 (1994).
4. J. Jackle, *Rep. Prog. Phys.* **49**, 171 (1999).
5. K. L. Ngai, *J. Non-Cryst. Solids* **275**, 7 (2000).
6. C. A. Angell, K. L. Ngai, G. B. McKenna, P. F. McMillan, and S. W. Martin, *J. Appl. Phys.* **88**, 3113 (2000).
7. P. G. Debenedetti and F. H. Stillinger, *Nature* **410**, 259 (2001).
8. M. D. Ediger and P. Harrowell, *J. Chem. Phys.* **137**, 080901 (2012).
9. H. J. Sillescu, *J. Non-Cryst. Solids* **243**, 81 (1999).
10. D. Chakrabarti and B. Bagchi, *Phys. Rev. Lett.* **96**, 187801 (2006).
11. S. Karmakar, C. Dasgupta, and S. Sastry, *Annu. Rev. Condens. Matter Phys.* **5**, 255 (2014).
12. C. A. Angell, *J. Phys. Chem. Solids* **49**, 863 (1988).
13. K. Schmidt-Rohr and H. W. Spiess, *Phys. Rev. Lett.* **66**, 3020 (1991).
14. A. Heuer, M. Wilhelm, H. Zimmermann, and H. W. Spiess, *Phys. Rev. Lett.* **75**, 2851 (1995).
15. U. Tracht, M. Wilhelm, A. Heuer, H. Feng, K. Schmidt-Rohr, and H. W. Spiess, *Phys. Rev. Lett.* **81**, 2727 (1998).
16. E. Vidal Russel and N. E. Israeloff, *Nature* **408**, 695 (2000).
17. G. Szamel and E. Flenner, *Europhys. Lett.* **67**, 779 (2004).

18. R. Richert, *J. Phys.: Condens. Matter* **14**, R703 (2002).
19. L. Berthier and G. Biroli, *Rev. Mod. Phys.* **83**, 587 (2011).
20. S. Karmakar, C. Dasgupta, and S. Sastry, *Rep. Prog. Phys.* **79**, 016601 (2016).
21. G. Hinze, *Phys. Rev. E* **57**, 2010 (1998).
22. R. Bohmer, G. Hinze, G. Diezemann, B. Geil, and H. Sillescu, *Europhys. Lett.* **36**, 55 (1996).
23. S. C. Kuebler, A. Heuer, and H. G. Spiess, *Phys. Rev. E* **56**, 741 (1997).
24. D. K. Sasmal, A. K. Mandal, T. Mondal, and K. Bhattacharyya, *J. Phys. Chem. B* **115**, 7781 (2011).
25. S. Patra and A. Samanta, *J. Phys. Chem. B* **116**, 12275 (2012).
26. A. H. Marcus, J. Schofield, and S. A. Rice, *Phys. Rev. E* **60**, 5725 (1999).
27. W. K. Kegel and A. van Blaaderen, *Science* **287**, 290 (2000).
28. Q. H. Wei, C. Bechinger, and P. Leiderer, *Science* **287**, 625 (2000).
29. H. E. Fisher, A. C. Barnes, and P. S. Salmon, *Rep. Prog. Phys.* **69**, 233 (2006).
30. H. Conrad, F. Lehmkuhler, B. Fischer, F. Westermeier, M. A. Schroer, Y. Chushkin, C. Gutt, M. Sprung, and G. Grubel, *Phys. Rev. E* **91**, 042309 (2015).
31. W. Gotze and L. Sjogren, *Rep. Prog. Phys.* **55**, 241 (1992).
32. S. Benkhof, A. Kudlik, T. Blochowicz, and E. Rossler, *J. Phys.: Condens. Matter* **10**, 8155 (1998).
33. W. Kob and H. C. Andersen, *Phys. Rev. E* **51**, 4626 (1995).
34. W. Kob and H. C. Andersen, *Phys. Rev. E* **52**, 4134 (1995).
35. W. Kob and H. C. Andersen, *Phys. Rev. Lett.* **73**, 1376 (1994).

36. G. Wahnstrom, *Phys. Rev. A* **44**, 3752 (1991).
37. R. D. Mountain, *Supercooled Liquids: ACS Symposium Series*, **676**, 122 (1997).
38. W. Kob, C. Donati, S. J. Plimpton, P. H. Poole, and S. C. Glotzer, *Phys. Rev. Lett.* **79**, 2827 (1997).
39. C. Donati, J. F. Douglas, W. Kob, S. J. Plimpton, P. H. Poole, and S. C. Glotzer, *Phys. Rev. Lett.* **80**, 2338 (1998).
40. C. Donati, S. C. Glotzer, P. H. Poole, and W. Kob, *Phys. Rev. E* **60**, 3107 (1999).
41. S. C. Glotzer and C. Donati, *J. Phys.: Condens. Matter* **11**, A285 (1999).
42. C. Donati, S. C. Glotzer, and P. H. Poole, *Phys. Rev. Lett.* **82**, 5064 (1999).
43. S. C. Glotzer, V. N. Novikov, and T. B. Schroder, *J. Chem. Phys.* **112**, 509 (2000).
44. B. Bernu, Y. Hiwatari, and J. P. Hansen, *J. Phys. C: Solid State Phys.* **18**, L371 (1985).
45. B. Bernu, J. P. Hansen, Y. Hiwatari, and G. Pastore, *Phys. Rev. A* **36**, 4891 (1987).
46. D. Coslovich and G. Pastore, *J. Phys.: Condens. Matter* **21**, 285107 (2009).
47. S. C. Glotzer, *J. Non-Cryst. Solids* **274**, 342 (2000).
48. N. Lacevic, F. W. Starr, T. B. Schroder, and S. C. Glotzer, *J. Chem. Phys.* **119**, 7372 (2003).
49. N. Lacevic, F. W. Starr, T. B. Schröder, V. N. Novikov, and S. C. Glotzer, *Relat. Interdiscip. Top.* **66**, 030101(R) (2002).
50. K. Kim and S. Saito, *J. Chem. Phys.* **138**, 12A506 (2013).
51. K. Kim and S. Saito, *J. Chem. Phys.* **133**, 044511 (2010).
52. B. Guchhait, S. Daschakraborty, and R. Biswas, *J. Chem. Phys.* **136**, 174503 (2012).
53. B. Guchhait, S. Das, S. Daschakraborty, and R. Biswas, *J. Chem. Phys.* **140**, 104514 (2014).

54. S. N. Tripathy, Z. Wojnarowska, J. Knapik, H. Shirota, and R. Biswas, *J. Chem. Phys.* **142**, 184504 (2015).
55. R. Biswas, A. Das, and H. Shirota, *J. Chem. Phys.* **141**, 134506 (2015).
56. B. Guchhait, H. A. R. Gazi, H. Kashyap, and R. Biswas, *J. Phys. Chem. B* **114**, 5066 (2010).
57. A. Das, S. Das, and R. Biswas, *Chem. Phys. Lett.* **581**, 47 (2013).
58. A. Das, S. Das and R. Biswas, *J. Chem. Phys.* **142**, 034505 (2015).
59. H. A. R. Gazi, B. Guchhait, S. Daschakraborty, and R. Biswas, *Chem. Phys. Lett.* **501**, 358 (2011).
60. A. Das and R. Biswas, *J. Phys. Chem. B* **119**, 10102 (2015).
61. A. Samanta, *J. Phys. Chem. B* **110**, 13704 (2006).
62. A. Samanta, *J. Phys. Chem. Lett.* **1**, 1557 (2010).
63. J. A. Ingram, R. S. Moog, N. Ito, and R. Biswas, *J. Phys. Chem. B* **107**, 5926 (2003).
64. S. Arzhantsev, H. Jin, and G. A. Baker, *J. Phys. Chem. B* **111**, 4978 (2007).
65. X. X. Zhang, M. Liang, and N. P. Ernsting, *J. Phys. Chem. B* **117**, 4291 (2013).
66. A. Stoppa, J. Hunger, R. Buchner, G. Hefter, A. Thoman, and H. Helm, *J. Phys. Chem. B* **112**, 4854 (2008).
67. J. Hunger, A. Stoppa, S. Schrödle, G. Hefter, and R. Buchner, *Chem. Phys. Chem.* **10**, 723 (2009).
68. S. Daschakraborty and R. Biswas, *J. Chem. Phys.* **140**, 014504 (2014).
69. S. Daschakraborty, T. Pal, and R. Biswas, *J. Chem. Phys.* **139**, 164503 (2013).
70. S. Daschakraborty and R. Biswas, *J. Chem. Phys.* **137**, 114501 (2012).
71. H. K. Kashyap and R. Biswas, *J. Phys. Chem. B* **112**, 12431 (2008).

72. H. K. Kashyap and R. Biswas, *J. Phys. Chem. B* **114**, 254 (2010).
73. S. Daschakraborty and R. Biswas, *Chem. Phys. Lett.* **510**, 202 (2011).
74. S. Daschakraborty and R. Biswas, *Chem. Phys. Lett.* **545**, 54 (2012).
75. H. K. Kashyap and R. Biswas, *J. Phys. Chem. B* **114**, 16811 (2010).
76. H. K. Kashyap and R. Biswas, *Indian J. Chem.* **49A**, 685 (2010).
77. X. X. Zhang, M. Liang, J. Hunger, R. Buchner, and M. Maroncelli, *J. Phys. Chem. B* **117**, 15356 (2013).
78. M. Liang, X. X. Zhang, A. Kaintz, and N. P. Ernsting, *J. Phys. Chem. B* **118**, 1340 (2014).
79. A. Stoppa, J. Hunger, G. Hefter, and R. Buchner, *J. Phys. Chem. B* **116**, 7509 (2012).
80. D. Chakrabarty, A. Chakraborty, D. Seth, and N. Sarkar, *J. Phys. Chem. A* **109**, 1764 (2005).
81. S. Daschakraborty and R. Biswas, *J. Phys. Chem. B* **115**, 4011 (2011).
82. S. Daschakraborty and R. Biswas, *J. Phys. Chem. B* **118**, 1327 (2014).
83. T. Pal and R. Biswas, *J. Chem. Phys.* **141**, 164502 (2014).
84. T. Pal and R. Biswas, *J. Phys. Chem. B* **119**, 15683 (2015).
85. D. V. Wagle, H. Zhao, and G. A. Baker, *Acc. Chem. Res.* **47**, 2299 (2014).
86. Q. Zhang, K. De Oliveira Vigier, S. Royer, and F. Jerome, *Chem. Soc. Rev.* **41**, 7108 (2012).
87. A. P. Abbott, G. Capper, D. L. Davies, R. K. Rasheed, and V. Tambyrajah, *Chem. Commun.* 70 (2003).
88. A. P. Abbott, D. Boothby, G. Capper, D. L. Davies, and R. K. Rasheed, *J. Am. Chem. Soc.* **126**, 9142 (2004).

89. M. Francisco, A. van den Bruinhorst, and M. C. Kroon, *Angew. Chem., Int. Ed.* **52**, 3074 (2013).
90. M. Francisco, A. van den Bruinhorst, and M. C. Kroon, *Green Chem.* **14**, 2153 (2012).
91. H. Zhao and G. A. Baker, *J. Chem. Technol. Biotechnol.* **88**, 3 (2013).
92. D. Carriazo, M. C. Serrano, M. C. Gutierrez, M. L. Ferrer, and F. del Monte, *Chem. Soc. Rev.* **41**, 4996 (2012).
93. R. D. Rogers and K. R. Seddon, *Science*, **302**, 792 (2003).
94. S. Zhu, Y. Wu, Q. Chen, Z. Yu, C. Wang, S. Jin, Y. Ding, and G. Wu, *Green Chem.* **8**, 325 (2006).
95. K. N. Marsh, J. A. Boxall, and R. Lichtenthaler, *Fluid Phase Equilibria* **219**, 93 (2004).
96. O. A. El Seoud, A. Koschella, L. C. Fidale, S. Dorn, and T. Heinze, *Biomacromolecules*, **8**, 2629 (2007).
97. A. S. Amarasekara, *Chem. Rev.* **116**, 6133 (2016).
98. J. F. Wishart, *Energy Environ. Sci.* **2**, 956 (2009).
99. G. van der Zwan and J. T. Hynes, *Chem. Phys.* **152**, 169 (1991).
100. G. van der Zwan and J. T. Hynes, *J. Chem. Phys.* **78**, 4174 (1983).
101. T. Pradhan and R. Biswas, *J. Phys. Chem. A* **111**, 11524 (2007).
102. R. A. Wallace, *Inorg. Chem.* **11**, 414 (1972).
103. G. Berchiesi, G. Vitali, P. Passamonti, and R. Plowiec, *J. Chem. Soc. Faraday Trans. 2* **79**, 1257 (1983).
104. G. Berchiesi, G. Vitali, R. Plowisc, and S. Barocci, *J. Chem. Soc. Faraday Trans. 2* **85**, 635 (1989).
105. G. Berchiesi, M. D. Angelis, G. Rafaiani, and G. Vitali, *J. Mol. Liq.* **51**, 11 (1992).

106. G. Berchiesi, F. Farhat, and M. D. Angelis, *J. Mol. Liq.* **54**, 103 (1992).
107. G. Berchiesi, G. Rifaiani, G. Vitali, and F. Farhat, *J. Therm. Anal.* **44**, 1313 (1995).
108. A. Amico, G. Berchiesi, C. Cametti, and A. D. Biasio, *J. Chem. Soc. Faraday Trans. 2* **83**, 619 (1987).
109. K. Mukherjee, A. Das, S. Choudhury, A. Barman, and R. Biswas, *J. Phys. Chem. B* **119**, 8063 (2015).
110. S. Das, R. Biswas, and B. Mukherjee, *J. Phys. Chem. B* **119**, 274 (2015).
111. S. Das, R. Biswas, and B. Mukherjee, *J. Phys. Chem. B* **119**, 11157 (2015).
112. S. Das, R. Biswas, and B. Mukherjee, *J. Chem. Phys.* (under review).
113. A. Amico, G. Berchiesi, C. Cametti, and A. Di Biasio, *J. Chem. Soc., Faraday Trans. 2* **83**, 619 (1987).
114. J. Hunger, T. Sonnleitner, L. Liu, R. Buchner, M. Bonn, and H. J. Bakker, *J. Phys. Chem. Lett.* **3**, 3034 (2012).

Chapter 2

Reorientational Jump Dynamics and Its Connections to Hydrogen Bond Relaxation in Molten Acetamide: An All-Atom Molecular Dynamics Simulation Study

2.1. Introduction

The presence of a peptide bond (-OC-NH-) and its occurrence as a repeat unit in polypeptides and proteins have rendered biological relevance to acetamide (CH_3CONH_2).^{1,2} In addition, the ability of CH_3CONH_2 to participate in hydrogen bonding (H-bonding) has made this molecule as an excellent model system for studying the role of H-bonding interactions in determining the three dimensional structures of proteins and nucleic acids.³⁻⁵ The presence of methyl, carbonyl, tautomeric hydroxyl, and amide groups in the same molecule has made acetamide an excellent solvent for a very large number of organic and inorganic substances.^{6,7} Interestingly, the high static dielectric constant ($\epsilon_0 \sim 60$) of molten acetamide (melting temperature ~ 350 K, and viscosity ~ 2.2 cP) coupled with its large dipole moment (3.7 D) have made acetamide an even better solvent than water for many ionic compounds.⁶⁻¹⁰ As a result, interaction and dynamics in acetamide and other simpler amides have been the subject of a large number of studies.¹¹⁻¹⁸ Of late, deep eutectic solvent (DES) systems containing acetamide have been studied using fast spectroscopic techniques and computer simulations in order to explore the interrelationship between solution structure and dynamics of these room temperature molten mixtures.¹⁹⁻²⁵ The utility of these DES systems as cheap replacements for ionic liquids as reaction media in chemical industries,^{26,27} and the application aspect of controlling reactions via understanding the relationship between dynamic solvent response and reaction rate^{28,29} in such media have further motivated research in this direction. Although the above combined spectroscopic and simulation studies have revealed some structural and dynamical aspects of acetamide in presence of electrolytes,

similar investigation for neat liquid acetamide is still unavailable and thus warrants an in-depth study.

Here, we have performed all-atom molecular dynamics simulations to study the orientational relaxation of neat liquid acetamide at 368 K and investigate whether orientational jumps, like in the case of liquid water,³⁰⁻³⁵ contribute substantially to the collective orientational relaxation. The interconnection between H-bond dynamics³⁶⁻⁴² of molten acetamide at this temperature and orientation jumps have been explored. In addition, the coupling between translation and rotation in neat liquid acetamide has been investigated. Both the simulated acetamide backbone and N-H vector orientational relaxations suggest presence of non-hydrodynamic reorientation mechanism. The presence of orientational jumps is revealed when the cosine of the angle made by the acetamide backbone with the Z-axis of the simulation box is followed over time. A broad distribution for the jump angle has been found along with a significant centre-of-mass displacement (~25-50% of acetamide diameter) during a jump of as large as 90°. Simulated waiting time (between two successive jumps) and jump time distributions have been found to be exponential at long time with the mean waiting time ~2.5 times longer than the mean jump time. As expected, the continuous H-bond lifetime has been found to be shorter than the jump time. The free energy barrier associated with orientation jumps has been found to be $\sim 0.7 k_B T$ which is approximately one-fourth of that reported^{30,31} for neat liquid water. The essential feature of this reorientation mechanism is the coupling between the orientation and the concerted centre-of-mass motion of the triad of molecules participating in the microscopic orientational jump. This feature is also shared by liquid water,^{30,31} making this translation-rotation coupling a universal feature of all H-bonded liquids.

2.2. Simulation Details

All-atom molecular dynamics simulations were performed using 256 CH₃CONH₂ molecules at 368 K (CH₃CONH₂ melts at ~ 350 K)⁴³ with DL_POLY version 2.20,⁴⁴ where the molecules interacted via the following potential function:⁴⁵

$$\begin{aligned}
U(\mathbf{R}) = & \sum_{\text{bonds}} K_r (r - r_{eq})^2 + \sum_{\text{angles}} K_\theta (\theta - \theta_{eq})^2 + \sum_{\text{dihedrals}} K_\phi [1 + \cos(n\phi - \delta)] + \sum_{i < j}^{\text{atoms}} \left(\frac{A_{ij}}{R_{ij}^{12}} - \frac{B_{ij}}{R_{ij}^6} \right) \\
& + \sum_{i < j}^{\text{atoms}} \frac{q_i q_j}{4\pi\epsilon_0 R_{ij}}. \tag{2.1}
\end{aligned}$$

In Equation 2.1, K_r is the bond constant with the equilibrium bond distance r_{eq} , K_θ is the angle constant with the equilibrium angle θ_{eq} , K_ϕ is the dihedral constant with periodicity n , dihedral angle ϕ and phase shift δ . R_{ij} is the distance between atoms i and j with partial charges q_i and q_j , respectively. The interaction parameters for the acetamide molecule were taken from the CHARMM⁴⁶ force field and summarized in Appendix A. The force field was constructed using DL_FIELD.⁴⁷ Such a construction was found earlier to generate a reasonable description of acetamide dynamics in molten mixtures.^{21,22} The short-range van der Waals interaction was represented by the Lennard-Jones (LJ) potential, and the long-range electrostatic potential was treated via Ewald summation technique⁴⁸ using an Ewald parameter of $\alpha = 0.2 \text{ \AA}^{-1}$ and a 6x6x6 k-point grid.

The initial configuration was built using Packmol⁴⁹ and equilibrated in NPT ensemble at 1 atm. pressure for 500 ps. Fidelity of the simulations was then checked by reproducing the experimental density (1.16 gm/cc)⁵⁰ at 353 K. Nose-Hoover thermostat⁵¹ and barostat⁵² were used to control the temperature and pressure with time constant of 0.5 and 1.0 ps, respectively. Subsequently, further equilibration of 1 ns followed by a production run of 5 ns was carried out in NVT ensemble. Periodic boundary conditions were employed in all three directions, and the equations of motion were integrated using a time step of 0.5 fs employing the velocity Verlet algorithm.⁴⁸ Snapshots were saved every 10 fs for data analyses and simulation results. Note that the simulations were carried out at 368 K in order to completely avoid complexities arising from being in close proximity to the melting temperature (~350 K).

2.3. Analysis Protocol

Figure 2.1 displays the time series of the cosine of the angle made by the backbone of a randomly chosen CH_3CONH_2 molecule (connecting the C (-CH₃) and N (-NH₂) atom) with

the Z axis of the simulation box. Clearly, the chosen CH_3CONH_2 molecule executes diffusive reorientation as well as angular jumps, with jump amplitude sometimes as large as 90° . Such features (diffusive reorientation punctuated by large amplitude angular jumps) are strongly reminiscent of the reorientation mechanism in liquid water.^{30,31,53} We have analysed microscopic trajectories generated from MD simulations for uncovering the details of the reorientation mechanism in molten acetamide.

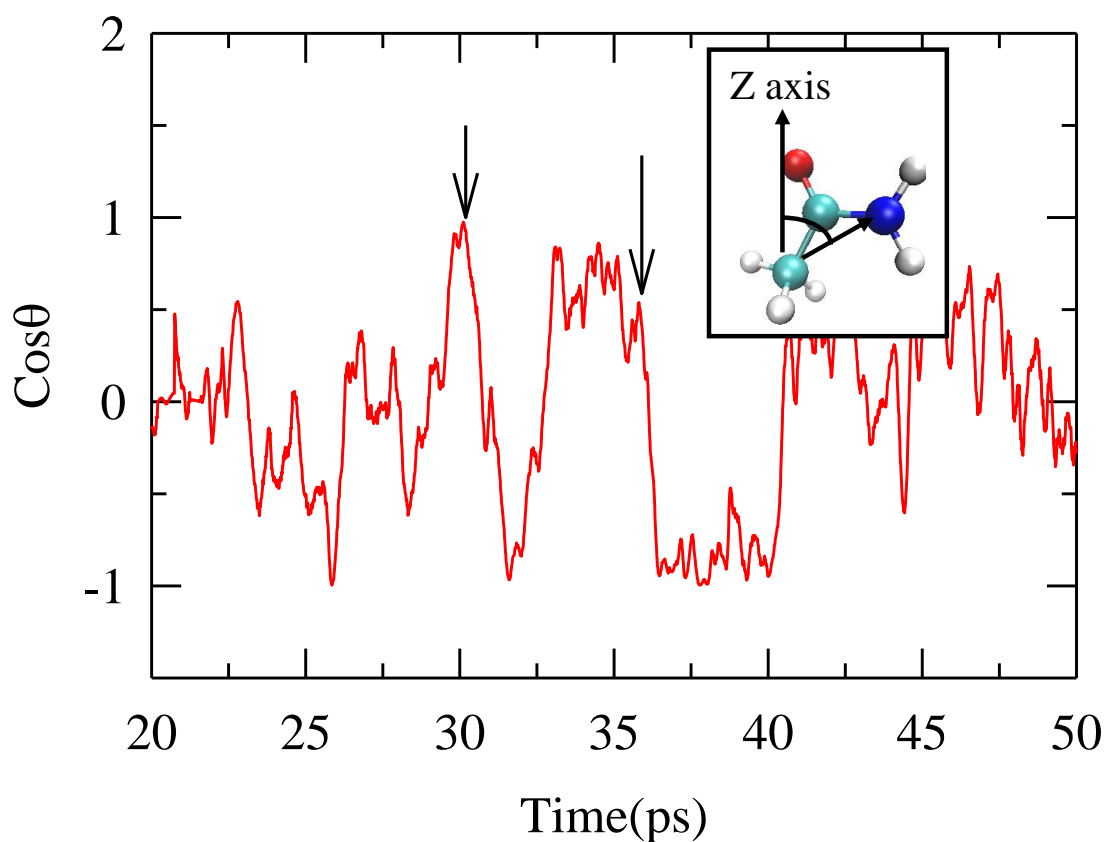


Figure 2.1: The plot shows the time series of the cosine of the angle which the backbone of a randomly chosen acetamide molecule makes with the Z axis of the simulation box. The reorientational dynamics exhibits diffusive reorientation as well as large amplitude orientational jumps (indicated by arrows).

A large amplitude angular jump involves a change in the hydrogen bond (H-bond) partners of the molecule in question. Pre-requisite for such identification is the knowledge of H-bond partners of a molecule in a given simulation snapshot. H-bonds can be defined in a number of ways based on geometric criteria, energy consideration or orbital occupancy.³² Here, we have chosen a widely accepted geometric definition based on a distance (R) and an angle ($^\circ$). Two CH_3CONH_2 molecules are considered to be H-bonded if the following criteria are satisfied: (i) distance between the oxygen and nitrogen atoms belonging to different CH_3CONH_2 molecules, R_{ON} , is less than a cut-off distance, $R_{\text{cut-off}}$ and (ii) angle between the vector joining nitrogen and amide hydrogen of one CH_3CONH_2 molecule, and the vector joining this nitrogen and an oxygen atom belonging to another acetamide molecule, θ_{ONH} , is less than 30° . $R_{\text{cut-off}}$ is taken as the distance at which appears the first minimum of the simulated radial distribution function ($g_{\text{ON}}(r)$) for the oxygen and the nitrogen atoms belonging to different CH_3CONH_2 molecules. In our simulations at 368 K, this has been found to be 4 \AA , as shown in Figure 2.2. Note the first peak of the simulated $g_{\text{ON}}(r)$ occurs at $\sim 3 \text{ \AA}$, which agrees well to the results from X-ray scattering measurements of CH_3CONH_2 .^{11,12} This agreement between simulations and experiments suggests validity of the interaction potential used.

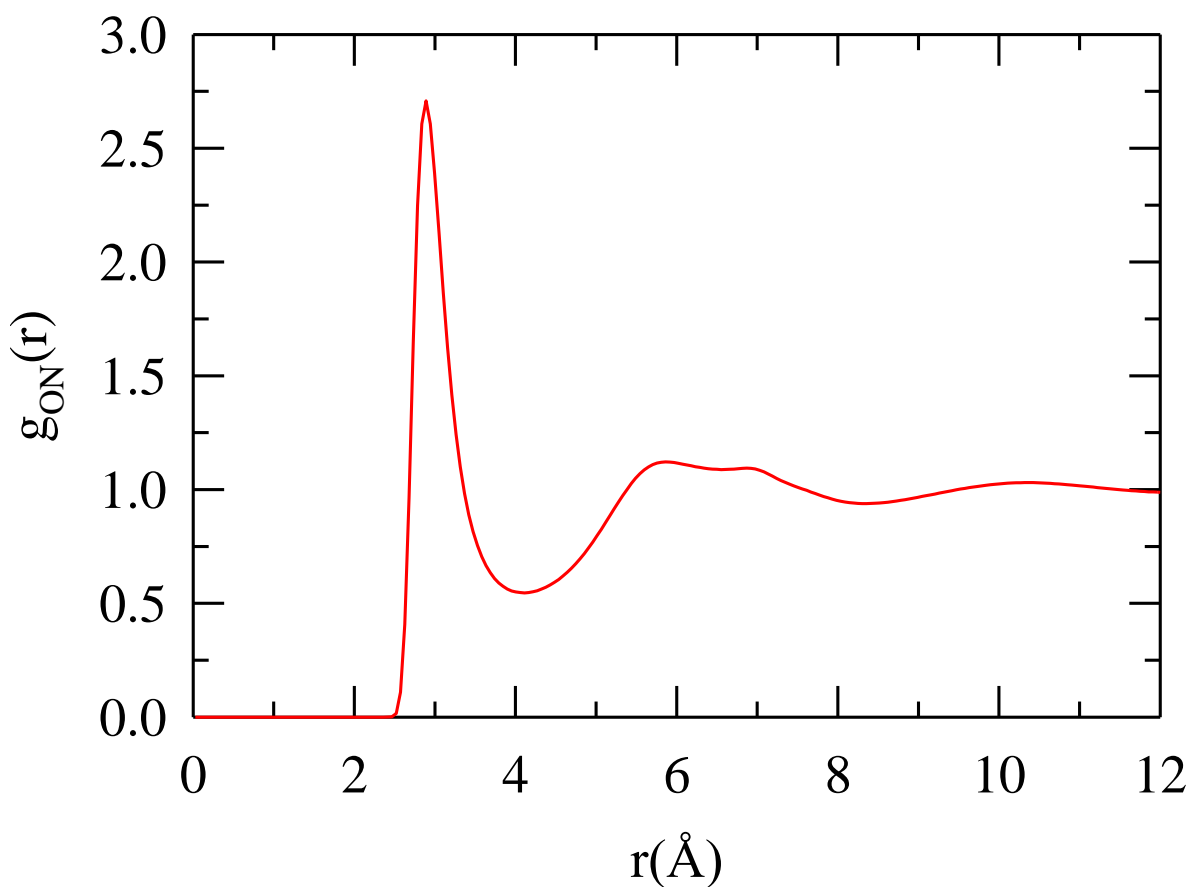


Figure 2.2: The radial distribution function, $g_{\text{ON}}(r)$, between the oxygen and the nitrogen atoms belonging to two different acetamide molecules. The cut-off distance (for the hydrogen bond definition) is taken at 4 Å, which corresponds to the first minima of the above $g_{\text{ON}}(r)$ and it measures the extent of the first solvation shell.

Since the criterion we have used for determining whether pairs of molecules are hydrogen bonded or not is somewhat arbitrary ($R_{\text{ON}} < 4 \text{ \AA}$ and $\theta_{\text{ONH}} < 30^\circ$), we decided to impose another H-bonding criterion for making our study robust. First, we search for pairs of molecules for which the distance between the nitrogen and oxygen, R_{ON} is less than 4 Å. Then we monitor the distance between the hydrogen atoms and oxygen atom for these pairs of molecules. The distribution, shown in Figure 2.3, is double peaked for the two hydrogen atoms of the chosen acetamide molecule signifying the most probable locations of them with respect to the oxygen atom of a neighbouring acetamide molecule. The probability

distribution for any of the two H-atoms which is at the nearest distance to the oxygen (of the neighbouring acetamide) is also shown in Figure 2.3. Considering these two distributions we have chosen a cut-off distance between O and H atoms of hydrogen bonded pairs of acetamide molecules as 2.5 Å. This cut-off distance of 2.5 Å correlates well with the hydrogen bond distance for N-H...O moiety estimated from X-ray and neutron diffraction measurements of a large number organic crystals possessing such an interaction.⁵⁴ With this added H-bonding criteria we have evaluated the waiting time distribution, which is sensitive to the definition of H-bond. Note this additional H-bond criterion has not altered the qualitative feature of the waiting time distribution (shown later) but induced a small change (~10-15%) in the numerical value of the mean waiting time. As a result, we stick to our first definition of H-bond for the rest of the calculations.

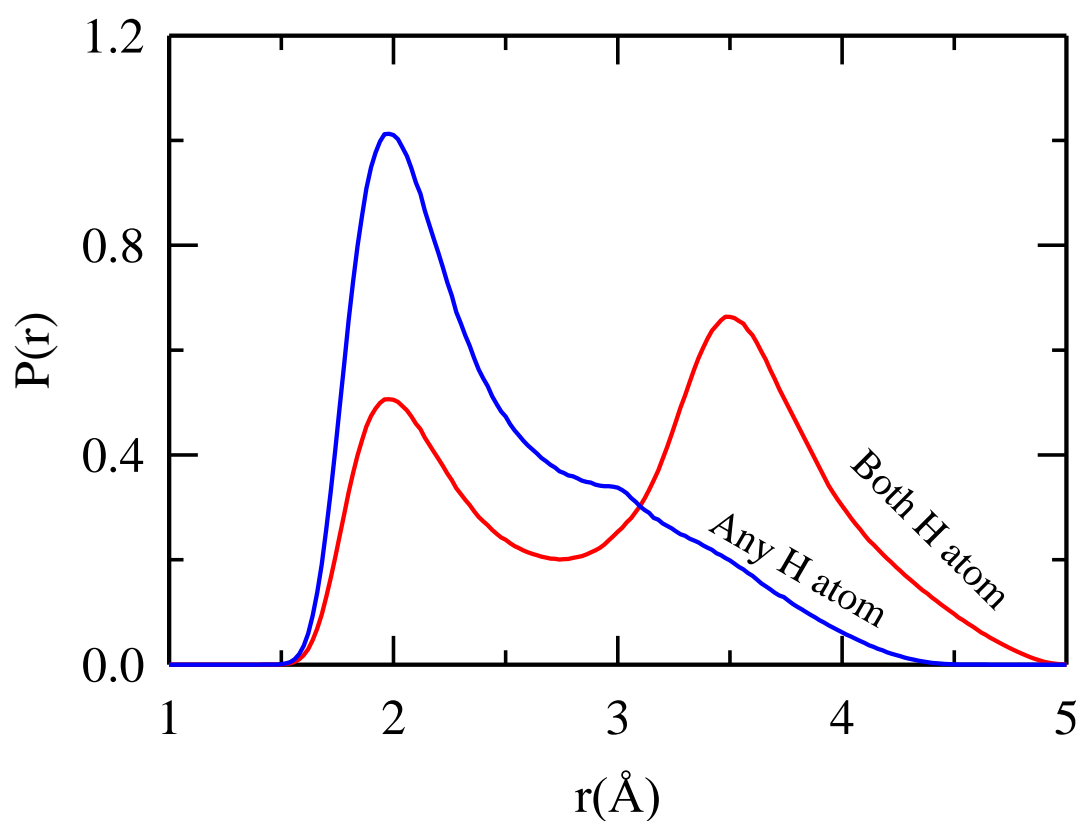


Figure 2.3: Distance distributions between hydrogen and oxygen atoms of a pair of nearby acetamide molecules. Modified hydrogen bond criteria is derived by choosing the cut-off distance between oxygen and hydrogen at 2.5 Å. Double peak (red curve) structure is

obtained when the locations of both the amide H-atoms (with respect to the oxygen atom of another participating acetamide molecule) are monitored. Monitoring of only the nearest H-atom leads to the blue curve possessing a peak and a shoulder.

Considering the first definition of H-bonding we have identified the H-bond switching events as follows. Two flags have been associated with each CH_3CONH_2 molecule, $\text{flag_H1}(i,t)$ and $\text{flag_H2}(i,t)$. Here ‘ i ’ denotes the index of the CH_3CONH_2 molecule and ‘ t ’ denotes the label for the simulation snapshot. The value of a flag of molecule ‘ i ’, if non-zero, denote the index of the acetamide molecule H-bonded to the i^{th} molecule. If its value is zero, it means that the particular hydrogen of molecule ‘ i ’ is not H-bonded to any other acetamide molecule. The two flags thus represent the H-bonding state of the two H atoms of the $-\text{NH}_2$ group since both H atoms are capable of forming H-bonds. Figure 2.4(a) shows a typical microscopic process extracted from our simulations, where the rotating molecule (in ball-and-stick representation) performs a large amplitude angular jump. It was initially H-bonded to molecule ‘A’, and it breaks this bond and rotates and forms a new H-bond with molecule ‘B’. Such a microscopic process can be translated to time-dependence of the flag variables. Figure 2.4(b) shows the same process in terms of the flag variables. The variable $\text{flag_H1}(i,t)$ initially has a non-zero value equal to ‘A’, which denotes that the rotating molecule ‘ i ’ is H-bonded to molecule ‘A’. Note that the H-bond between ‘ i ’ and ‘A’ can break temporarily and then reform, which is signified by the value of the flag jumping discontinuously from ‘A’ to zero and back to ‘A’. These are examples of temporal H-bond fluctuations and do not involve large amplitude angular jumps. The events that we are interested in identifying are the ones where the identity of the H-bonding partners changes resulting in a large orientational displacement. The ‘start’ time (t_{start} in Figure 2.4(b)) is the last instant when molecule ‘ i ’ was H-bonded to its initial partner ‘A’. Similarly, the end-time, t_{end} , is the first instant when molecule ‘ i ’ forms a H-bond with its final partner molecule ‘B’.

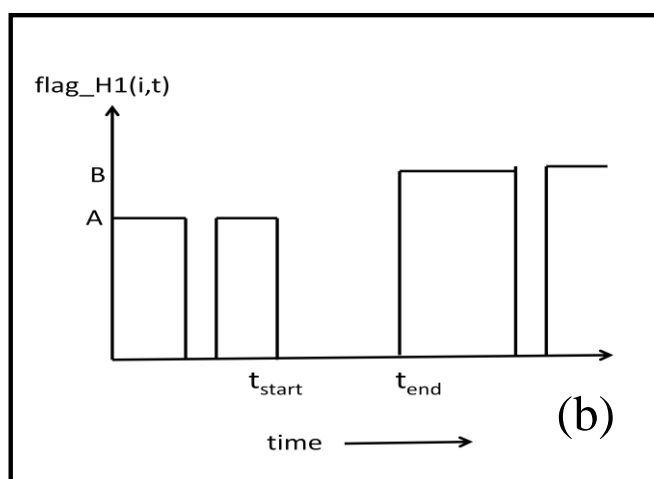
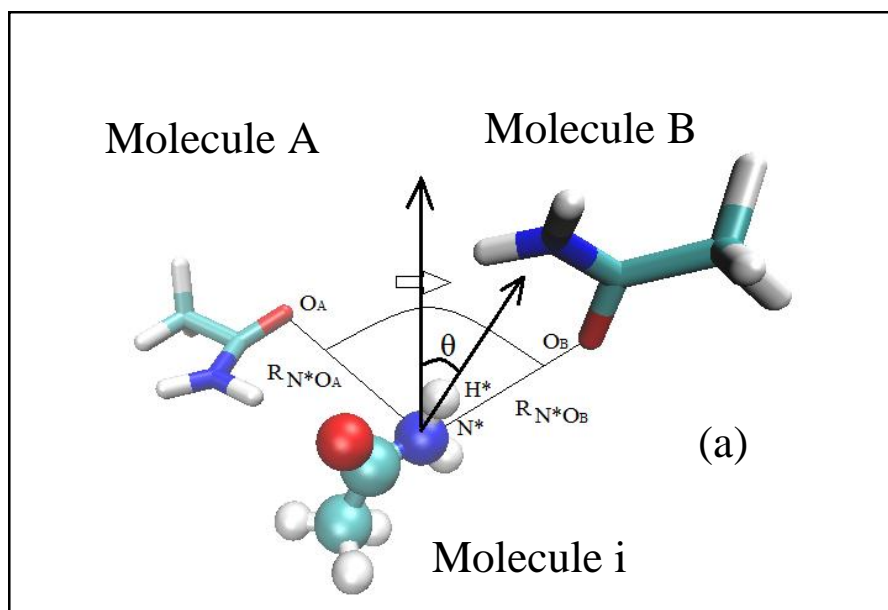


Figure 2.4: Top panel shows an intermediate configuration while an orientational jump occurs. The N^*H^* vector of the rotating molecule (shown in ball and stick representation) is initially bonded to oxygen atom O_A of molecule A. It breaks this hydrogen bond, simultaneously orients and then forms hydrogen bond to atom O_B of molecule B. Bottom panel shows how the above process can be represented by the change in the value of a flag variable. This flag variable has a value of A (the index of the molecule to which it is hydrogen bonded to) initially, later, it attains a value of B (new hydrogen bonding partner). The times at which the jump starts and ends are also identified.

Subsequently, we construct a time series of $flag_H1(i,t)$ and $flag_H2(i,t)$ for all molecules at all instants during the production run. From such time series we identify all t_{start} and t_{end} where the microscopic jumps start and end. The identification of these times allows us to

calculate the distributions of the waiting time between jumps and the distribution of the time required to complete the jumps. We then compare the timescales associated with these distributions with those obtained from the simulated H-bond time correlation functions. The knowledge of the start and end times also allows us to calculate the orientational displacement of the molecules during these times. The transition state of the orientational jump occurs when $R_{N^*O_A}$ equals $R_{N^*O_B}$ (see Figure 2.4(a) for these geometrical definitions). For each microscopic jump, we search between times t_{start} and t_{end} when $R_{N^*O_A}$ becomes equal to $R_{N^*O_B}$. For this we numerically estimate the minimum value of the modulus of $(R_{N^*O_A} - R_{N^*O_B})$. The value of the angle $O_A N^* O_B$ at the transition state is a good descriptor of the jump angle of the rotating $N^* - H^*$ vector. This choice may seem odd, but this is the only way one can remove the effects arising from the librational motion of the $N^* - H^*$ vector of the rotating acetamide molecule. Naively one may consider that the angular displacement can be estimated easily by calculating the angular displacement of the $N^* - H^*$ vector of the rotating acetamide molecule in the time interval between t_{start} and t_{end} . This is incorrect as this does not exclude the error arising from the librational motion of the rotating $N^* - H^*$ vector, which can be significant compared to the jump angle that one wants to determine. However, in the case of orientational displacement of the backbone, where the effects of libration are minimal, we have followed this simpler method.

For the calculation of the average trajectory, we choose jumps in the following way: a single molecule can perform several orientational jumps within the simulation time window. Once the transition times for all jumps of a particular molecule are known, we choose those jumps whose transition times differ by more than 340 fs, with the transition time at the centre of this time window (170 fs preceding and 170 fs following the transition time). This time interval (340 fs) has been decided by monitoring whether the distances and angles reach their corresponding saturation values at the beginning and end of the average trajectories. We ensure that within this 340 fs interval the particular molecule does not participate in any other hydrogen bond switching event apart from the chosen one. We do this for all the molecules in the system and finally a ‘coherent average’ is taken for all the relevant geometrical quantities defining the microscopic trajectory. During the ‘coherent averaging’, the transition state is chosen as the origin of time at the centre of the average trajectory with the jump starting at -

170 fs and ending at +170 fs. In this fashion where one coincides the transition times of all the microscopic trajectories considered ('coherent averaging'), one can extract generic features from microscopic trajectories, without the important features being swamped by the presence of inherent thermal fluctuations. The geometrical quantities for which the 'average' temporal dependence are calculated are: distances $R_{N^*O_A}$, $R_{N^*O_B}$ and the angle formed by the projection of the $N^* - H^*$ vector on the $O_A N^* O_B$ plane and the angle bisector of angle $O_A N^* O_B$ (see 2.4(a) for these geometrical definitions). These distances and angles describing the average trajectory have been obtained by coherent averaging over microscopic trajectories exhibiting H-bond jumps.

Finally, we have estimated the free energy barrier associated with an average reorientational trajectory. Following the method devised earlier for liquid water,^{30,31} we construct a three dimensional free energy profile, which depends on the difference of the H-bond coordination numbers of initial donor and final donor, Δn_{HB} , the difference in the distance between N^* (N atom belonging to the rotating CH_3CONH_2 molecule) and O_A (O atom belonging to the initial H-bond acceptor), and N^* and O_B (O atom belonging to the final H-bond acceptor), ΔR , and one angular coordinate θ (defined in Figure 2.4(a)). A probability distribution function (histogram), $P(\Delta n_{HB}, \Delta R, \theta)$ was first calculated based on these three coordinates. This calculation proceeds in the following way: Refer to Figure 2.5, which shows a typical jump event whose t_{start} and t_{end} have been identified by the above protocol. The nitrogen atom of the rotating CH_3CONH_2 molecule is denoted by N^* and $N^* - H^*$ vector is initially H-bonded to the oxygen atom O_A of the neighbouring molecule. During the jump, this H-bond breaks and the molecule rotates and $N^* - H^*$ forms a H-bond with atom O_B of another CH_3CONH_2 in the vicinity of the rotating neighbour. Suppose this is the j^{th} orientational jump of the chosen molecule and its t_{start} and t_{end} are denoted by $t_{start}(j)$ and $t_{end}(j)$. We calculate the contributions to the probability distribution function, $P(\Delta n_{HB}, \Delta R, \theta)$ only during three types of time intervals: (i) $t_{end}(j-1) < t < t_{start}(j)$, (ii) $t_{start}(j) < t < t_{end}(j)$, and (iii) $t_{end}(j) < t < t_{start}(j+1)$. During these intervals we calculate the value of the variables Δn_{HB} , ΔR , and θ from the microscopic MD trajectories and construct a histogram by binning them. The sizes of the bins used in this calculation are $\Delta R = 0.1 \text{ \AA}$, $\Delta n = 1$, and $\Delta \theta = 3^\circ$.

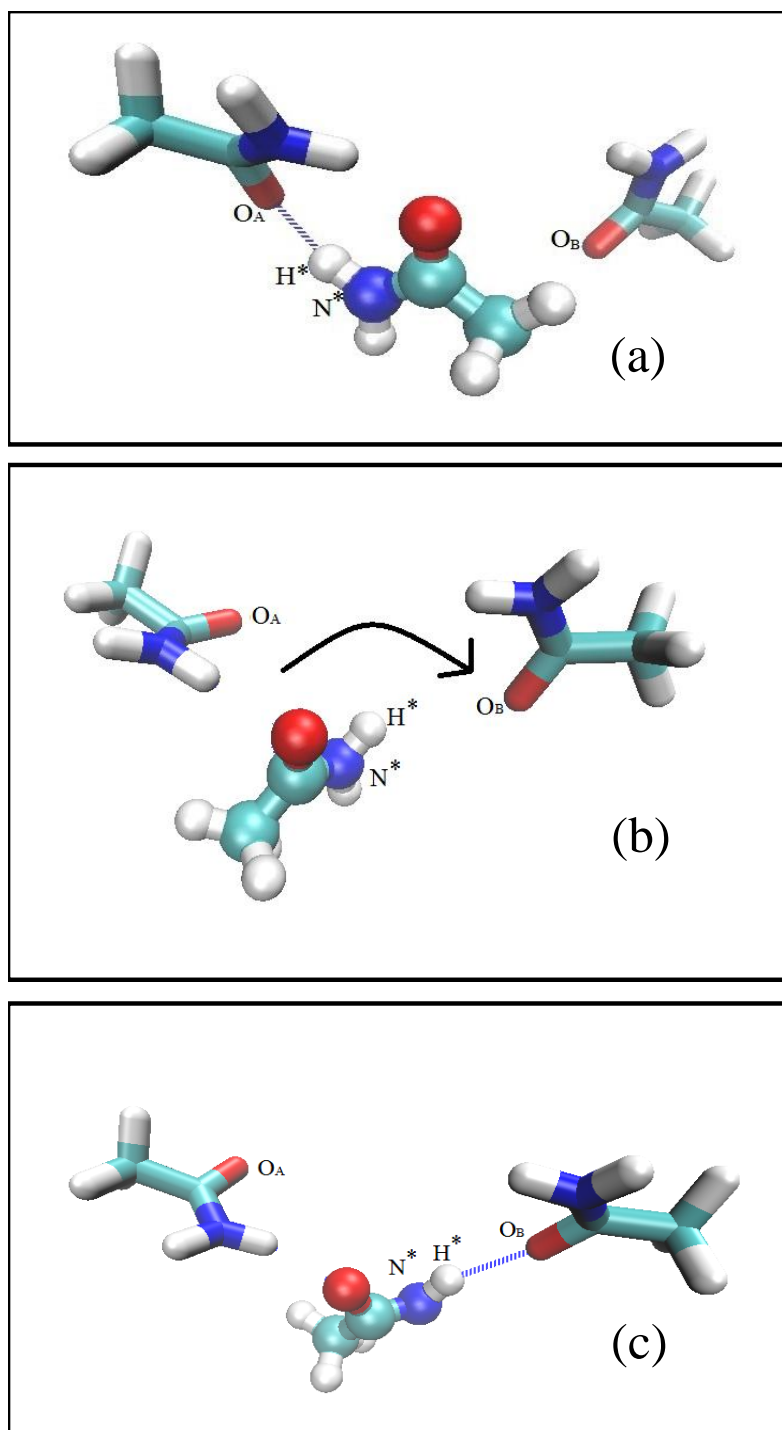


Figure 2.5: The orientational jump mechanism in liquid acetamide: the vector $N^* - H^*$ undergoes an orientational jump. Initially it is hydrogen bonded to oxygen O_A (panel (a)),

which belongs to acetamide A, it breaks the hydrogen bond (panel (b)) and finally forms a new hydrogen bond with oxygen O_B , belonging to acetamide B, (panel (c)).

Contributions arising from interval (i) contribute to the initial free energy minima (on the reactant side, these orientational jumps can also be viewed as a chemical reaction^{30, 31} even though in this case only migration of hydrogen bonds, rather than formation and breakage of covalent bonds, is involved). Contributions from interval (ii) contribute to the regions around the transition state of this reaction, and contributions from interval (iii) contribute to the final free energy minima (product side of the reaction). This procedure is then followed for all the molecules in the system to yield the probability distribution function, $P(\Delta n_{\text{HB}}, \Delta R, \theta)$. Finally the free energy $G(\Delta n_{\text{HB}}, \Delta R, \theta)$ is determined using the following expression,

$$G(\Delta n_{\text{HB}}, \Delta R, \theta) = -k_B T \ln[P(\Delta n_{\text{HB}}, \Delta R, \theta)]. \quad (2.2)$$

This calculation protocol ensures that the prediction of the free energy surface and its sections are symmetric with respect to the reactant and product states.

2.4. Results and Discussion

Figure 2.6 shows the time-evolution of $R_{N^*O_A}$ and $R_{N^*O_B}$ with time during an average H-bond switching event. The behaviour of the average trajectory shows that the molecule containing atom O_A moves from the first coordination shell to the second coordination shell, whereas, the molecule containing atom O_B moves in from the second coordination to the first. The coordination shells can be identified from the radial distribution function between the oxygen and nitrogen atoms belonging to different CH_3CONH_2 molecules (see Figure 2.2). As in the case of liquid water, the role played by the translational motion of amide O_A and O_B is very important, and the symmetric configuration when both $R_{N^*O_A}$ and $R_{N^*O_B}$ are equal is the transition state.^{30,31} The magnitude of translational displacement of the oxygen atoms of the initial and final H-bond acceptors during the ‘average’ orientational jump is $\sim 2 \text{ \AA}$. The bottom panel of Figure 2.6 shows that the average trajectory of the angle formed by the projection of the $N^* - H^*$ vector on the $O_A N^* O_B$ plane and the angle bisector of angle $O_A N^* O_B$. This average angle exhibits a sharp transition from an angle of -45° to $+45^\circ$,

signifying a jump of about 90° . This angle is zero at the transition state and is negative before the transition state and positive after it crosses the transition state.

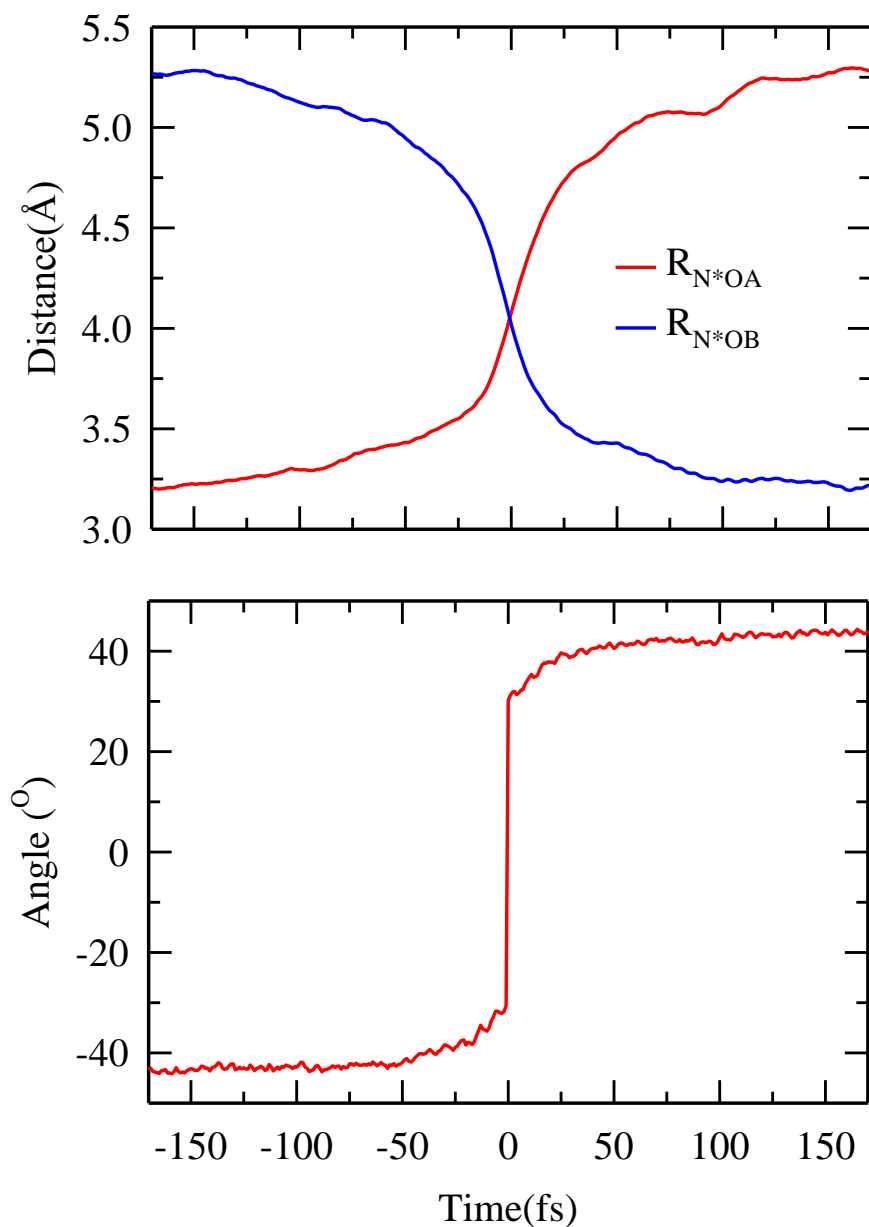


Figure 2.6: Top panel shows the time evolution of the distances R_{N^*OA} (red curve) and R_{N^*OB} (blue curve), calculated for the average jump trajectory. The oxygen of the initial acceptor, moves out from the first solvation shell to the second solvation shell, whereas, the final acceptor moves in from the second to the first shell. The solvation shells are evident

from the radial distribution function (see Figure 2.2) between the oxygen atom and the nitrogen atom belonging to two different acetamide molecules. The bottom panel shows how angle θ (defined in Figure 2.4(a)) varies in an average trajectory. It jumps from a value of -45° to $+45^\circ$, showing a jump of about 90° .

In order to estimate the effects these orientational jumps have on the centre-of-mass (COM) coordinates, we have recalculated the above average trajectories using the COM coordinates of the triad of molecules (the rotating molecule, the initial and the final H-bond acceptors). O_A , N^* and O_B have been replaced by the COM of the three chosen molecules. Figure 2.7 shows the average trajectory calculated using the centre of mass coordinates, the definition of the angle also changes similarly. The translational displacement associated with the average orientational jump is $\sim 0.8 \text{ \AA}$ in a time interval of 340 fs (the extent of the time axis in Figure 2.7). One can estimate the value of translational diffusion coefficient (D_T) of liquid acetamide from the Stokes-Einstein relation,⁵⁵ $D_T = k_B T / 4\pi\eta r$, $k_B T$ being the Boltzmann constant times the absolute temperature and r the radius of the diffusing molecule. Using a value of viscosity²³ ($\eta \sim 2 \text{ cP}$) and $r \sim 2 \text{ \AA}$, we find $D_T \sim 10 \times 10^{-5} \text{ \AA}^2/\text{fs}$. The diffusive displacement estimated from the relation,⁵⁵ $\Delta r^2 = 6D_T t$, turns out to be $\Delta r \sim 0.4 \text{ \AA}$ in 340 fs. In reality (in presence of orientational jumps) the magnitude of COM translational displacement is $\sim 0.8 \text{ \AA}$ (see the upper panel of Figure 2.7) which is nearly double the value of Δr . This COM displacement and the translational displacement of the oxygen atom displayed in Figure 2.6 ($\sim 2 \text{ \AA}$) jointly suggest that the translational motion of the nitrogen and oxygen atoms is significantly influenced by the orientational jumps. This shows the natural coupling which is always present between translational and orientational modes in such complex systems.

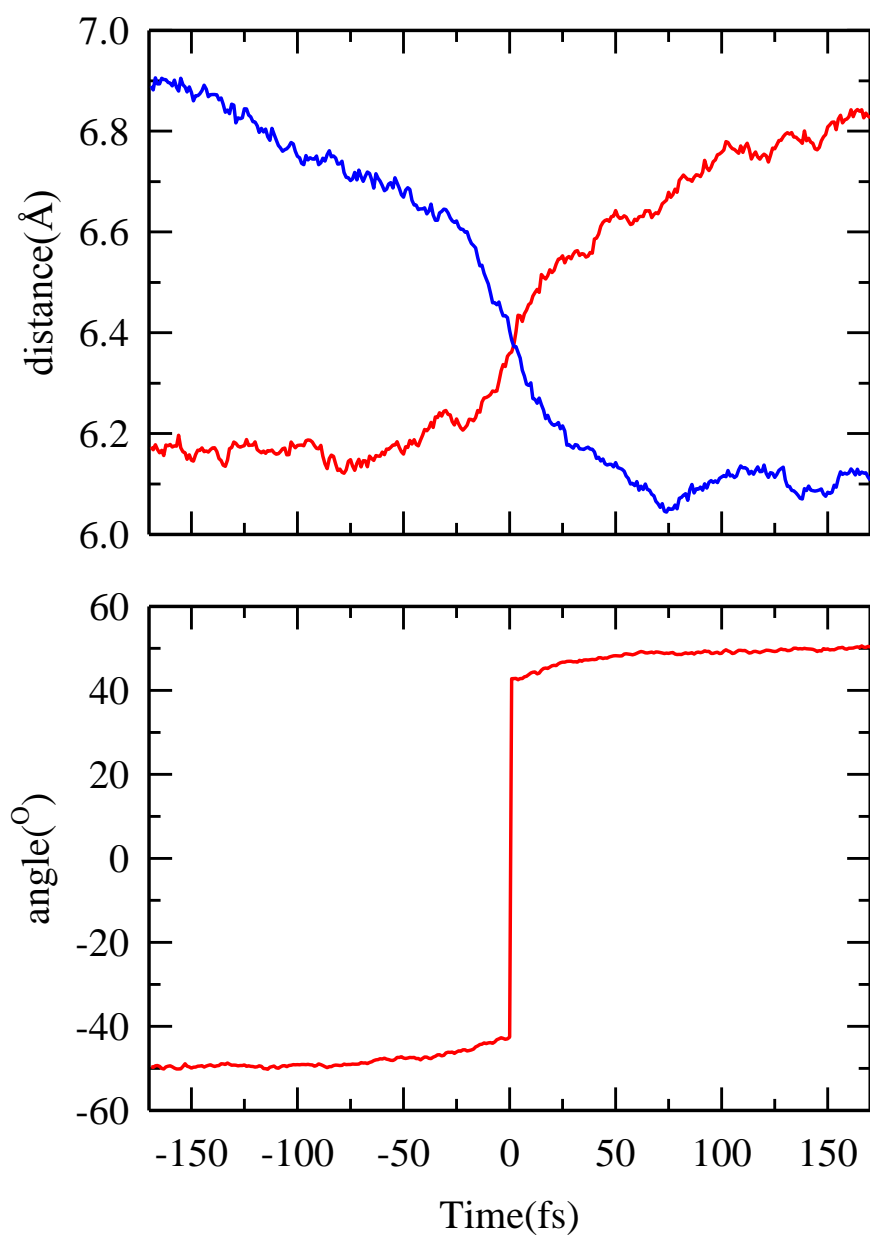


Figure 2.7: Average trajectory calculated in terms of the distance between centre-of-mass (COM) of the rotating acetamide and its initial (red curve) and final (blue curve) H-bond acceptors (top panel). The bottom panel shows how angle θ (defined in Figure 2.4(a)) varies in an average trajectory.

Figure 2.8 (main panel) demonstrates the jump angle distribution calculated from the orientational displacements of the backbone of the acetamide molecules between the starting and ending times of the microscopic jumps. The curve peaks at around 5° but displays a long tail extending towards larger jump angles. A more magnified view of the jump angle distribution can be accessed via considering the angular motion of the $N^* - H^*$ vector. The jump angle, in such a description, is the angle $O_A N^* O_B$ at the transition state when $R_{N^*O_A} = R_{N^*O_B}$ (see Figure 2.4(a)). Inset of Figure 2.8 shows this distribution which peaks at $\sim 60^\circ$ and again displays a long tail extending to large angles. This clearly indicates that large amplitude jumps are associated with angular dynamics of the $N^* - H^*$ vector. This means that the $N^* - H^*$ vector probably first undergoes the orientational jump and the rest of the molecule then follows. Intuitively, this can be understood if we consider that the volume associated with backbone rotation is much larger than that associated with $N^* - H^*$ rotation.

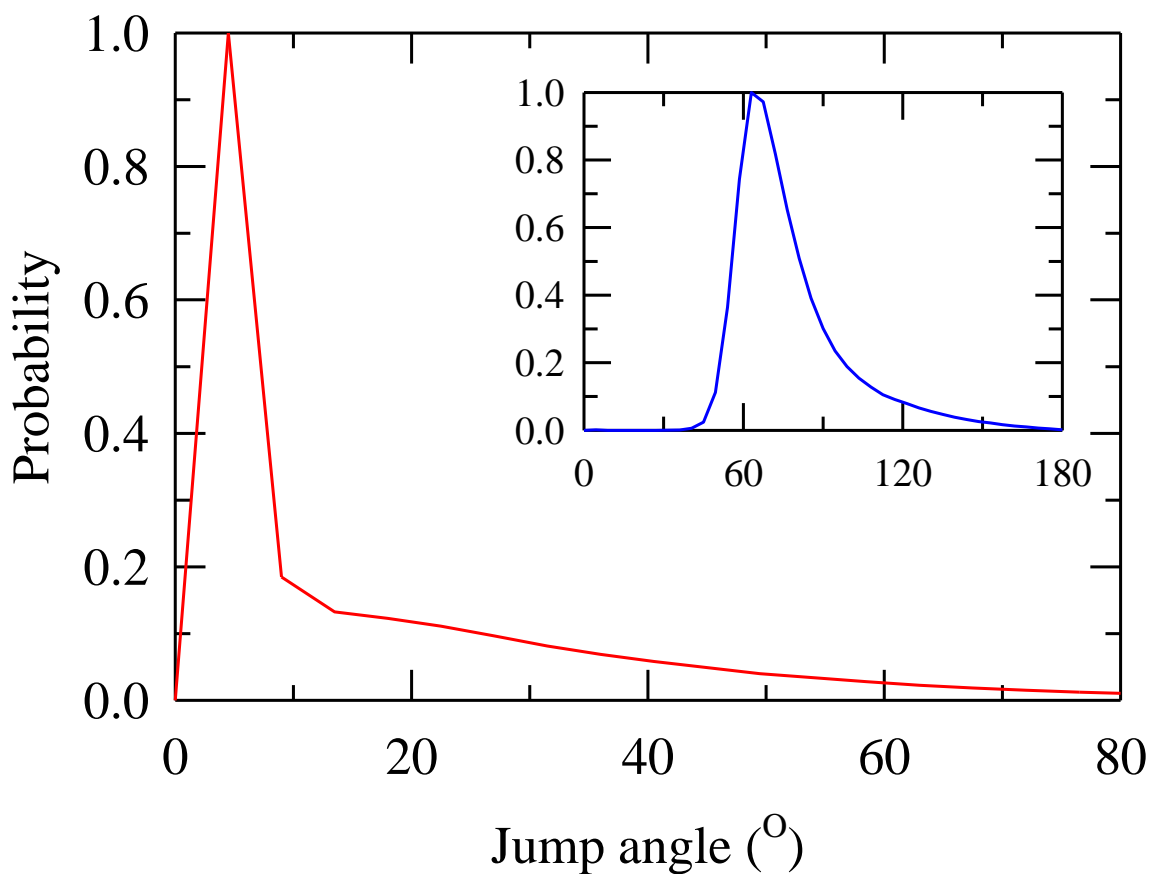


Figure 2.8: Jump angle distributions for acetamide at 368 K from simulations. Main panel shows the jump angle distribution for the backbone of the acetamide molecule, whereas the inset presents the jump angle distribution of the $N^* - H^*$ vector, which participates in the exchange of hydrogen bonding partner.

We have calculated the average number of H-bonds associated with a rotating CH_3CONH_2 molecule, the initial H-bond acceptor and the final H-bond acceptor along the average trajectory (see Figure 2.9). The number of H-bonds associated with the initial and the final donors is ~ 2.8 . Incidentally, each CH_3CONH_2 molecule offers three hydrogen bonding sites, the two amide H-atoms can act as donors, whereas the carbonyl oxygen can act as an acceptor. As time proceeds, due to inherent thermal fluctuations in the system, the initial H-bond acceptor gets over-coordinated and the final H-bond acceptor becomes under-coordinated before it prepares for an orientational jump. The jump then helps release the internal stress developed due to the deviation from the average co-ordination. Figure 2.9 shows the time evolution of the H-bond co-ordination numbers of the initial acceptor, the final acceptor and the rotating CH_3CONH_2 . One typical order parameter which is responsible for driving this microscopic transition (jump) is the difference between the coordination of the initial and the final H-bond acceptors. The blue curve in Figure 2.9 shows the time evolution of this difference, Δn_{HB} . It crosses suddenly from a positive value to a negative one at the transition state.

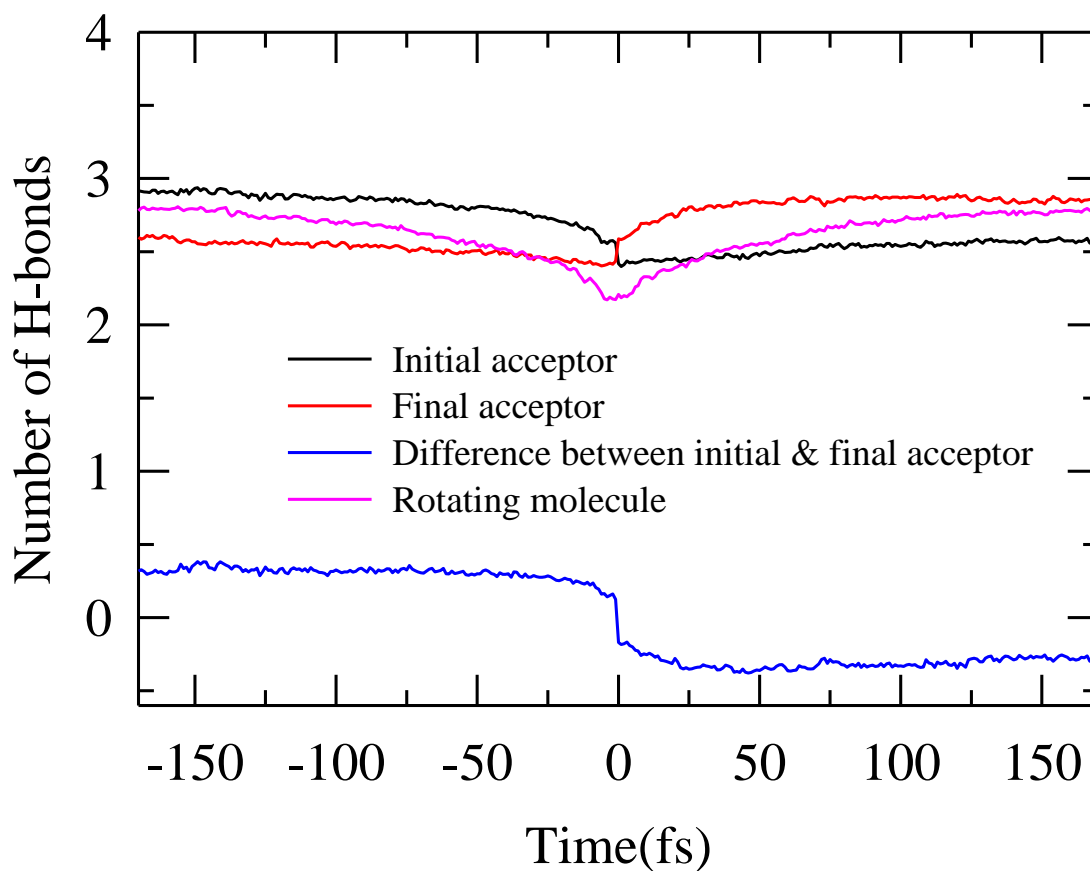


Figure 2.9: Time-evolution of the number of the hydrogen bonds (counting both the number of bonds donated and accepted) for the rotating molecule, the initial hydrogen bond acceptor (black curve) and the final hydrogen bond acceptor (red curve). The jump is driven by the fluctuation in the number of hydrogen bonds: the blue curve shows the difference between hydrogen bond coordination of the initial and the final hydrogen bond acceptors.

The above observations clearly demonstrate that orientational relaxation occurs in liquid acetamide via large amplitude jumps. This jump dynamics also affects the behaviour of the experimentally accessible orientational correlation functions, $C_\ell(t)$. The orientational dynamics of the CH_3CONH_2 molecules has been examined via simulating the reorientational correlation functions defined as⁵⁵

$$C_\ell(t) = \frac{\langle P_\ell(\mathbf{u}(0) \cdot \mathbf{u}(t)) \rangle}{\langle P_\ell(\mathbf{u}(0) \cdot \mathbf{u}(0)) \rangle}, \quad (2.3)$$

where P_ℓ denotes the Legendre polynomial of rank ℓ and \mathbf{u} is a unit vector connecting the C(-CH₃) and N(-NH₂) atoms of a given CH₃CONH₂ molecule. From Debye's model of diffusive reorientation in homogeneous media,^{56,57} the ℓ -th rank correlation function can be expressed as a mono-exponential function, and the corresponding reorientation time τ_ℓ can be obtained as follows

$$\tau_\ell = \frac{1}{\ell(\ell+1)D_R}, \quad (2.4)$$

where D_R is the rotational diffusion constant. For a Debye-like behaviour, $\tau_1/\tau_2 \approx 3$.^{56,57} Deviation from a value of 3 may be attributed to the presence of a large amplitude angular jumps.⁵⁷ Figure 2.10 (top panel) shows the normalized $C_\ell(t)$ decays simulated for $\ell=1$ (first rank) and 2 (second rank) associated with the backbone (connecting the C and N atoms of CH₃CONH₂). The bottom panel of Figure 2.10 shows the corresponding normalized $C_\ell(t)$ decays for the N* - H* vector of CH₃CONH₂. Multi-exponential fit parameters for these $C_\ell(t)$ decays are provided in Table 2.1. For the backbone reorientation, the ratio between the longest time constants, $(\tau_{\ell=1}/\tau_{\ell=2})^{\text{longest}}$, has been found to be ~ 1.5 . For N* - H* vector, this value is ~ 1.7 . Such a value (deviation from three) strongly suggests presence of non-Debye reorientation mechanism which could be large amplitude angular jumps.

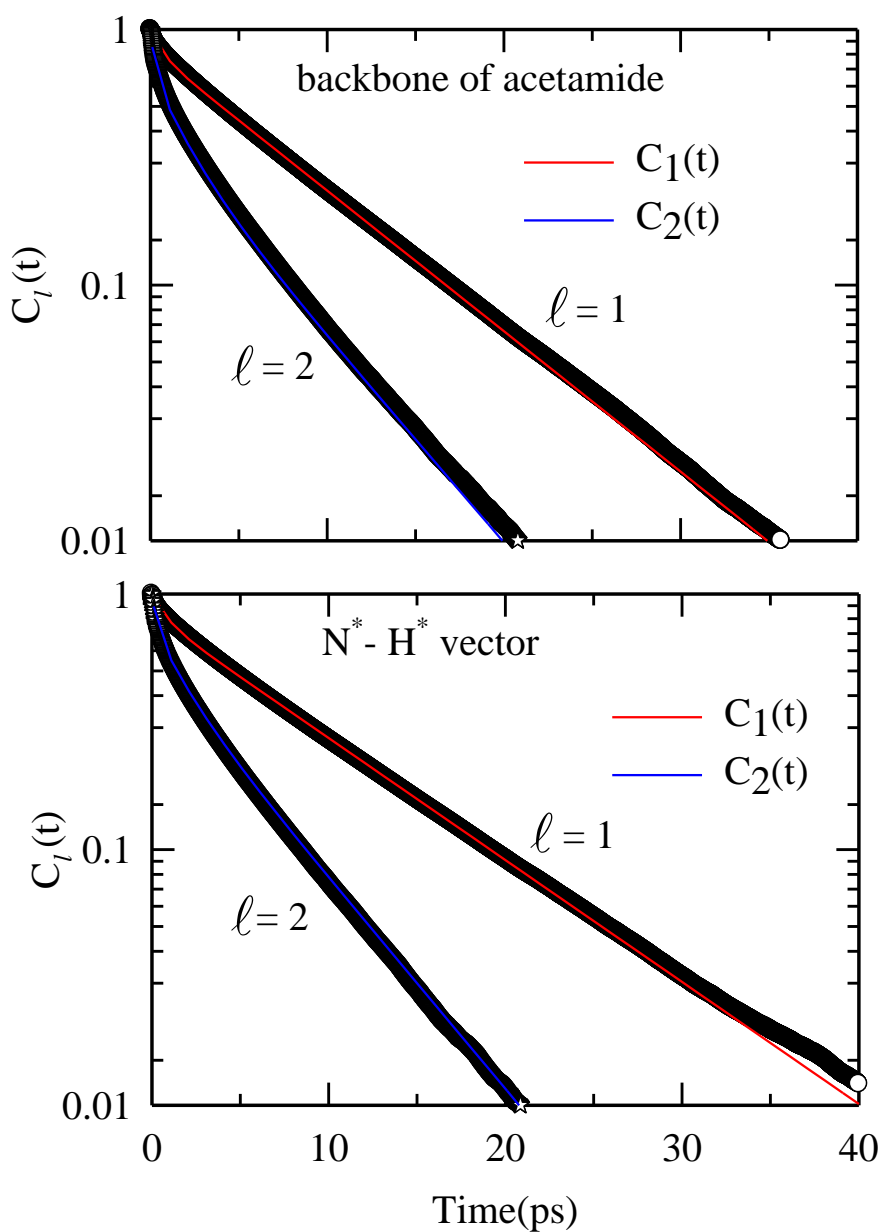


Figure 2.10: Simulated reorientational correlation functions of first ($l=1$) and second ranks ($l=2$) for molten acetamide at 368 K, and their fits. Fit parameters are provided in **Table 2.1**.

Table 2.1: Multi-exponential fit parameters for the simulated rank dependent orientational correlation functions at 368K for (a) backbone (C-N vector) and (b) N^{*}-H^{*} vector.

(a)

Rank(ℓ)	a ₁	t ₁ (ps)	a ₂	t ₂ (ps)	a ₃	t ₃ (ps)	τ (ps)
$\ell = 1$	0.17	0.63	0.83	7.9	-	-	6.7
$\ell = 2$	0.30	0.19	0.30	1.7	0.40	5.4	2.7

(b)

Rank(ℓ)	a ₁	t ₁ (ps)	a ₂	t ₂ (ps)	a ₃	t ₃ (ps)	τ (ps)
$\ell = 1$	0.18	0.8	0.82	9.1	-	-	7.6
$\ell = 2$	0.23	0.23	0.25	1.6	0.52	5.26	3.2

In Figure 2.11, we present the distribution of the waiting time between jumps and the time required to complete the jump (jump time). Both distributions are exponential at long times and the average timescale associated with jump ($\tau_{\text{jump}} \sim 0.9$ ps) is shorter compared to the average waiting time between jumps ($\tau_{\text{wait}} \sim 2.09$ ps). Incorporation of additional hydrogen bond criterion also leads to a very similar average waiting time ($\tau_{\text{wait}} \sim 2.3$ ps). This suggests that the jumps are relatively faster events punctuated by longer periods of rest between them.

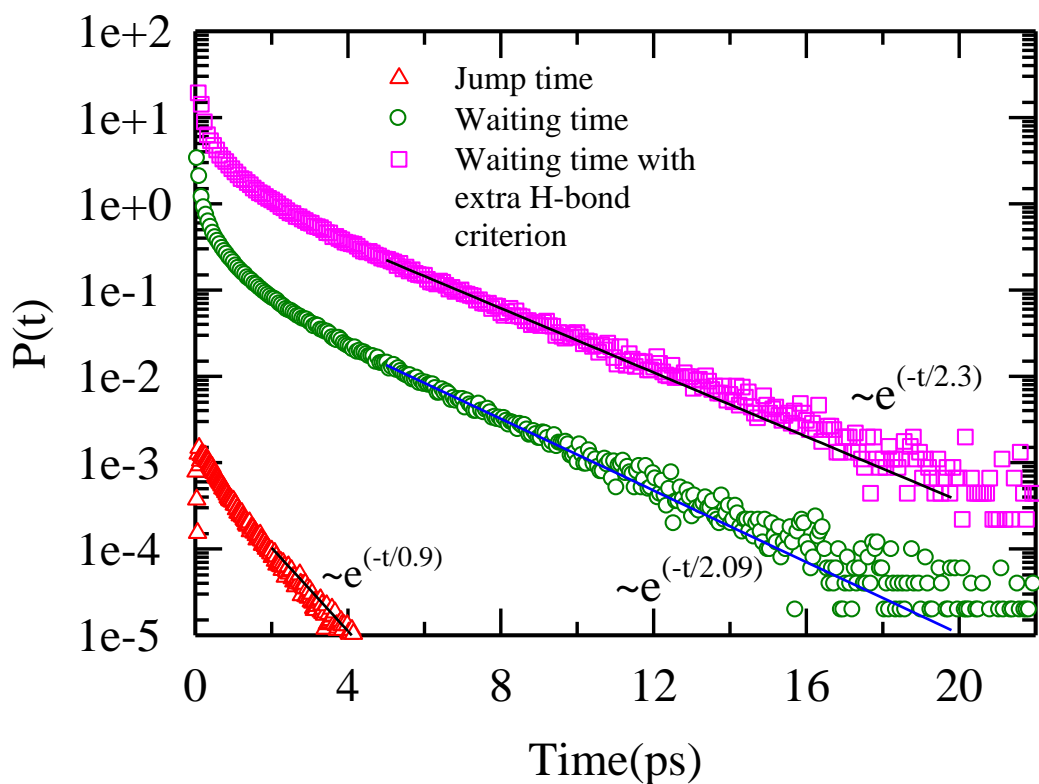


Figure 2.11: Distributions of waiting times between jumps (green circles and pink squares) and of the time required to complete the jump (red triangles). Both distributions are exponential at long times with the mean waiting time (2.09 ps) much longer than the mean jump time (0.9 ps). For clarity, the waiting time distribution using the additional (extra) H-bond criterion has been translated up vertically (data represented by pink squares).

It would be instructive to compare these timescales with more conventional measures of timescales of H-bond correlations. We have calculated two well-known H-bond correlation functions $S_{\text{HB}}(t)$ and $C_{\text{HB}}(t)$. They are defined in the following way,³⁶⁻³⁸

$$S_{\text{HB}}(t) = \langle h(0)H(t) \rangle / \langle h \rangle, \quad (2.5)$$

where $h(t')$ is a variable defined for a pair of CH_3CONH_2 molecules at all times, $h(t') = 1$ if the pair is hydrogen bonded at time t' , it is zero otherwise. $H(t)$ is a history dependent function of $h(t')$ and it is unity if $h(t')$ is continuously 1 between times t_0 and $(t_0 + t)$, where t_0 is an arbitrary origin of time. If this condition is violated, $H(t)$ is set to zero. Thus,

$S_{\text{HB}}(t)$ describes the probability that a pair of CH_3CONH_2 molecules remains continuously H-bonded for certain duration. The corresponding average relaxation time, τ_{HB} , can be treated as the average life-time of H-bonds. Another correlation function which does not require pairs to remain H-bonded continuously, but allows them to be broken fleetingly at intermediate times is defined below,^{36,37,39,40}

$$C_{\text{HB}}(t) = \langle h(0)h(t) \rangle / \langle h \rangle . \quad (2.6)$$

The associated average relaxation time constant, τ_{CB} , provides an estimate of the H-bond survival time. Clearly, $C_{\text{HB}}(t)$ associates with structural relaxation due to translational diffusion. The top panel of Figure 2.12 shows the time dependence of $S_{\text{HB}}(t)$, whereas the bottom panel shows $C_{\text{HB}}(t)$. Multi-exponential fit parameters for these simulated decays are shown inside each of these panels. The longest timescale associated with $S_{\text{HB}}(t)$ is 0.4 ps, whereas the decay of $C_{\text{HB}}(t)$ is much slower, the longest timescale being ~ 54 ps. This ~ 50 ps timescale is qualitatively similar to the center-of-mass translation timescale of an acetamide molecule at this temperature and suggests a connection to structural relaxation. The sub-picosecond timescale is close to τ_{jump} and the other timescale (~ 8 ps) is close to τ_{wait} shown in Figure 2.11. This explains the microscopic origin for the different multi-exponential behaviours of $C_{\text{HB}}(t)$ and $S_{\text{HB}}(t)$ decays.

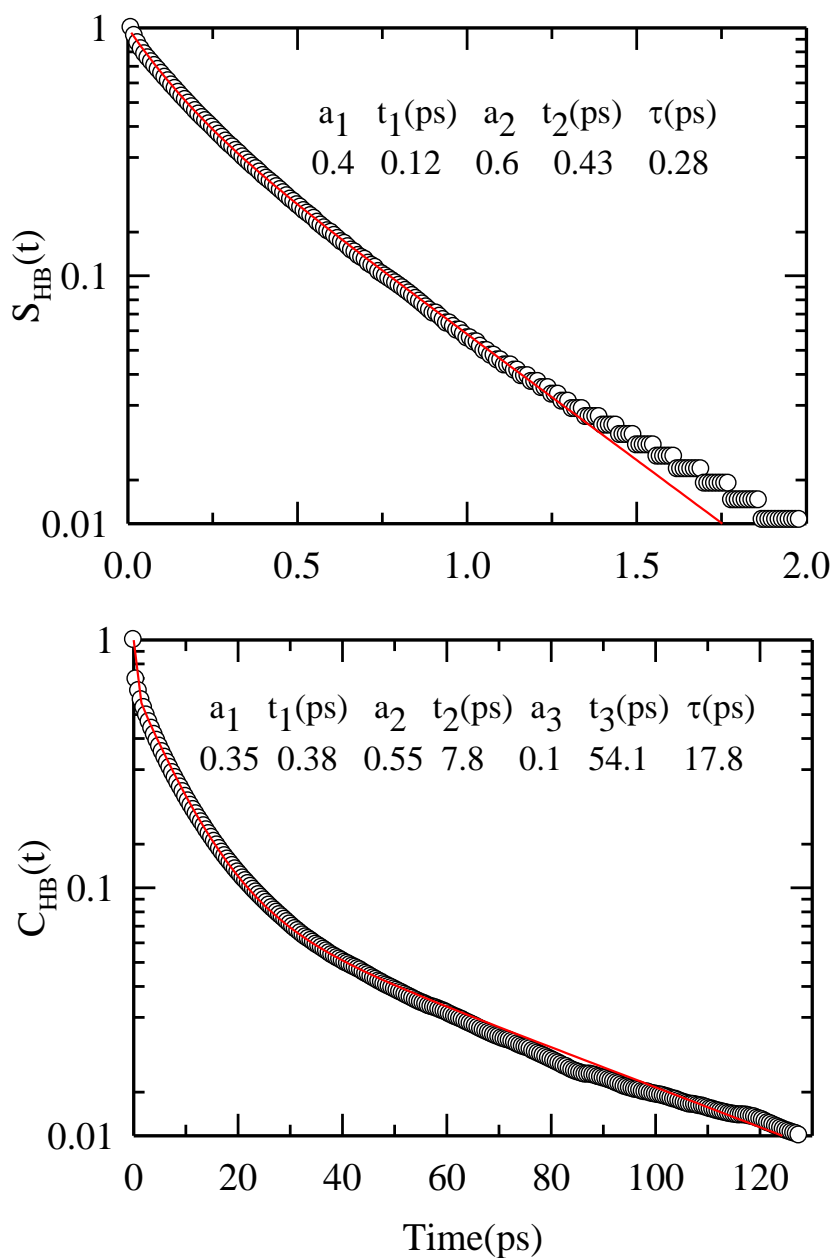


Figure 2.12: Simulated decay of the hydrogen bond correlation functions, $S_{\text{HB}}(t)$ and $C_{\text{HB}}(t)$. Multi-exponential function fit parameters are shown inside the panels.

The free-energy profile of the average trajectory (see Figure 2.13), which has been discussed above, can be found by projecting the average trajectory on the free energy surface. In this calculation we have neglected the fluctuation in difference of the H-bond coordination, Δn_{HB} , a contribution, which is known to be small from similar calculations in liquid water^{30,31} and have only collected the contributions arising from ΔR and θ . The value of the free energy has been arbitrarily chosen to be zero at the beginning and end of the average trajectory. The free energy barrier estimated from this free-energy profile is about 0.5 kcal/mole ($\sim 0.7 k_{\text{B}}T$). This value is approximately one-fourth of what has been estimated for liquid water at room temperature.^{30,31} This difference (from water) is expected if one considers the qualitative difference of the H-bond networks between liquid acetamide and liquid water. Figure 2.14 shows various sections of the free energy surface as a function of θ for different values of ΔR ($\Delta n_{\text{HB}} = 0$). At negative values of ΔR , the free energy has a single minimum at negative θ . This signifies that the $\text{N}^* - \text{H}^*$ vector of the rotating acetamide molecule is H-bonded to its initial partner. Only when the transition state is reached ($\Delta R = 0$), the free energy section attains a symmetric double well structure (black curve in Figure 2.14). This feature is very similar to that observed for liquid water and emphasizes that the crossing of the barrier by angular jumps can only happen when the surrounding has prepared itself by situating the initial and the final H-bond acceptor oxygen atoms at equal distances from the nitrogen atom (N^*) of the rotating acetamide molecule.

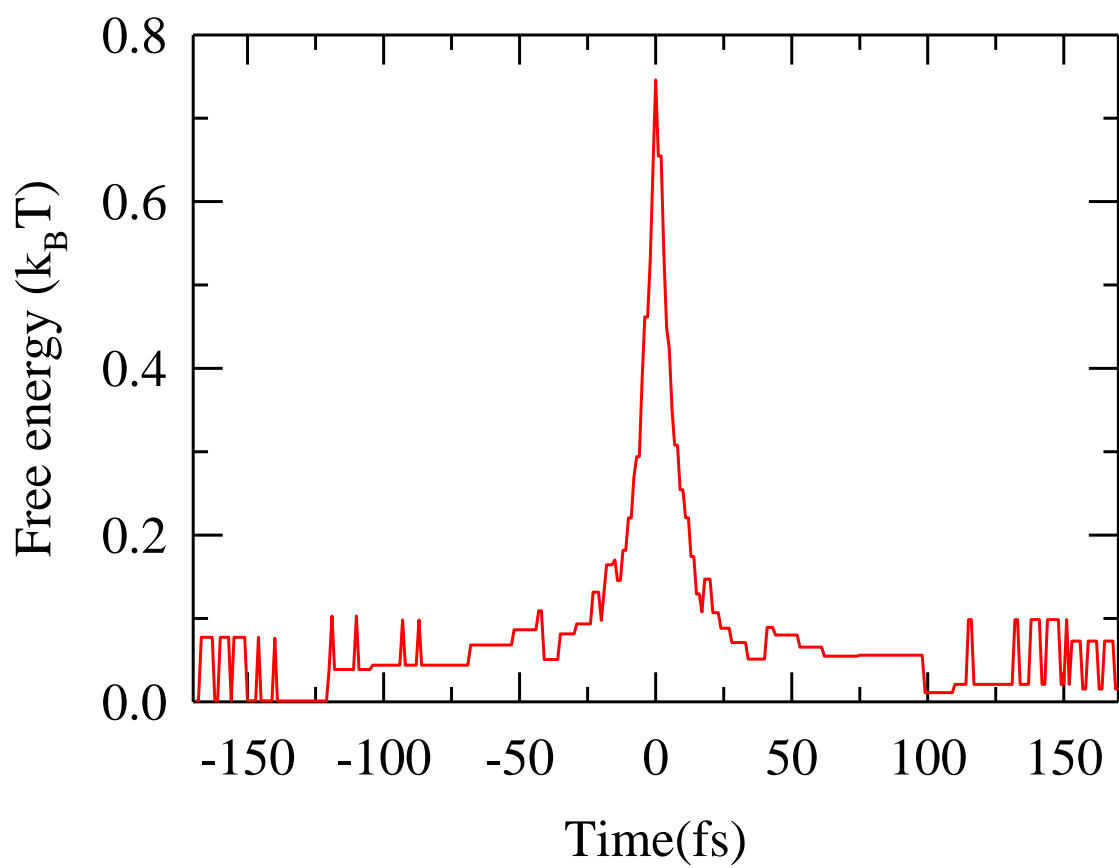


Figure 2.13: Free energy as a function of time along the average jump trajectory shown in **Figure 2.5**. The transition state has the highest free energy with the two stable minima on both sides of the transition state.

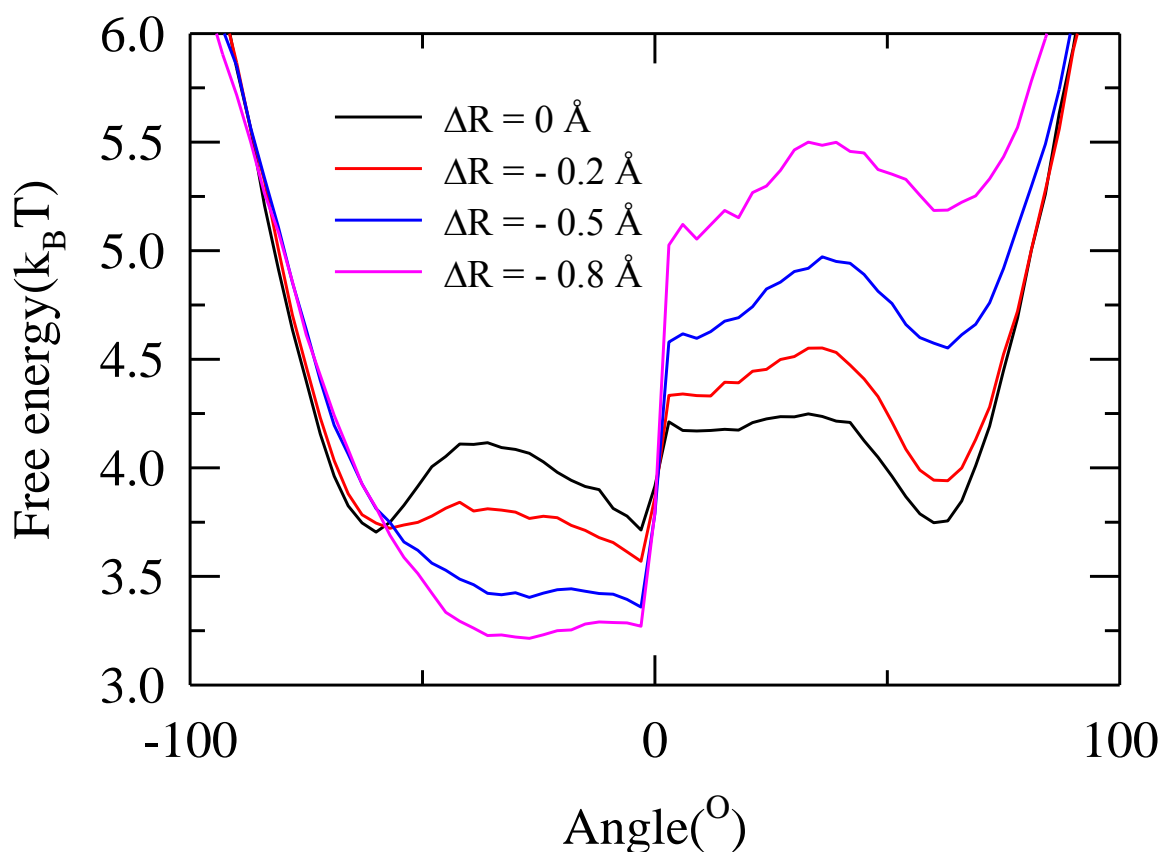


Figure 2.14: Cuts of the free energy surface, as a function of θ , are shown for various values of $\Delta R = (R_{N^*O_A} - R_{N^*O_B})$ and $\Delta n_{HB} = 0$. The function becomes symmetric about $\theta = 0$ for $\Delta R = 0$ (black curve). At other negative values of ΔR (red, blue, and pink curves), the cut of the free energy surface has a minima at a negative value of θ . The kinks near $\theta = 0$ are due to insufficient statistics in the close proximity to the transition state.

2.5. Conclusions

In summary, the present study has revealed presence of orientational jumps in molten acetamide and a significant translation-rotation coupling. The barrier to the orientation jumps has been estimated to be around $0.7 k_B T$ which is a factor of ~ 4 less than that reported for liquid water at ~ 300 K. The jump and waiting time distributions are exponential at long time with time constants correlating well with those obtained from continuous and structural hydrogen bond relaxation dynamics. Jump angle distributions for both the acetamide

backbone and the amide vectors are asymmetric with long tails extended towards large angles. The ratios of the longest time constants associated with the first and second rank orientational correlation functions simulated for the backbone and amide vectors exhibit deviations from diffusive orientational diffusion and suggest, much like in the case of liquid water,^{30-31,58} presence of angular jumps.

The interconnection between jump reorientations and H-bond dynamics can be extended to room temperature ionic liquids (RTILS) and their binary mixtures with protic solvents as they possess highly heterogeneous solution structure and exhibit non-exponential relaxation kinetics.⁵⁹⁻⁶⁷ It would be interesting to explore how spatial heterogeneity in such systems affects the jump dynamics and H-bond relaxations and modifies the interconnection between them. Likewise, characterization of jumps and their dynamics for interfacial water confined in carbon nanotubes,⁶⁸ microemulsions⁶⁹⁻⁷⁰ and vesicles⁷¹ and the relationship with H-bond dynamics would be worth investigation.

References

1. D. A. Dixon, K. D. Dobbs, and J. J. Valentini, *J. Phys. Chem.* **51**, 13435 (1994).
2. J. B. O. Mitchell and S. L. Price, *Chem. Phys. Lett.* **154**, 267 (1989).
3. P. Jedlovszky, *J. Chem. Phys.* **113**, 9113 (2000).
4. M. W. Wong and K. B. Wiberg, *J. Phys. Chem.* **96**, 668 (1992).
5. R. Ludwig, F. Weinhold, and T. C. Farrar, *J. Chem. Phys.* **107**, 499 (1997).
6. D. H. Kerridge, *Chem. Soc. Rev.* **17**, 181 (1988).
7. O. F. Stafford, *J. Am. Chem. Soc.* **55**, 3987 (1933).
8. L. F. Yntema and L. F. Audrieth, *J. Am. Chem. Soc.* **52**, 2693 (1930).
9. L. R. Dawson, P. G. Sears, and R. H. Graves, *J. Am. Chem. Soc.* **77**, 1986 (1955).
10. R. A. Wallace, *J. Phys. Chem.* **75**, 2687 (1971).
11. S. Nasr, M. Ghédira, and R. Cortés, *J. Chem. Phys.* **110**, 10487 (1999).
12. S. Nasr, *J. Chem. Phys.* **115**, 6569 (2001).
13. S. Trabelsi and S. Nasr, *J. Chem. Phys.* **121**, 6380 (2004).
14. F. Hammami, S. Nasr, and M. C. Bellissent-Funel, *J. Chem. Phys.* **122**, 064505 (2005).
15. S. Trabelsi, M. Bahri, and S. Nasr, *J. Chem. Phys.* **122**, 024502 (2005).
16. H. K. Kashyap, T. Pradhan, and R. Biswas, *J. Chem. Phys.* **125**, 174506 (2006).
17. S. K. Pattanayak, N. Prashar, and S. Chowdhuri, *J. Chem. Phys.* **134**, 154506 (2011).
18. R. Biswas and B. Bagchi, *J. Phys. Chem.* **100**, 1238 (1996).
19. R. Biswas, A. Das, and H. Shirota, *J. Chem. Phys.* **141**, 134506 (2014).
20. B. Guchhait, S. Das, S. Daschakraborty, and R. Biswas, *J. Chem. Phys.* **140**, 104514 (2014).
21. A. Das, S. Das, and R. Biswas, *Chem. Phys. Lett.* **581**, 47 (2013).
22. B. Guchhait, S. Daschakraborty, and R. Biswas, *J. Chem. Phys.* **136**, 174503 (2012).
23. B. Guchhait, H. A. R. Gazi, H. K. Kashyap, and R. Biswas, *J. Phys. Chem. B* **114**, 5066 (2010).
24. T. Pal and R. Biswas, *Chem. Phys. Lett.* **517**, 180 (2011).
25. H. A. R. Gazi, B. Guchhait, S. Daschakraborty, and R. Biswas, *Chem. Phys. Lett.* **501**, 358 (2011).
26. Q. Zhang, K. De Oliveira Vigier, S. Royer, and F. Jérôme, *Chem. Soc. Rev.* **41**, 7108 (2012).

27. D. V. Wagle, H. Zhao, and G. A. Baker, *Acc. Chem. Res.* **47**, 2299 (2014).
28. G. van der Zwan and J. T. Hynes, *Chem. Phys.* **152**, 169 (1991).
29. G. van der Zwan and J. T. Hynes, *J. Chem. Phys.* **78**, 4174 (1983).
30. D. Laage and J. T. Hynes, *Science* **311**, 832 (2006).
31. D. Laage and J. T. Hynes, *J. Phys. Chem. B* **112**, 14230 (2008).
32. D. Laage and J. T. Hynes, *Proc. Natl. Acad. Sci. U.S.A.* **104**, 11167 (2007).
33. D. Laage, G. Stirnemann, and J. T. Hynes, *J. Phys. Chem. B* **113**, 2428 (2009).
34. G. Stirnemann, J. T. Hynes, and D. Laage, *J. Phys. Chem. B* **114**, 3052 (2010).
35. D. Laage and J. T. Hynes, *J. Phys. Chem. B* **112**, 7697 (2008).
36. D. C. Rapaport, *Mol. Phys.* **50**, 1151(1983).
37. A. Chandra, *Phys. Rev. Lett.* **85**, 768 (2000).
38. A. Luzar, *J. Chem. Phys.* **113**, 10663 (2000).
39. A. Luzar, *Nature* **379**, 55 (1996).
40. A. Luzar and D. Chandler, *Phys. Rev. Lett.* **76**, 928 (1996).
41. R. Kumar, J. R. Schmidt, and J. L. Skinner, *J. Chem. Phys.* **126**, 204107 (2007).
42. S. Indra and R. Biswas, *Molecular Simulation* **41**, 471 (2014).
43. J. A. Mitchell and E. E. Reid, *J. Am. Chem. Soc.* **53**, 1879 (1931).
44. W. Smith and T. R. Forster, *The DL_POLY Molecular Simulation Package*, Daresbury Laboratory, Cheshire, U. K. (1999).
45. J. Habasaki and K. L. Nagi, *J. Chem. Phys.* **129**, 194501 (2008).
46. A. D. MacKerell Jr., J. Wiorkiewicz-Kuczera, and M. Karplus, *J. Am. Chem. Soc.*, **117**, 11946 (1995).
47. C. W. Yong, DL_FIELD, STFC Daresbury Laboratory http://www.cse.scitech.ac.uk/ccg/software/DL_FIELD (2011).

48. M. P. Allen and D. J. Tildesley, *Comput. Simulations Liq.* Oxford University Press, New York, (1987).
49. L. Martinez, R. Andrade, E. G. Birgin, and J. M. Martinez, *J. Comput. Chem.* **30**, 2157 (2009).
50. <http://en.wikipedia.org/wiki/Acetamide>
51. S. A. Nose, *J. Chem. Phys.* **81**, 511 (1984).
52. W. G. Hoover, *Phys. Rev. A* **31**, 1695 (1985).
53. D. Laage and J. T. Hynes, *Chem. Phys. Lett.* **433**, 80 (2006).
54. R. Taylor, O. Kennard, and W. Versichel, *J. Am. Chem. Soc.* **106**, 244 (1984).
55. J. P. Hansen and I. R. McDonald, *Theory of Simple Liquids*, 3rd edition, Academic, San Diego, (2006).
56. P. Debye, *Polar Molecules*. The Chemical Catalog Company: New York, (1929).
57. K. Seki, B. Bagchi, and M. Tachiya, *Phys. Rev. E* **77**, 031505 (2008).
58. R. Ludwig, *Chem. Phys. Chem.* **8**, 44 (2007).
59. T. Pal and R. Biswas, *J. Chem. Phys.* **141**, 104501 (2014).
60. T. Pal and R. Biswas, *Theor. Chem. Acc.* **132**, 1348 (2013).
61. S. Daschakraborty and R. Biswas, *J. Chem. Phys.* **140**, 014504 (2014).
62. S. Daschakraborty, T. Pal and R. Biswas, *J. Chem. Phys.* **139**, 164503 (2013).
63. S. Daschakraborty and R. Biswas, *J. Chem. Phys.* **137**, 114501 (2012).
64. S. Daschakraborty and R. Biswas, *J. Phys. Chem. B* **118**, 1327 (2014).
65. S. Daschakraborty and R. Biswas, *J. Phys. Chem. B* **115**, 4011 (2011).
66. T. Pal and R. Biswas, *J. Chem. Phys.* **141**, 164502 (2014).
67. K. M. Barra, R. P. Sabatini, Z. P. McAtee, and M. P. Heitz, *J. Phys. Chem. B* **118**, 12979 (2014).
68. B. Mukherjee, P. K. Maiti, C. Dasgupta, and A. K. Sood, *J. Phys. Chem. B* **113**, 10322 (2009).

69. B. Guchhait, R. Biswas, and P. Ghorai, *J. Phys. Chem. B* **117**, 3345 (2013).
70. R. Biswas, A. R. Das, T. Pradhan, D. Touraud, W. Kunz, and S. Mahiuddin, *J. Phys. Chem. B* **112**, 6620 (2008).
71. N. Sarma, J. M. Borah, S. Mahiuddin, H. A. R. Gazi, B. Guchhait, and R. Biswas, *J. Phys. Chem. B* **115**, 9040 (2011).

Chapter 3

Oriental Jumps in (Acetamide + Electrolyte) Deep Eutectics: Anion Dependence

3.1. Introduction

Minimum ecological foot-print via bio-degradation, economic viability through cheaper preparation protocol, extended moisture stability, and easy alteration of physico-chemical properties are the principal requirements that a solvent or a class of solvents must satisfy to demand large-scale industrial applications. Deep eutectic solvents (DESs), solvents that are molten mixtures of a few components of high individual melting points, meet several or all of the above stringent criteria for large-scale applications.¹⁻⁵ DESs made of amide and electrolytes constitute an example of one such class of solvents that have found of late several industrial and technological applications.⁶⁻¹⁰ Extensive inter-species hydrogen bonding (H-bonding) and entropic gain in the subsequent process are believed to bring the high melting solid components in liquid phase. Acetamide, by virtue of possessing several functional groups, large molecular dipole moment ($\mu = 3.7\text{D}^{11}$) and high dielectric constant in molten condition ($\epsilon_0 \sim 61$ at $\sim 367\text{K}^{11,12}$), can dissolve a wide range of organic and inorganic compounds except cellulose.¹³ It is only natural then that molten mixtures which offer acetamide in liquid phase near room temperature will be a subject of intense research. In addition, engineering these media for tailoring chemical reactions demands a molecular level understanding of medium effects on chemical reactions.¹⁴⁻¹⁶

Although (acetamide + electrolyte) DESs have been used in a few industrial applications, microscopic understanding of interaction and dynamics of these media are still lacking. Previous dielectric¹⁷⁻¹⁹ and other relaxation experiments²⁰⁻²² have interpreted measured data in terms of micro-heterogeneity in these systems, although no structural measurements at molecular length-scales exist to contest such a view. In the last few years several studies employing time-resolved fluorescence²³⁻²⁷ and optical Kerr spectroscopic²⁸ measurements have revealed information on

collective interaction and dynamics of these systems. A few simulation studies^{23,24,29} have revealed the nature of viscosity coupling of diffusive dynamics in these DESs and helped interpreting departure from hydrodynamics of diffusive timescales observed in time-resolved fluorescence measurements. However, no study exists that dissects the experimentally observed ensemble-averaged total information into the separate contributions from acetamide molecules that are interacting with the electrolyte present in such a medium, and from those which are not. Conventional time-resolved fluorescence and other frequency-dependent relaxation experiments cannot separate out these contributions as response measured by them is averaged over contributions from all length-scales.³⁰ However, such a study can be conducted via computer simulations, and we focus here on revealing the orientational features of acetamide molecules that are H-bonded to ions present in these DESs, and those which are H-bonded only to other acetamide molecules.

In order to carry out the proposed study we have considered three different deep eutectics, namely, ($\text{CH}_3\text{CONH}_2 + \text{LiBr}$), ($\text{CH}_3\text{CONH}_2 + \text{LiNO}_3$) and ($\text{CH}_3\text{CONH}_2 + \text{LiClO}_4$), all at 78:22 mole ratio and at 303 K. This mole ratio has been chosen as several measurements exist for these DESs at this composition.^{23,24,26,28} Reorientation jumps of acetamide molecules in these media have been monitored via a method that closely follows the framework developed earlier for studying water reorientation dynamics in a variety of environments,³¹⁻⁴² and employed later for molten neat acetamide.⁴³ The anion dependence is explored via simulating jump angle and jump time distributions, free energy barrier at the transition state (involved in H-bond switching), changes in radial and angular distances during successful jumps, and difference in H-bond coordination between the initial and the final acceptors. Since these ions are varying in both shape and size, effects are expected to be more complex than arising from excluded volumes alone.^{34,44} As observed earlier,^{32,43,45} H-bond switching events in these systems have also been found to be associated with a significant amount of translation-rotation coupling.

3.2. Simulation details

All-atom simulations were performed at a temperature of 303 K using the package DL_POLY version 2.20.⁴⁶ Each mixture comprised of 512 molecules, of which there were 400 acetamide and 56 pairs of Li^+ and X^- where X^- denotes the identity of the anion. This provides a mole ratio of 78:22 between acetamide and electrolyte. The potential function used has the following form:

$$U(\mathbf{R}) = \sum_{\text{bonds}} K_r (r - r_{\text{eq}})^2 + \sum_{\text{angles}} K_\theta (\theta - \theta_{\text{eq}})^2 + \sum_{\text{dihedrals}} K_\phi [1 + \cos(n\phi - \delta)] + \sum_{i < j}^{\text{atoms}} \left(\frac{A_{ij}}{R_{ij}^{12}} - \frac{B_{ij}}{R_{ij}^6} \right) + \sum_{i < j}^{\text{atoms}} \frac{q_i q_j}{4\pi\epsilon_0 R_{ij}}. \quad (3.1)$$

Note this particular form of potential function has been used earlier for modeling DESs.^{23,24,47} In Equation 3.1, K_r and K_θ are respectively the bond and angle constants, r_{eq} and θ_{eq} the equilibrium bond length and angle. K_ϕ denotes the dihedral constant, n the periodicity, ϕ the dihedral angle, and δ the phase shift. R_{ij} is the distance between atoms i and j with partial charges q_i and q_j respectively. The interaction parameters for the acetamide molecule were taken from the CHARMM⁴⁸ force field. The force field parameters for Li^+ , Br^- , NO_3^- , ClO_4^- were taken from the existing literature.⁴⁹⁻⁵¹ Note these force field parameters, summarized in Appendix A and Appendix B (Table B1-Table B4, Figure B1-Figure B2) were used earlier to simulate acetamide dynamic structure factors in the DESs that successfully explained fractional viscosity dependence of diffusive timescales observed in time-resolved fluorescence measurements.^{23,24} The force field was constructed with DL_FIELD.⁵² The short-range van der Waals interaction was represented by the Lennard-Jones (LJ) potential.⁵³ The long-range electrostatic potential was treated via Ewald summation technique⁵³ using an Ewald parameter of $\alpha = 0.2 \text{ \AA}^{-1}$ and a 6x6x6 k-point grid.

The initial configurations were built using Packmol⁵⁴ and equilibrated in the NPT ensemble at 1 atm. pressure for 500 ps. The simulated densities for all the three systems were found to be in good agreement with those from experiments^{23,28} (Appendix B, Table B5). Nose-Hoover thermostat and barostat^{55,56} were used to control the temperature and pressure with time

constants of 0.4 ps and 1.0 ps, respectively. Subsequently, further equilibration of 2 ns followed by a production run of 5 ns was carried out in the NVT ensemble. Periodic boundary conditions were employed in all three directions, and the equations of motion were integrated using a time step of 0.5 fs employing the velocity Verlet algorithm.⁵³ Snapshots were saved every 10 fs for data analyses. For some calculations, particularly those related to estimation of free energy barriers, snapshots were saved every 2 fs.

3.3. Analysis Protocol

The presence of angular jumps in the reorientational dynamics of acetamide molecules present in all these ionic DESs is evident in Figure 3.1, which shows the time series of the cosine of the angle made by the backbone of a randomly chosen CH_3CONH_2 molecule (connecting the C (- CH_3) and N(- NH_2) atom) with the Z axis of the simulation box. As found previously for molten neat acetamide,⁴³ acetamide backbone in these deep eutectics also executes diffusive Brownian motion with occasional large amplitude jumps. It is observed that the cosine of the angle fluctuates from -0.75 to +1.0 in presences of both Br^- and ClO_4^- . However, in presence of NO_3^- the fluctuation is significantly reduced (spanning values only between +0.25 and 1.0), indicating much restricted large amplitude jumps for acetamide in ($\text{CH}_3\text{CONH}_2 + \text{LiNO}_3$) deep eutectics. The qualitative difference in reorientational jump dynamics of acetamide molecules in presence of different anions in these DESs originates from the chemical nature of these anions leading to differences in interaction with the surrounding acetamide molecules. The implication of this difference will be reflected later when we present and discuss various other simulated quantities.

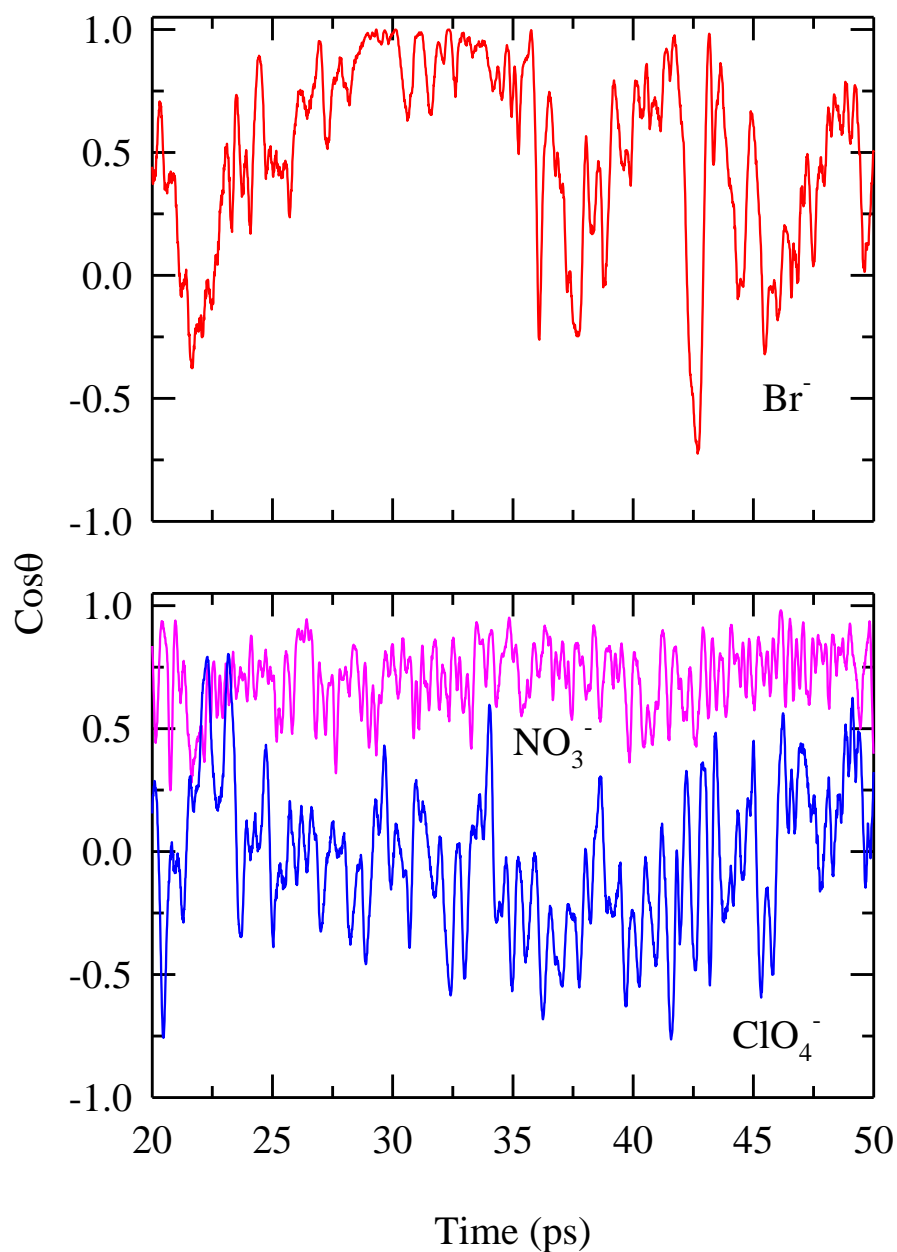


Figure 3.1. This figure shows the time series of the cosine of the angle, which a randomly chosen acetamide molecule makes with the Z axis of the simulation box in DESs studied here at 303 K. The upper panel shows the results for DES that contains lithium Bromide. Lower panel presents data for the same in systems containing lithium perchlorate (blue line) and lithium nitrate (pink line).

The analysis protocol is similar to what has been previously⁴³ employed but with a few technical modifications to allow for the interaction of the ions. Amide hydrogens of acetamide molecules can form hydrogen bonds (H-bonds) with both neighboring acetamide molecules and anions in these DESs. This microscopic consideration then allows one to study separately orientational dynamics of acetamide for the following three different (at least) types: (i) one that involves acetamide molecules, which were initially bonded to other acetamide molecules, break the H-bonds, reorient and form new H-bonds with different neighboring acetamide molecules. (ii) The second type involves acetamide molecules, originally H-bonded to other acetamide molecules, finding anions as a partners for reformation of H-bonds after reorientation. (iii) The third type are those acetamide molecules, which had initially anions as partners through H-bonding, reforms H-bond with neighboring acetamide molecules leaving these anions. For better statistics and averaging, we have bracketed the second and the third types into one single category (note number of ions is much less than that of acetamide), and subsequently analyzed the reorientational dynamics of two main types: one involves only acetamide molecules, and the other acetamide and ion. Note effects of interaction of cation (Li^+ here) with acetamide molecules (via the carbonyl oxygen) on orientational jumps have not been separately analyzed here although present simulations include this interaction. Similarly, anion shape effects have also not been separated out and investigated.

It is expected that microscopic events associated with the above two different types (acetamide-acetamide and acetamide-ion) would exhibit different molecular details along with signatures of anion dependence. Since the reorientation process for both types requires an exchange of H-bonded partners, one needs to define a criterion for the existence of H-bond first. The H-bond can be defined in a number of different ways based on geometric criteria, energy consideration or orbital occupancy.³³ Here we have followed the widely accepted geometric criterion that depends on a distance (R) and an angle (θ).⁵⁷⁻⁶¹ Two CH_3CONH_2 molecules are considered to be H-bonded only when (i) distance between the oxygen and nitrogen atoms of different CH_3CONH_2 molecules, R_{ON} , is less than a cut-off distance, $R_{\text{cut-off}}$ and (ii) angle between the vector joining nitrogen and amide hydrogen of one CH_3CONH_2 molecule, and the vector joining this nitrogen and an oxygen atom belonging to another acetamide molecule, θ_{ONH} , is less than 30° . $R_{\text{cut-off}}$ is

selected where the first minimum of the simulated radial distribution function ($g_{\text{ON}}(r)$) for the oxygen and the nitrogen atoms of two different CH_3CONH_2 molecules appears. Following Figure 3.2 we have taken $R_{\text{cut-off}} = 4 \text{ \AA}$ for calculating acetamide-acetamide jump characteristics in all these DESs. For acetamide-anion cases, the distance considered is between nitrogen atom of the CH_3CONH_2 and X^- , R_{NX} and the angle, θ_{XNH} between the vector joining nitrogen and X^- of the anion and the vector joining this nitrogen and amide hydrogen of the CH_3CONH_2 molecule. For ClO_4^- and NO_3^- , however, there exist more than one possible H-bonding sites. Here we initially calculate the distance between all oxygen atoms of the anion and the nitrogen atom of acetamide molecule and then determine the minimum among these distances. This minimum distance is then compared to the cut-off distance, $R_{\text{cut-off}}$. Once again $R_{\text{cut-off}}$ has been chosen based on the first minimum of the simulated radial distribution function (RDF) between the nitrogen atom of the acetamide molecule and the anions of the salt. Figure B3–Figure B5, Appendix B depict the simulated RDFs between the amide nitrogen and anions for these deep eutectics. These figures indicate $R_{\text{cut-off}} = 4.7 \text{ \AA}$ for LiBr, 4.0 \AA for LiClO_4 and 2.5 \AA for LiNO_3 . The angle cut-off has been kept fixed for all the anions at $\theta_{\text{XNH}} = 30^\circ$. Note this particular way of defining a H-bond with an anion has been used earlier to study H-bond reorientation³³ in aqueous electrolyte solutions.

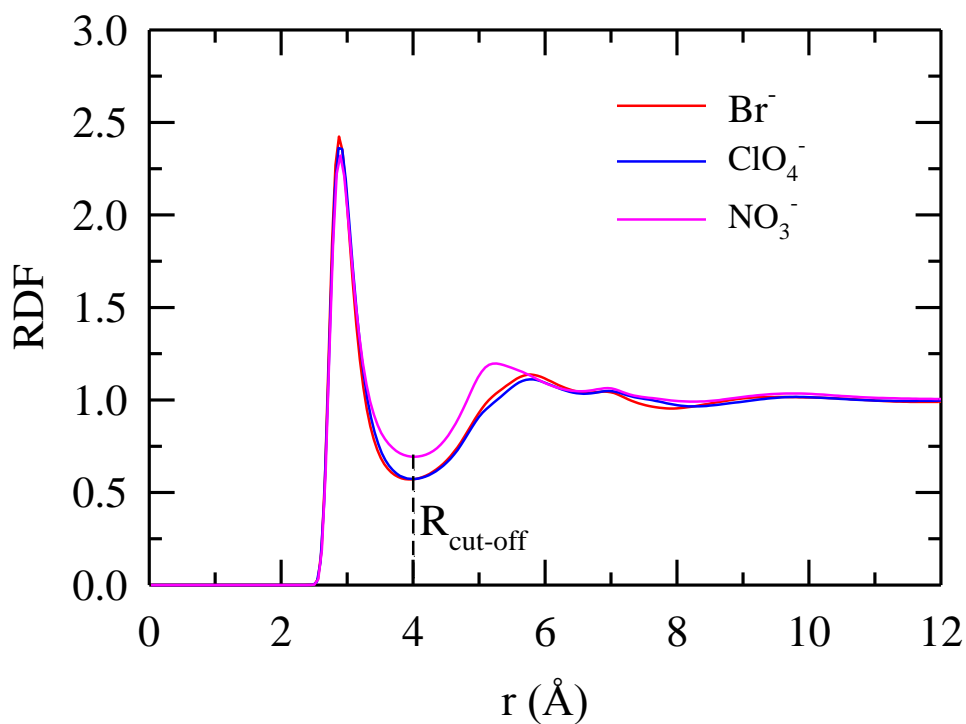


Figure 3.2. The above figure shows the simulated radial distribution function (RDF) calculated for the distance between the nitrogen atom of one acetamide molecule and the carbonyl oxygen belonging to another acetamide molecule. RDFs are presented for all three mixtures of acetamide and the lithium salts at 303 K. The cut-off distance (shown by the vertical line), identified as the distance where the first minima of the RDF occurs is used in the criteria for deciding whether pairs of acetamide molecules are H-bonded or not.

Based on the above H-bond definition we have identified the pairs of molecules involved in H-bonding. Then we assign a flag to each molecule like $\text{flag_H1}(i,t)$ for the first hydrogen atom of the acetamide molecule in question, where i is the index of the acetamide molecule and t is the snapshot of the simulation. If atom H1 of the i^{th} acetamide participates in H-bonding at time t , then the value of $\text{flag_H1}(i,t)$ gives the index of the acetamide molecule which is H-bonded to the i^{th} molecule. If the H1 atom does not participate in H-bonding, then the flag value is zero. Similarly, $\text{flag_H2}(i,t)$ is assigned for the second hydrogen atom of the i^{th} acetamide molecule as

both the H atoms of $-\text{NH}_2$ group of CH_3CONH_2 are capable of forming H-bond. In a similar way we can assign a flag value to X^- participating in H-bond. Since we have a mixture, where acetamide molecules can also form H-bonds with ions, we have devised a scheme of assigning the values of the flag. If the flag variables have a value between one and four hundred (the total number of acetamide molecules present in the system), it indicates that the chosen acetamide molecule forms a H-bond with another acetamide. Values of the flag between four hundred one and four hundred fifty six (fifty six ion pairs in the system) denote H-bonding with an anion. The cations of the salt can also participate in H-bond type interaction with the carbonyl oxygen of the acetamide molecules. This interaction is accounted for via a third flag, $\text{flag_c6O}(i,t)$, associated with each acetamide molecule.

Following this scheme, it is possible to construct a series of flag value for all molecules at all time instants. A representative picture is shown in Figure 3.3, where $\text{flag_H1}(i,t)$ has an initial value A which means the molecule with index number A was initially bonded to the molecule with index number i. Due to thermal fluctuations this H-bond breaks and the molecule with index number i performs a jump to bond with another molecule with index number B. Note there can be other processes where the H-bonds between a pair of molecules can temporarily break and then reform. These do not involve any change of H-bonding partner and, as a result, are not associated with large amplitude jumps. Here we are interested in the former set of microscopic processes which involve change of H-bond partner.

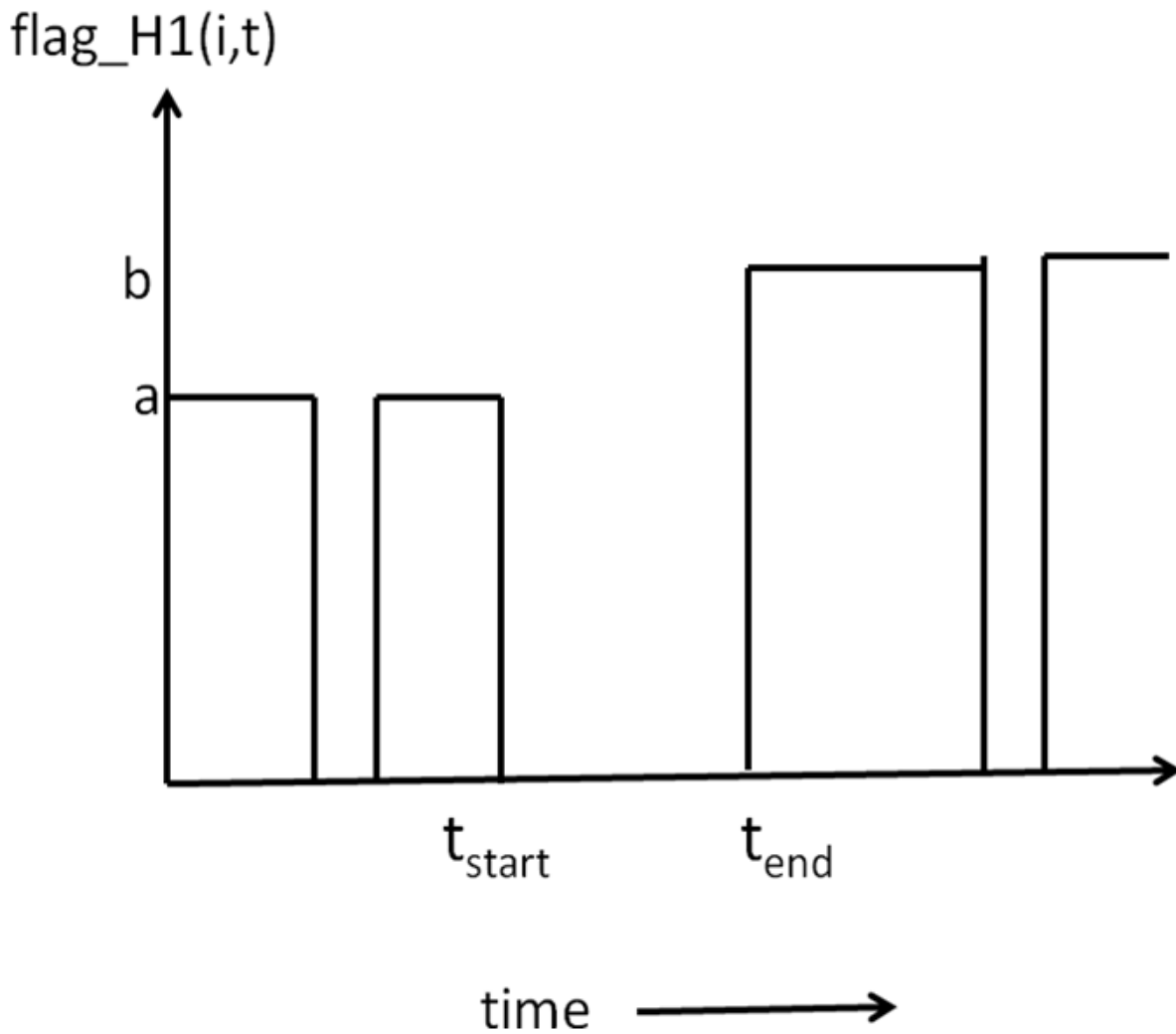


Figure 3.3. A schematic representation of the time-series of a typical flag variable associated with a randomly chosen acetamide molecule. It depicts a H-bond acceptor switching process, which is associated with large angular jumps of the chosen acetamide molecule. The starting and the ending times are also identified.

From the time series of flag values it is also possible to identify the starting (t_{start}) and the ending times (t_{end}) of each microscopic jump process as shown in Figure 3.4. The starting time (t_{start}) is defined as the last instant when the molecule with index “i” H-bonded to its initial acceptor, the molecule with index number A. Similarly, the ending time (t_{end}) is the first instant when the molecule with index number i is H-bonded to its final H-bond acceptor with

index number B. Note that if both indices A and B are less than or equal to 400, then it corresponds to a jump event between a pair of acetamide molecules (represented in left column of Figure 3.4). If the index number A is less than or equal to 400 and that of B is greater than 400, then it is an acetamide-ion jump (right column of Figure 3.4), and the reverse corresponds to an ion-acetamide jump.

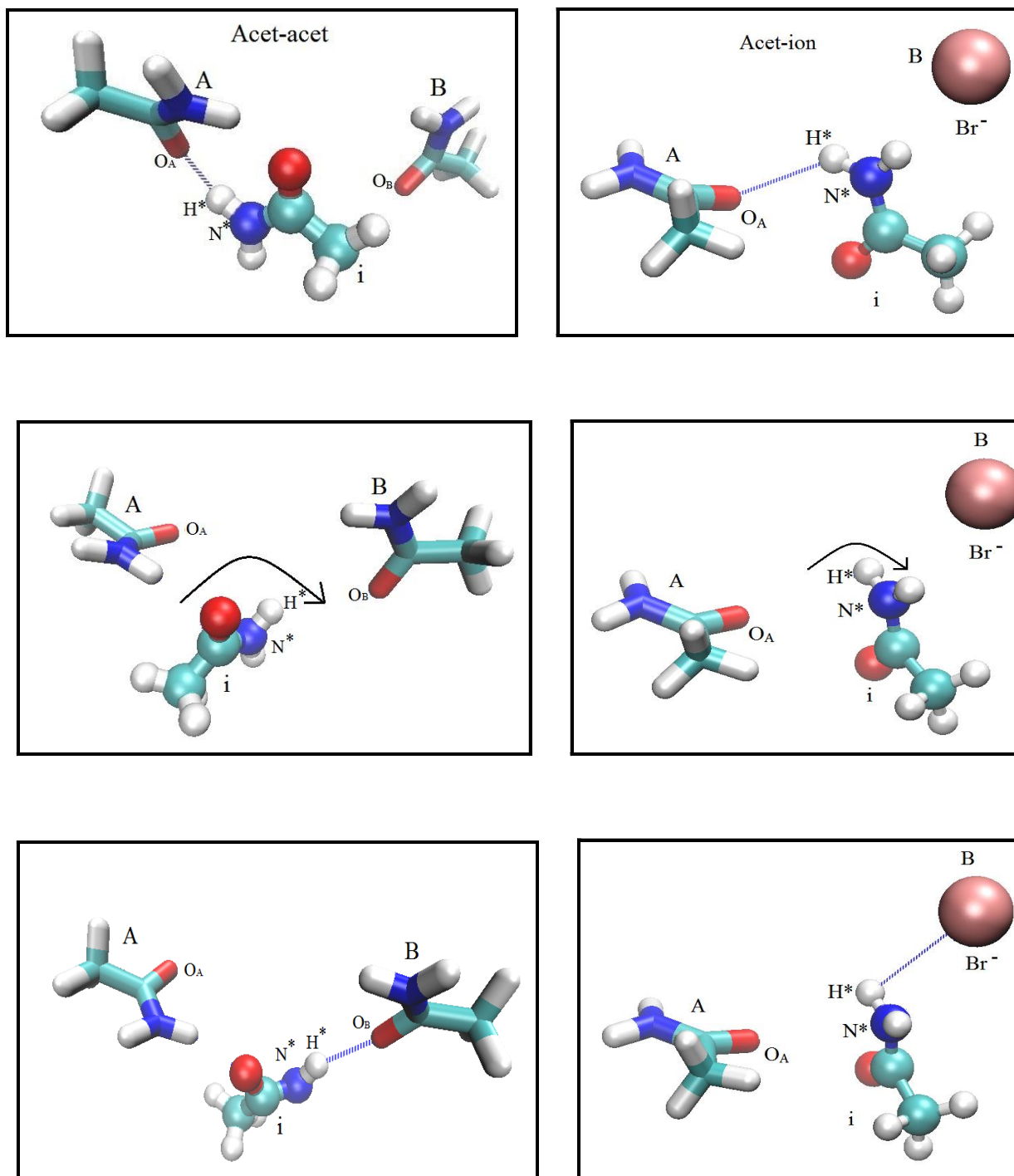


Figure 3.4. The three panels on the left show a microscopic jump process extracted from the simulations at 303 K, showing the i^{th} acetamide molecule (shown in ball and stick representation) undergoing a large angular jump resulting in a change of the identity of its H-bond acceptor. Molecule i is initially H-bonded to molecule A (uppermost panel) and finally to molecule B

(lowermost panel). The panels on the right show a similar process where molecule i is initially H-bonded to an acetamide molecule, but finally gets H-bonded to Br^- .

From analyzing the time-series of the two flag variables separately we find the identity of the initial and final H-bond acceptors of all the microscopic jump processes, and also their starting and ending times. Once we have identified the starting and ending times for all successful jumps, it is possible to compute various distributions like the distribution of jump time and waiting time for both acetamide-acetamide and acetamide-ion jumps. Suppose we are considering the j -th jump for i -th molecule. The microscopic jump time is the difference between $t_{\text{end}}(i,j)$ and $t_{\text{start}}(i,j)$. On the other hand, the microscopic waiting time is the difference between $t_{\text{start}}(i,j+1)$ and $t_{\text{end}}(i,j)$. During this waiting time H-bonds formed by molecule i remain intact, whereas during the jump a single H-bond is broken and a new one is formed, resulting in an exchange of the H-bond acceptor and molecule i performs a large amplitude angular jump. Further, these time distributions can be grouped into two types: the acetamide-acetamide and the acetamide-ion jump and waiting time distributions.

The identification of the transition state requires a simultaneous monitoring of the translational and the orientational coordinates. For the acetamide-acetamide jump it is defined as one occurring at that instant when the nitrogen atom of the rotating acetamide molecule, N^* , is equidistant from the oxygen atoms of both the initial and the final H-bond acceptors, O_A and O_B . To identify the transition state numerically we calculate the difference of the distances $R_{\text{N}^*\text{O}_A}$ and $R_{\text{N}^*\text{O}_B}$ within t_{start} and t_{end} , and identify the time instant when this difference is zero (within the prescribed numerical precision). The angle formed by the oxygen atom of the initial H-bond acceptor, O_A , the nitrogen atom of the rotating acetamide molecule, N^* , and the oxygen atom of the final H-bond acceptor, O_B , is the transition angle at the transition state. Schematic representations of these distances and angles associated with acetamide-acetamide and acetamide-ion jumps are provided in Figure 3.5.

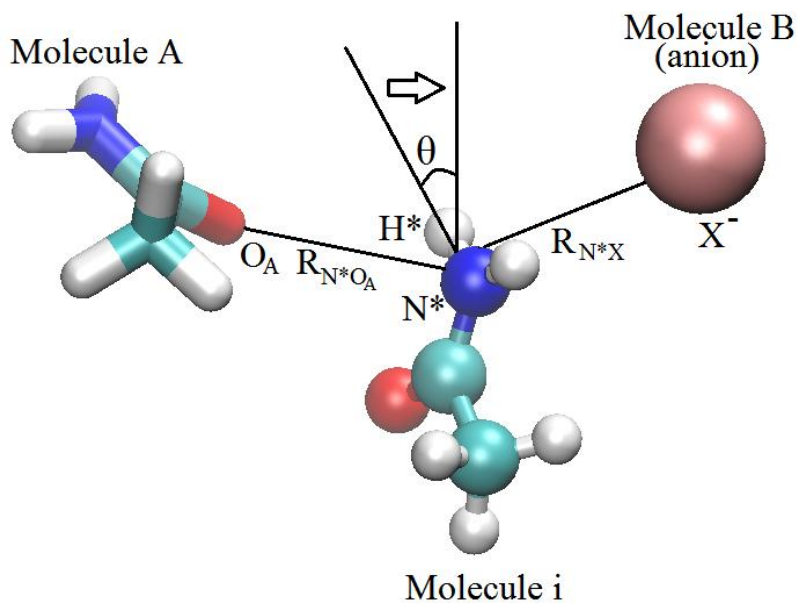
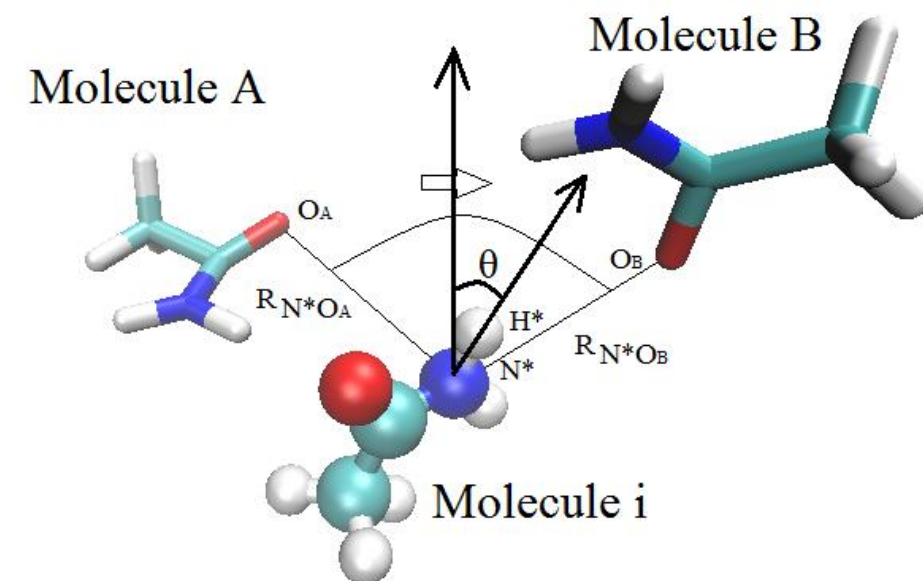


Figure 3.5. This figure shows the distance and angles which describe a jump process where the rotating acetamide molecule (ball and stick representation, molecule i) its initial H-bond acceptor (molecule A) and its final H-bond acceptor (molecule B). The distance between the nitrogen

atoms of molecule i and the oxygen atom O_A of molecule A, and oxygen atom O_B of molecule B are denoted by $R_{N^*O_A}$ and $R_{N^*O_B}$, respectively. The angle between the projection of the $N^* - H^*$ vector on the $O_A N^* O_B$ plane and the bisector of the angle $O_A N^* O_B$ is also marked. Both the initial and final acceptors are acetamide molecules in the top panel. The bottom panel shows the same distances and angles for a situation where the final acceptor is an anion (Br^- in this case).

Once the transition state is identified one can calculate the time evolution of average trajectory which is quantified in terms of three geometrical quantities, namely, $R_{N^*O_A}$, $R_{N^*O_B}$, and the angle formed by the projection of the $N^* - H^*$ vector on the $O_A N^* O_B$ plane and the bisector of the angle $O_A N^* O_B$ (see upper panel, Figure 3.5). In case of ion-acetamide or acetamide-ion jumps, identities of the initial or the final H-bond acceptors get suitably modified (see lower panel, Figure 3.5). Another important concept which goes into the calculations of the average trajectory is that of “coherent averaging”. During the “coherent averaging”, the transition states of the microscopic orientational jumps are chosen as the origin of time at the centre of the average trajectory with the jump starting at -250 fs and ending at +250 fs. In this fashion where one coincides the transition states of all the microscopic trajectories considered, one can extract the generic picture of orientational jump from microscopic trajectories, without loss of any important feature due to inherent thermal fluctuations. The duration of the time window of 500 fs has been decided by monitoring whether the distances and angles achieve their corresponding saturation values at the beginning and end of the average trajectories.

Finally, we have calculated the free energy associated with acetamide-acetamide and acetamide-ion orientational jumps. The free energy depends on three factors: (i) Δn_{HB} , the difference in coordination number of initial and final H-bond acceptors, (ii) ΔR , the difference in the distances between N^* and O_A , and N^* and O_B for acetamide-acetamide jumps (for acetamide-ion jumps the identity of the initial and the final H-bond acceptors are suitably modified), and (iii) an angular co-ordinate θ which is defined in Figure 3.5. A probability distribution

function, $P(\Delta n_{\text{HB}}, \Delta R, \theta)$ is then constructed. The procedure is similar to the one followed for liquid water³² and molten neat acetamide.⁴³ Consider the j^{th} orientational jump of a chosen molecule, and its starting and ending times are denoted by $t_{\text{start}}(j)$ and $t_{\text{end}}(j)$. We calculate the contributions to the probability distribution function, $P(\Delta n_{\text{HB}}, \Delta R, \theta)$ from three time intervals: (i) $t_{\text{end}}(j-1) < t < t_{\text{start}}(j)$, (ii) $t_{\text{start}}(j) < t < t_{\text{end}}(j)$, and (iii) $t_{\text{end}}(j) < t < t_{\text{start}}(j+1)$. Contributions arising from interval (i) contribute to the initial free energy minimum, contributions from interval (ii) contribute to the regions around the transition state of this reaction, and contributions from interval (iii) contribute to the final free energy minimum. During these intervals we calculate the value of the variables Δn_{HB} , ΔR and θ from microscopic MD trajectories, and construct a histogram by binning them. The sizes of the bins used in these calculations are $\Delta R = 0.1 \text{ \AA}$, $\Delta n = 1$, and $\Delta \theta = 3^\circ$. Finally, the free energy $G(\Delta n_{\text{HB}}, \Delta R, \theta)$ is determined using the following expression,^{32,43}

$$G(\Delta n_{\text{HB}}, \Delta R, \theta) = -k_{\text{B}} T \ln[P(\Delta n_{\text{HB}}, \Delta R, \theta)], \quad (3.2)$$

where $k_{\text{B}}T$ is the Boltzmann constant (k_{B}) times the absolute temperature (T).

3.4. Results and Discussion

Figures 3.6 and 3.7 show the time evolution of average trajectories for successful reorientation jumps for acetamide-acetamide and acetamide-ion couples, respectively. These average trajectories with error bars are presented in the Appendix B (Figure B6-FigureB11), which provide a sense of fluctuations in distance and angle during orientational jump. The upper panels of Figure 3.6 depict the time evolution of $R_{\text{N}^*\text{O}_\text{A}}$ and $R_{\text{N}^*\text{O}_\text{B}}$ for acetamide-acetamide reorientation jumps while the lower panels present the same for the angle formed by the projection of $\text{N}^*\text{-H}^*$ on the $\text{O}_\text{A}\text{N}^*\text{O}_\text{B}$ plane and the angle bisector of the angle $\text{O}_\text{A}\text{N}^*\text{O}_\text{B}$ (as represented in Figure 3.5). These trajectories exhibit a symmetric transition state, which occurs when $R_{\text{N}^*\text{O}_\text{A}}$ equals $R_{\text{N}^*\text{O}_\text{B}}$. Additionally, at this transition state, the projection of $\text{N}^*\text{-H}^*$ on the $\text{O}_\text{A}\text{N}^*\text{O}_\text{B}$ plane and the angle bisector of the angle $\text{O}_\text{A}\text{N}^*\text{O}_\text{B}$ coincide (angle between these lines is zero). This underlines the inherent translation-rotation coupling which is present in H-bonded

systems, and has already been observed for liquid water^{32,45} and molten acetamide.⁴³ For acetamide-ion reorientation jumps, the time evolution of $R_{N^*O_A}$ is shown in the upper panel of Figure 3.7, while the lower panel depicts the same for the angle formed by the projection of N^*H^* vector on the $O_A N^* X / X N^* O_A$ plane and the angle bisector of the angle $O_A N^* X / X N^* O_A$. The average trajectories for the acetamide-ion orientational jumps (Figure 3.7) appear to exhibit a transition state that is symmetric. This does not generally occur for a binary system, as observed in simulations of water in the first hydration shells of fluoride and iodide ions.⁶² However, it appears here because we have calculated the average trajectory by combining ion-acetamide and acetamide-ion events, both of which are equally probable.

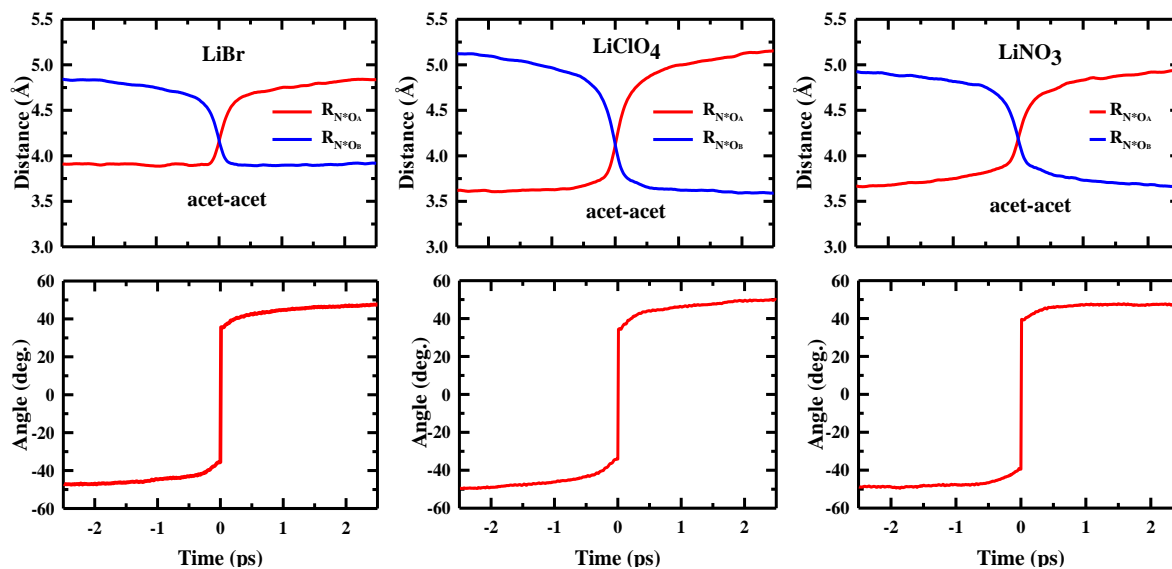


Figure 3.6. The average trajectory in terms of the geometrical quantities (see Figure 3.5) at 303 K. Columns starting from left show data from simulations of mixture of acetamide and lithium bromide, perchlorate and nitrate, respectively. The top panels show the time-evolution of separation between the rotating acetamide and its initial H-bond acceptor (red curve) and the final H-bond acceptor (blue curve). The bottom panel shows the time evolution of the angle which defines the angular jump (see Figure 3.5 for definition). Here both the initial and the final H-bond acceptors are acetamide molecules. All plots show data for acetamide-acetamide orientational jumps.

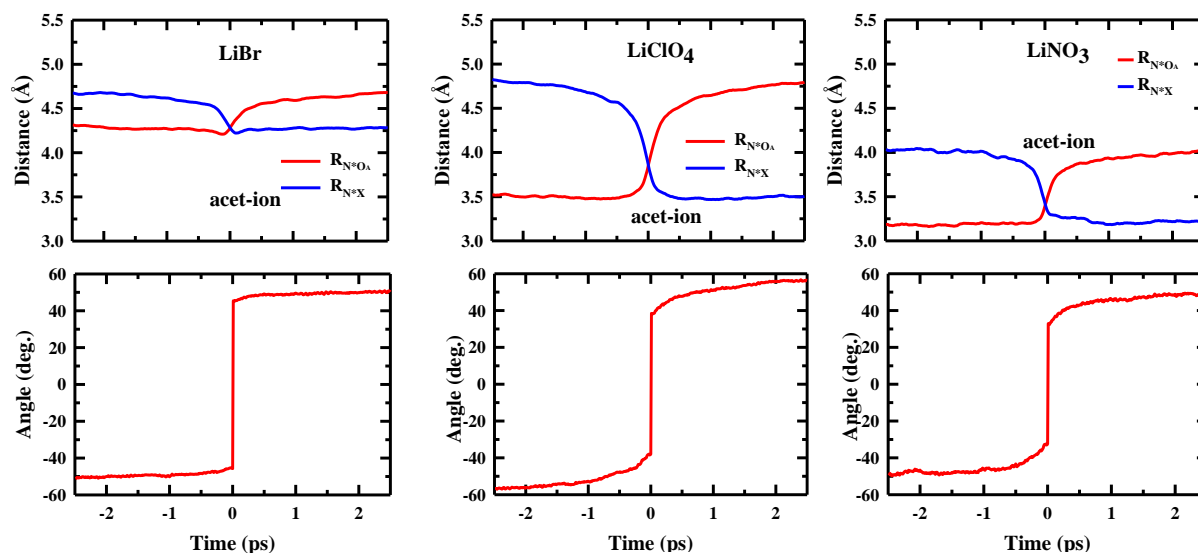


Figure 3.7. Average trajectories similar to those shown in Figure 3.6, but are calculated for acetamide-ion orientational jumps at 303 K.

Since variables associated with translation and orientation which define the average trajectories, saturate both at the beginning and at the end of the trajectories, it is possible to define a mean translational and orientational displacement associated with each average trajectory. Table 3.1 shows a comparison of the anion dependence of the change in the separation between the rotating acetamide molecule and its initial and final hydrogen bond acceptors, and in the angle associated with average trajectories. It appears that the change in displacement is more prominent than that in angle, irrespective of the nature of anion for both acetamide-acetamide and acetamide-ion jumps. In addition, these changes reflect the following ascending sequence: $\text{Br}^- < \text{NO}_3^- < \text{ClO}_4^-$, which follows the size-sequence of these ions.²¹ The correlation between displacement (radial distance) amplitude and ion size (see Table 3.1) suggests excluded volume effects on orientational jumps. The extent of displacement is smaller for acetamide-ion jumps than that for acetamide-acetamide in all these cases. Stronger electrostatic interaction between acetamide molecules and anions may be a reason for this. Among the anions, the displacement is the largest for ClO_4^- and smallest for Br^- with NO_3^- in between for both

acetamide-acetamide and acetamide-ion reorientation. Note this depicts a trend reverse of viscosity (η) values of these (acetamide + LiX) deep eutectics: η (cP) = 1300, 210 and 158 when the anions (X^-) are Br^- , NO_3^- and ClO_4^- , respectively.^{23,26}

Table 3.1: Anion dependence of changes in radial distance and angle during orientation jumps in (Acetamide + LiX) DESs.

Anion (X^-)	Radius (\AA)	Acetamide-Acetamide			Acetamide-Ion		
		Distance ($\Delta R / \text{\AA}$)	$\Delta R / \sigma_{\text{acet}}$	Angle (degree)	Distance ($\Delta R / \text{\AA}$)	$\Delta R / \sigma_{\text{acet}}$	Angle (degree)
Br^-	1.82 ^b	0.91	0.20 ^a	94	0.35	0.08	100
ClO_4^-	2.4	1.53	0.34	100	1.29	0.28	112
NO_3^-	1.96	1.25	0.27	96	0.85	0.19	98

a) $\sigma_{\text{acet}} = 4.52 \text{\AA}$ (from Refs.25). b) ion radii are from Ref. 23

Figure 3.8 shows the time evolution of the number of H-bonds. Error-bars associated with these trajectories are provided in Appendix B (Figure B12-Figure B14). Note the overlapping error-bars in these figures indicate that H-bond coordination numbers indeed saturate at long times to their corresponding equilibrium values. The upper panel shows the change in number of H-bonds for acetamide-acetamide reorientation and the lower panel shows the same for acetamide-ion

reorientation. On an average, the number of H-bonds formed by the initial and final donors for acetamide-acetamide reorientation are ~ 2.4 , ~ 3.0 and ~ 3.0 in presence of Br^- , NO_3^- and ClO_4^- , respectively. This number remains almost the same for acetamide-ion reorientation as well. Table 3.2 shows the change in number of H-bonds for successful jump reorientations. The fluctuation in H-bond network is one of the main driving forces for jump reorientation of acetamide molecules. Due to fluctuations in H-bond network, the initial donor, O_A becomes over-coordinated while the final donor O_B/X becomes under-coordinated. This facilitates the motion of N^*-H^* to shift from initially over-coordinated donor to under coordinated final donor. It is evident from Table 3.2 that the change in number of H-bond coordination is higher for acetamide-acetamide jumps ($\Delta n_{\text{HB}} \sim 0.2$) than that associated with acetamide-ion jumps ($\Delta n_{\text{HB}} \sim 0.1$). The fact that this difference is almost negligible for acetamide-ion jumps for LiBr is nicely reflected in the distribution of jump time (shown below) and the shape of the corresponding free energy barrier (discussed later).

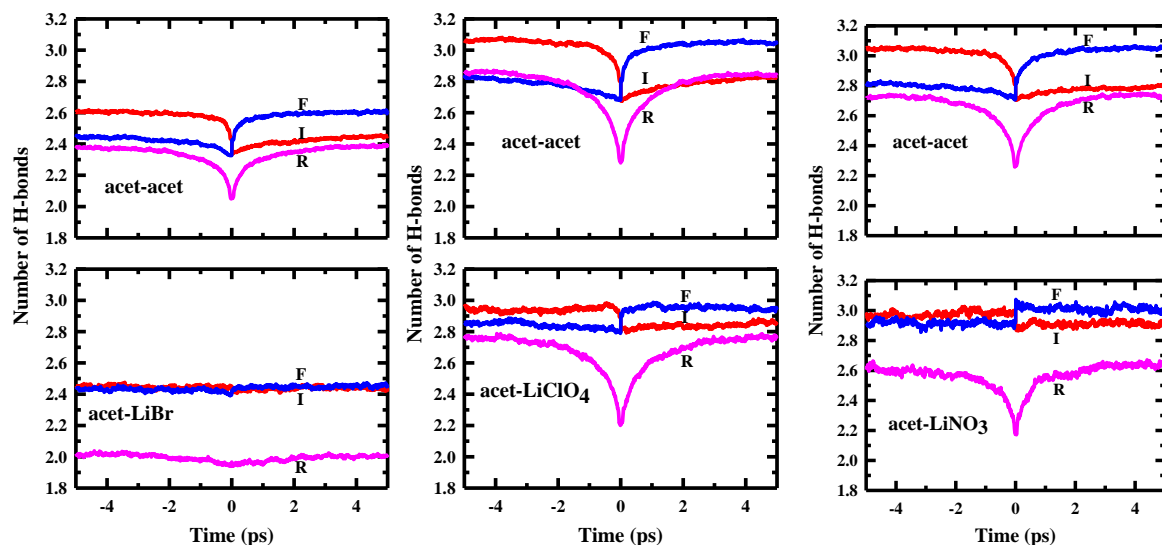


Figure 3.8. This figure shows the time evolution of the H-bond coordination number at 303 K. Columns starting from left show data from simulations of mixture of acetamide and lithium bromide, perchlorate and nitrate, respectively. The upper panels show the time evolution of the H-bond coordination number for the acetamide-acetamide orientational jumps and the bottom

panel shows the same for acetamide-ion jumps. The red curves denote H-bond coordination for the initial (“T”) acceptor, the blue curves denote the final (“F”) acceptor and the pink lines denote the same for the rotating (“R”) acetamide molecule.

Table 3.2: Anion dependence of changes in hydrogen bond coordination number, Δn_{HB} , for acetamide in (acetamide + LiX) DESs.

Anion (X^-)	Acetamide-Acetamide	Acetamide-Ion
Br^-	0.2	0.0
ClO_4^-	0.2	0.1
NO_3^-	0.2	0.1

The simulated jump time distributions for acetamide-acetamide and acetamide-ion are shown in Figure 3.9. As mentioned earlier, the microscopic jump time is the difference between the first instant when the rotating acetamide molecule is H-bonded to its final acceptor and the last instant when it was H-bonded to its initial acceptor. The dependence on anion is evident in both the panels where the slowest long-time tail appears for deep eutectics containing LiBr, and the fastest for the system that contains LiClO_4 . As the fits indicate, these distributions at long times follow a power-law dependence of the type, $P(t_{\text{jump}}) \propto A(t_{\text{jump}}/\tau)^{-\beta}$, where both β and τ shows considerable anion dependence. This is further quantified in the fit parameters summarized in the insets of Figure 3.9. Such a power-law dependence of long-time tail suggests dynamic heterogeneity,⁶³⁻⁶⁵ and is the origin for fractional viscosity dependence of average relaxation times measured earlier via time-resolved fluorescence measurements.²³⁻²⁷ Note for molten neat acetamide⁴³ the corresponding distribution was single-exponential, reflecting homogeneous dynamics. Values for both β and τ obtained here follow, similar to radial and angular displacements, a sequence inverse to the viscosity trend (that is, $\eta_{\text{LiBr}}^{\text{DES}} > \eta_{\text{LiNO}_3}^{\text{DES}} > \eta_{\text{LiClO}_4}^{\text{DES}}$) for these DESs. This is expected because search for a H-bond acceptor during ‘flight’ involves angular

displacements through the medium. Interestingly, the long-time decay rates for acetamide-acetamide jump-time distribution are slower than the corresponding acetamide-ion jump-time distributions. The presence of electronic charge on the anions may facilitate the search for an appropriate H-bond acceptor and effectively reduce the search-time for those jumps that involve breaking an acetamide-acetamide bond and the subsequent formation of acetamide-ion bond. The reverse process that involves breaking of an acetamide-ion bond will also be a part of the total jump distributions, but contribution of this process is expected to be less because of enhanced stability of such bonds.

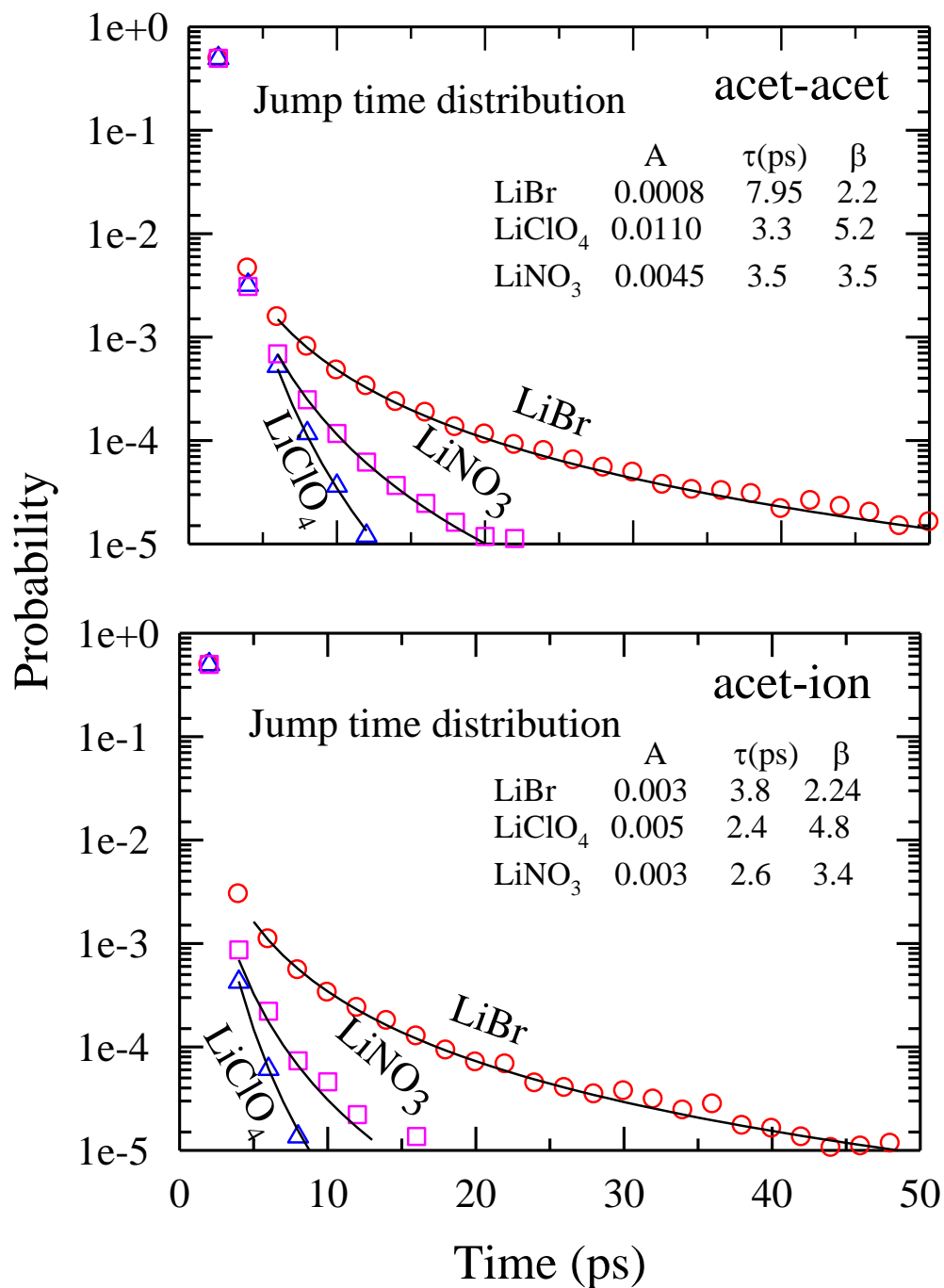


Figure 3.9. This figure shows the distribution of the jump times for the acetamide-acetamide (upper panel) and the acetamide-ion jumps (lower panel) for these DESs at 303 K. Fit parameters required for describing the power law dependence of long-time tails of jump time distributions are summarized in the insets.

Figure 3.10 demonstrates the jump angle distributions for acetamide molecules calculated between starting and ending time of the microscopic jumps. The upper panel shows the anion dependence of jump angle distribution for acetamide-acetamide jump while the lower panel shows the same for acetamide-ion jump. For comparison, simulated jump angle distribution for molten neat acetamide⁴³ is also shown. Note the acetamide-acetamide jump angle distributions in these DESs, although possess similar shape as that for molten acetamide, are shifted toward relatively lower angles, reflecting electrolyte effects. In addition, the dependence on anion identity of these distributions is weak, with the jump angles peaking around $\sim 55^\circ$ for NO_3^- , and ClO_4^- , and $\sim 59^\circ$ for Br^- . Also, these distributions in presence of electrolytes are broader than that for molten acetamide, with the maximum width for DES containing ClO_4^- . Except for the case of Br^- , the distributions for acetamide-ion jumps are relatively narrower and shifted to lower angles compared to that for molten acetamide-acetamide case. The peak position in jump angle distribution is around 54° for NO_3^- and ClO_4^- like the corresponding acetamide-acetamide jumps. Note a shoulder at a larger angle ($\sim 80^\circ$) appears for acetamide-ion jumps in case of ClO_4^- . Interestingly, the distribution in presence of Br^- for acetamide-ion jumps is bimodal with peaks of nearly equal intensity at $\sim 64^\circ$ and $\sim 88^\circ$, and is completely different in shape from other distributions. However, the primary peak of the double-peak distribution almost coincides with the distribution for molten acetamide.⁴³ To understand what kind of local structure renders this bimodality, we have selected two snapshots depicting the jump angles of the peak. Figure 3.11 presents the transition state configurations of the acetamide-ion jumps corresponding to above-mentioned orientational jumps in (acetamide + LiBr) DES. For ClO_4^- containing DES, similar configuration is also present and renders shoulder at higher angle. Such a diversity in jump angle distribution indicates complexity of interactions of these anions with acetamide molecules.

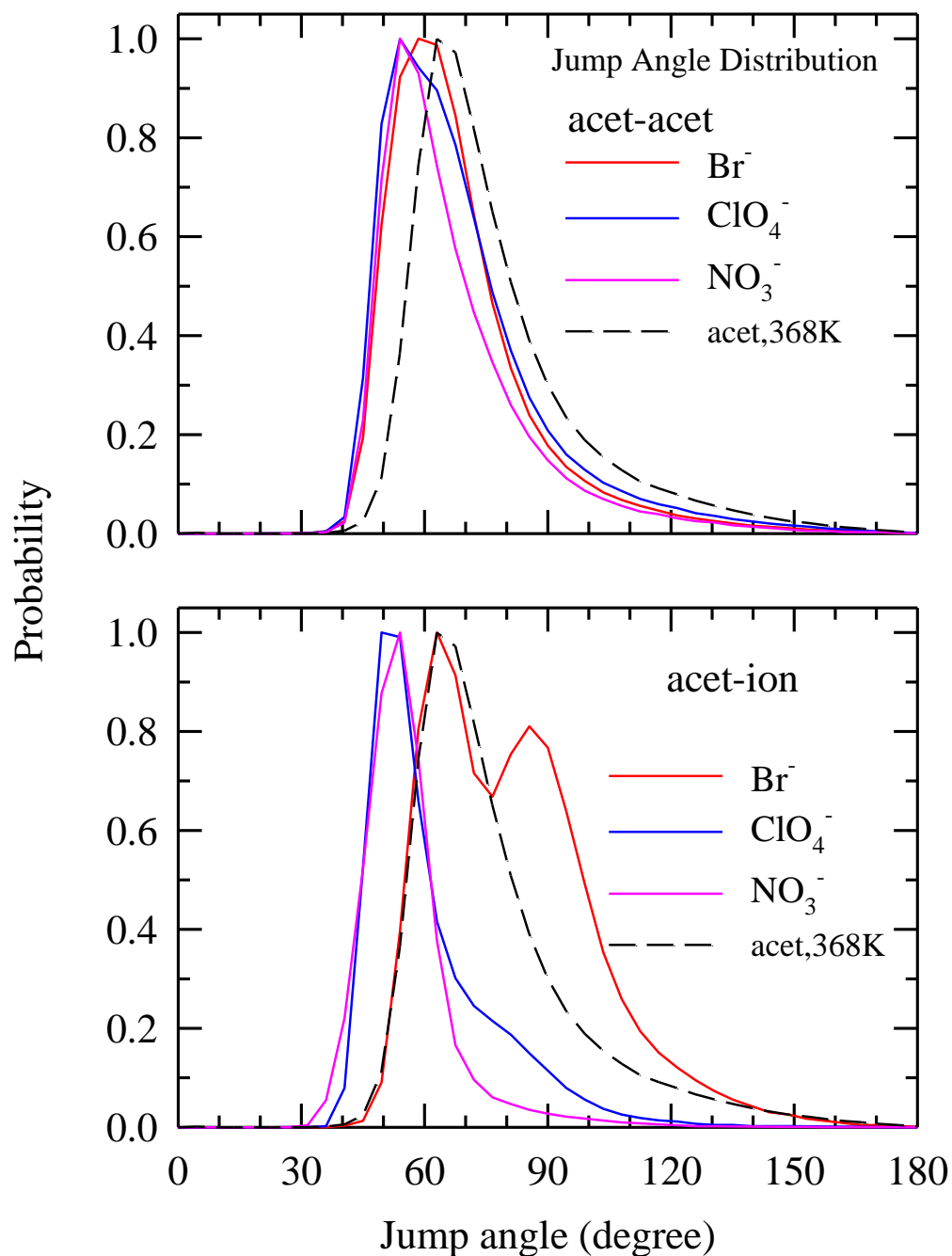


Figure 3.10. Simulated jump angle distribution of the N*-H* vector for the acetamide-acetamide (upper panel) and acetamide-ion jumps (lower panel) at 303 K. For comparison, jump angle distribution for molten neat acetamide is also shown (dashed line) in both the panels.

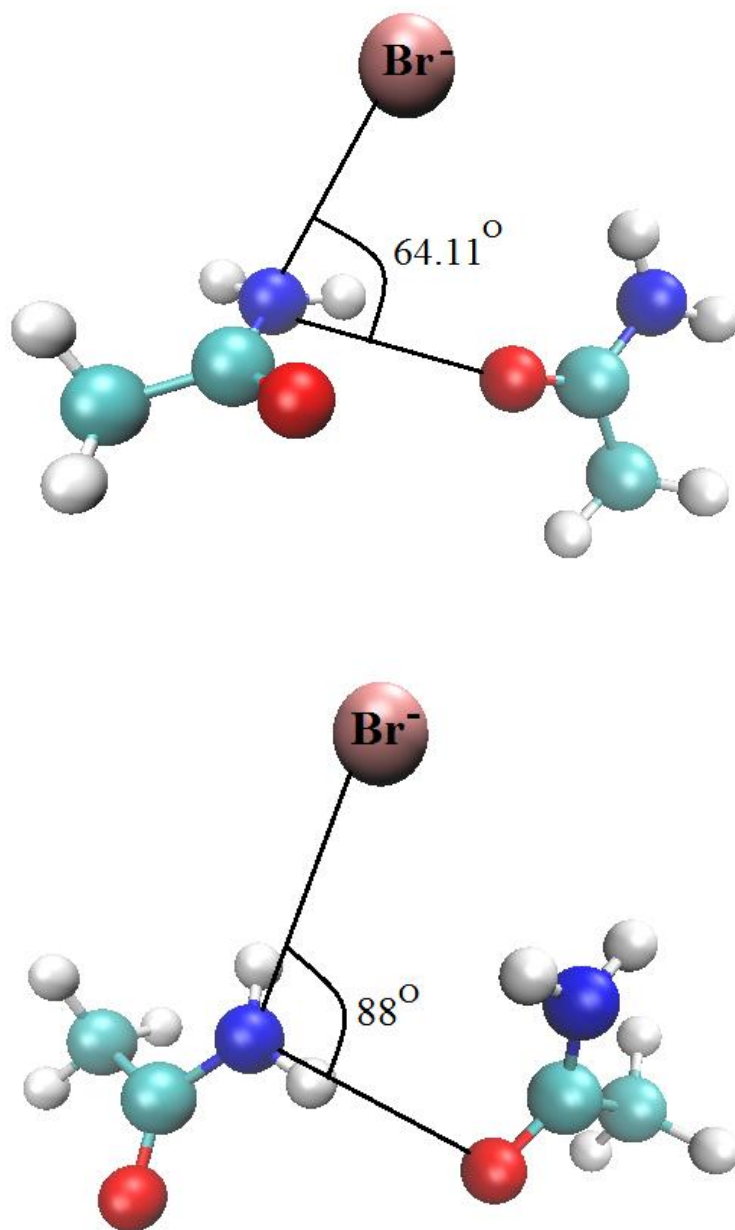


Figure 3.11. Transition state configurations corresponding to the two peaks of the bimodal, acetamide-ion jump angle distribution for DES made of acetamide and lithium bromide at 303 K.

Figure 3.12 shows the free energy (in the units of $k_B T$) as a function of time along the average jump trajectories shown in Figures 3.6 and 3.7. Note these free energies have been obtained via projection of the average trajectory on the full free energy surface described by Equation 3.2. It is possible to perform projections once we have calculated the free energy surface and the time dependence of the geometrical quantities characterizing the average trajectories. For each time instant of the average trajectory, we find the values of the reaction coordinates (ΔR , θ , Δn) and the corresponding free energies. This process is then repeated for the whole length of the average trajectory for obtaining an average free energy which is a function of time. We have chosen a convention similar to the one which has been used to calculate the average trajectories, where all transition states have been chosen to occur at time, $t = 0$. This process of obtaining time-dependent free energies has been executed for both acetamide-acetamide and acetamide-ion jumps. The upper panel shows anion-dependent free energy profile for acetamide-acetamide jumps, and the lower panel presents the same for the ion-acetamide jumps. While the acetamide-acetamide free energy barrier is weakly dependent on ion-identity, the ion-acetamide free energy barrier shows a significant anion dependence, with the free energy barrier for NO_3^- being the highest ($\sim 1.0 K_B T$) and ~ 2 times as large as that for ClO_4^- ($\sim 0.5 K_B T$). Table 3.3 summarizes the anion dependent free energy barriers for orientation jumps in these DESs. Note the free energy barrier simulated for acetamide-acetamide jumps in these DESs is, on an average, very similar to the barrier ($\sim 0.7 k_B T$) found for molten neat acetamide.⁴³ The free energy profile in presence of Br^- is not as sharp as in presence of the other two anions. This can be connected to the lowest values for ΔR , and Δn (see Tables 3.1 and 3.2) in presence of Br^- which creates a relatively shallower and more flat free energy surface for the corresponding acetamide-ion jumps.

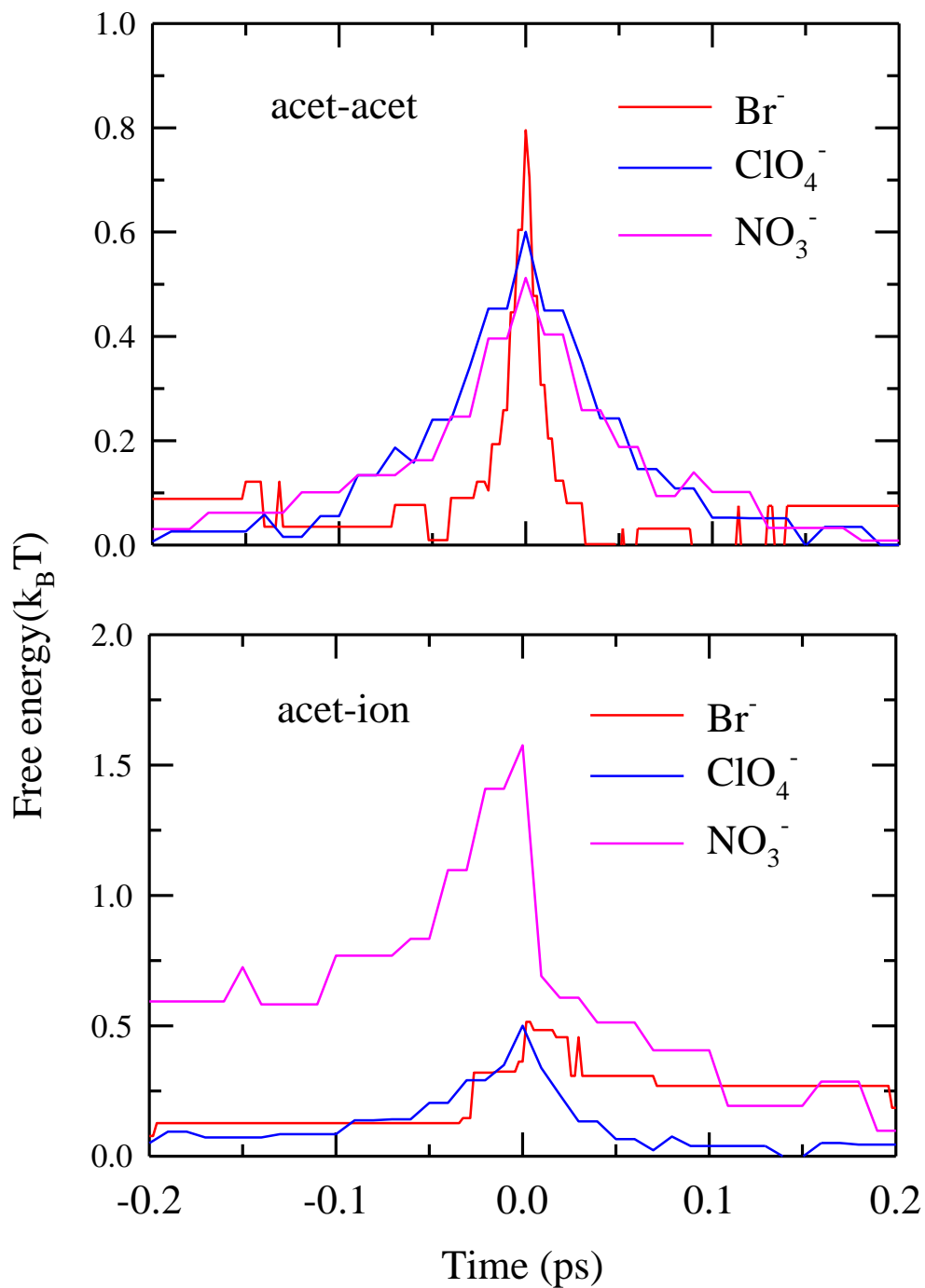


Figure 3.12. Temporal evolution of the free energies corresponding to the average trajectories associated with acetamide-acetamide (upper panel) and acetamide-ion (lower panel) orientational jumps in these DESs at 303 K. Anion dependence of the barrier is summarized in **Table 3.3**.

Table 3.3: Anion dependent free energy barrier for orientation jumps in (Acetamide + LiX) DESs.

Anion (X^-)	Acetamide-Acetamide (in $k_B T$ unit)	Acetamide-Ion (in $k_B T$ unit)
Br^-	0.8	0.4
ClO_4^-	0.6	0.5
NO_3^-	0.5	1.0

3.5. Concluding Remarks

We summarize by stating that orientational jump characteristics of acetamide depends significantly on the identity of the anion present in these (acetamide + LiX) DESs. Jump reorientations have been separated into acetamide-acetamide and acetamide-ion contributions, and electrolyte effects have been observed for both the components. Large angle jumps are found to be more frequent in systems containing ClO_4^- and Br^- than those in NO_3^- . Acetamide-acetamide jump angle distributions are narrower and shifted to lower angles compared to that in molten neat acetamide.⁴³ Interestingly, these distributions for acetamide-ion species show a bimodality for Br^- and a shoulder for ClO_4^- but no such features in case of NO_3^- . Substantial translation-rotation coupling has been observed for jump reorientation in all these systems with the extent depending on identity of the anion. In addition, change in relative radial distance (ΔR) and difference in H-bond coordination number (Δn_{HB}) between initial and final acceptors have been found to be significantly less than those found in molten neat acetamide.⁴³ Jump time distributions follow power-law dependence at long-times reflecting dynamic heterogeneity in these systems, with the tail decay rate being the slowest for Br^- containing DES among the three such systems studied here. Free energy barrier for orientational jumps also registers electrolyte dependence with the electrolyte effects more pronounced on acetamide-ion jumps than that involves acetamide-acetamide jumps.

Although the present work have separated out acetamide-acetamide and acetamide-ion jumps, the effects due to interaction between cation (Li^+) and carbonyl oxygen of acetamide molecules on these jumps have not been analyzed. Also, exchange of H-bond partners between anions and subsequent effects on jump characteristics need to be investigated. Orientational relaxation in these heterogeneous molten mixtures and its connection to waiting time distribution would be interesting as that would provide microscopic picture for understanding experimental dielectric relaxation (DR) data. These and other DESs, being industrially relevant and rich in important basic scientific aspects, warrant further experimental and simulation study not only for smarter large scale applications but also for examining the applicability of the language that describe dynamics of supercooled liquids.⁶³⁻⁶⁵ Exploring the interconnection between orientational relaxation and jumps for confined water,⁶⁶⁻⁶⁸ and that between non-exponentiality in dielectric relaxation of ionic liquids^{69,70} and orientation jumps would also be exciting future problems.

It is to be mentioned here that the simulation results presented here have been obtained by using non-polarizable potential functions. Inclusion of polarizabilities, therefore, may alter the angular displacement mechanism reflected by the presented analyses.⁷¹ Interestingly, very recent DR measurements of these and a few other DESs in the frequency window $0.2 \leq \nu/\text{GHz} \leq 50$ have indeed revealed a strong dependence on ion identity of both static dielectric constant and relaxation times.⁷² The average ion-dependent DR relaxation times have been found to deviate strongly from the hydrodynamic predictions, hinting at orientation mechanisms that are different from Brownian rotational moves. In addition, reorientation jump picture for water have been found to remain unaltered even after inclusion of polarizability in the interaction potential.³³ All these seem to indicate that the orientational jump mechanism for acetamide molecules in these DESs reflected by the present simulations may not be drastically altered upon inclusion of polarizability. Contribution of the orientation-coupled centre-of-mass movements on the total translational dynamics⁷³ of ions and acetamide molecules needs to be separated out for a quantitative understanding of mass transport in these heterogeneous and industrially important solvents.

References

1. D. V. Wagle, H. Zhao, and G. A. Baker, *Acc. Chem. Res.* **47**, 2299 (2014).
2. Q. Zhang, K. De Oliveira Vigier, S. Royer, and F. Jérôme, *Chem. Soc. Rev.* **41**, 7108 (2012).
3. A. P. Abbott, G. Capper, D. L. Davies, R. K. Rasheed, and V. Tambyrajah, *Chem. Commun.* 70 (2003).
4. A. P. Abbott, D. Boothby, G. Capper, D. L. Davies, and R. K. Rasheed, *J. Am. Chem. Soc.* **126**, 9142 (2004).
5. M. Francisco, A. van den Bruinhorst, and M. C. Kroon, *Angew. Chem. Int. Ed.* **52**, 3074 (2013).
6. A. P. Abbott, G. Capper, D. L. Davies, H. L. Munro, R. K. Rasheed, and V. Tambyrajah, *Chem. Commun.* 2010 (2001).
7. A. P. Abbott, G. Capper, D. L. Davies, and R. Rasheed, *Inorg. Chem.* **43**, 3447 (2004).
8. A. P. Abbott, G. Capper, D. L. Davies, R. K. Rasheed, and V. Tambyrajah *Green Chem.* **4**, 24 (2002).
9. A. P. Abbott, G. Capper, D. L. Davies, and R. K. Rasheed, *Chem. Eur. J.* **10**, 3769 (2004).
10. A. P. Abbott, K. E. Ttaib, G. Frisch, K. J. McKenzie, and K. S. Ryder, *Phys. Chem. Chem. Phys.* **11**, 4269 (2009).
11. R. A. Wallace, *Inorg. Chem.* **11**, 414 (1972).
12. D. H. Kerridge, *Chem. Soc. Rev.* **17**, 181 (1988).
13. O. F. Stafford, *J. Am. Chem. Soc.* **55**, 3987 (1933).
14. G. van der Zwan and J. T. Hynes, *J. Chem. Phys.* **78**, 4174 (1983).
15. G. van der Zwan and J. T. Hynes, *Chem. Phys.* **152**, 169 (1991).

16. T. Pradhan and R. Biswas, *J. Phys. Chem. A* **111**, 11524 (2007).
17. G. Berchiesi, *J. Mol. Liq.* **83**, 271 (1999).
18. A. Amico, G. Berchiesi, C. Cametti, and A. D. Biasio, *J. Chem. Soc., Faraday Trans. 2*, **83**, 619 (1987).
19. G. Berchiesi, F. Farhat, and M. de Angelis, *J. Mol. Liq.* **54**, 103 (1992).
20. G. Berchiesi, G. Vitali, P. Passamonti, and R. Plowiec, *J. Chem. Soc., Faraday Trans. 2*, **79**, 1257 (1983).
21. G. Berchiesi, G. Rifaiani, G. Vitali, and F. Farhat, *J. Therm. Anal.* **44**, 1313 (1995).
22. F. Farhat and G. Berchiesi, *J. Mol. Liq.* **54**, 131 (1992).
23. B. Guchhait, S. Das, S. Daschakraborty, and R. Biswas, *J. Chem. Phys.* **141**, 104514 (2014).
24. A. Das, S. Das, and R. Biswas, *Chem. Phys. Lett.* **581**, 47 (2013).
25. B. Guchhait, H. A. R. Gazi, H. K. Kashyap, and R. Biswas, *J. Phys. Chem. B* **114**, 5066 (2010).
26. B. Guchhait, S. Daschakraborty, and R. Biswas, *J. Chem. Phys.* **136**, 174503 (2012).
27. H. A. R. Gazi, B. Guchhait, S. Daschakraborty, and R. Biswas, *Chem. Phys. Lett.* **501**, 358 (2011).
28. R. Biswas, A. Das, and H. Shirota, *J. Chem. Phys.* **141**, 134506 (2014).
29. T. Pal and R. Biswas, *Chem. Phys. Lett.* **517**, 180 (2011).
30. B. Bagchi, *Molecular Relaxation in Liquids*, Oxford University Press, (2012).
31. D. Laage and J. T. Hynes, *Science* **311**, 832 (2006).
32. D. Laage and J. T. Hynes, *J. Phys. Chem. B* **112**, 14230 (2008).
33. D. Laage and J. T. Hynes, *Proc. Natl. Acad. Sci. U.S.A.* **104**, 11167 (2007).
34. D. Laage, G. Stirnemann, and J. T. Hynes, *J. Phys. Chem. B* **113**, 2428 (2009).

35. G. Stirnemann, J. T. Hynes, and D. Laage, *J. Phys. Chem. B* **114**, 3052 (2010).
36. D. Laage and J. T. Hynes, *J. Phys. Chem. B* **112**, 7697 (2008).
37. G. Stirnemann, E. Wernersson, P. Jungwirth, and D. Laage, *J. Am. Chem. Soc.* **135**, 11824 (2013).
38. D. Laage, G. Stirnemann, F. Sterpone, R. Rey, and J. T. Hynes, *Annu. Rev. Phys. Chem.* **62**, 395 (2011).
39. G. Stirnemann, P. J. Rossky, J. T. Hynes, and D. Laage, *Faraday Discuss.* **146**, 263 (2010).
40. G. Stirnemann, S. R. V. Castrillón, J. T. Hynes, P. J. Rossky, P. J. Debenedetti, and D. Laage, *Phys. Chem. Chem. Phys.* **13**, 19911 (2011).
41. F. Sterpone, G. Stirnemann, and D. Laage, *J. Am. Chem. Soc.* **134**, 4116 (2012).
42. B. Mukherjee, P. K. Maiti, C. Dasgupta, and A. K. Sood, *J. Phys. Chem. B* **113**, 10322 (2009).
43. S. Das, R. Biswas, and B. Mukherjee, *J. Phys. Chem. B* **2015**, 119, 274-283.
44. A. A. Vartia, K. R. Mitchell-Koch, G. Stirnemann, D. Laage, and W. H. Thompson, *J. Phys. Chem. B* **115**, 12173 (2011).
45. G. Stirnemann, F. Sterpone, and D. Laage, *J. Phys. Chem. B* **115**, 3254 (2011).
46. W. Smith and T. R. Forster, *The DL_POLY Molecular Simulation Package*, Daresbury Laboratory: Cheshire, U. K (1999).
47. A. Das, S. Das, and R. Biswas, *J. Chem. Phys.* **142**, 034505 (2015).
48. A. D. MacKerellJr., J. Wiorcikiewicz-Kuczera, and M. Karplus, *J. Am. Chem. Soc.* **117**, 11946 (1995).
49. K. P. Jensen and W. L. Jorgensen, *J. Chem. Theory Comput.* **2**, 1499 (2006).
50. C. Cadena and E. J. Maginn, *J. Phys. Chem. B* **110**, 18026 (2006).

51. J. N. C. Lopes and J. Deschamps, *J. Phys. Chem. B* **108**, 2038 (2004).
52. C. W. Yong, *DL_FIELD*, STFC Daresbury Laboratory: Cheshire, U.K. (2011), http://www.cse.scitech.ac.uk/ccg/software/DL_FIELD.
53. M. P. Allen and D. J. Tildesley, *Comput. Simulations Liq.*; Oxford University Press: New York, (1987).
54. L. Martinez, R. Andrade, E. G. Birgin, and J. M. Martinez, *J. Comput. Chem.* **30**, 2157 (2009).
55. S. Nose, *J. Chem. Phys.* **81**, 511 (1984).
56. W. G. Hoover, *Phys. Rev. A* **31**, 1695 (1985).
57. A. Luzar, *Faraday Discuss.* **103**, 29 (1996).
58. T. C. Berkelbach, H. S. Lee, and M. E. Tuckerman, *Phys. Rev. Lett.* **103**, 238302 (2009).
59. A. Chandra, *Phys. Rev. Lett.* **85**, 768 (2000).
60. S. Balasubramanian, S. Pal, and B. Bagchi, *Phys. Rev. Lett.* **89**, 115505 (2002).
61. S. Indra and R. Biswas, *Molecular Simulations.* **41**, 471 (2015).
62. J. Boisson, G. Stirnemann, D. Laage, and J. T. Hynes, *Phys. Chem. Chem. Phys.* **13**, 19895 (2011).
63. E. Flenner and G. Szamel, *Phys. Rev. E* **72**, 011205 (2005).
64. P. G. Wolynes and V. Lubchenko, (Eds.) *Structural Glasses and Supercooled Liquids: Theory, Experiment, and Application*, John Wiley and Sons: New York (2012).
65. B. Bagchi, *Mol. Phys.* **112**, 1 (2014).
66. N. Sarma, J. M. Borah, S. Mahiuddin, H. A. R. Gazi, B. Guchhait, and R. Biswas, *J. Phys. Chem. B* **115**, 9040 (2011).
67. R. Biswas, A. R. Das, T. Pradhan, D. Touraud, W. Kunz, and S. Mahiuddin, *J. Phys. Chem. B* **112**, 6620 (2008).
68. B. Guchhait, R. Biswas, and P. K. Ghorai, *J. Phys. Chem. B* **117**, 3345 (2013).
69. S. Daschakraborty and R. Biswas, *J. Chem. Phys.* **140**, 014504 (2014).

70. J. Hunger, A. Stoppa, S. Schrodle, G. Hefter, and R. Buchner, *R. Chem. Phys. Chem.* **10**, 723 (2009).
71. R. Ludwig, *Chem. Phys. Chem.* **8**, 44 (2007).
72. K. Mukherjee, A. Das, S. Choudhury, A. Barman, and R. Biswas, *J. Phys. Chem. B* **119**, 8063 (2015).
73. B. Mukherjee, *J. Chem. Phys.* **143**, 054503 (2015).

Chapter 4

Collective Dynamic Dipole Moment Fluctuations, Cooperative Hydrogen Bond Relaxations and Their Connections to Dielectric Relaxation in Ionic Acetamide Deep Eutectics: Microscopic Insight from Simulations

4.1. Introduction

In-depth study of molecular relaxation processes is critical to the understanding of interaction and dynamics of complex solvent systems that ranges from molecular liquids to the modern ionic liquids and deep eutectic solvents.¹⁻⁹ The typical experiments which investigate molecular relaxation processes involve energy and/or momentum exchange between the studied system and an external perturbation.¹ Although the experimental sophistication to study microscopic dynamical processes in liquids has reached new levels during the last few decades, the basic theoretical approach¹⁰⁻¹³ to understand the phenomenon has remained largely unchanged. Among these the methods which established relations between the transport coefficients and time correlation functions and the projection-operator formalism deserve special mention.^{11-12, 14-15}

Dielectric relaxation (DR) experiments probe the time dependent change in the collective dipole moment autocorrelation function,¹⁶ $\frac{d}{dt}\langle\mathbf{M}(0)\cdot\mathbf{M}(t)\rangle$, where the collective dipole moment, $\mathbf{M}(t) = \sum_i \boldsymbol{\mu}_i(t)$, $\boldsymbol{\mu}_i(t)$ representing the dipole moment of the molecule 'i' at a time, t. Therefore, DR measurements are associated with the collective (that is, wavenumber $k\sigma \rightarrow 0$ limit, where σ is the diameter of the rotating species) polarization fluctuations and the measured response depicts the collective orientational relaxation in dipolar systems. Consequently, DR measurements cannot probe the wave-number dependence of orientational relaxation of polar molecules and thus angular dynamics at the level of a few to ~1000 molecules remains inaccessible.¹

Several conceptual difficulties arise when one attempts to connect the collective reorientation timescale, τ_{DR} , obtained from DR measurements to the single molecule reorientation time, τ_{M} . Single molecule reorientation time can readily be estimated from either the Stokes-Einstein-Debye (SED) relation or molecular dynamics (MD) simulations. It is to be noted here that this τ_{M} calculated from MD simulations or SED relation contains multi-body effects. In the SED, the multi-body effects enter via medium viscosity whereas in MD simulations the reorientation time is calculated in an ‘exact’ manner from the dynamics of a single molecule relaxing in the environment created by the neighboring molecules. A connection between the microscopic single particle orientation time, τ_{M} , and the macroscopic dielectric relaxation time, τ_{DR} , can be expressed as follows¹⁷⁻¹⁹

$$\tau_{\text{M}} = \frac{n^2 + 2}{\varepsilon_0 + 2} \tau_{\text{DR}}, \quad (4.1)$$

where n and ε_0 are the refractive index and the static dielectric constant of the medium, respectively. The above expression works well for weakly polar non-associated solvents; for strongly polar solvents, the following modified relation is used²⁰⁻²²

$$\tau_{\text{M}} = \frac{\varepsilon_{\infty} + 2\varepsilon_0}{3\varepsilon_0} \times \frac{\tau_{\text{DR}}}{g}, \quad (4.2)$$

where ε_{∞} represents the infinite frequency dielectric constant of the solvent (treated as a continuum), and g is a measure of the short-range solvent-solvent static orientational correlation (Kirkwood’s g factor)²³. One of the earliest molecular level theories, which incorporated solvent molecularity via the wavenumber dependent spatial and orientational static correlations, was found to be successful in predicting the experimental DR in normal polar solvents of varying polarity.^{17, 24-26} Moreover, this theory was found to reduce correctly to the Debye relation at low frequencies and to the Onsager-Glarum expression^{20,27} at the high ε_0 limit.

As mentioned earlier, continuum hydrodynamics allows one to relate the single particle reorientation time to the medium viscosity via the relation,²⁸⁻³⁰

$$\tau_M = \frac{3V_m\eta}{k_B T}, \quad (4.3)$$

where V_m is the molecular volume of the rotating species, η the medium viscosity, and $k_B T$ the Boltzmann constant times the absolute temperature. Rank (ℓ) dependence enters into the orientation times via the relation,^{1,31} $\tau_{DR} = [\ell(\ell + 1)/2]\tau_M$. For DR, $\ell = 1$, and therefore, $\tau_{DR} = \tau_M$. In highly viscous liquids, the effective volume (V_{eff}) that associates with the measured orientational relaxation is often found to be smaller than the molecular volume (V_m). For example, measured DR times for aluminate ILs and imidazolium ILs suggest V_{eff} to be $\sim 4\%$ and $\sim 1\%$ of their respective V_m .^{18-19,32-33} The small value for such V_{eff} can be justified in the following manner. Within the framework of hydrodynamics this can be explained either by assuming complete rotation of a tiny fraction of the total number of dipolar molecules present in the system, or by invoking partial collective rotation of several molecules together. A more microscopic consideration, however, assumes presence of non-hydrodynamic moves, such as angular jumps,³⁴⁻³⁷ effecting a complete breakdown of the hydrodynamic. This then allows a certain degree of decoupling between the molecular rotation and the medium viscosity leading to a reduction of V_m .

The experimental DR spectra of dipolar media, which is often limited by the accessible frequency range of the employed experimental set-up, exhibit multiple relaxation timescales.³⁸⁻⁴¹ Identifying a connection between the collective DR timescales and molecular rotation times at the single-particle level in complex systems is a non-trivial task and continuously stimulates fundamental academic interest. The present study attempts to address this issue by studying the reorientational relaxations in acetamide/electrolyte deep eutectic solvents (DESs)⁴²⁻⁴⁷ employing molecular dynamics simulations, and juxtaposing the simulated data against the available experimental DR results.³¹ In addition, we explore the effects of the cooperative relaxation of H-bond network on the simulated reorientational relaxation and the measured DR dynamics. The relevance to H-bond relaxation arises because liquid acetamide (CH_3CONH_2) is an extensively H-bonded system. The electrolytes that we have considered are lithium salts of nitrate (LiNO_3), bromide (LiBr) and perchlorate (LiClO_4). These DESs have been chosen because of the availability of experimental DR data for these systems,³¹ although the frequency coverage in these measurements was limited,

$0.2 \leq \nu/\text{GHz} \leq 50$. DESs considered here are multi-component molten mixtures which form stable liquid phase at temperatures much lower than the individual melting temperatures of the constituents.^{31,42-50} These solutions can be prepared easily by simply mixing the individual components and gently heating the mixture. Given that some of the DESs are biodegradable, these solvent systems are increasingly used in industry as ‘green solvents’.^{5,9,51-54} Academic and technological interest for these systems arises from the solvent control of chemical reactions⁵⁵⁻⁵⁷ and the flexibility to design reaction media for tailoring reactions.

The primary timescale which governs the orientational dynamics in H-bonded fluids is the typical waiting time between orientational jumps.³⁴⁻³⁵ During these intervals of waiting, the H-bond connectivity remains intact and they undergo rapid, stochastic changes which results in exchange of H-bond partners due to which angular reorientations occur via large angular jumps. This exchange of the H-bond partners occurs during a much smaller time-interval which is the jump time (time of flight), whose distribution and its dependence on the anion identity has already been discussed in detail in our earlier studies.³⁶⁻³⁷ We calculate two varieties of waiting time intervals, depending on whether the tagged acetamide molecule is H-bonded to another acetamide or to an anion during the period of waiting. Then we monitor the unconditional and conditional orientational and H-bond correlation functions, and analyze these functions to trace the origin of different relaxation timescales. The decay of the orientational correlation function depends on the angle between the axes of the tagged molecule at an arbitrary time-origin and at a later time. By placing several conditions depending on the nature of the neighbors to which the tagged molecule is hydrogen bonded (at the arbitrary time origin), we have been able to show that a variety of relaxation times can arise depending on the type of the H-bond neighbors at the time-origin. Similar classification procedure has also been followed for the calculations of the H-bond coordination fluctuations.

4.2. Simulation Details

All-atom simulations were performed at a temperature of 303 K using DL_POLY version 2.20.⁵⁸ Each system comprised of 512 molecules, of which there were 400 acetamide and 56 pairs of Li^+ and X^- where X^- denotes the identity of the ion (Br^- , NO_3^- and ClO_4^-). This

provides, as in experiments, a mole ratio of 78:22 between acetamide and electrolyte. The potential function used has the following form:

$$U(\mathbf{R}) = \sum_{\text{bonds}} K_r (r - r_{\text{eq}})^2 + \sum_{\text{angles}} K_\theta (\theta - \theta_{\text{eq}})^2 + \sum_{\text{dihedrals}} K_\phi [1 + \cos(n\phi - \delta)] + \sum_{i < j}^{\text{atoms}} \left(\frac{A_{ij}}{R_{ij}^{12}} - \frac{B_{ij}}{R_{ij}^6} \right) + \sum_{i < j}^{\text{atoms}} \frac{q_i q_j}{4\pi\epsilon_0 R_{ij}}. \quad (4.4)$$

Note this particular form of potential function has been used earlier for modeling DESs^{36-37,43,47-48}. In Eq. 4.4, K_r and K_θ are respectively the bond and angle constants, r_{eq} and θ_{eq} the equilibrium bond length and angle. K_ϕ denotes the dihedral constant, n the periodicity, ϕ the dihedral angle, and δ the phase shift. R_{ij} is the distance between atoms i and j with partial charges q_i and q_j , respectively. The interaction parameters for the acetamide molecule were taken from the CHARMM⁵⁹ force field. The force field parameters for Li^+ , Br^- , NO_3^- and ClO_4^- were taken from the existing literature.⁶⁰⁻⁶² Note these force field parameters, summarized in Appendix A and Appendix B (Table B1-Table B4, Figure B1-Figure B2) were used earlier to simulate acetamide dynamic structure factors⁴⁷⁻⁴⁸ and for studying orientational jumps in these DESs.³⁶⁻³⁷ The force field was constructed with DL_FIELD.⁶⁴ The short-range van der Waals interaction was represented by the Lennard-Jones (LJ) potential.⁶⁵ The long-range electrostatic potential was treated via Ewald summation technique⁶⁵ using an Ewald parameter of $\alpha = 0.2 \text{ \AA}^{-1}$ and a 6x6x6 k-point grid.

The initial configurations were built using Packmol⁶⁶ and equilibrated in the NPT ensemble at 1 atm. pressure for 500 ps. The simulated densities for all the three systems were found to be in good agreement with those from experiments^{43,44} (Table B5 of Appendix B). Nose-Hoover thermostat and barostat⁶⁷⁻⁶⁸ were used to control the temperature and pressure with time constants of 0.4 and 1.0 ps, respectively. Subsequently, further equilibration of 2 ns followed by a production run of 100 ns was carried out in the NVT ensemble. Periodic boundary conditions were employed in all three directions, and the equations of motion were integrated using a time step of 2 fs employing the velocity Verlet algorithm.⁶⁵ SHAKE algorithm⁶⁹ was applied to constrain the bonds. The snapshots were saved after every 100 fs for data analysis.

4.3. Analysis Protocol

Reorientations of CH_3CONH_2 molecules involve breaking and making of H-bonds, and therefore a criterion is required for determining whether a pair of entities are H-bonded. We have defined H-bonds based on the widely accepted geometric condition^{36-37,70} which considers distance (R) and angle (θ). Two CH_3CONH_2 molecules are considered to be H-bonded only when (i) the distance between the oxygen and nitrogen atoms of different CH_3CONH_2 molecules, R_{ON} , is less than a cut-off distance, $R_{\text{cut-off}}$ (that is, $R_{\text{ON}} < R_{\text{cut-off}}$) and (ii) the angle between the vector joining nitrogen and amide hydrogen of one CH_3CONH_2 molecule, and the vector joining this nitrogen and an oxygen atom belonging to another acetamide molecule, θ_{ONH} , is less than 30° (that is, $\theta_{\text{ONH}} < 30^\circ$). Following our previous work,³⁷ we have taken $R_{\text{cut-off}} = 4 \text{ \AA}$ for calculating the acetamide-acetamide jump characteristics in all these DESs. For acetamide-anion pairs, the distance considered is between nitrogen atom of the CH_3CONH_2 and X^- , R_{NX} , and the angle, θ_{XNH} , between the vector joining nitrogen and X^- of the anion and the vector joining this nitrogen and amide hydrogen of the CH_3CONH_2 molecule. For ClO_4^- and NO_3^- , however, there exist more than one possible H-bonding sites. In such cases, the least of the distances at which the first minimum of the corresponding radial distribution function appears is accepted³⁷ as $R_{\text{cut-off}}$. Following our earlier works,³⁷ we have taken $R_{\text{cut-off}} = 4.7 \text{ \AA}$ for LiBr , 4.0 \AA for LiClO_4 and 2.5 \AA for LiNO_3 with the angle cut-off fixed at $\theta_{\text{XNH}} = 30^\circ$ for all the anions.

Using the above criteria for determining whether acetamide-acetamide and acetamide-ion pairs are H-bonded, we set up a scheme to determine the identity of the H-bonded neighbors of each acetamide molecule at all time instants. To achieve this, we define two flag variables associated with the two hydrogen atoms of each acetamide molecule in the system. The value of $\text{flag_H1}(i,t)$ denotes the index of the acetamide molecule to which it is H-bonded via H1 of molecule “ i ” at time “ t ”. If molecule “ i ” does not form any H-bond via H1 at time “ t ”, then the value of this flag is zero. Since these DESs contain anions which can also form H-bonds with the i^{th} acetamide molecule, the following protocol has been utilized: values of the flag variables between one and four hundred (the total number of acetamide molecules present in the system) indicates that the chosen acetamide molecule forms a H-bond with another

acetamide. Values of the flag between four hundred one and four hundred fifty six (fifty six ion pairs in the system) denote H-bonding with an anion. A similar procedure is followed for assigning values for flag_H2(i,t). The cations of the salt can also interact with the carbonyl oxygen of the acetamide molecules and affect the reorientational dynamics. This interaction is accounted for via a third flag, flag_c6O(i,t), associated with each acetamide molecule.

Using this scheme it is possible to monitor the time-series associated with each flag variable over time. By locating pairs of discontinuities in the flag variables (flag_H1(i,t) and flag_H2(i,t)) one is able to identify all the H-bond partner exchange events. These H-bond partner exchange events are involved with the large amplitude orientational jumps.³⁶⁻³⁷ The location of the discontinuities in the flag variables are associated with the starting time (t_{start} , which is defined as the last instant during which the i^{th} molecule remains H-bonded to its initial acceptor) and the ending time (t_{end} , which is defined as the first instant when the molecule becomes H-bonded to its final acceptor). Following the time series of the flags over the entire simulation span, one is able to identify the starting and the ending times of all microscopic H-bond exchange events. These are then recorded as $t_{\text{start}}(i, j)$ and $t_{\text{end}}(i, j)$, where 'i' is the index of the tagged molecule and 'j' the index describing the jump. This identification scheme is recursively carried out over all molecules present in the system. During the waiting time interval, $t_{\text{end}}(i, j) < t < t_{\text{start}}(i, j+1)$, molecule 'i' remains H-bonded to some neighbor, which can either be another acetamide molecule or an anion. Keeping this in mind, we have computed two types of waiting time distributions, one where the tagged molecule is H-bonded to an acetamide molecule and another where it is H-bonded to an anion in the system.

The reorientational relaxation of acetamide can be characterized via monitoring the orientational correlation function, $C_\ell(t)$, defined by⁷¹⁻⁷²

$$C_\ell(t) = \frac{\langle P_\ell | \mathbf{u}(0) \cdot \mathbf{u}(t) \rangle}{\langle P_\ell | \mathbf{u}(0) \cdot \mathbf{u}(t) \rangle}, \quad (4.5)$$

where P_ℓ denotes the Legendre polynomial of rank ℓ and \mathbf{u} is a unit vector which connects the C(-CH₃) and N(-NH₂) atoms of an acetamide molecule (backbone C-N vector)³⁶ at a time t and the angular brackets denote averaging over molecules and time-origins. Given that there are three sites in the acetamide molecule through which it can form H-bonds (H-bond

donation via the two amide hydrogen atoms and H-bond acceptance via the carbonyl oxygen atom, see Figure 4.1), we have simulated a variety of orientational correlation functions depending on the H-bonding states of the tagged acetamide at the arbitrary time origin, $t = 0$. These $C_l(t)$ correspond to (i) tagged acetamide molecules which are bonded to Li^+ at $t = 0$, and (ii) tagged acetamide molecules which are not bonded to Li^+ at $t = 0$. We further subdivide each of the above types into two parts, (a) arising from the tagged acetamide molecule H-bonded to another acetamide molecule at $t = 0$, and (b) the tagged acetamide molecule H-bonded to an anion at $t = 0$. This allows us to separate the individual contributions (to the over-all orientational relaxation) from those acetamide molecules which are H-bonded to the ions (cation or anion), and those H-bonded to the other acetamide molecules. Similar dis-entangling procedure has already been followed to understand heterogeneous dynamics of water under confinement.⁷³⁻⁷⁴

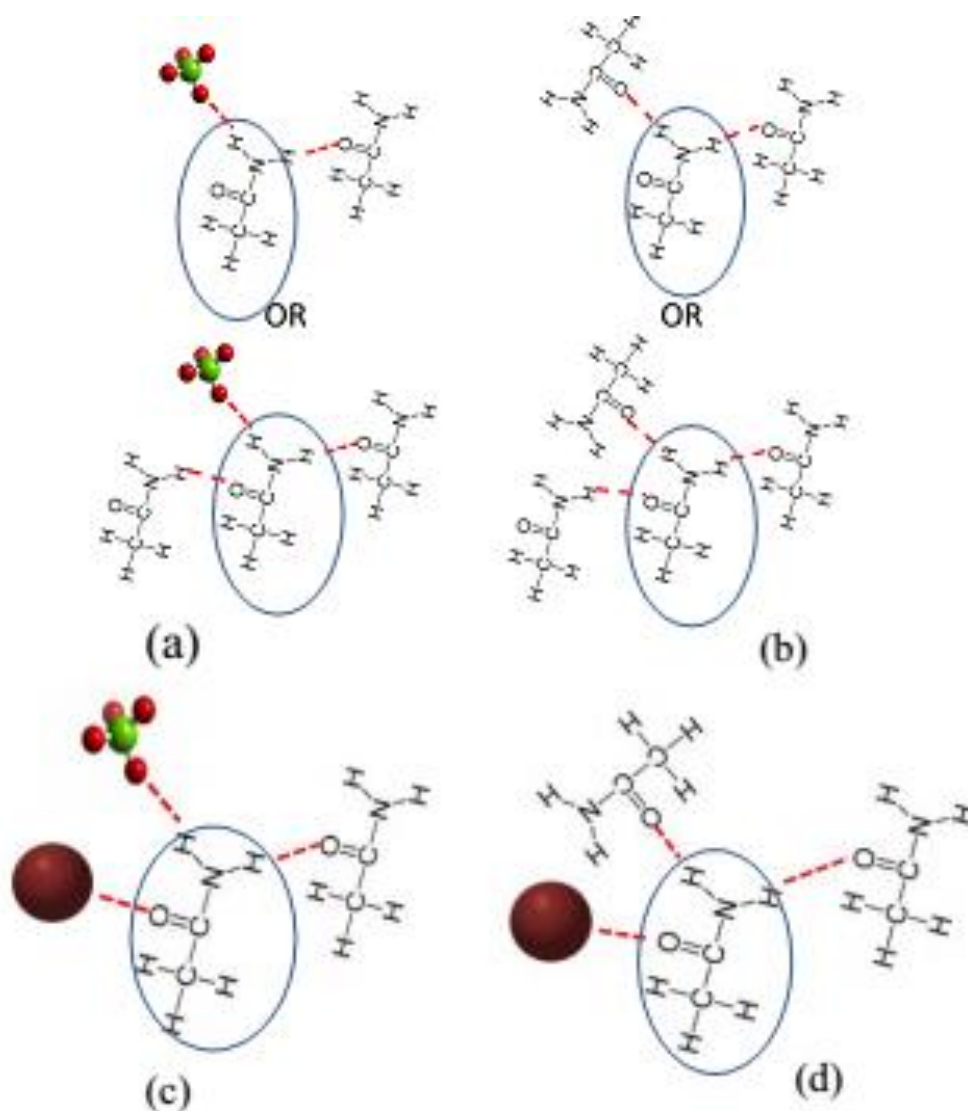


Figure 4.1: (a) acetamide-anion and (b) acetamide-acetamide pairs at the arbitrary time-origin, $t = 0$, which contribute to the two types of orientational correlation functions for the tagged central acetamide molecule. Tagged acetamide molecule may also be H-bonded (c) to the Li^+ simultaneously to the anion, and (d) to the Li^+ simultaneously to another acetamide molecule.

The procedure employed is depicted in Figure 4.1. From the values of $\text{flag_c6_O}(i,t)$, we have identified those acetamide molecules which are bonded to Li^+ at each simulation snapshot. From the $\text{flag_H1}(i,t)$ and $\text{flag_H2}(i,t)$ values, we have information about the acetamide molecules which are either H-bonded to another acetamide molecule or to an anion, at all the time frames. We have calculated $C_\ell(t)$ for acetamide molecules whose $\text{flag_c6_O}(i,t)$ is non-zero with the additional condition of possessing both $\text{flag_H1}(i,t)$ and $\text{flag_H2}(i,t)$ values less than or equal to four hundred at $t = 0$. This corresponds to orientational relaxation of acetamide molecules H-bonded to Li^+ . If the value of the $\text{flag_c6_O}(i,t)$ is non-zero at $t = 0$ simultaneously with values of one of the flag variables ($\text{flag_H1}(i,t)$ and $\text{flag_H2}(i,t)$) less than four hundred and the other greater than four hundred at $t = 0$, then the corresponding reorientation process involves those acetamide molecules H-bonded to Li^+ . For analyzing reorientation of acetamide molecules which are not H-bonded to a Li^+ ion, we choose those acetamide molecules for which $\text{flag_c6_O}(i,t)$ is equal to zero at $t = 0$. Now looking at the $\text{flag_H1}(i,t)$ and $\text{flag_H2}(i,t)$ value and following the same procedure, it is possible to obtain the acetamide-acetamide and acetamide-ion reorientations which do not involve H-bonding Li^+ .

Similarly, we have calculated the timescales associated with several types of H-bond relaxation functions. There are two varieties of the H-bond relaxation functions, one measures timescales corresponding to continuously present H-bonds, those bonds which do not rupture (due to librations) during the interval during which they are monitored. The continuous H-bond correlation function, $S_{\text{HB}}(t)$ is defined in the following way⁷⁵⁻⁷⁸,

$$S_{\text{HB}}(t) = \langle h(0)H(t) \rangle / \langle h \rangle, \quad (4.6)$$

where, $h(t')$ is a variable defined for a pair of molecules and $h(t') = 1$ is H-bonded at time t' , it is zero otherwise. $H(t)$ is a history dependent function of $h(t')$ and it is unity if $h(t')$ is continuously unity between times t_0 and $t_0 + t$, where t_0 is an arbitrary origin of time. The timescale characterizing the decay of $S_{HB}(t)$ can be identified with the average lifetime of the H-bonds. The other H-bond relaxation function, $C_{HB}(t)$, arising from structural relaxation due to translational and orientational diffusion is defined in the following manner^{75-77,79-80},

$$C_{HB}(t) = \langle h(0)h(t) \rangle / \langle h \rangle \quad (4.7)$$

where $h(t')$ is again a variable defined for a pair of molecules and $h(t') = 1$ if the pair is H-bonded at time t' . The angular brackets denote averaging over time origins and molecules. $C_{HB}(t)$ describes the relaxation of a pair which were H-bonded at time $t = 0$, remains intact at time t , with the possibility of breaking and reformation of H-bond in the intermediate period with the same or a different neighboring partner.⁷⁸ Thus, $C_{HB}(t)$ involves structural relaxation and the associated timescale is typically one order of magnitude larger than the timescale associated with the continuous H-bond relaxation function, $S_{HB}(t)$. Owing to the presence of the acetamide and the ions (anions and cations) in these systems, the pair can be chosen in several ways. The possibilities are shown schematically in Figures 4.2 and 4.3. Figure 4.2 schematically shows the pairs for the indices “i” and “j” for the variable $h_{ij}(0, t)$, which enters the H-bond correlation function calculations. The variable $h_{ij}(0, t)$ can take values of either zero or one, depending on whether the entities with indices “i” and “j” are hydrogen bonded or not, at the respective times. It is clear that the choice of the pair of entities can be classified in three different categories. In presence of cation and anion the following pairs at $t = 0$ may be present : (a) an acetamide and another Li^+ ion (b) an acetamide molecule and an anion, and (c) an acetamide and another acetamide. Moreover, (b) and (c) types of pairs can be of two varieties (i) when the acetamide of the pair is complexed to a Li^+ ion at $t = 0$ and (ii) when the acetamide of the pair is not complexed to a Li^+ at $t = 0$. The molecular arrangements in this second level of subdivision are represented in Figure 4.3.

$$\sum_{i=1}^{N_{acet} + N_{salt}} \sum_{j=1}^{N_{acet} + N_{salt}} h_{ij}(0, t)$$

$$h_{ij}(0, t) = 0 \text{ or } 1$$

(a) $i \in \text{Acetamide}, j \in \text{Li}^+$

(b) $i \in \text{Acetamide}, j \in \text{Anion}$

(c) $i \in \text{Acetamide}, j \in \text{Acetamide}$

Figure 4.2: A schematic for the various choices of the pair of molecules for the calculation of the hydrogen bond time correlation functions.

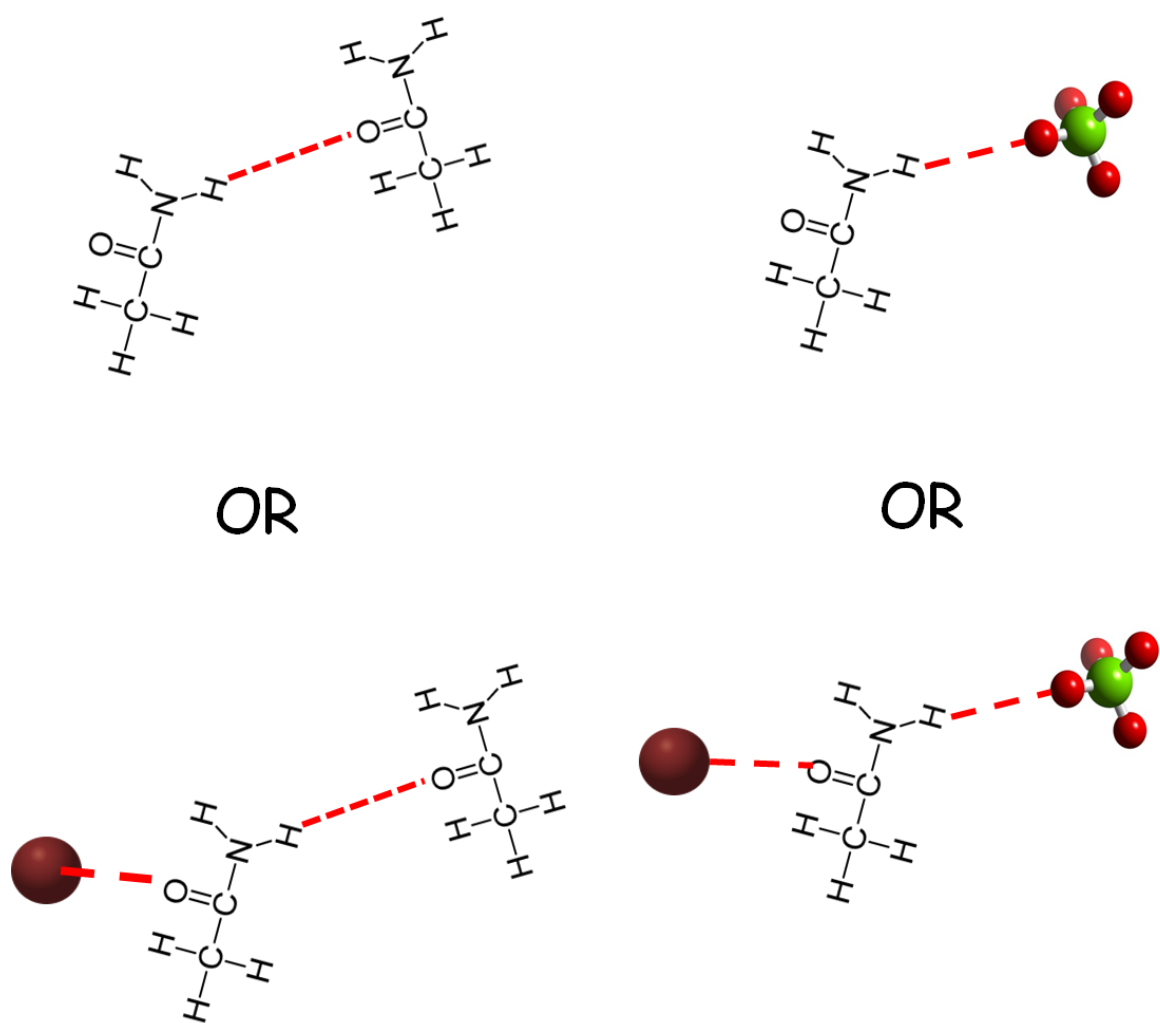


Figure 4.3: Types of pairs for the calculation of H-bond correlation functions. Left panel shows a pair of acetamide molecules in the absence and presence of Li^+ , whereas the right panel shows pairs that are H-bonded to an anion in the absence and presence of Li^+ .

4.4. Results and Discussion

4.4.1. Reorientational correlation relaxation: effects of electrolyte and anion dependence

Figure 4.4 displays the simulated decays of $C_1(t)$ and $C_2(t)$ for acetamide molecules (backbone vector) in $\text{CH}_3\text{CONH}_2 + \text{LiBr}/\text{NO}_3/\text{ClO}_4$ DESs at 303 K. These decays contain contributions from all acetamide molecules that are interacting and not interacting with the ions present in the respective DESs. For comparison, the corresponding decays for neat molten acetamide at 368 K are also shown in the respective panels. Clearly, the orientational

relaxation of acetamide in these deep eutectics is not only significantly slowed down compared to that for neat molten acetamide but the relaxation patterns are also remarkably different. For example, $C_1(t)$ and $C_2(t)$ for acetamide in these deep eutectics extend to a few nanoseconds and display stretched exponential relaxation whereas those for neat molten acetamide are complete within ~ 30 ps with no trace of distributed kinetics. While the temperature difference (303 K versus 368 K) may account partly for the observed retardation, interaction between electrolyte and acetamide can play a significant role in slowing down the relaxation rate in these ionic DESs. In addition, the relaxation rates for $C_1(t)$ and $C_2(t)$ depend upon the identity of the anion present in these systems. Note in Figure 4.4 both stretched exponential and multi-exponential fits to the DES data have been shown which suggest neither of these functions performs better over the other in analytically describing these simulated relaxations. In addition, fit parameters summarized in Table 4.1 reflect that the average relaxation times ($\langle \tau \rangle$ and $\langle \tau_{\text{long}} \rangle$) produced by these two different fit functions do not match exactly with each other. However, a consideration of the ‘economy-of-fit-parameters’ leads to the choice of stretched exponential description, although either of these two, as was done previously for ionic liquids,^{19,33,81-84} can be considered for comparison purpose. Interestingly, the stretched exponential description relates well to the dynamic heterogeneity feature of these deep eutectics discussed already in previous works,⁴³ whereas the nanosecond timescale reflected in multi-exponential fits to $C_1(t)$ qualitatively matches with the slowest DR timescale reported for these systems.

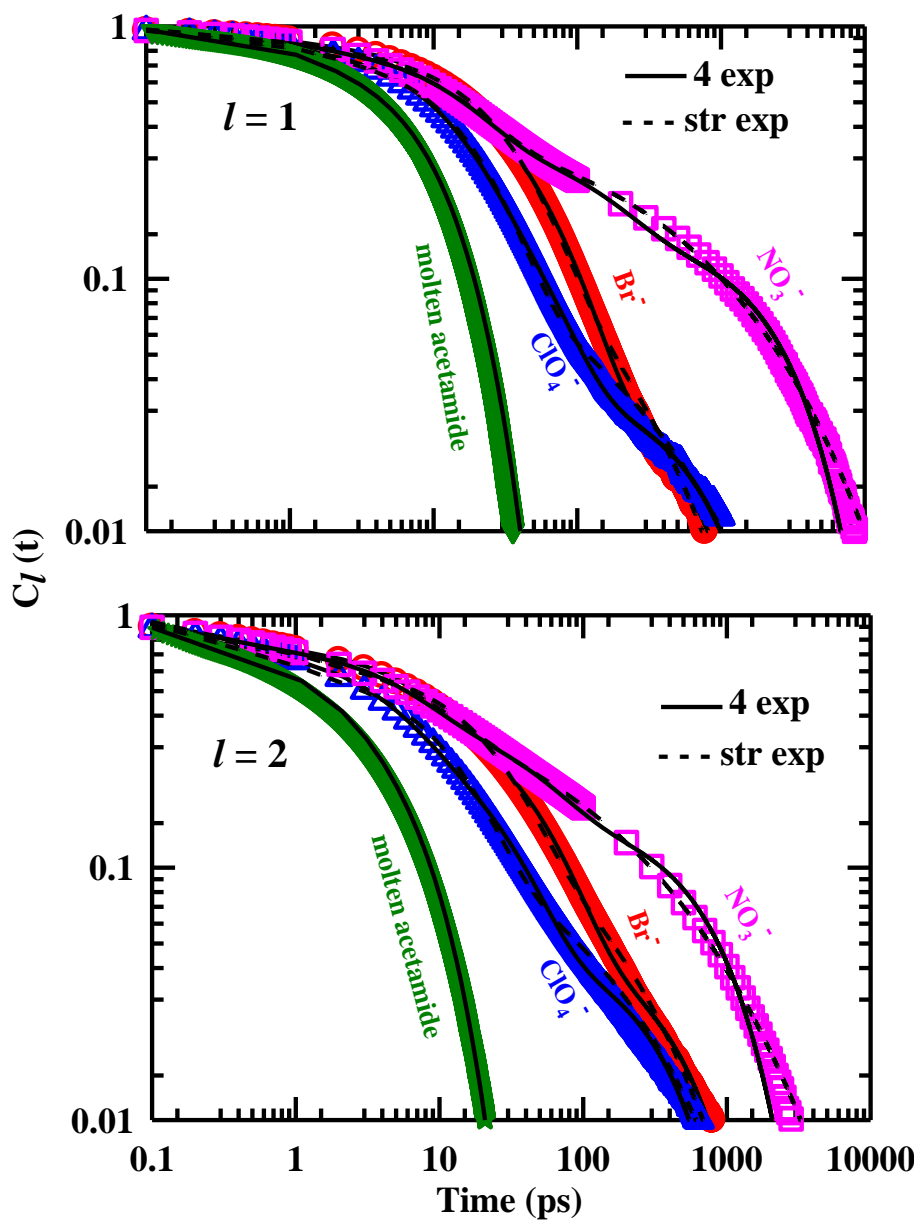


Figure 4.4: Simulated reorientational correlation functions $C_1(t)$ (upper panel) and $C_2(t)$ (lower panel) for the three DES mixtures studied here along with the multi-exponential (solid lines) and stretched exponential (dashed lines) fits. For comparison, simulated reorientational correlation functions for molten acetamide are also shown.

Table 4.1: Stretched- and/or Multi-exponential fit parameters for the simulated first ($\ell = 1$) and second ($\ell = 2$) rank orientational relaxation functions, $C_1(t)$ and $C_2(t)$, for acetamide in (acetamide + $\text{LiNO}_3/\text{Br}/\text{ClO}_4$) DESs, and in neat molten acetamide.

DES ^a	Rank (ℓ)	Fit Function	a_1	τ_1 (ps)	a_2	τ_2 (ps)	a_3	τ_3 (ps)	a_4	τ_4 (ns)	β	$\langle \tau \rangle$ (ps)	$\langle \tau_{\text{long}} \rangle$ (ps) ^c	$\langle \tau \rangle^{\ell=1} / \langle \tau \rangle^{\ell=2}$	η (cP) ^e
NO_3^-	1	Stretched	0.11	0.98	0.42	16.0	0.47	339.0	-	-	0.40	536.5	530.5	3.15(3.03) ^d	210
	1	Multi-exp	0.15	0.80	0.50	15.0	0.20	148.0	0.15	2.52	1.0	415.0	378.0	3.13(3.15)	
	2	Stretched	0.15	0.50	0.23	9.1	0.62	50.4	-	-	0.34	170.4	175.0		
	2	Multi-exp	0.23	0.24	0.37	5.7	0.24	44.0	0.16	0.75	1.0	132.4	120.0		
Br^-	1	Stretched	0.11	0.90	0.61	33.0	0.28	51.0	-	-	0.45	55.6	35.3	1.32(1.10)	1312
	1	Multi-exp	0.11	0.60	0.35	15.4	0.49	52.9	0.05	0.59	1.0	60.8	29.5	1.49(1.31)	
	2	Stretched	0.30	0.64	0.43	22.7	0.27	51.0	-	-	0.46	42.2	32.1		
	2	Multi-exp	0.23	0.30	0.35	7.1	0.37	41.8	0.05	0.45	1.0	40.7	22.5		
ClO_4^-	1	Stretched	0.15	0.95	0.66	18.0	0.19	51.0	-	-	0.36	56.4	43.9	1.79(1.73)	160
	1	Multi-exp	0.14	0.60	0.57	11.9	0.25	42.2	0.04	0.77	1.0	48.2	30.8	1.84(1.76)	
	2	Stretched	0.35	0.52	0.47	11.6	0.18	51.7	-	-	0.43	31.6	25.4		
	2	Multi-exp	0.24	0.20	0.41	4.3	0.3	23.7	0.05	0.35	1.0	26.2	17.5		
Molten ^b Acetamide	1	Multi-exp	0.17	0.63	0.83	7.9	-	-	-	-	1.0	6.7	6.56	2.50(3.04)	2
	2	Multi-exp	0.30	0.19	0.30	1.7	-	-	-	-	1.0	2.7	2.16		

a) Acetamide+LiX (X= NO₃⁻, Br⁻, ClO₄⁻) DES are at 303 K; b) Molten acetamide at 368 K; c) $\langle \tau_{\text{long}} \rangle$ denotes amplitude-weighted time constant associated with the slowest component; for stretched exponential fits, $\langle \tau_{\text{long}} \rangle = \tau \Gamma(\beta^{-1})/\beta$; d) numbers in parenthesis represent $\langle \tau_{\text{long}} \rangle^{\ell=1} / \langle \tau_{\text{long}} \rangle^{\ell=2}$; e) η values are from Refs. 31, 36, 42 and 43.

Let us now compare the molecular rotation time, τ_M , obtained via Eq. 4.3 with the simulated average reorientational relaxation time ($\langle\tau\rangle^{\ell=1}$) summarized in Table 4.1. Considering an acetamide molecule as a sphere with diameter³¹ of 4.5Å, we find τ_M values to be ~720 ps, ~4500 ps and ~550 ps for NO_3^- , Br^- and ClO_4^- containing systems, respectively. These hydrodynamic rotation times are, however, much different from the simulated average reorientational relaxation times, deviation being particularly dramatic for the Br^- contacting system. Similar observation is also made when one compares the anion dependent τ_M values calculated from Eq. 4.3 with those from Eq. 4.2 using the slowest of the measured DR times³¹ and approximating the Kirkwood g factor to be unity. This indicates that the orientational relaxation in these complex chemical systems cannot be described merely in terms of viscosity-controlled single particle rotation; one needs to account for the cooperative relaxation of the collective H-bond network and the ion-acetamide interaction at the molecular level.

We next examine the viscosity (η) coupling of the average orientational relaxation timescales in these media. Relative to neat molten acetamide, the average times ($\langle\tau\rangle$ and $\langle\tau_{\text{long}}\rangle$ for $\ell = 1$ and 2) are slower by a factor of ~50-80 for NO_3^- containing DES, and ~8-16 for Br^- and ClO_4^- containing systems. In contrast, the viscosity ratios,^{31,42-43} $\eta^{\text{DES}} / \eta^{\text{acetamide}}$, are ~105, ~656, and ~80 for NO_3^- , Br^- and ClO_4^- containing deep eutectics, respectively. This clearly indicates a substantial decoupling between the average times and viscosity coefficients, suggesting heterogeneous dynamics and break-down of hydrodynamics. Our earlier simulation studies have indeed revealed presence of large angle orientation jumps with dynamic heterogeneity (DH) being more pronounced for Br^- containing DES than in the other two systems considered.³⁷ The ratios between the simulated average times, $\langle\tau\rangle^{\ell=1} / \langle\tau\rangle^{\ell=2}$ or $\langle\tau_{\text{long}}\rangle^{\ell=1} / \langle\tau_{\text{long}}\rangle^{\ell=2}$, for Br^- and ClO_4^- containing systems are in the range ~1-2 which is much deviated from 3 predicted^{1,85} on the basis of stochastic Brownian dipolar rotations. This reflects presence of temporal heterogeneity in these systems and provides support to the conclusions drawn from time-resolved fluorescence results.^{42-43,47} It is interesting to note that the ratio of these rank dependent average times is nearly 3 for the

NO_3^- containing DES although fluorescence measurements revealed substantial fractional viscosity dependence⁴² for the average solvation and rotation times of a dissolved dipolar solute in this system.

Effects of anion on orientational relaxation of acetamide in these ionic deep eutectics can be realized by correlating $\langle \tau \rangle$ or $\langle \tau_{\text{long}} \rangle$ to η in these systems. For example, the ratio of average times between Br^- and ClO_4^- containing DESs is within ~ 0.8 - 1.5 although the Br^- containing DES is approximately 8 times more viscous than the ClO_4^- counter-part. In contrast, the average times for NO_3^- containing system are ~ 3 - 15 times longer than those for Br^- containing DES although the former is ~ 6 times less viscous than the latter. Similarly, average times in NO_3^- containing DES are ~ 5 - 12 times slower than those in the corresponding ClO_4^- system despite their viscosity coefficients being not too different ($\eta_{\text{NO}_3^-} / \eta_{\text{ClO}_4^-} \sim 1.3$). Such a dependence on anion may arise from anion-specific interactions with acetamide molecules where pinning of acetamide molecules by Li^+ (cation solvation) through the carbonyl oxygen atom of acetamide can also contribute. This effect of cation solvation by acetamide is expected to be electrolyte dependent because of difference in degree of dissociation⁸⁶ which, in turn, adds to the anion dependence. Interestingly, the simulation observation here that the NO_3^- containing DES is the slowest among these three has also been reflected in dielectric relaxation³¹ and steady state fluorescence⁴² spectroscopic measurements.

4.4.2. Microscopic origin of the slow long-time relaxation: Role of ion-acetamide interaction

Next we explore the possible origin of the slow longtime component of the simulated ‘overall’ $C_l(t)$ decays (shown in Figure 4.4) by separating out the individual relaxation contributions that arise from the reorientation of (i) acetamide molecules that are not interacting with either of the ions (Li^+ or the corresponding anion) and H-bonded only to other neighboring acetamide molecules, (ii) acetamide molecules that are H-bonded to anion but not interacting with Li^+ , (iii) acetamide molecules that are interacting with Li^+ (through

carbonyl oxygen atom) but not H-bonded to any anion, and (iv) acetamide molecules that are interacting simultaneously with Li^+ and the corresponding anion. These individual relaxation contributions are displayed in Figures 4.5, 4.6 and 4.7 respectively for nitrate, bromide and perchlorate deep eutectics investigated here. Best fits through the simulated data, multi-exponential or stretched or both, are also shown along with the fit parameters summarized in Table 4.2. $C_\ell(t)$ decays simulated for neat molten acetamide at 368 K are also shown in these figures. Visually it is quite clear that the over-all slowing down of the acetamide orientational relaxation in these DESs arises from both the presence of electrolyte (via η which is a collective quantity) and interaction at the molecular level with the ions. More interestingly, the extent of slowing down of these individual relaxation components depends on the identity of the anion.

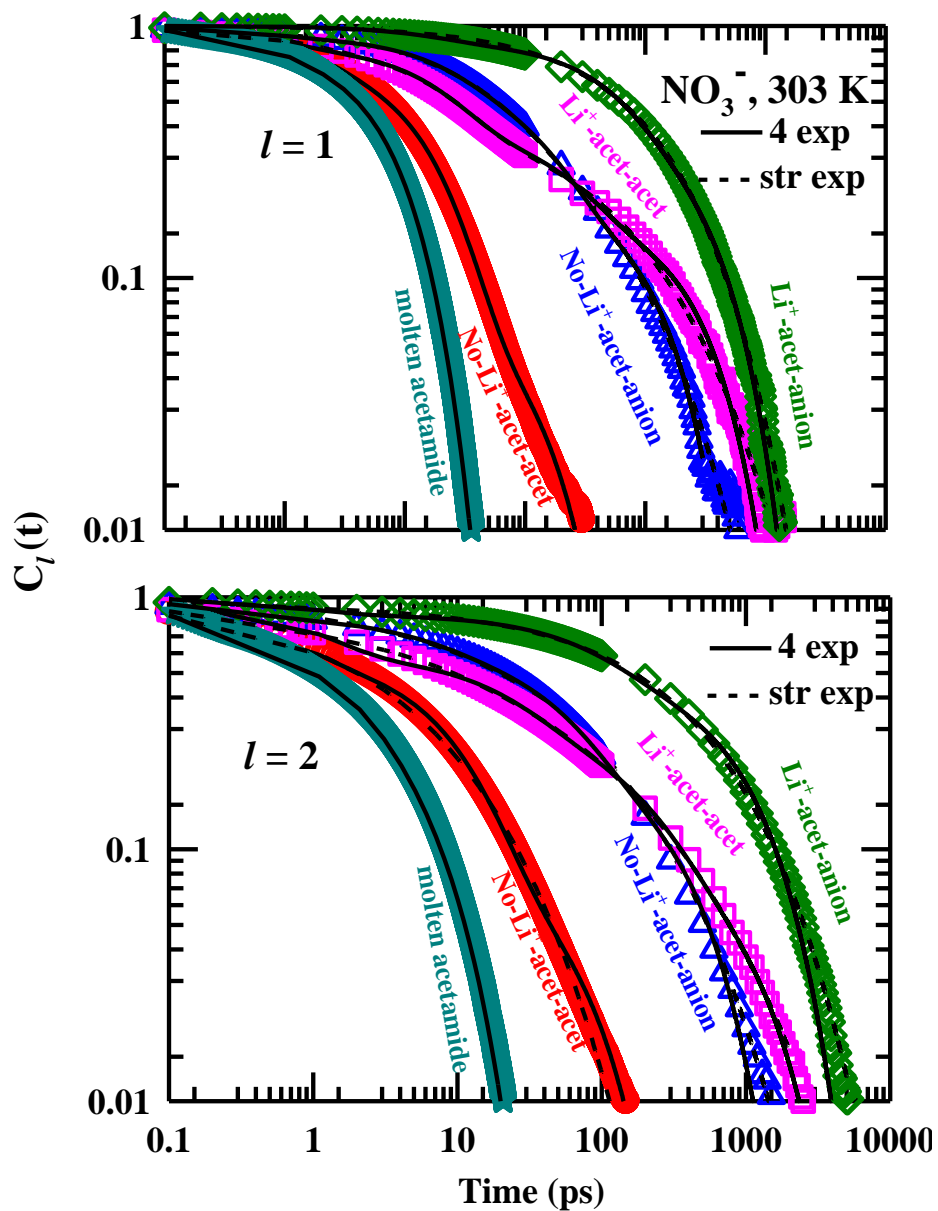


Figure 4.5: Separated out reorientational correlation functions, $C_1(t)$ (upper panel) and $C_2(t)$ (lower panel) for acetamide/ LiNO₃ deep eutectics along with the fits. Simulated data and fits through them for molten neat acetamide are also shown.

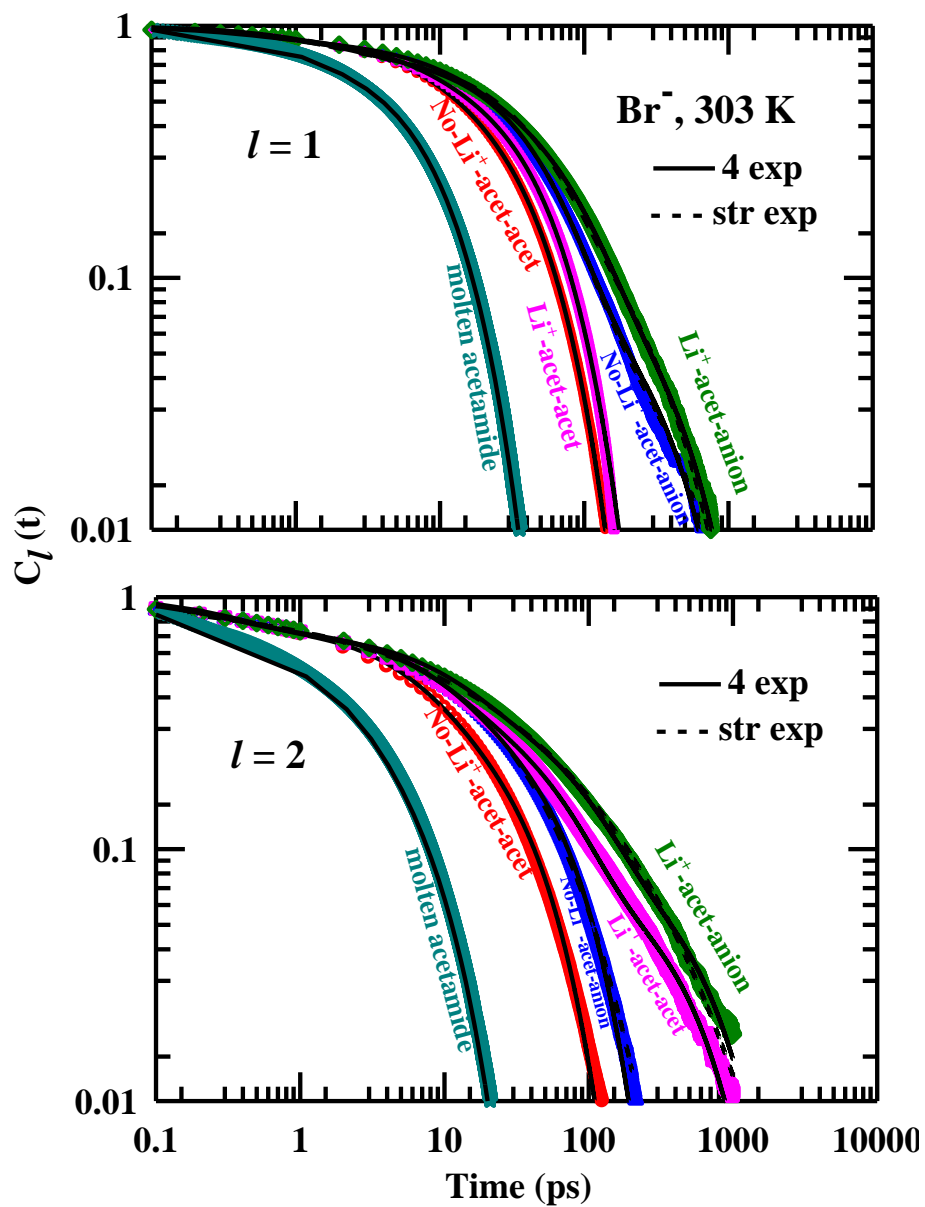


Figure 4.6: Separated out reorientational correlation functions for acetamide/ LiBr deep eutectics along with the fits.

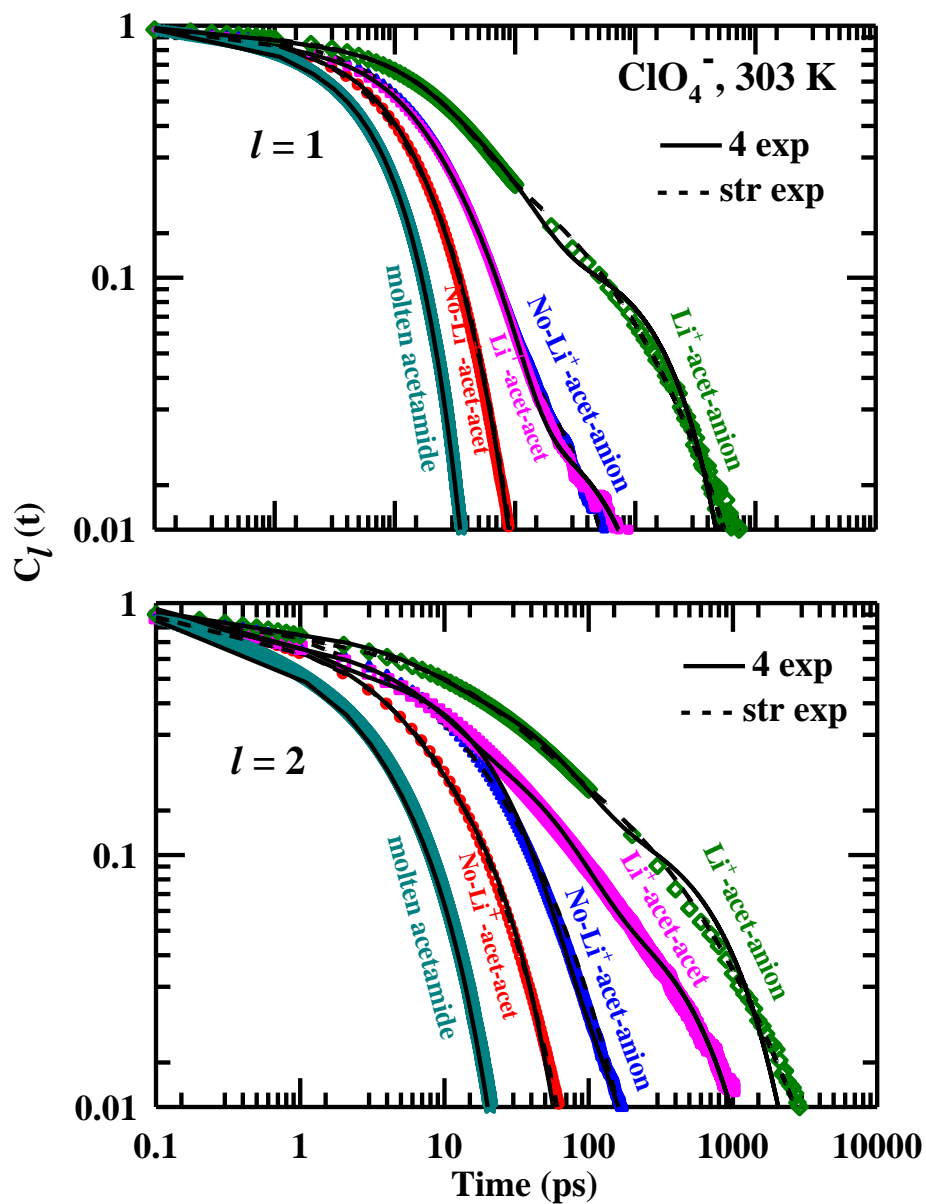


Figure 4.7: Separated out reorientational correlation functions for acetamide/ LiClO_4 deep eutectics along with the fits.

Table 4.2: Stretched/Multi-exponential fit parameters for the simulated first ($\ell = 1$) and second ($\ell = 2$) rank orientational relaxation functions, $C_1(t)$ and $C_2(t)$, for separated out pairs - acetamide attached to another acetamide or to an anion, in the absence and presence of Li^+ in (acetamide + $LiNO_3/Br/ClO_4$) DESs.

DES		Rank (l)	Fit Function	Li^+	a_1	τ_1 (ps)	a_2	τ_2 (ps)	a_3	τ_3 (ps)	a_4	τ_4 (ps)	β	$\langle \tau \rangle$ (ps)
NO_3^-	Acet-acet	1	Multi-exp	absent	0.26	1.8	0.66	16.2	0.08	131.6	-	-	1	21.7
	Acet-anion	1	Multi-exp	absent	0.09	0.7	0.28	23.5	0.41	137	0.22	1250	1	337.8
			Stretched	absent	0.04	19.9	0.20	64.8	0.76	181.5	-	-	0.44	373.1
	Acet-acet	1	Multi-exp	present	0.17	0.8	0.44	21.9	0.21	238.5	0.18	2900	1	581.9
			Stretched	present	0.12	1.5	0.36	23.4	0.52	476.2	-	-	0.43	688.7
	Acet-anion	1	Multi-exp	present	0.13	18.9	0.44	588.2	0.43	3333.3	-	-	1	1694.6
			Stretched	present	1	1164	-	-	-	-	-	-	-	0.6
	Acet-acet	2	Multi-exp	absent	0.41	0.6	0.5	9.3	0.09	64.5	-	-	1	10.7
			Stretched	absent	1	4.4	-	-	-	-	-	-	-	0.47
	Acet-	2	Multi-	absent	0.16	0.2	0.2	6.4	0.41	51.6	0.23	357.6	1	104.7

	anion		exp											
			Stretched	absent	1	44.8	-	-	-	-	-	-	0.44	116.1
	Acet-acet	2	Multi-exp	present	0.41	1.0	0.28	24.8	0.21	180.8	0.1	1016	1	146.9
			Stretched	present	0.07	0.4	0.04	11.5	0.89	37.5	-	-	0.35	168.3
	Acet-anion	2	Multi-exp	present	0.15	0.8	0.35	97.1	0.5	1000	-	-	1	534.1
			Stretched	present	0.07	0.2	0.93	385.5	-	-	-	-	0.57	578.7
<i>Br⁻</i>	Acet-acet	1	Multi-exp	absent	0.08	0.3	0.23	7.8	0.69	33.1	-	-	1	24.6
	Acet-anion	1	Multi-exp	absent	0.2	1.5	0.7	40	0.1	270.3	-	-	1	55.3
			Stretched	absent	0.2	1.6	0.68	40.8	0.12	200	-	-	0.74	57
	Acet-acet	1	Multi-exp	present	0.08	0.3	0.2	6.2	0.72	40.7	-	-	1	30.6
	Acet-anion	1	Multi-exp	present	0.11	0.5	0.23	11.5	0.54	58.4	0.12	312.5	1	71.7
			Stretched	present	0.2	1.4	0.54	41.2	0.26	150	-	-	0.75	69.3
	Acet-acet	2	Multi-exp	absent	0.22	0.3	0.37	5.8	0.41	29.7	-	-	1	14.4

	Acet-anion	2	Multi-exp	absent	0.24	0.3	0.35	8.7	0.41	51	-	-	1	24	
			Stretched	absent	0.15	0.2	0.85	20	-	-	-	-	0.62	24.4	
	Acet-acet	2	Multi-exp	present	0.25	0.3	0.34	7.8	0.33	48.1	0.08	416.7	1	51.9	
			Acet-anion	2	Multi-exp	present	0.27	0.4	0.33	10.9	0.3	71.9	0.1	526.3	1
	Stretched	present			1	20.6	-	-	-	-	-	-	0.38	79.2	
	ClO_4^-	Acet-acet	1	Multi-exp	absent	0.13	0.5	0.53	9.3	0.34	25.0	-	-	1	13.5
				Stretched	absent	1	11.1	-	-	-	-	-	-	0.7	14
		Acet-anion	1	Multi-exp	absent	0.1	0.4	0.33	9.3	0.51	31.8	0.06	294.1	1	37
Acet-acet		1	Multi-exp	present	0.15	0.6	0.43	11.6	0.4	41.3	0.02	714.3	1	35.9	
Acet-anion		1	Multi-exp	present	0.12	0.6	0.37	16.5	0.38	82.3	0.13	1827.3	1	275	
			Stretched	present	0.4	27.3	0.6	106.4	-	-	-	-	0.35	331.9	
Acet-acet		2	Multi-exp	absent	0.24	0.2	0.4	3.2	0.36	15.3	-	-	1	6.8	
			Stretched	absent	0.11	0.1	0.89	5.6	-	-	-	-	0.63	7.9	

	Acet-anion	2	Multi-exp	absent	0.43	0.8	0.52	20	0.05	98.8	-	-	1	15.7
			Stretched	absent	1.00	8.1	-	-	-	-	-	-	-	0.5
	Acet-acet	2	Multi-exp	present	0.29	0.3	0.40	6.7	0.24	48.8	0.07	500	1	49.5
			Multi-exp	present	0.21	0.2	0.29	6.1	0.36	51.5	0.14	769.2	1	128
			Stretched	present	0.14	0.5	0.20	20	0.66	50.2	-	-	0.36	155

We now quantify the roles of individual ions in slowing down the over-all acetamide orientational relaxation by comparing the decay timescales obtained from multi-exponential fits summarized in Tables 4.1 and 4.2. The slowest timescale (τ_4) in the over-all $C_1(t)$ decay shown in Figure 4.4 for the NO_3^- system is ~ 2.5 ns which is quite similar to the longest timescale found in the corresponding individual relaxations of Li^+ -coordinated acetamide molecules (2.9 ns) and acetamide molecules that are simultaneously interacting with both Li^+ and NO_3^- (~ 3.3 ns). Note the ratio between the slowest time constants associated with $C_1(t)$ relaxations for NO_3^- system and molten acetamide is ~ 312 and nearly three times larger than the corresponding viscosity ratio ($\eta^{\text{NO}_3^- \text{DES}} / \eta^{\text{acetamide}} = 210/2 = 105$). This further supports the view that a molecular-level ion-acetamide interaction is responsible for the dramatic slowing down of orientational relaxation of acetamide in these media. Likewise, the half-a-nanosecond relaxation component in the over-all $C_1(t)$ relaxation for acetamide in Br^- containing DES arises from the orientational relaxations of acetamide molecules that are H-bonded to Br^- in the absence and presence of Li^+ (~ 300 ps). It is quite interesting to notice that interaction of Br^- and Li^+ with acetamide molecules does not slow down the $C_1(t)$ relaxation as much as the interaction of NO_3^- and Li^+ with acetamide does. This difference in interaction at the molecular level produces the electrolyte dependence of acetamide orientational relaxation in these deep eutectics. For ClO_4^- containing DES, the slowest component of the over-all $C_1(t)$ relaxation is characterized by a time constant of ~ 0.8 ns and is arising, as in the above cases, from the relaxation of acetamide molecules which are either coordinated to Li^+ or interacting simultaneously with ClO_4^- and Li^+ (see Figure 4.7 and Table 4.2). Similar analyses of the longtime component in the over-all $C_2(t)$ relaxation shown in Figure 4.4 also confirm that ion-coordinated acetamide molecules are responsible for the nanosecond relaxation component. It may therefore be concluded that in all these DESs the slowest relaxation component arises from those acetamide molecules which are coordinated to ions.

We next investigate the origin of the other timescales found in the multi-exponential fits to the simulated $C_\ell(t)$. Data in Table 4.1 indicate that the fastest time constant (τ_1) for $C_\ell(t)$ decays in these DESs is nearly a picosecond which is also the finding for molten neat

acetamide. In fact, the separated out acetamide-acetamide relaxation (category (i) discussed earlier) in these deep eutectics also reflects a similar timescale at early times. Therefore, the sub-picosecond to picosecond relaxation component in these systems can be attributed to the orientational relaxation of acetamide molecules which are not interacting with any ions but H-bonded only to other neighboring acetamide. In addition, relaxation of these acetamide molecules also predominantly contributes to the ~5-20 ps timescale (see Table 4.1 and Table 4.2) of the $C_i(t)$ decays in these systems. This component is present in the orientational relaxation of neat molten acetamide and, therefore, origin of the other two slower components in these DES can be assigned exclusively to the ion-acetamide interactions.

An interesting scenario emerges when the ratios between the average times ($\langle \tau \rangle^{\text{comp}}$) from individual relaxation components (as described by categories (i), (ii), (iii) and (iv)) and those from neat molten acetamide are compared against the viscosity ratios for these DESs. For example, the ratio, $R^{\text{comp}} = \langle \tau \rangle^{\text{comp}} / \langle \tau \rangle^{\text{acetamide}}$, covers the range ~3-250 for the NO_3^- system, ~4-30 for the Br^- system and ~2-50 for the ClO_4^- system. The viscosity ratios, $\eta^{\text{DES}} / \eta^{\text{acetamide}}$, are 105, 606 and 80 for NO_3^- , Br^- and ClO_4^- containing systems, respectively. Note the lower end of the R^{comp} range is associated with the relaxation of category (i) and the higher end with that of category (iv) in each case. This suggests that the orientational relaxation of acetamide molecules that are not interacting with the ions (category (i)) is decoupled from the medium viscosity to the largest extent in each of these DESs. This decoupling may occur via large angle orientation jumps³⁶⁻³⁷ of the acetamide backbone of the relaxing molecule. The R^{comp} range being narrower for the Br^- and ClO_4^- deep eutectics than their NO_3^- counterpart then suggests that the jump events are more frequent in these two deep eutectics than in the NO_3^- system. Interestingly, such an observation has already been made in simulation studies of anion dependent orientation jumps in these DESs.³⁷

4.4.3. Orientation jump and waiting time distributions: Anion dependence of the characteristic timescales

The primary timescale that dictates the time-span of $C_\ell(t)$ (or the average reorientation time

$\langle \tau_\ell \rangle = \int_0^\infty dt C_\ell(t)$) is the duration of waiting between two consecutive orientational jumps,

τ_{wait} . The problem of calculating $C_\ell(t)$ for a rotor performing stochastic angular jumps in a three dimensional (3D) space with a constant amplitude and frequency was solved and the following expression interconnecting τ_{wait} and $\langle \tau_\ell \rangle$ derived⁸⁷

$$\langle \tau_\ell \rangle = \tau_{\text{wait}} \left\{ 1 - \frac{1}{2\ell + 1} \frac{\sin(\ell + 1/2)\Delta\theta}{\sin(\Delta\theta/2)} \right\}^{-1}, \quad (4.8)$$

where $\Delta\theta$ is the jump angle. This model, however, assumed that the direction of the rotor is frozen between two consecutive reorientational jumps; subsequent extension of this model removed this lacunae and explained the timescales associated with the reorientational dynamics of liquid water.⁸⁷ We have already shown³⁶⁻³⁷ that large amplitude orientational jumps play an important role during an exchange of H-bonding partner for the reorienting molecule. This description naturally allows the presence of at least two different timescales characterizing the dynamics. The angular jumps are typically fast and are punctuated by relatively longer periods of waiting. The distribution of jump time (t_{jump} , the flight-time during which an angular jump takes place) has already been shown to follow a power law dependence on time, $P(t_{\text{jump}}) \sim A(t_{\text{jump}}/\tau)^{-\gamma}$, with both γ and τ showing substantial anion dependence.³⁷ It is to be noted here that in neat, molten acetamide at 368 K, the jump time and waiting time are 0.9 ps and 2.1 ps, respectively.³⁶ The power law dependence of these characteristic time distributions is a reflection of strong structural and dynamical heterogeneities in these DESs. The anion dependence of waiting time distribution, $P(\tau_{\text{wait}})$, simulated for these systems is now reported below.

Figure 4.8 shows the simulated waiting time distributions where the long time tails are fitted to the functional form, $P(\tau_{\text{wait}}) \sim A(\tau_{\text{wait}}/\tau)^{-\lambda}$. Fit parameters, summarized in the insets, quantify the anion dependence for orientation jumps associated with both the acetamide-acetamide and acetamide-ion specie. As before,³⁷ the power law dependence arises due to the intrinsic heterogeneity of these systems. Similar to $C_\ell(t)$ decays, presence of the ions gives rise to a long tail in the waiting time distribution and NO_3^- , among these anions, generates the longest tail. In addition, for both acetamide-acetamide and acetamide-ion specie the power-

law exponent (λ) assumes the lowest value for the NO_3^- system. This provides an indirect support to the steady state fluorescence spectroscopic observation that the interconversion between solvation configurations is the slowest in the NO_3^- DES among the three systems considered here.⁴²⁻⁴³

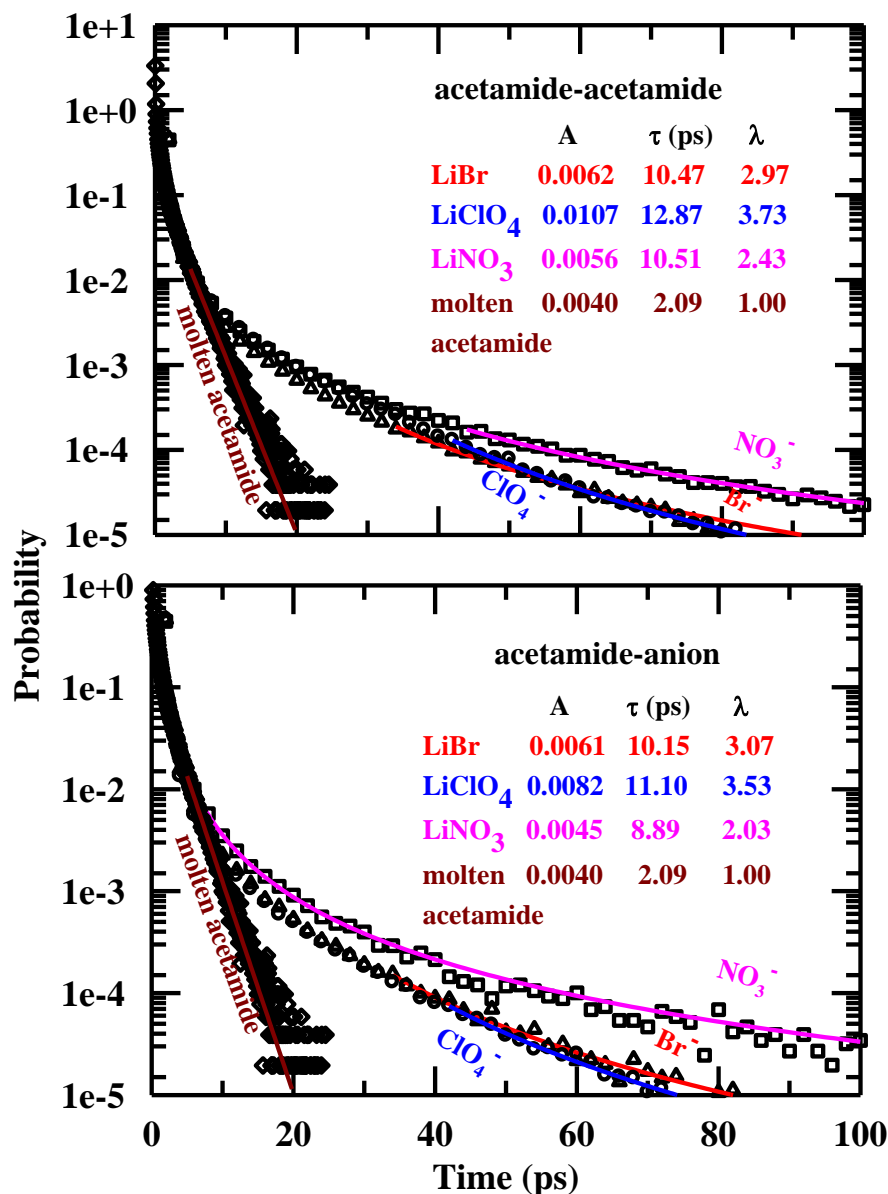


Figure 4.8: Waiting time distributions for acetamide-acetamide (upper panel) and the acetamide-anion (lower panel) for these DESs along fits of the long-time part of the distributions to a power law expression, $P(\tau_{\text{wait}}) \sim A(\tau_{\text{wait}} / \tau)^{-\lambda}$. Fit parameters are summarized in the inset.

Table 4.3: Mean and root mean square deviation times from the waiting and jump time distributions for acetamide in (acetamide + LiNO₃/Br/ClO₄) DESs. ‘Acet-anion’ refers to acetamide molecules interacting with anion irrespective of being complexed and not complexed with Li⁺.

DES	Mean waiting time ($\langle \tau_{waiting} \rangle$) (ps)		Mean jump time ($\langle \tau_{jump} \rangle$) (ps)		Waiting time RMSD ($\sigma_{waiting}$) (ps)		Jump time RMSD (σ_{jump}) (ps)	
	Acet-acet	Acet-anion	Acet-acet	Acet-anion	Acet-acet	Acet-anion	Acet-acet	Acet-anion
<i>Br</i> ⁻	1.32	1.26	1.06	1.04	2.9	2.5	1.46	1.26
<i>ClO</i> ₄ ⁻	1.41	1.23	1.00	1.00	3.0	2.3	0.74	0.71
<i>NO</i> ₃ ⁻	1.60	1.61	1.01	1.00	6.3	6.9	0.78	0.73

Next we have estimated the mean and the root mean squared deviation (RMSD) times associated with these waiting time distributions in order to generate an idea of the timescales that are intrinsic to the jump events in these DESs. The mean time has been calculated numerically by using the relation, $\langle \tau_{\text{wait}} \rangle = \int_0^{\infty} d\tau_{\text{wait}} \tau_{\text{wait}} P(\tau_{\text{wait}})$. The RMSD of the waiting time distribution is then obtained from the relation, $\sigma_{\text{wait}} = \left[\int_0^{\infty} d\tau_{\text{wait}} (\tau_{\text{wait}} - \langle \tau_{\text{wait}} \rangle)^2 P(\tau_{\text{wait}}) \right]^{1/2}$. Anion dependent $\langle \tau_{\text{wait}} \rangle$ and σ_{wait} so calculated for acetamide-acetamide and acetamide-ion pairs are listed in Table 4.3. Notice here that $\langle \tau_{\text{wait}} \rangle$ are very similar (~1-2 ps) for these ionic DESs although σ_{wait} differs significantly for the NO_3^- system (~6 - 7 ps) from the other two (~2-3 ps). This provides a partial explanation (see Eq. 4.5) to the unexpectedly longer $\langle \tau_{\ell} \rangle$ for the nitrate DES compared to those for the other two systems. The estimated mean and the RMSD times ($\langle \tau_{\text{jump}} \rangle$ and σ_{jump}) from the jump time distributions shown in Ref.37 are also presented in Table 4.3 for a comparison. As observed for $\langle \tau_{\text{wait}} \rangle$, $\langle \tau_{\text{jump}} \rangle$ also show insensitivity to the anion identity. However, $\langle \tau_{\text{jump}} \rangle$ are faster than $\langle \tau_{\text{wait}} \rangle$, and the estimated σ_{wait} values suggest jump time distributions are significantly narrower than the waiting time distributions. This indicates that it is the waiting time rather than the jump time that dominates the dynamics heterogeneity aspect of these systems.

4.4.4. Hydrogen bond correlation functions, $S_{\text{HB}}(t)$ and $C_{\text{HB}}(t)$: Connection to orientational relaxations

Figure 4.9 presents the simulated over-all $S_{\text{HB}}(t)$ and $C_{\text{HB}}(t)$ decays along with their multi-exponential fits in these ionic deep eutectics at 303 K. These H-bond relaxation functions have been obtained after averaging over all acetamide molecules that are interacting and not interacting with ions. Fit parameters are summarized in Table 4.4 and Table 4.5. For a comparison, corresponding simulated decays for neat molten acetamide at 368 K are also shown in the respective panels. Clearly, both the H-bond relaxations are slower in these DESs

than those in neat molten acetamide. Notice that both $S_{\text{HB}}(t)$ and $C_{\text{HB}}(t)$ decays exhibit anion dependence. Interestingly, the anion dependence for $S_{\text{HB}}(t)$ follows the viscosity trend of these media ($\eta_{\text{Br}^-} > \eta_{\text{NO}_3^-} > \eta_{\text{ClO}_4^-}$) while that for $C_{\text{HB}}(t)$ reflects the trend shown by $C_\ell(t)$. Fit parameters summarized in Table 4.4 indicate that the over-all $C_{\text{HB}}(t)$ decay contains a component (~10 -15%) that has a time constant in ~0.5-5 ns regime. This is qualitatively similar to the nanosecond component (~0.4-2.5 ns with ~5-15% amplitude) observed in the simulated over-all $C_\ell(t)$ decays for these DESs. This similarity highlights the interconnection between $C_{\text{HB}}(t)$ and $C_\ell(t)$, and arises from the participation of orientational structural rearrangement in $C_{\text{HB}}(t)$. Moreover, presence of such a slow decay in the $C_{\text{HB}}(t)$ suggests that the nanosecond component (~0.6-0.8 ns with nearly 70% amplitude)³¹ observed in the relevant DR measurements may derive contribution from the collective relaxation of the H-bond network involving acetamide molecules in these DESs. Data in these tables also reflect that for these DESs the average continuous H-bond relaxation times are ~6-16 times and the average structural H-bond relaxation times are ~6-47 times slower than those for neat molten acetamide. Consequently, we next investigate the role of anion-acetamide interactions in slowing down the $S_{\text{HB}}(t)$ and $C_{\text{HB}}(t)$ relaxation rates and effects of Li^+ on them in these media.

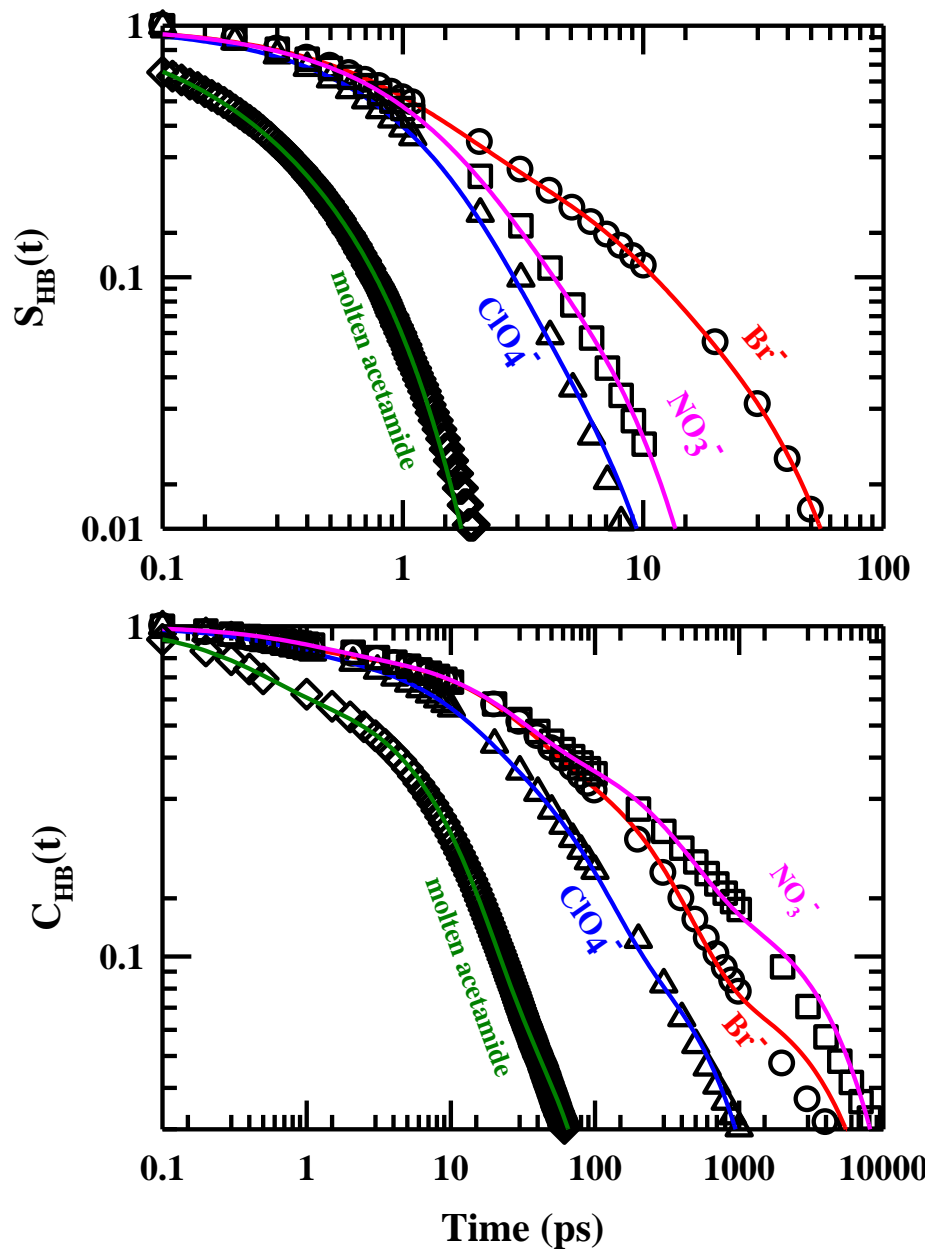


Figure 4.9: Simulated continuous H-bond relaxation function, $S_{HB}(t)$ (upper panel) and structural H-bond relaxation function, $C_{HB}(t)$ (lower panel) in the three ionic acetamide deep eutectics studied. Note the anion dependence of these relaxation functions.

Table 4.4: Multi-exponential fit parameters for the simulated $S_{HB}(t)$ for the separated out pairs that are H-bonded either to another acetamide or to an anion in the absence and presence of Li^+ in (acetamide + $LiNO_3/Br/ClO_4$) DESs, and for the neat molten acetamide. ‘All’ refers to all acetamide molecules in a given DES.

DES	Type	Li^+	a_1	τ_1 (ps)	a_2	τ_2 (ps)	a_3	τ_3 (ps)	a_4	τ_4 (ps)	β	$\langle\tau\rangle$ (ps)
NO_3^-	All	-	0.83	1	0.17	3.7	-	-	-	-	1	1.4
	Acet-acet	absent	0.82	1	0.18	3.6	-	-	-	-	1	1.4
	Acet-anion	absent	0.73	1.1	0.27	5	-	-	-	-	1	2.1
	Acet-acet	present	0.83	1	0.17	3.7	-	-	-	-	1	1.4
	Acet-anion	present	0.73	1.1	0.27	5.3	-	-	-	-	1	2.1
Br^-	All	-	0.82	0.9	0.18	3.3	-	-	-	-	1	1.3
	Acet-acet	absent	0.82	0.9	0.18	3.3	-	-	-	-	1	1.3
	Acet-anion	absent	0.47	0.8	0.3	5	0.23	19.6	-	-	1	6.4
	Acet-	present	0.82	0.9	0.18	3.2	-	-	-	-	1	1.3

	acet											
	Acet-anion	present	0.46	0.8	0.3	5.3	0.24	20.7	-	-	1	6.9
ClO_4^-	All	-	0.86	1	0.14	3.6	-	-	-	-	1	1.3
	Acet-acet	absent	0.86	1	0.14	3.6	-	-	-	-	1	1.4
	Acet-anion	absent	0.86	0.9	0.14	3.2	-	-	-	-	1	1.2
	Acet-acet	present	0.85	1	0.15	3.6	-	-	-	-	1	1.4
	Acet-anion	present	0.85	0.9	0.15	3.2	-	-	-	-	1	1.2
Molten acetamide	-	-	0.4	0.12	0.6	0.43	-	-	-	-	1	0.28

Table 4.5: Multi-exponential fit parameters for the simulated $C_{HB}(t)$ for separated out pairs that are H-bonded either to another acetamide or to an anion in the absence and presence of Li^+ in (acetamide + $LiNO_3/Br/ClO_4$) DESs, and for neat molten acetamide. ‘All’ refers to all acetamide molecules in a given DES.

DES	Type	Li^+	a_1	τ_1 (ps)	a_2	τ_2 (ps)	a_3	τ_3 (ps)	a_4	τ_4 (ps)	β	$\langle\tau\rangle$ (ps)
NO_3^-	all	-	0.16	0.7	0.37	12.4	0.38	88.5	0.09	833.1	1	113.3
	Acet- acet	absent	0.15	0.7	0.32	10.1	0.39	64.1	0.14	500	1	98.3
	Acet- anion	absent	0.11	1.1	0.25	30.3	0.38	625	0.26	5000	1	1545.2
	Acet- acet	present	0.16	0.7	0.32	10.1	0.39	64.5	0.13	500	1	93.5
	Acet- anion	present	0.10	1.1	0.21	36.2	0.41	714.3	0.28	5000	1	1700.6
Br^-	all	-	0.16	0.6	0.32	12.5	0.39	74.6	0.13	769.2	1	133.2
	Acet- acet	absent	0.16	0.6	0.27	10.2	0.42	58.8	0.15	555.6	1	110.9
	Acet- anion	absent	0.14	0.7	0.35	29.1	0.4	312.5	0.11	5000	1	685.3
	Acet- acet	present	0.16	0.6	0.28	10.4	0.41	59.5	0.15	555.6	1	110.7

	acet											
	Acet-anion	present	0.14	0.8	0.35	35.1	0.41	400	0.1	10000	1	1176.4
ClO_4^-	all	-	0.16	0.7	0.39	10.1	0.37	58.8	0.08	526.3	1	67.9
	Acet-acet	absent	0.16	0.7	0.35	9.1	0.37	45.4	0.12	333.3	1	60.1
	Acet-anion	absent	0.17	0.7	0.38	15.4	0.33	135.1	0.12	1666.7	1	250.6
	Acet-acet	present	0.16	0.7	0.34	9.1	0.37	45.7	0.13	344.8	1	64.9
	Acet-anion	present	0.16	0.7	0.34	16.6	0.36	158.7	0.14	2000	1	342.9
Molten acetamide	-	-	0.35	0.38	0.55	7.8	0.1	54.1	-	-	1	17.8

4.4.5. Separation of $S_{\text{HB}}(t)$ and $C_{\text{HB}}(t)$ relaxations into acetamide-acetamide and acetamide-anion components: Effects of Li^+ and origin of slowing down

Figure 4.10 shows the effects of Li^+ on $S_{\text{HB}}(t)$ (shown in Figure 4.9) by separating out the acetamide-acetamide and acetamide-ion relaxation components in these three deep eutectics. Because Li^+ can interact via the carbonyl oxygen of acetamide forming these pairs (acetamide-acetamide and acetamide-anion), one can further dissect a given pair into two sets: one set where Li^+ is complexed with acetamide and the other where it is not. Upper panels of Figure 4.10 presents the $S_{\text{HB}}(t)$ relaxations of acetamide-acetamide pairs in the presence and the absence of Li^+ . Simulated decays in these panels and fit parameters summarized in Table 4.4 indicate that $S_{\text{HB}}(t)$ relaxation involving only the acetamide-acetamide pairs depends neither on anion identity nor on complexation of acetamide with Li^+ , although the average relaxation rate ($\langle \tau \rangle^{-1}$) becomes ~ 5 times slower than that in neat molten acetamide. However, the relaxation involving acetamide-anion pair does depend on the anion identity (see lower panels and Table 4.4) but again remains largely insensitive to the presence of Li^+ in the medium. Note the the average relaxation rate of $S_{\text{HB}}(t)$ involving the acetamide-anion pairs is slower (~ 5 -25 times) than that corresponding to acetamide-acetamide pairs, suggesting that acetamide-anion interaction contributes considerably to the over-all slowing down of $S_{\text{HB}}(t)$ relaxation in these ionic acetamide deep eutectics.

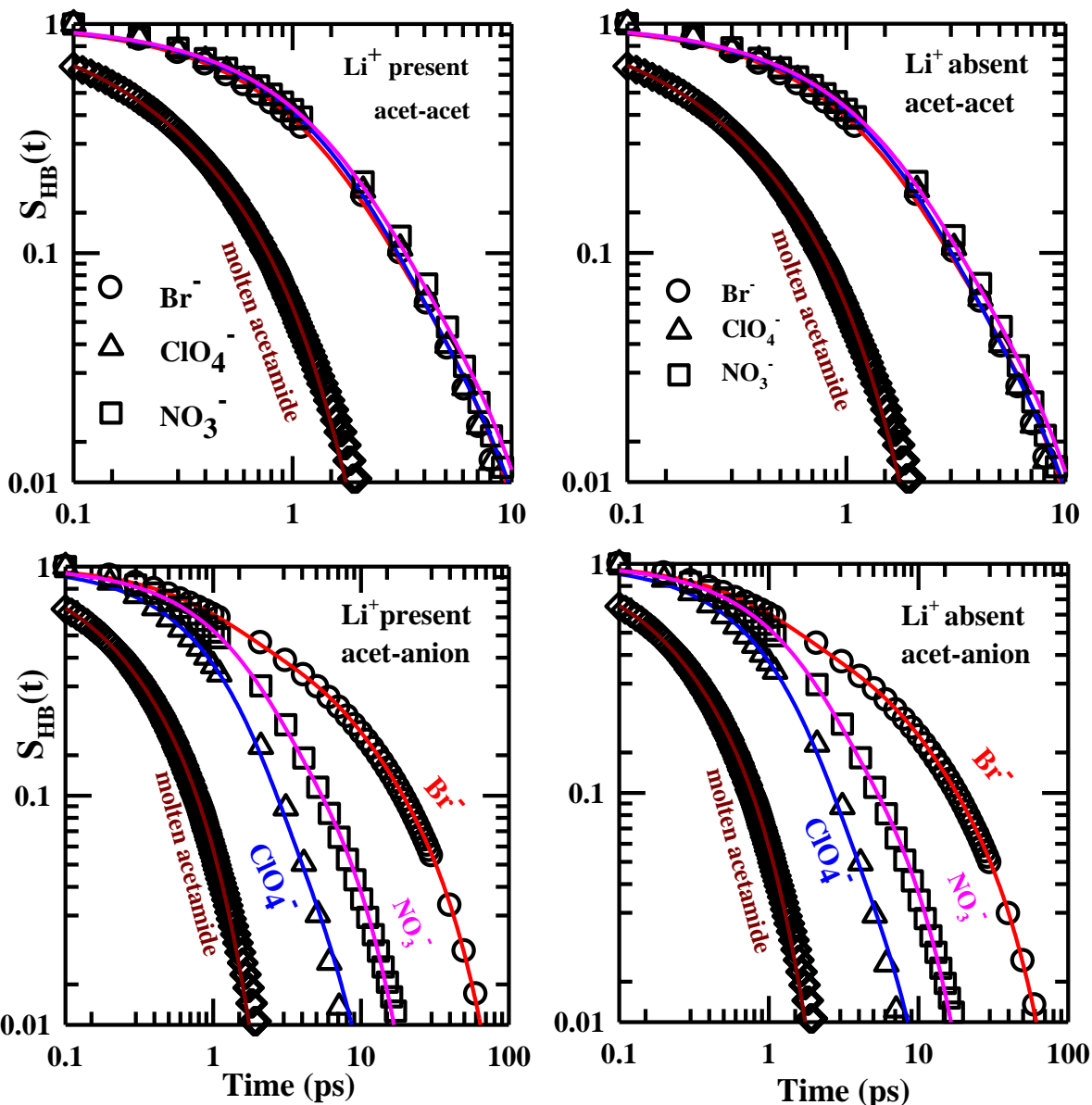


Figure 4.10: Continuous H-bond relaxation involving acetamide-acetamide (‘acet-acet’) and acetamide-anion (‘acet-anion’) pairs in the presence and absence of Li^+ . Note the anion dependence of the relaxation involving acetamide-anion species.

Figure 4.11 presents the similar analyses as shown above for $C_{\text{HB}}(t)$. Fit parameters in Table 4.5 suggest a slowing down of the average rate for $C_{\text{HB}}(t)$ involving only the acetamide-acetamide pairs by a factor of ~ 3 -6 over that of neat molten acetamide with a small contribution coming from Li^+ complexation. However, this factor becomes ~ 14 -96 for the relaxation of acetamide-anion pairs with a relatively larger contribution to the slowing down arising from complexation of Li^+ with acetamide. Also, an extremely slow component (~ 10 -

25%) with time constant of $\sim 2\text{-}10$ ns characterizes acetamide-anion $C_{\text{HB}}(t)$ relaxation. This component, therefore, provides the over-all $C_{\text{HB}}(t)$ relaxation a slow component that brings a similarity to the longtime rate of the simulated over-all $C_l(t)$ decay for acetamide molecules in these deep eutectics.

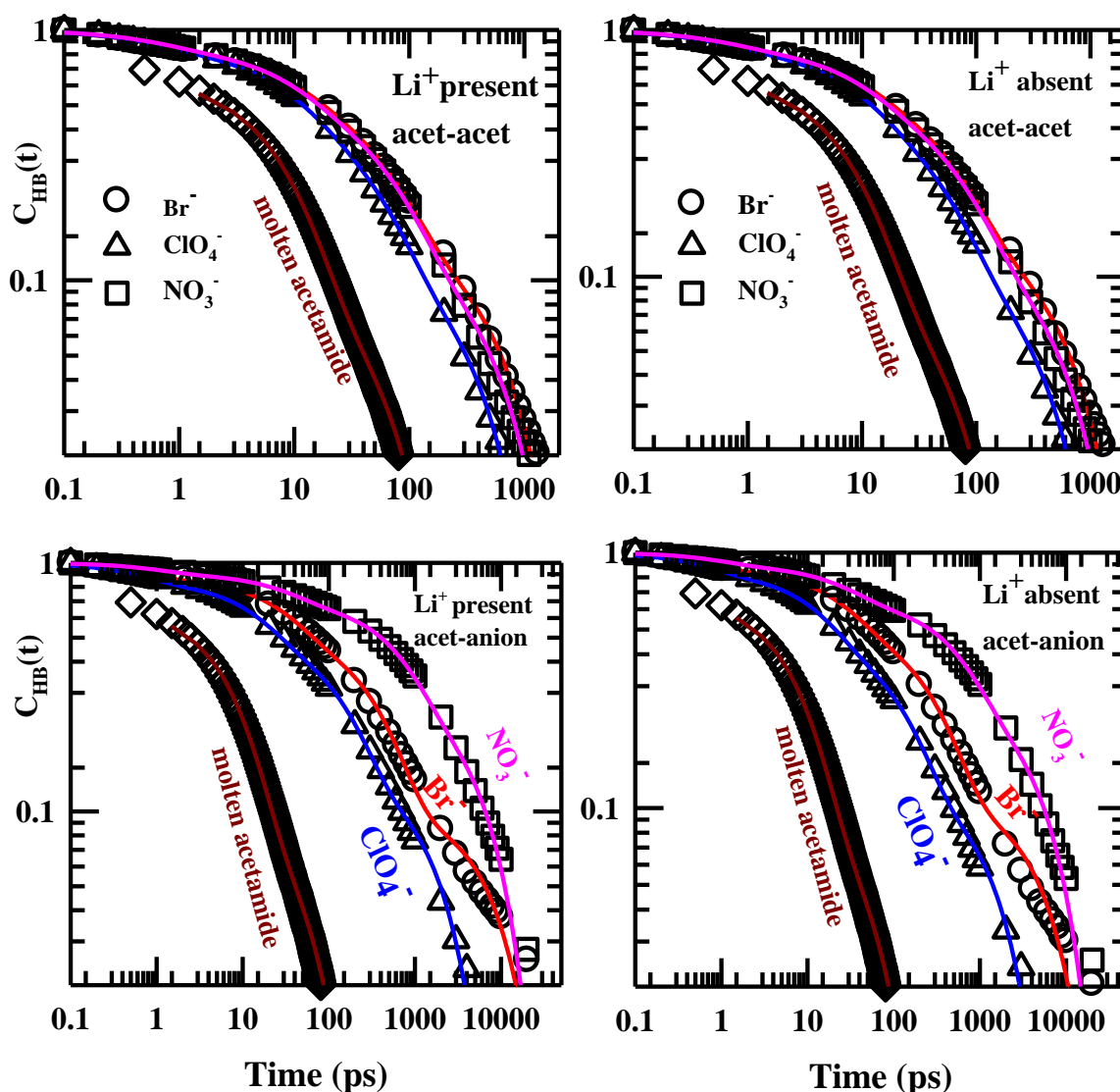


Figure 4.11: Structural H-bond relaxation involving acetamide-acetamide (‘acet-acet’) and acetamide-anion (‘acet-anion’) pairs in the presence and absence of Li^+ . Note the anion dependence of relaxation that involves acetamide-anion species.

A natural question arises in this context regarding how long the complex formed between Li^+ and acetamide via electrostatic interaction survives without changing the interaction site

(carbonyl oxygen) of the initial partner (acetamide molecule), and after changing but receiving within the interaction distance another carbonyl oxygen of a different acetamide molecule. This distance is determined from the simulated radial distribution function between Li^+ and carbonyl oxygen of acetamide in these deep eutectics (Figure C1 of Appendix C⁶³). Using similar conditions as employed for $S_{\text{HB}}(t)$ and $C_{\text{HB}}(t)$ temporal profiles for the survival period of acetamide- Li^+ complex have been generated. They are the continuous survival profile, $S_{\text{cont.}}^{\text{complex}}(t)$, and the structural survival profile, $C_{\text{str.}}^{\text{complex}}(t)$. These profiles are shown in Figure 4.12 along with multi-exponential fits and average survival times. Individual fit parameters are summarized in Table C1 and Table C2 of Appendix C.⁶³ Note the anion dependence of average survival times produced by these profiles follow the viscosity trend of these media. Interestingly, the average structural survival times are in ~3-12 ns range, with slow time constants in the ~10-20 ns regime (see Table C2 of the Appendix C⁶³). Such slow times are much longer than the slow dynamics probed by the DR measurements in the frequency window of $0.2 \leq \nu/\text{GHz} \leq 50$, and may therefore be responsible for the reported reduction of the static dielectric constant of molten acetamide in presence of these lithium salts (due to ‘irrotationally’ bound acetamide molecules to Li^+).³¹ In addition, DR measurements probing the dynamics at the mega-Hertz (MHz) range have reported a relaxation time of ~30 ns at ~300 K for acetamide/sodium thiocyanate (NaSCN) DES.⁸⁸ This provides a qualitative support for the simulated slow time constant of ~10-20 ns in these ionic DESs. In addition, this observation suggest that assumption of formation of nano-sized domains is not required to explain the relaxation timescales reported by MHz DR measurements for these media.

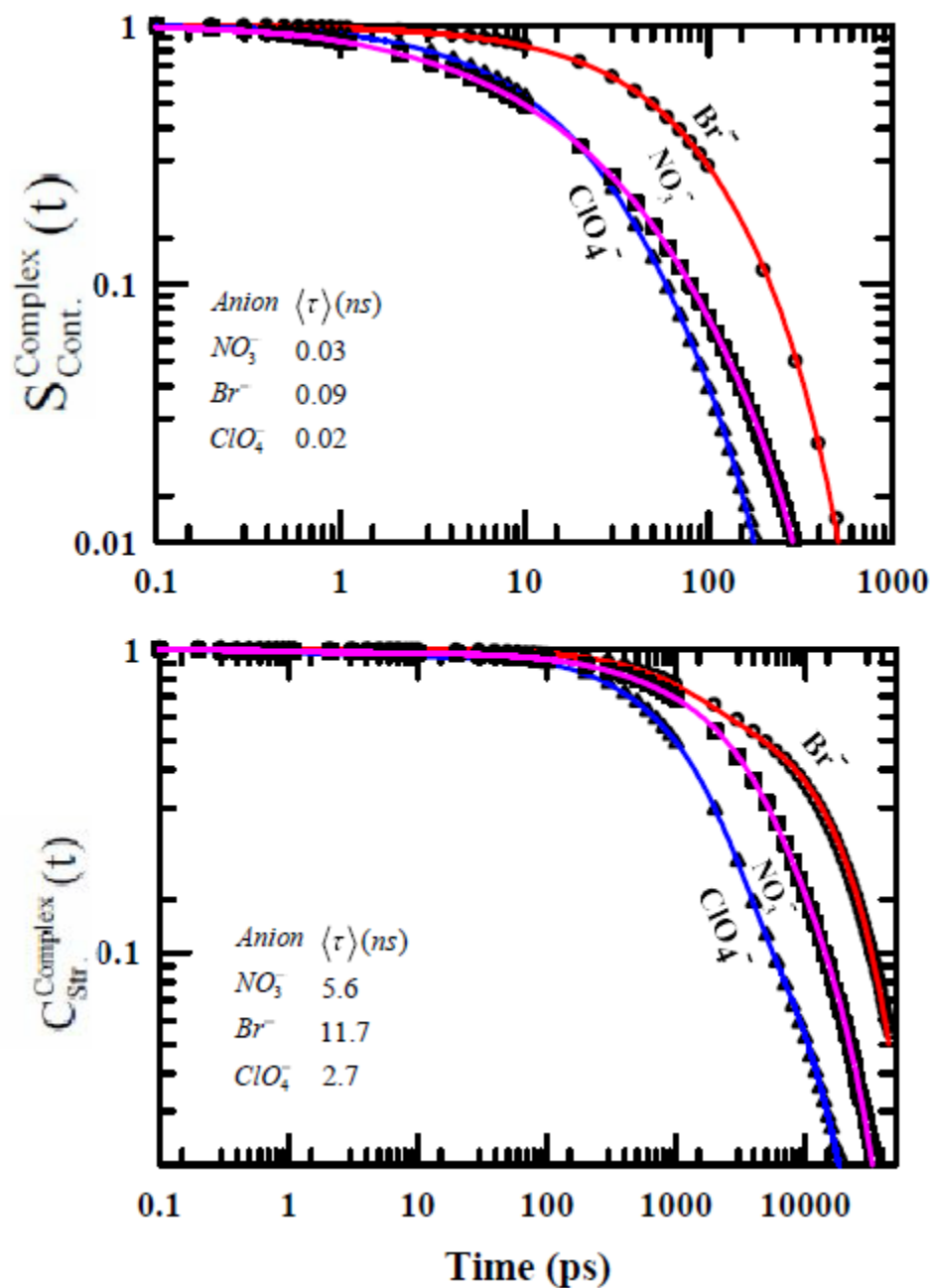


Figure 4.12: Simulated continuous and structural survival profiles for Li⁺-acetamide complex in the three ionic acetamide DESs studied here. Note the anion dependence, and difference in timescales between $S_{\text{Cont.}}^{\text{Complex}}(t)$ and $C_{\text{Str.}}^{\text{Complex}}(t)$.

4.5. Conclusions

To summarize, we have explored, via extensive analysis of MD simulation trajectories, the anion dependence of the reorientational relaxation in acetamide/LiBr/NO₃/ClO₄ deep

eutectics and probed the connection between the H-bond fluctuation dynamics and reorientational relaxation in these complex media. Simulated results indicated break-down of the single particle level hydrodynamic description of viscous resistance to the rotational diffusion of acetamide, and revealed ion-acetamide direct interaction. This ion-acetamide interaction is found to be the reason for the slow nanosecond component in the simulated reorientational relaxation in these systems. Average relaxation times do not follow the viscosity trend of these media, and support dynamic heterogeneity view and presence of orientation jumps. Simulated structural H-bond relaxation dynamics reflects a nanosecond component establishing thereby an interconnection between the orientational relaxation and H-bond fluctuations in these systems. In addition, these simulated results suggest that the nanosecond timescale found in DR measurements derive significant contribution from the cooperative relaxation of the H-bond network involving acetamide molecules in these deep eutectics. Simulated survival time for the acetamide-Li⁺ complex appears to correlate well with the DR measurements in the MHz range, and provides a possible justification of ion-induced reduction of static dielectric constant of molten acetamide. Waiting time distributions reveal the most persistent tail for the nitrate containing system, producing the longest root mean square deviation time among the three deep eutectics studied here. This and other simulation observation provide microscopic explanation to results obtained earlier via steady state and time-resolved fluorescence measurements of these media. Anion dependence of dynamic heterogeneity via four-point correlations⁸⁹⁻⁹¹ together with an extensive structural analysis is what is required now for further understanding of these multi-component molten systems. Investigation of coupling between ion translations and acetamide jump reorientations⁹²⁻⁹⁴ in these ionic deep eutectics can be another interesting future problem.

References:

1. B. Bagchi, *Molecular Relaxation in Liquids* (Oxford University Press, New York, 2012).
2. B. Bagchi and R. Biswas, *Adv. Chem. Phys.* **109**, 207 (1999).
3. A. Samanta, *J. Phys. Chem. Lett.* **1**, 1557 (2010).
4. E. W. Castner Jr., C. J. Margulis, M. Maroncelli, and J. F. Wishart, *Annu. Rev. Phys. Chem.* **62**, 85 (2011).
5. Q. Zhang, K. De Oliveira Vigier, S. Royer, and F. Jerome, *Chem. Soc. Rev.* **41**, 7108 (2012).
6. D. V. Wagle, H. Zhao, and G. A. Baker, *Acc. Chem. Res.* **47**, 2299 (2014).
7. A. P. Abbott, D. Boothby, G. Capper, D. L. Davies, and R. K. Rasheed, *J. Am. Chem. Soc.* **126**, 9142 (2004).
8. A. P. Abbott, G. Capper, D. L. Davies, R. K. Rasheed, and V. Tambyrajah, *Chem. Commun.* 70 (2003).
9. M. Francisco, A. van den Bruinhorst, and M. C. Kroon, *Angew. Chem. Int. Ed.* **52**, 3074 (2013).
10. R. Kubo, *J. Phys. Soc. Jpn.* **12**, 570 (1957).
11. R. Zwanzig, *Phys. Rev.* **124**, 983 (1961).
12. H. Mori, *Prog. Theor. Phys.* **33**, 423 (1965).
13. R. Zwanzig, *Annu. Rev. Phys. Chem.* **16**, 67 (1965).
14. R. Zwanzig, *J. Chem. Phys.* **33**, 1338 (1960).
15. R. Zwanzig, *Nonequilibrium Statistical Mechanics* (Oxford University Press, Oxford, **2001**)
16. C. J. F. Bottcher, *Theory of Electric Polarization*, 2nd Ed. (Elsevier, Amsterdam, **1973**, Vol. 1).
17. B. Bagchi and A. Chandra, *Adv. Chem. Phys.* **80**, 1 (1991).
18. S. Daschakraborty and R. Biswas, *J. Chem. Phys.* **140**, 014504 (2014).
19. S. Daschakraborty and R. Biswas, *J. Chem. Phys.* **144**, 104505 (2016).
20. J. G. Powles, *J. Chem. Phys.* **21**, 633 (1953).
21. J. M. Deutch, *Faraday Symp. Chem. Soc.* **11**, 26 (1977).

22. P. Madden and D. Kivelson, *Adv. Chem. Phys.* **56**, 467 (1984).
23. J. G. Kirkwood, *J. Chem. Phys.* **7**, 911 (1939).
24. A. Chandra and B. Bagchi, *J. Chem. Phys.* **91**, 1829 (1989).
25. B. Bagchi and A. Chandra, *Phys. Rev. Lett.* **64**, 455 (1990).
26. A. Chandra and B. Bagchi, *J. Phys. Chem.* **95**, 2529 (1991).
27. S. H. Glarum, *J. Chem. Phys.* **33**, 1371 (1960).
28. M.-L. Horng, J. A. Gardecki, and M. Maroncelli, *J. Phys. Chem. A* **101**, 1030 (1997).
29. A. Das, R. Biswas, and J. Chakrabarti, *J. Phys. Chem. A* **115**, 973 (2011).
30. A. Das, R. Biswas, and J. Chakrabarti, *J. Chem. Phys.* **136**, 014505 (2012).
31. K. Mukherjee, A. Das, S. Choudhury, A. Barman, and R. Biswas, *J. Phys. Chem. B* **119**, 8063 (2015).
32. M.-M. Huang, S. Bulut, I. Krossing, and H. Weingartner, *J. Chem. Phys.* **133**, 101101 (2010).
33. J. Hunger, A. Stoppa, S. Schrodle, G. Hefter, and R. Buchner, *ChemPhysChem.* **10**, 723 (2009).
34. D. Laage and J. T. Hynes, *Science* **311**, 832 (2006).
35. D. Laage and J. T. Hynes, *J. Phys. Chem. B* **112**, 14230 (2008).
36. S. Das, R. Biswas, and B. Mukherjee, *J. Phys. Chem. B* **119**, 274 (2015).
37. S. Das, R. Biswas, and B. Mukherjee, *J. Phys. Chem. B* **119**, 11157 (2015).
38. T. Chen, G. Hefter, and R. Buchner, *J. Phys. Chem. A* **107**, 4025 (2003).
39. J. T. Jindt and C. A. Schmuttenmaer, *J. Phys. Chem.* **100**, 10373 (1996).
40. M. Mizoshiri, T. Nagao, Y. Mizoguchi, and M. Yao, *J. Chem. Phys.* **132**, 164510 (2010).
41. C. Schroder, J. Hunger, A. Stoppa, J. Buchner, and O. Steinhauser, *J. Chem. Phys.* **129**, 184501 (2008).

42. B. Guchhait, S. Daschakraborty, and R. Biswas, *J. Chem. Phys.* **136**, 174503 (2012).
43. B. Guchhait, S. Das, S. Daschakraborty, and R. Biswas, *J. Chem. Phys.* **140**, 104514 (2014).
44. S. N. Tripathy, Z. Wojnarowska, J. Knapik, H. Shirota, R. Biswas, and M. Paluch, *J. Chem. Phys.* **142**, 184504 (2015).
45. R. Biswas, A. Das, and H. Shirota, *J. Chem. Phys.* **141**, 134506 (2015).
46. B. Guchhait, H. A. R. Gazi, H. Kashyap, and R. Biswas, *J. Phys. Chem. B* **114**, 5066 (2010).
47. A. Das, S. Das, and R. Biswas, *Chem. Phys. Lett.* **581**, 47 (2013).
48. A. Das, S. Das, and R. Biswas, *J. Chem. Phys.* **142**, 034505 (2015).
49. H. A. R. Gazi, B. Guchhait, S. Daschakraborty, and R. Biswas, *Chem. Phys. Lett.* **501**, 358 (2011).
50. A. Das and R. Biswas, *J. Phys. Chem. B* **119**, 10102 (2015).
51. P. G. Jessop, D. A. Jessop, D. Fu, and L. Phan, *Green Chem.* **14**, 1245 (2012).
52. Y. Dai, J. van Spronsen, G.-J. Witkamp, R. Verpoorte, and Y. H. Choi, *Anal. Chim. Acta.* **766**, 61 (2013).
53. C. Rub and B. Konig, *Green Chem.* **14**, 2969 (2012).
54. M. Francisco, A. van den Bruinhorst, and M. C. Kroon, *Green Chem.* **14**, 2153 (2012).
55. G. van der Zwan and J. T. Hynes, *J. Chem. Phys.* **78**, 4174 (1983).
56. G. van der Zwan and J. T. Hynes, *Chem. Phys.* **152**, 169 (1991).
57. T. Pradhan and R. Biswas, *J. Phys. Chem. A* **111**, 11524 (2007).
58. W. Smith and T. R. Forester, The DL_POLY Molecular Simulation Package, Daresbury Laboratory, Cheshire, U.K., **1999**.
59. A. D. MacKerell Jr., J. Wiorcikiewicz-Kuczera, and M. Karplus, *J. Am. Chem. Soc.* **117**, 11946 (1995).
60. K. P. Jensen and W. L. Jorgensen, *J. Chem. Theory Comput.* **2**, 1499 (2006).
61. C. Cadena and E. J. Maginn, *J. Phys. Chem. B* **110**, 18026 (2006).
62. J. N. Canongia Lopes, J. Deschamps, and A. A. H. Padua, *J. Phys. Chem. B* **108**, 2038 (2004).

63. See Appendix C for simulated radial distribution functions between Li^+ and carbonyl oxygen of acetamide, multi-exponential fits and average survival times of $S_{\text{cont.}}^{\text{complex}}(t)$ and $C_{\text{str.}}^{\text{complex}}(t)$ in these deep eutectics.
64. C. W. Yong, DL_FIELD, STFC Daresbury Laboratory, **2011**.
65. M. P. Allen and D. J. Tildesley, *Computer Simulation of Liquids* (Oxford University Press, New York, **1987**).
66. L. Martinez, R. Andrade, E. G. Birgin, and J. M. Martinez, *J. Comput. Chem.* **30**, 2157 (2009).
67. S. Nose, *J. Chem. Phys.* **81**, 511 (1984).
68. W. G. Hoover, *Phys. Rev. A* **31**, 1695 (1985).
69. J.-P. Ryckaert, G. Ciccotti, and H. J. C. Berendsen, *J. Comput. Phys.* **23**, 327 (1977).
70. D. Laage and J. T. Hynes, *Proc. Natl. Acad. Sci. U.S.A.* **104**, 11167 (2007).
71. J. P. Hansen and I. R. McDonald, *Theory of Simple Liquids*, 3rd ed. (Academic, San Diego, **2006**).
72. T. Pal and R. Biswas, *Theor. Chem. Acta.* **132**, 1348 (2013).
73. D. Laage and W. H. Thompson, *J. Chem. Phys.* **136**, 044513 (2012).
74. A. C. Fogarty, E. Duboue-Dijon, D. Laage, and W. H. Thompson, *J. Chem. Phys.* **141**, 18C523 (2014).
75. D. C. Rapaport, *Mol. Phys.* **50**, 1151 (1983).
76. A. Chandra, *Phys. Rev. Lett.* **85**, 768 (2000).
77. A. Luzar, *J. Chem. Phys.* **113**, 10663 (2000).
78. S. Indra and R. Biswas, *Mol. Simul.* **41**, 471 (2015).
79. A. Luzar and D. Chandler, *Nature.* **379**, 55 (1996).
80. A. Luzar and D. Chandler, *Phys. Rev. Lett.* **76**, 928 (1996).
81. X.-X. Zhang, M. Liang, J. Hunger, R. Buchner, and M. Maroncelli, *J. Phys. Chem. B* **117**, 15356 (2013).
82. S. Daschakraborty and R. Biswas, *J. Phys. Chem. B* **118**, 1327 (2014).
83. X.-X. Zhang, M. Liang, N. P. Ernstring, and M. Maroncelli, *J. Phys. Chem. B* **117**, 4291 (2013).
84. S. Daschakraborty, T. Pal, and R. Biswas, *J. Chem. Phys.* **139**, 164503 (2013).
85. R. Biswas and B. Bagchi, *J. Phys. Chem. B* **100**, 1238 (1996).
86. C. K. Kim, J. Won, H. S. Kim, Y. S. Kang, H. G. Li, and C. K. Kim, *J. Comput. Chem.* **22**, 827 (2001).

87. E. N. Ivanov, *Sov. Phys. JETP* **18**, 1041 (1964).
88. A. Amico, G. Berchiesi, C. Cametti, and A. Di Biasio, *J. Chem. Soc., Faraday Trans. 2* **83**, 619 (1987).
89. T. Pal and R. Biswas, *J. Phys. Chem. B* **119**, 15683 (2015).
90. T. Pal and R. Biswas, *Chem. Phys. Lett.* **517**, 180 (2011).
91. S. Indra, B. Guchhait, and R. Biswas, *J. Chem. Phys.* **144**, 124506 (2016).
92. J. C. Araque, R. P. Daly, and C. J. Margulis, *J. Chem. Phys.* **144**, 204504 (2016).
93. J. C. Araque, S. K. Yadav, M. Shadeck, M. Maroncelli, and C. J. Margulis, *J. Phys. Chem. B* **119**, 7015 (2015).
94. P. Banerjee, S. Yashonath, and B. Bagchi, arXiv preprint, arXiv:1605.00790, **2016**.

Chapter 5

Structural Aspects of Amide Deep Eutectics: A Molecular Dynamics Investigation

5.1. Introduction

Deep eutectic solvents (DESs), an alternative to room temperature ionic liquids¹⁻² (RTILs), have recently found a considerable attention because of various fundamental and technological importance.³⁻¹⁰ DESs are mainly mixtures of hydrogen bond acceptors (HBA) like quaternary phosphonium, ammonium cation with hydrogen bond donors (HBD) such as glycerol, urea, ethylene glycol etc.⁶ When they are mixed at a particular mole fraction the mixture becomes liquid at a temperature less than their individual melting temperatures. Several interesting properties of DESs like low vapour pressure, high thermal stability, low melting point, non-toxicity, cheaper cost make them suitable for various chemical and industrial applications.¹¹⁻¹⁵ In chemical industry they are widely used as eco-friendly reaction media and catalysis.^{4,6} Also, DESs are finding several novel applications in bio-industry such as dissolution of biopolymers,¹⁶ extraction of aromatic compounds from plants,¹⁷ extraction of proteins¹⁸ etc. Given the importance of DESs, a proper and in-depth understanding of structural and dynamical aspects are required for smarter use of these media. In addition, an understanding of the static and dynamic medium effects on chemical reactions¹⁹⁻²¹ is required for using these solvents for solvent engineering.

Various DESs comprised of amide and electrolyte have been investigated via time-resolved fluorescence measurements,²²⁻²⁸ dielectric relaxation experiments,²⁹ optical kerr effect spectroscopy³⁰ and molecular dynamics simulations.^{22,23,31} Time-resolved fluorescence measurements have reported fractional viscosity dependence and decoupling of the translational and rotation rates of a dissolved dipolar solute probe in these mixtures. This has been explained in terms of dynamic heterogeneity and supported by the stretched exponential decay of the simulated wave-vector dependent amide dynamic structure factors. The dipolar orientational mechanism of molten acetamide³² as well as acetamide in presence of these electrolytes has been analysed.³³ Also, the orientational polarization relaxation and its

connection to the hydrogen bond fluctuation dynamics have been discussed just recently.³⁴ Both these orientational relaxation and hydrogen bond dynamics have been separated into (a) amide-amide and (b) ion-amide parts in order to quantify the individual contributions arising from different interactions. Thus the dynamics of these systems were analysed systematically; however, the structural aspects have remained largely unexplored. The work presented here therefore focuses on the structural aspect of amide deep eutectics and the role of ions for inducing additional complexity to it.

The solvation of Li^+ in organic medium which directly influences its transport properties has immense industrial importance.³⁵⁻³⁸ Li^+ battery with high specific energy storage capability is often used as attractive power sources. However, Li^+ battery has some limitations for large scale application in automobile industry. The limitation is mainly due to their poor ionic conductivity arising out of strong co-ordination of Li^+ by the solvent. Thus there is a growing need in industry to design suitable solvents to overcome those shortcomings. Note transport properties such as diffusion, conductance, viscosity crucially depend on solvation structure. Molecular dynamics simulations in this case can provide molecular-level information regarding the solvation structure around the ion, and its transport mechanism. Several room temperature ionic liquids (RTILs) have been investigated³⁹⁻⁴¹ via MD simulations in order to examine the local structure. It has been found that, on an average, the coordination number for Li^+ is four. However, the co-ordination number can differ depending upon the identity of the anion and solvent. Since the first co-ordination shell of Li^+ is highly stable, it diffuses along with its first solvation shell as a ‘solvent-dressed’ entity with a hydrodynamic radius much larger than its crystallographic ionic radius.⁴²⁻⁴⁴

In the present study we have carried out all-atom molecular dynamic simulations of amide/electrolyte DESs containing CH_3CONH_2 as the amide and three different types of electrolytes, namely, lithium bromide ($LiBr$), lithium nitrate ($LiNO_3$) and lithium perchlorate ($LiClO_4$) at 303 K and 350 K. First we have shown how the acetamide structure changes on adding electrolytes and its dependence on ion identity. Then we have examined the micro-structures that have formed in these mixtures and the roles played by the ions (both cation and anion). Next, we have investigated the cluster size and lifetime distributions with

an aim to generate a qualitative understanding of solution heterogeneity. These distributions are then separated into individual components pertaining to (a) $CH_3CONH_2 - CH_3CONH_2$, (b) $Li^+ - CH_3CONH_2$ and (c) $Li^+ - X^-$ interactions.

5.2. Simulation Details

All-atom molecular dynamics simulations were carried out with 512 number of total molecules with the composition $[0.78 CH_3CONH_2 + 0.22 LiX]$ ($X^- = Br^-, NO_3^-, ClO_4^-$) at two temperatures 303 K and 350 K with DL_POLY version 2.20.⁴⁵ Additionally, all-atom simulation was carried with 256 number of acetamide molecules at 368 K in order to compare structural differences with DESs. As the melting temperature of acetamide is around 353 K,⁴⁶ the pure acetamide system was simulated at a higher temperature. The potential function used has the following general form:

$$U(R) = \sum_{bonds} K_r(r - r_{eq})^2 + \sum_{angles} K_\theta(\theta - \theta_{eq})^2 + \sum_{dihedrals} K_\phi(1 + \cos[\eta\phi - \delta]) + \sum_{i < j}^{atoms} \left(\frac{A_{ij}}{R_{ij}^{12}} - \frac{B_{ij}}{R_{ij}^6} \right) + \sum_{i < j}^{atoms} \frac{q_i q_j}{4\pi\epsilon_0 R_{ij}} \quad (5.1)$$

In Eq. 5.1, K_r denotes the bond constant with the equilibrium bond distance r_{eq} , K_θ the angle constant with the equilibrium angle θ_{eq} , K_ϕ the dihedral constant with periodicity n , dihedral angle ϕ and phase shift δ . R_{ij} is the distance between i and j atoms with partial charges q_i and q_j , respectively. The force field parameters for CH_3CONH_2 were taken from the CHARMM⁴⁷ force field and the same for Li^+ , Br^- , NO_3^- , ClO_4^- were taken from the existing literature.⁴⁸⁻⁵⁰ These force field parameters were used previously to study reorientational dynamics³²⁻³⁴ and density relaxation of these DESs.²²⁻²³ Since the simulated results could successfully explain the experimental observations, we continued to use those force field parameters here also. All the force field parameters are summarized in Appendix A and Appendix B (Table B1-Table B4, Figure B1-Figure B2). The force field was constructed using DL_FIELD.⁵¹ The short-range van der Waals interaction was considered via the Lennard-Jones potential.⁵² Ewald summation technique⁵² was employed to treat the long-range electrostatic interactions.

The initial configuration of the simulated mixture was constructed using Packmol⁵³ with large simulation box length. Then each system was equilibrated in NPT ensemble at 1 atm pressure for 5 ns to reach the experimental density.^{22,30} The simulated densities were found to be in good agreement with the experimental values (Table D1, Appendix D). Nose-Hoover thermostat⁵⁴ and barostat⁵⁵ were used to control the temperature and pressure with time constant of 0.4 and 1.0 ps, respectively. After a further equilibration of 5 ns in NVT ensemble with Nose-Hoover thermostat⁵⁴ with time constant of 0.4 ps, the final production run was carried out for 100 ns in NVT ensemble. The periodic boundary condition was employed in all the three directions and the equation of motion was integrated with a time step of 0.5 fs using the velocity Verlet algorithm.⁵² The trajectories were saved every 0.1 ps for further analyses. All the snapshots shown in this study were constructed using the VMD⁵⁶ package.

5.3. Results and Discussion

5.3.1. Radial Distribution Function

Study of radial distribution function (RDF) gives a molecular insight about the solution structure. Several studies⁵⁷⁻⁵⁹ have revealed that the Li^+ containing electrolytes, when added into homogeneous solutions, produce heterogeneous environments. To analyse the role played by Li^+ and its ion counterpart in forming and stabilizing different kinds of aggregates, several RDFs of the three DESs have been compared. But before that, in order to understand how the homogeneous local environment changes into heterogeneous one in the presence of an added electrolyte, a comparison among several RDFs have been shown. The RDF has been calculated from the following equation:

$$g_{ij}(r) = \frac{1}{\rho N} \left\langle \sum_{ij} \delta(r - r_{ij}) \right\rangle \quad (5.2)$$

where N is the number of particles in the system, ρ the number density, i and j are two different types of particles and the brackets indicate the ensemble average.

Hydrogen bond, one of the most important and widely studied intermolecular interactions⁶¹⁻⁶⁶ plays a lead role in the structure and dynamics of the amide compounds. Diffraction

techniques⁶⁷⁻⁷¹ both in the solid state and gaseous phase have been applied to study the structure of acetamide. Two different types of crystal structures exist⁷⁰⁻⁷¹ for acetamide molecules - rhombohedral and orthorhombic forms. But in both the structures acetamide molecules are connected through the hydrogen bonds via $H(-CONH_2)\dots O(-CONH_2)$ interaction. The representative RDF is shown in Figure 5.1. A snapshot is presented inside

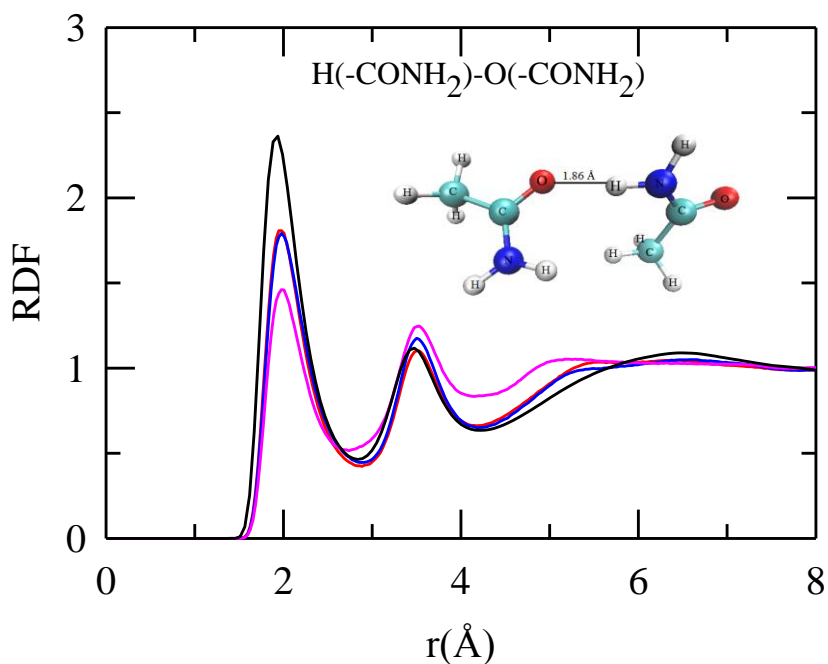


Figure 5.1: Simulated RDFs for $H(-CONH_2) - O(-CONH_2)$ for all DESs at 303 K and also for molten acetamide at 368 K. The black line is for molten acetamide, red line for Br^- , blue line for ClO_4^- and pink for NO_3^- . Snapshot is provided inside the figure for better understanding.

the figure which shows the geometrical position of acetamide molecules engaged in hydrogen bonding interaction. When compared with RDFs of the DESs at 303K, it is found that the peak height decreases substantially in presence of the electrolyte indicating the collapse in the hydrogen bonding network among the acetamide molecules. It should be noted that the comparison is made between molten acetamide simulated at 368K and the DESs at 303K which further enhances the effect of the electrolyte. The length of the

$H(-CONH_2)\dots O(-CONH_2)$ bond found from the structural investigation of the liquid acetamide is 3.03\AA ⁶⁹⁻⁷⁰ which matches pretty well with the 1st peak minima of the RDF. The peak height for the DESs increases as $Br^- \approx ClO_4^- > NO_3^-$ implying that the $H(-CONH_2)\dots O(-CONH_2)$ interaction among acetamide molecules is the least in presence of NO_3^- . However, this does not contradict the popular belief of $LiClO_4$ as H-bond breakers.⁷²⁻⁷³ It should be noted that density relaxation studies of these DESs at various length scales suggest that the dynamics of the system is the fastest in presence of ClO_4^- .²² Similar conclusion has also been drawn from the orientational and H-bond dynamics study of these DESs.³⁴

The RDF of $O(-CONH_2) - O(-CONH_2)$ shown in Figure 5.2 is quite interesting and clearly depicts the structural changes of acetamide taking place in presence of an electrolyte. The RDF for all shows the main peak at around 4.90\AA and a small hump before the main peak at

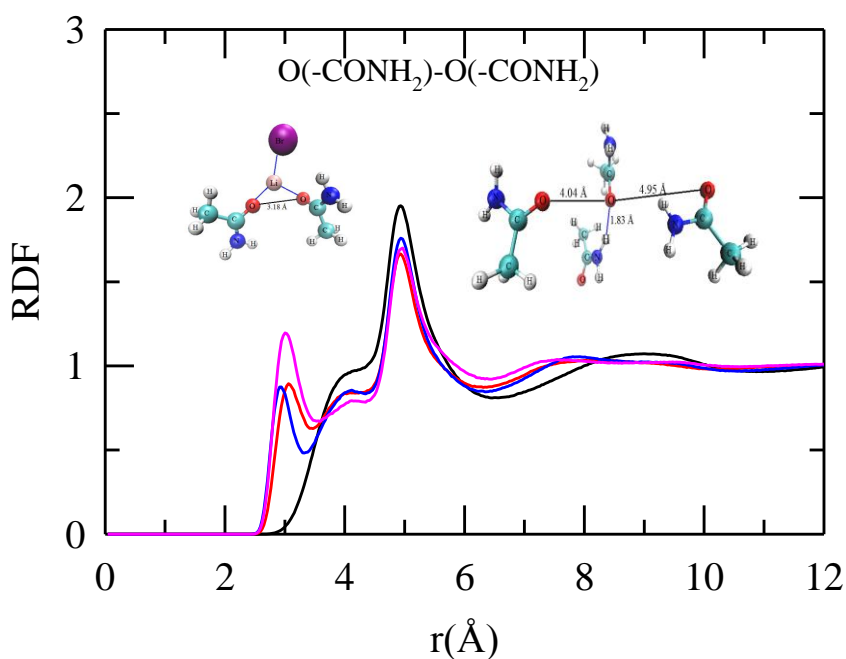


Figure 5.2: Simulated RDFs for $O(-CONH_2) - O(-CONH_2)$ for all DESs at 303 K and also for molten acetamide at 368 K. The black line is for molten acetamide, red line for Br^- , blue line for ClO_4^- and pink for NO_3^- . Various snapshots are provided at different length scales for better understanding.

around 4 Å. The main peak height is the highest in molten acetamide and decreases in presence of electrolyte. Interestingly all the electrolyte mixtures show an additional peak around 3 Å which is absent in the pure acetamide mixture. This closer approach of the $O(-CONH_2)$ atoms between acetamide molecules reflects the enhanced interaction in presence of the electrolytes. In order to have the molecular level understanding of the local geometry we have taken snapshots around peak values. The peak value around 5 Å comes when two $O(-CONH_2)$ atoms of two different acetamides faces each other with one $H(-CONH_2)$ atom belonging to one of those acetamides comes in between them. Interestingly the distance of $O(-CONH_2)$ with this $H(-CONH_2)$ is ~ 1.9 Å which is around the peak value of $O(-CONH_2) - H(-CONH_2)$ RDF. Therefore, this peak evolves as the main peak as it facilitates the hydrogen bonding interaction between two acetamide molecules and hence the peak order is similar to Figure 5.1. The hump around 4 Å arises when there is no $H(-CONH_2)$ moiety in between them. Next, we explain the peak position around 3 Å which is observed only in the presence of electrolytes. It is evident from the snapshot that the closest approach between two $O(-CONH_2)$ atoms is possible when there is one Li^+ in between them interacting with both the $O(-CONH_2)$ atoms. This interaction between Li^+ and $O(-CONH_2)$ is further enhanced when the ions (X^-) attached to Li^+ interacts with the $H(-CONH_2)$ atoms. NO_3^- , with its three oxygen atoms and planar geometry, probably fits as the best candidate and hence, shows an enhanced peak at this distance as compared to the other two ions.

Figure 5.3 gives RDF for $CH_3CONH_2 - CH_3CONH_2$. Note the $C(-CONH_2)$ atom has been considered as the centre of mass of CH_3CONH_2 for calculating the RDF. It is interesting to see that the correlation among acetamide molecules extends up to 15 Å which is ~ 3 times of the diameter of acetamide.²² Note similar correlation length also has been found for ionic liquids from the analysis of four-point correlation function.⁷⁴ The peak height is similar for molten acetamide and in presence of NO_3^- , is slightly higher than Br^- and ClO_4^- . A closer look at the RDFs suggests the presence of three distinct solvation shells, the first of which appears at ~ 4.6 Å, second at ~ 9 Å and the third at ~ 13 Å. At a distance smaller than 4.6 Å

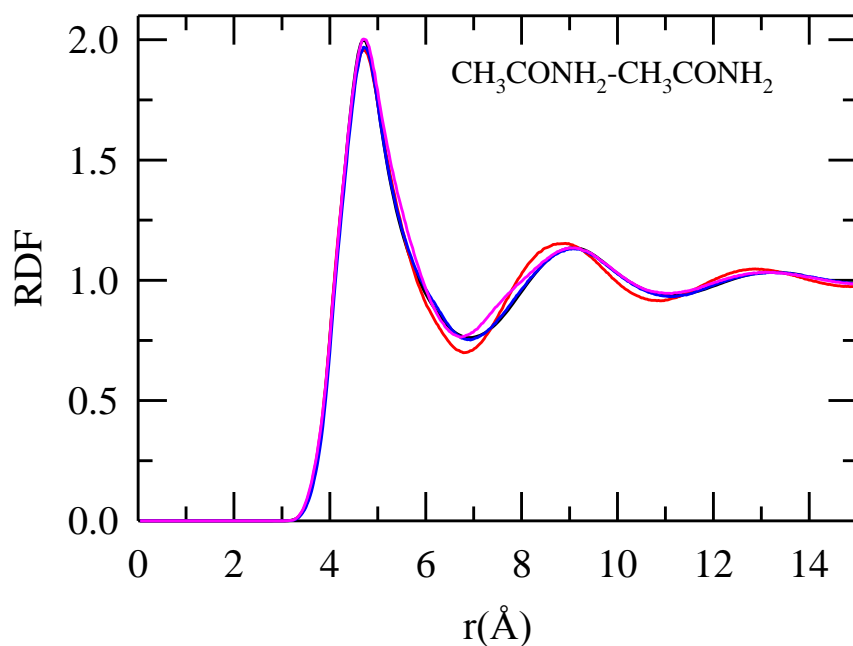


Figure 5.3: Simulated RDFs for $CH_3CONH_2 - CH_3CONH_2$ for all DESs at 303 K and also for molten acetamide at 368 K. The black line is for molten acetamide, red line for Br^- , blue line for ClO_4^- and pink for NO_3^- .

Li^+ and its counter ion are expected to interact with the acetamide molecule. The strong peak in the RDF of $Li^+ - O(-CONH_2)$ as observed in Figure 5.4 indicates that Li^+ ion is strongly co-ordinated to the $O(-CONH_2)$ atom of the amide group to form Li^+ assisted aggregation of acetamide molecules. This strong interaction with Li^+ has also been observed for other Li^+ containing systems.⁷⁵

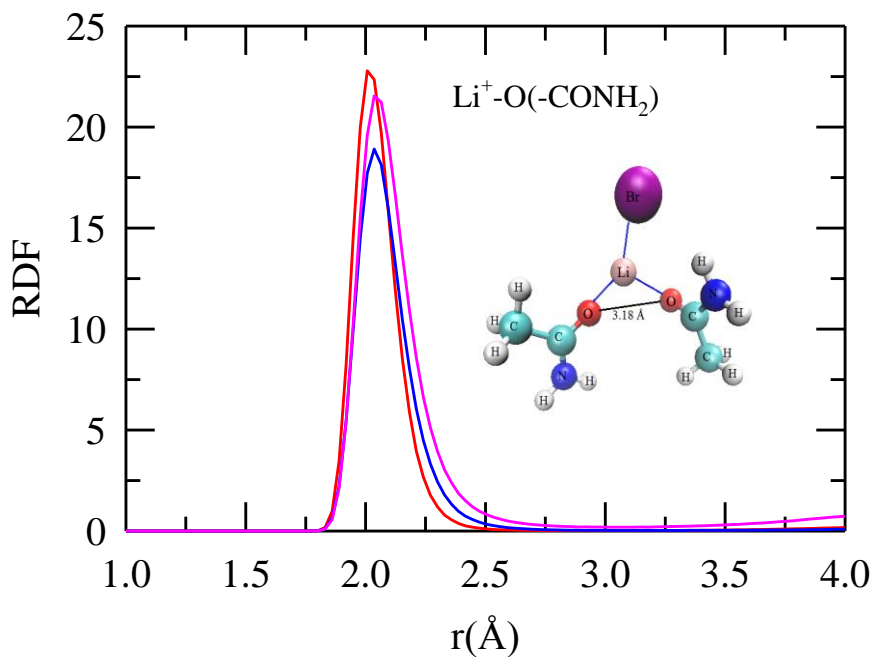


Figure 5.4: Simulated RDFs for $\text{Li}^+ - \text{O}(-\text{CONH}_2)$ for all DESs at 303 K. A snapshot is provided inside the plot. The red line is for Br^- , blue line for ClO_4^- and pink for NO_3^- .

The $\text{Li}^+ - \text{Li}^+$ RDF in Figure 5.5 is very interesting and provides useful structural information on these molten mixtures. The $\text{Li}^+ - \text{Li}^+$ distance is governed by a variety of factors including binding with the $\text{O}(-\text{CONH}_2)$ moiety of the acetamide molecules. It is expected that the $\text{Li}^+ - \text{Li}^+$ distance would increase if the acetamide molecules can successfully break the strong electrostatic interaction between Li^+ and its counter anion. So the nearest peak in Figure 5.5 comes from the $\text{Li}^+ - \text{O}(-\text{CONH}_2)$ interaction to form the Li^+ -amide complex. And the other peaks arise from the interaction with the anions of the electrolytes. It is likely that if the conformation of the anion is such that Li^+ can bind with the anion of the electrolyte in more than one way then the $\text{Li}^+ - \text{Li}^+$ distance would vary, and depending on the conformation of the anion of the electrolyte, more than one peak would appear at longer distances. First we mention the general observations. There are three distinct

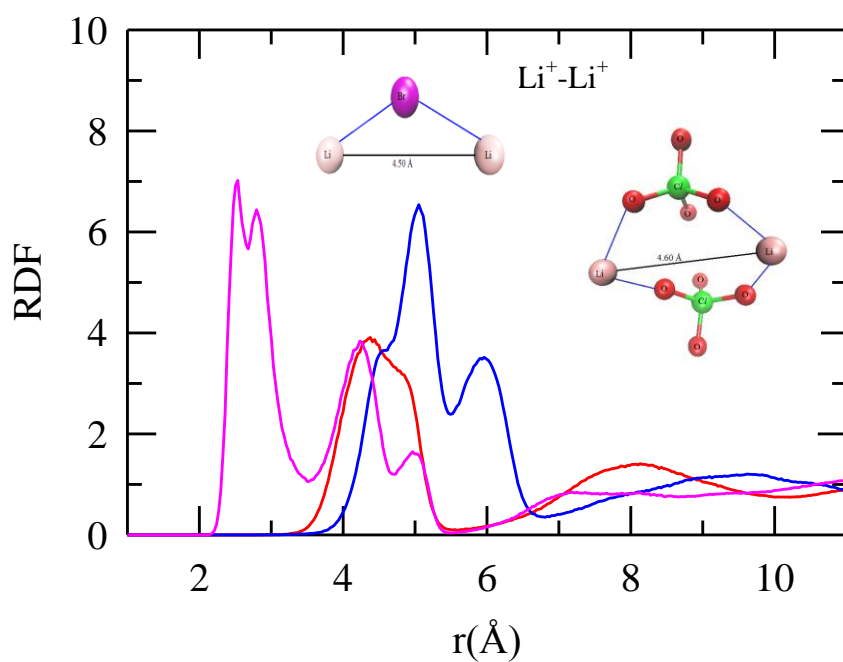
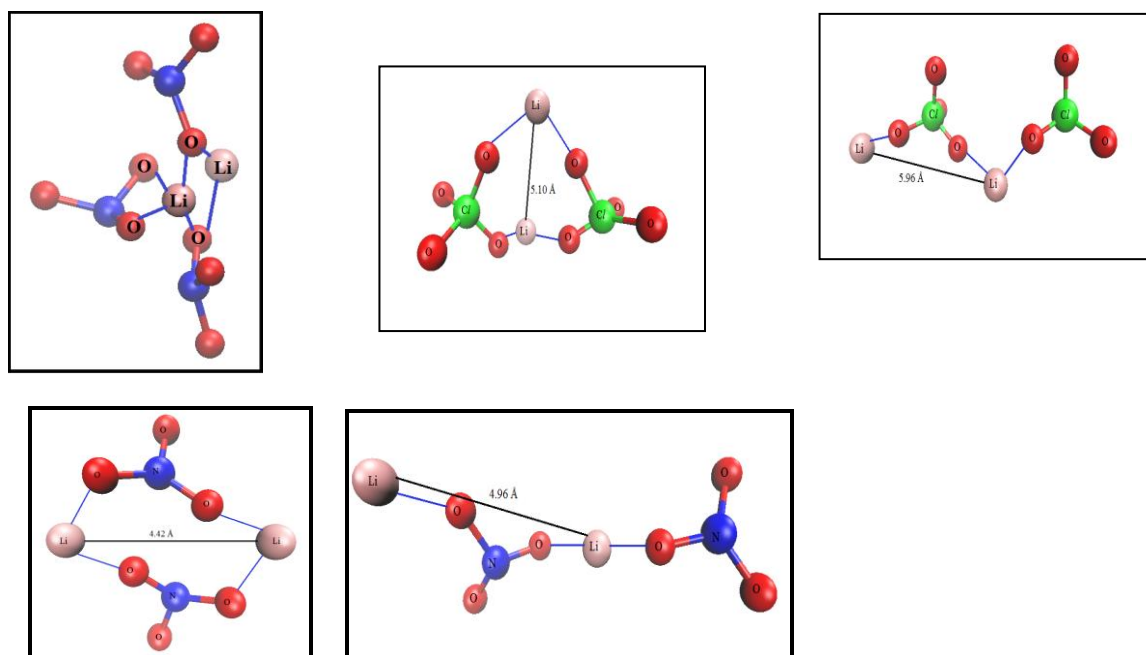


Figure 5.5: Simulated RDFs for $Li^+ - Li^+$ for all DESs at 303 K. The red line is for Br^- , blue line for ClO_4^- and pink for NO_3^- . Various snapshots at different length scales are provided inside the figure for better understanding.

regions of inhomogeneous distribution as observed from $Li^+ - Li^+$ RDF (i) at low distance where the RDF is notably structured due to the interaction with $O(-CONH_2)$ and anion

counterpart, (ii) the missing of a long-range ordering at longer distance and (iii) an intermediate region where practically the correlation is missing. This very pattern of Li^+ organization has been observed in various other heterogeneous environments.⁷⁶⁻⁷⁷ Now we would explain the individual characteristics. In presence of Br^- only one peak is observed around 4.3 Å followed by a small shoulder around 5 Å. Geometry analysis suggests that this peak arises when a Br^- sits in between two Li^+ . A broad second peak also appears at a larger distance around 8 Å. Note this second peak position follows the size of the anion that is $NO_3^- > Br^- > ClO_4^-$. In presence of NO_3^- , the first peak appears around 2.80 Å and bifurcated in nature. The second peak develops at longer distances, 4.25 Å followed by another small peak at 5.0 Å. We have captured snapshots at these distances in order to understand the local geometry. The first peak appears when both Li^+ interact simultaneously with multiple NO_3^- and CH_3CONH_2 molecules resulting in complex aggregates. A slight change in the local geometry to avail the multiple co-ordination sites results in the bifurcation as observed in the RDF. Note this peak is observed only in the presence of NO_3^- due to following reasons: (1) NO_3^- has the smallest size among the ions. So it can fit easily inside the cavity and (2) NO_3^- , being planar, its three $O(-NO_3^-)$ atoms can interact in more effective way to $H(-CONH_2)$ atoms of acetamide molecules which provide extra stabilization to the resulting complex as compared to the other ions. The other two peaks arise due to various anion conformations. The peak around 4.3 Å appears when Li^+ interacts with two NO_3^- to form an eight member closed ring. The next peak around 5 Å arises both Li^+ interacts with NO_3^- to form a linear chain like structure. This various pattern of interactions reflect the inherent complexity of the system. Similar trend is also observed for ClO_4^- . Note multiple peaks are not observed in presence of Br^- as the multiple anion conformation is not possible here.

Figure 5.6 shows the RDF of Li^+ with CH_3CONH_2 . The interaction between Li^+ and CH_3CONH_2 is quite strong as evident from the peak height mainly due to the strong electrostatic interaction with $O(-CONH_2)$. Hence, the ordering of the peak height follows the ordering of the RDF between Li^+ and $O(-CONH_2)$.

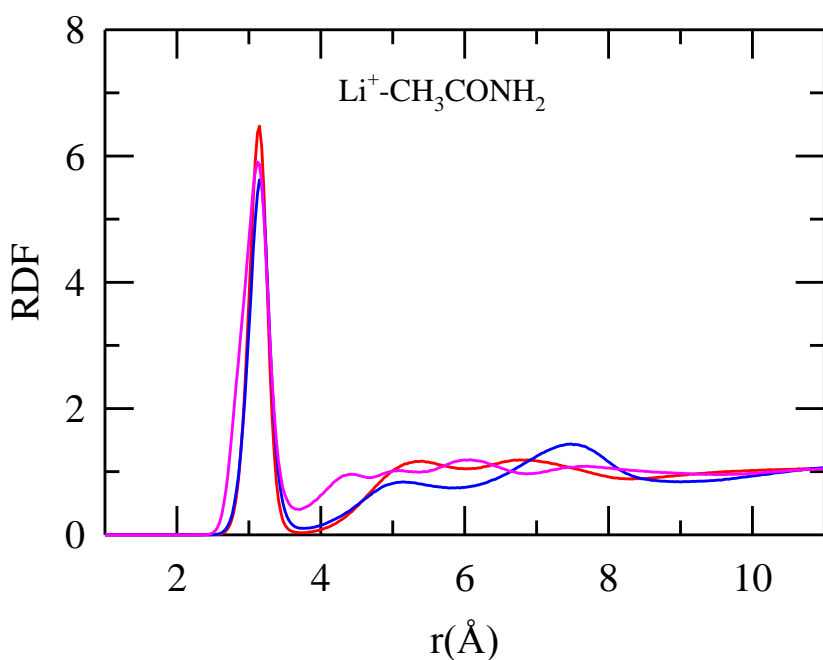


Figure 5.6: Simulated RDFs for $Li^+ - CH_3CONH_2$ for all DESs at 303 K. The red line is for Br^- , blue line for ClO_4^- and pink for NO_3^- .

Next we discuss the RDF between X^- and CH_3CONH_2 as shown in Figure 5.7. Here also the closest approach is possible in case of NO_3^- with smallest size giving rise to the peak at the smallest length scale. Note similar to the $Li^+ - Li^+$ RDF, the RDFs here also are bifurcated in presence of NO_3^- and ClO_4^- due to different anion conformations. It should be mentioned that the RDF between Li^+ and CH_3CONH_2 gives the peak around 3 Å and then around 4 Å the RDF between X^- and CH_3CONH_2 develops. At a slightly longer distance around 5 Å the principal peak of $CH_3CONH_2 - CH_3CONH_2$ RDF grows. This suggests that Li^+ interacts strongly with X^- to form an ion-pair type complex and this complex is solvated by the acetamide molecule. This may be the pre-cursor for inducing inhomogeneity to the solution structure.

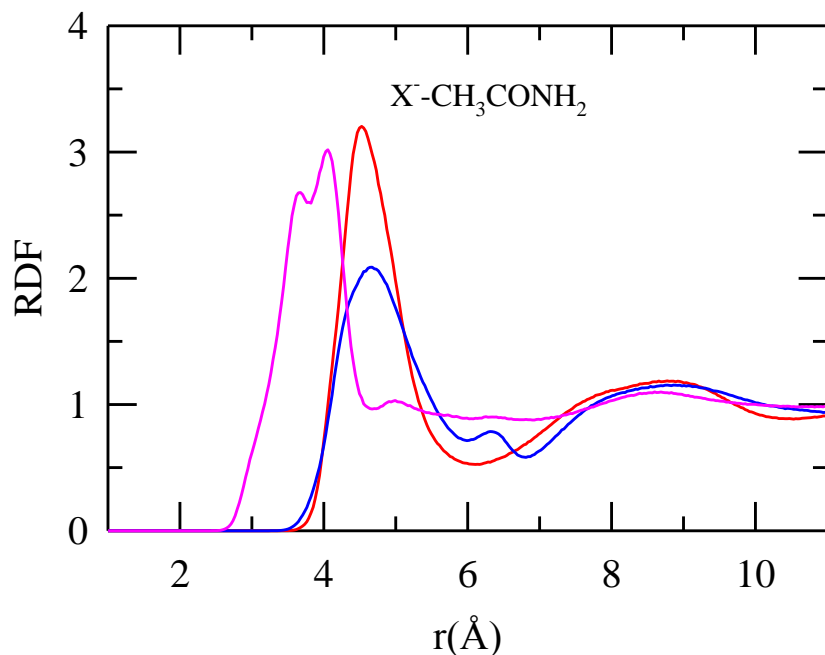


Figure 5.7: Simulated RDFs for $X^- - CH_3CONH_2$ for all DESs at 303 K. The red line is for Br^- , blue line for ClO_4^- and pink for NO_3^- .

5.3.2. Cluster Size and Lifetime Analysis

It is clear from the RDF analyses that different kinds of clusters are formed inside the mixtures which gives rise to the inherent complexity. Here we have separated three different types of clusters: (a) $CH_3CONH_2 - CH_3CONH_2$, (b) $Li^+ - CH_3CONH_2$ and (c) $Li^+ - X^-$. Then we have analysed their size and lifetime distributions. The clusters have been defined based on the corresponding RDFs. Specifically, CH_3CONH_2 molecules are assigned in the same cluster if the centre of mass distance between two CH_3CONH_2 molecules is less than or equal to the first minima following the first peak of the $CH_3CONH_2 - CH_3CONH_2$ RDF (7 Å for all the DESs). Note, CH_3CONH_2 molecules are connected via a hydrogen bond network joining $O(-CONH_2)$ atom of one CH_3CONH_2 and $H(-CONH_2)$ of the other. This H-bond between two CH_3CONH_2 molecules has been defined previously³²⁻³³ based on well accepted distance (R) and angle criteria (deg) and validity of the definition also has been checked

successfully. Two CH_3CONH_2 molecules are considered to be H-bonded if (1) the distance between the oxygen and the nitrogen atoms of two different CH_3CONH_2 molecules, R_{ON} , is less than the first minima of corresponding RDF ($R_{cut-off}$) and (2) the angle between the vector joining nitrogen and amide hydrogen atom of one CH_3CONH_2 molecule and the vector joining this nitrogen atom and oxygen atom of the other CH_3CONH_2 molecule, θ_{ONH} is less than 30° . For all the ions at both the temperature $R_{cut-off}$ is found to be 4 Å. Since the criterion we have employed here does not include any of this, we have checked the validity of our cluster definition. First we selected pair of CH_3CONH_2 molecules whose centre of mass distance is less than 7 Å. Then we calculated the distribution of R_{ON} and θ_{ONH} for these selected pair of molecules. The ion dependence of this distance and angle probability distribution at 303 K is provided in Appendix D, Figure D1. It is evident from the plot that the selected pair of CH_3CONH_2 molecules also includes pair of CH_3CONH_2 molecules which are hydrogen bonded. So, we continue to use this definition to calculate cluster size distribution among acetamide molecules. Similarly, for defining a cluster between $Li^+ - CH_3CONH_2$ and $Li^+ - X^-$ pairs, the cut-off distance has been selected based on first minima of the corresponding RDF. This distance is 3.8 Å for $Li^+ - CH_3CONH_2$ pairs. For $Li^+ - X^-$ clusters, the cut-off distance is 3.2 Å, 4.0 Å and 3.2 Å for Br^- , ClO_4^- and NO_3^- respectively. Note similar cluster definition has been used frequently for other systems also.⁷⁸⁻⁷⁹

Figure 5.8 shows the anion dependence of cluster size distribution for $CH_3CONH_2 - CH_3CONH_2$ cluster. The upper panel shows the distribution at 303 K and the lower panel shows the same at 350 K. Note the cluster size distribution has been calculated as a fraction of the total number of clusters that is if the number of cluster of size i is $P(i)$ then total number of clusters $P = \sum_i P(i)$. Then the comparison has been made between the cluster of size 1 that is not bonded to any other neighbour and cluster of larger size. It is evident from Figure 5.8 that $CH_3CONH_2 - CH_3CONH_2$ cluster size distribution does not depend either on the anion identity or the temperature. The distribution extends upto ~25-30 CH_3CONH_2 molecules or ~100-120 Å (considering the diameter of $CH_3CONH_2 \sim 4$ Å).²⁵

However beyond 6 CH_3CONH_2 molecules the probability is found to be even less than 20%. Also, 33% CH_3CONH_2 molecule does not form any cluster with the neighbours. This indicates a substantial breakdown of the H-bond network among CH_3CONH_2 molecules in presence of electrolytes.

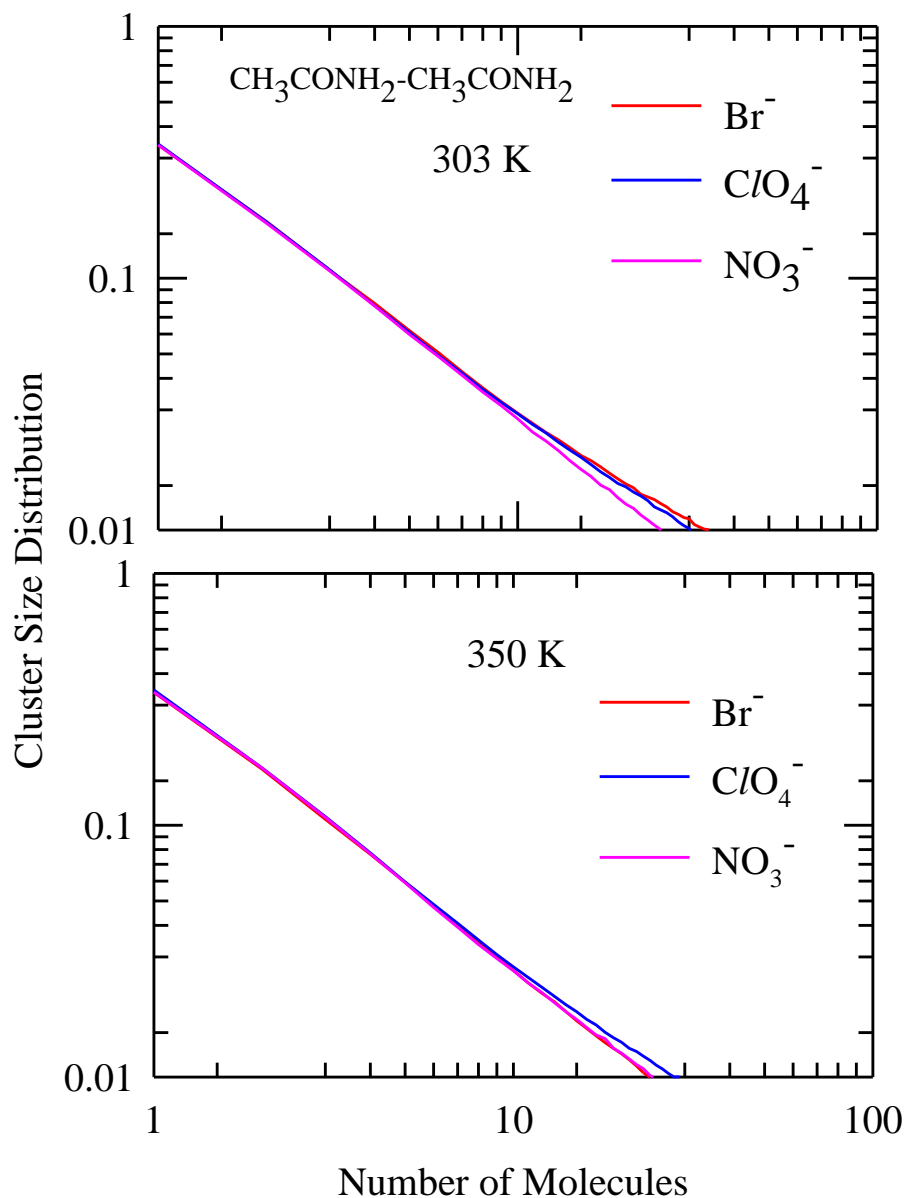


Figure 5.8: Cluster size distribution of $CH_3CONH_2 - CH_3CONH_2$ for all DESs. The upper panel shows the distribution at 303 K and the lower panel shows the same at 350 K.

Next we discuss the cluster size distribution of $\text{Li}^+ - \text{CH}_3\text{CONH}_2$. Figure 5.9 shows the distribution at both the temperatures. The similar anion dependence is evident from both the plots. It appears that in the presence of NO_3^- maximum clustering is achieved as compared to the other two anions. In presence of NO_3^- , the cluster size extends up to 35 number of molecules followed by ClO_4^- and Br^- . With increase in temperature, the clustering ability decreases only slightly for all the anions.

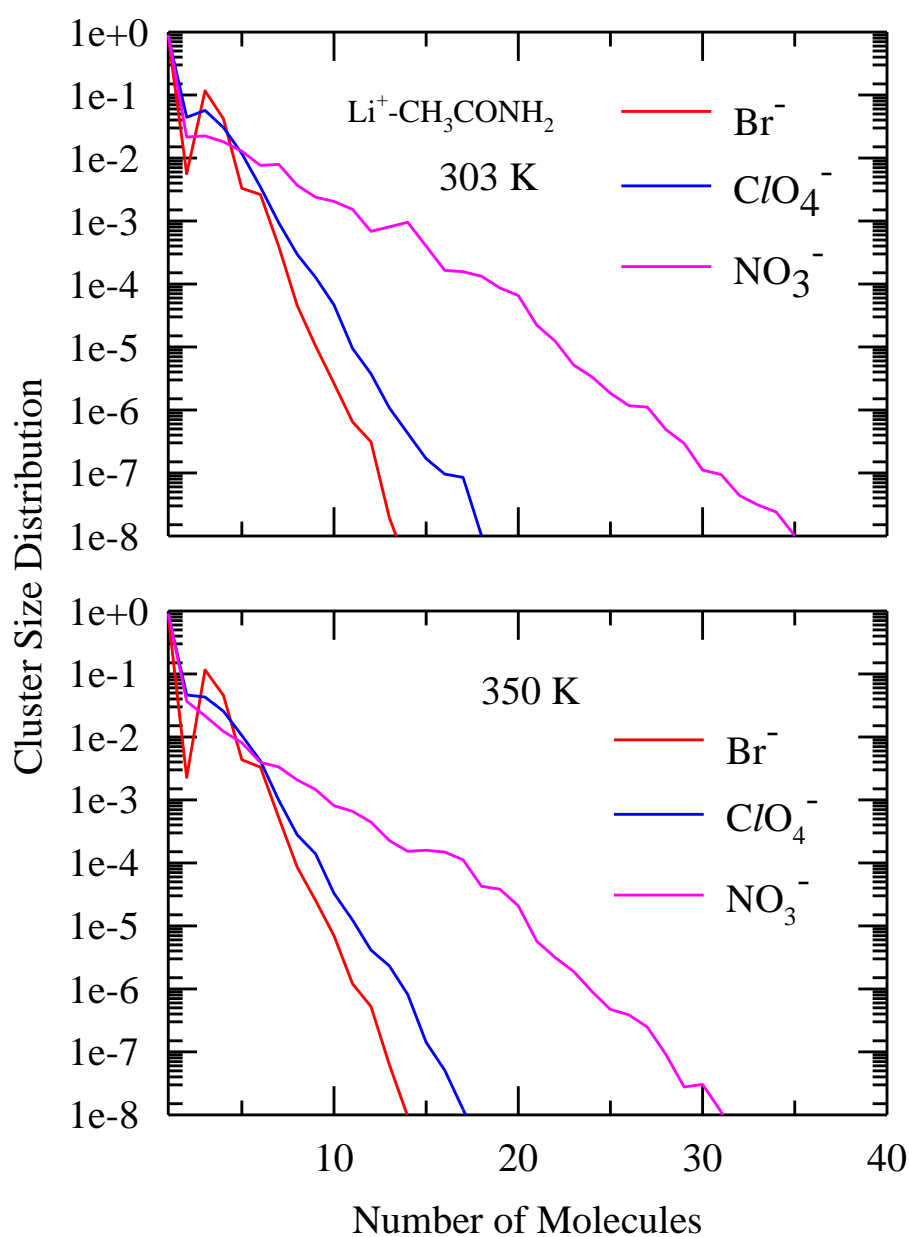


Figure 5.9: Cluster size distribution of $Li^+ - CH_3CONH_2$ for all DESs. The upper panel shows the distribution at 303 K and the lower panel shows the same at 350 K.

Next we comment on the cluster size distribution of $Li^+ - X^-$. Figure 5.10 shows the cluster size distribution of $Li^+ - X^-$ at 303 K for all DESs and Figure 5.11 gives the same at 350 K. The distribution in this case is slightly different as compared to the other two. For $CH_3CONH_2 - CH_3CONH_2$ and $Li^+ - CH_3CONH_2$ cluster size distributions, the probability is found to decrease as the number of molecule increases. However, here the distribution is random for all the ions and show significant anion dependence. For example, in presence of Br^- the distribution stretches up to 25 numbers of molecules but the distribution broadens in presence of ClO_4^- . Even after 35 numbers of molecules the distribution does not decay completely. This shows significant presence of $Li^+ - ClO_4^-$ clusters in the mixture. However in presence of NO_3^- , the cluster size distribution ceases completely after 15 numbers of molecules. At the elevated temperature we find that the distribution is somewhat regular for Br^- and ClO_4^- though significant percentage of large clusters exists for both of them.

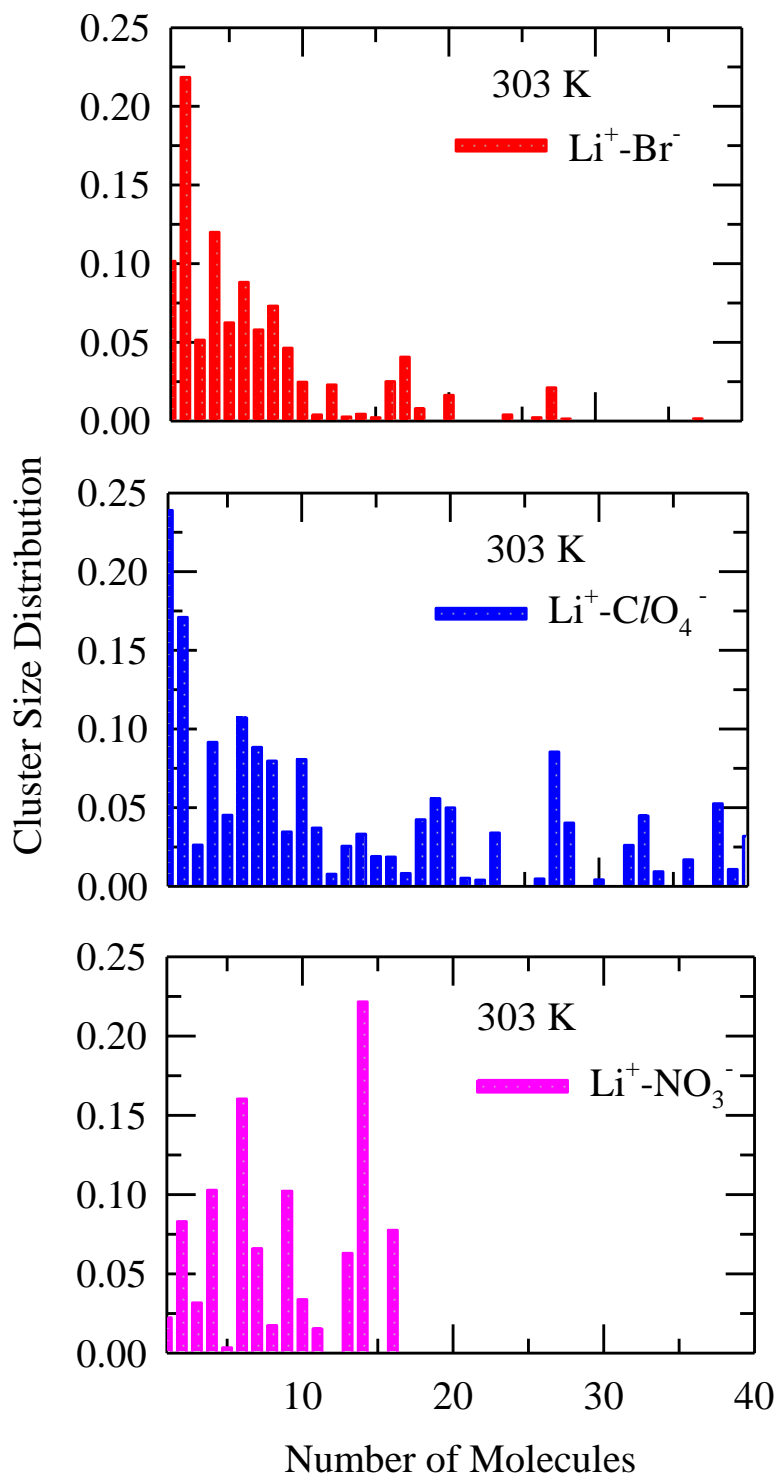


Figure 5.10: Cluster size distribution of $\text{Li}^+ - \text{X}^-$ for all DESs at 303 K.

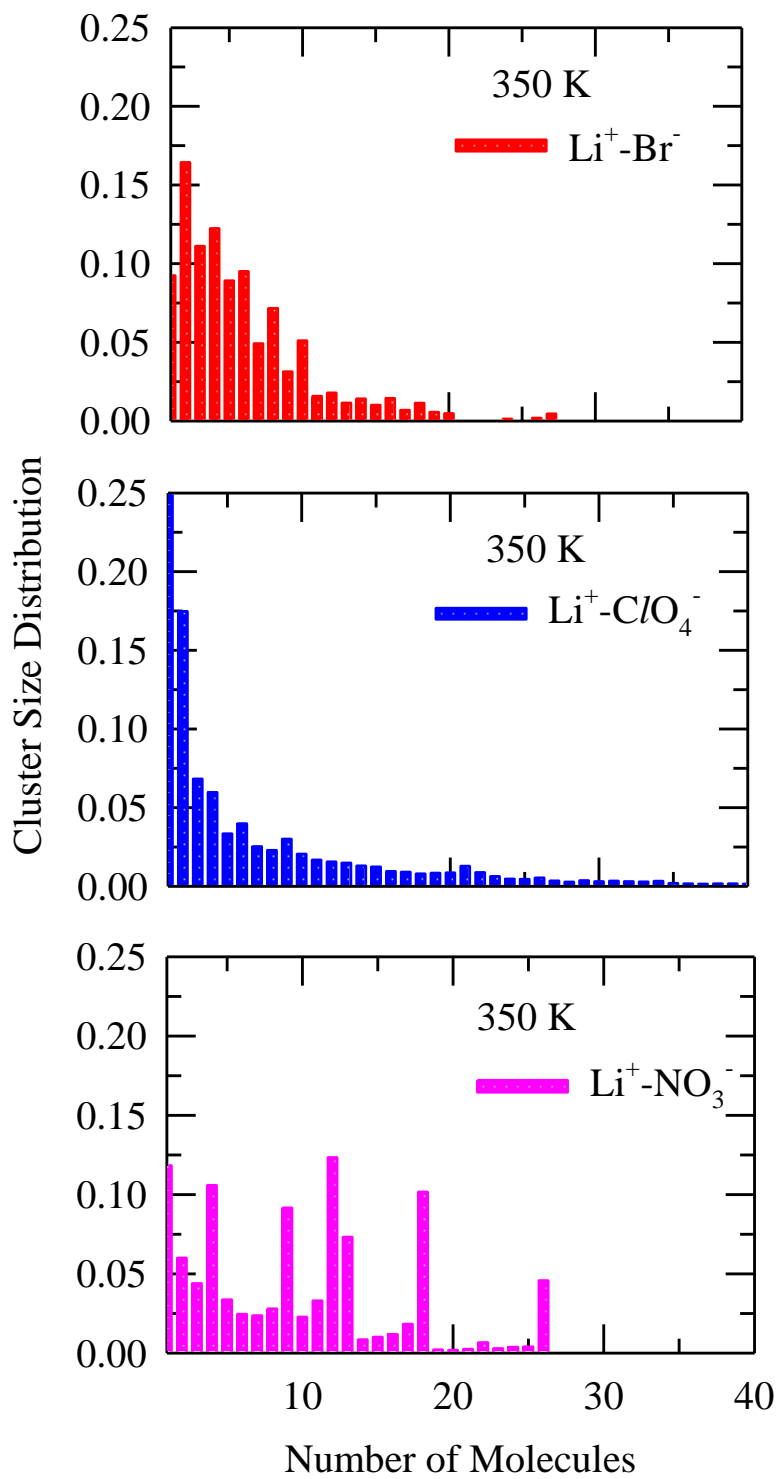


Figure 5.11: Cluster size distribution of $\text{Li}^+ - \text{X}^-$ for all DESs at 350 K.

Next we discuss about cluster lifetime. We have calculated cluster lifetime distributions for $CH_3CONH_2 - CH_3CONH_2$, $Li^+ - CH_3CONH_2$ and $Li^+ - X^-$ clusters at both the temperatures. The procedure we have employed here to calculate the lifetime distribution is similar to the hydrogen bond lifetime $S_{HB}(t)$.⁸⁰⁻⁸² The lifetime can be defined as:

$$P(t) = \langle h(0)H(t) \rangle / \langle h \rangle \quad (5.3)$$

$h(t')$ is a time dependent variable for a pair of CH_3CONH_2 molecules. If the centre of mass distance between two CH_3CONH_2 molecules is less than or equal to the cut-off distance, then $h(t') = 1$ or zero otherwise. $H(t)$ is a history dependent function and $H(t) = 1$ if $h(t')$ is unity upto time t from any arbitrary time origin else zero. So, $P(t)$ describes the probability that two CH_3CONH_2 molecules remains continuously hydrogen bonded for time t . So, the average relaxation time can be treated as the average lifetime of the CH_3CONH_2 clusters. Similarly, one can also define cluster lifetime for $Li^+ - CH_3CONH_2$ and $Li^+ - X^-$ clusters.

Figure 5.12 shows the ion dependence of cluster lifetime probability for $CH_3CONH_2 - CH_3CONH_2$ clusters. The upper panel shows the probability at 303 K and the lower panel shows the same at 350 K. The effect of the anion identity is prominent at the lower temperature. The probability distributions have been fitted with multi-exponential parameters which give timescales ranging from picoseconds to nanoseconds. The average lifetimes are provided in Table 5.1 and the fitting parameters are provided in Appendix D, Table D2. $CH_3CONH_2 - CH_3CONH_2$ clusters survive longer in presence of Br^- as compared to NO_3^- and ClO_4^- . In fact, the average lifetime is ~ 15 times higher in presence of Br^- . The longest time constant found is ~ 15 ns which signify the presence of slow dynamics. When the temperature is increased to 350 K, the average lifetime decreases to ~ 30 ps, however a \sim ns component is still observed for all the anions. Figure 5.13 shows the lifetime distribution for $Li^+ - CH_3CONH_2$ clusters at both the temperatures. Here also, the cluster survives longer in presence of Br^- as compared to the other two ions. Figure 5.14 gives the lifetime distribution for $Li^+ - X^-$ clusters. Here the average lifetime is highest in presence of NO_3^- followed by Br^- and ClO_4^- . The average lifetime is ~ 4.5 ns at 303 K and ~ 1 ns at 350 K for NO_3^- . This

signifies the strength of the $Li^+ - NO_3^-$ clusters which results from favourable planar arrangement of NO_3^- interacting with Li^+ as discussed before. The average lifetime for all the three different types of clusters does not follow any regular pattern which signifies the inherent complexity of these systems.

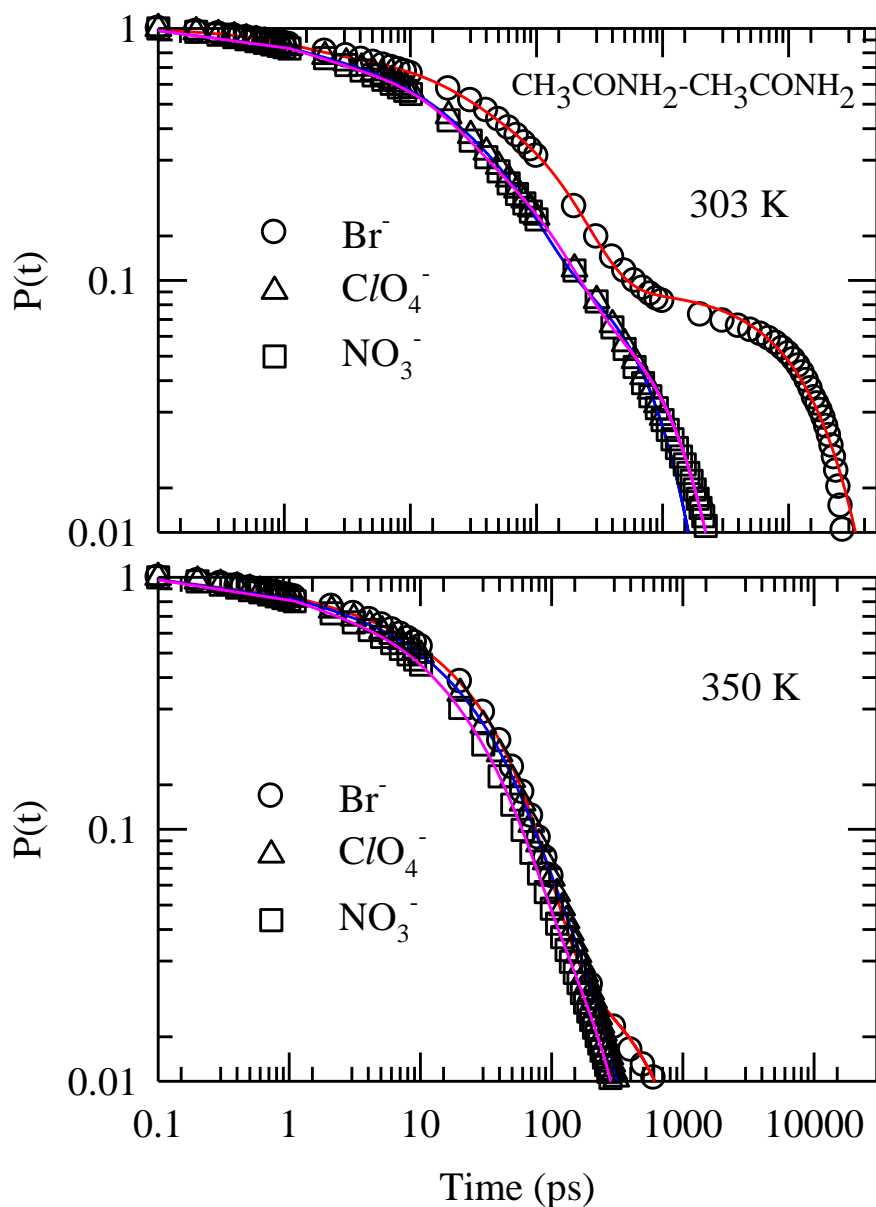


Figure 5.12: Simulated cluster lifetime distribution of $CH_3CONH_2 - CH_3CONH_2$ for all DESs. The upper panel shows the distribution at 303 K and the lower panel shows the same at 350 K.

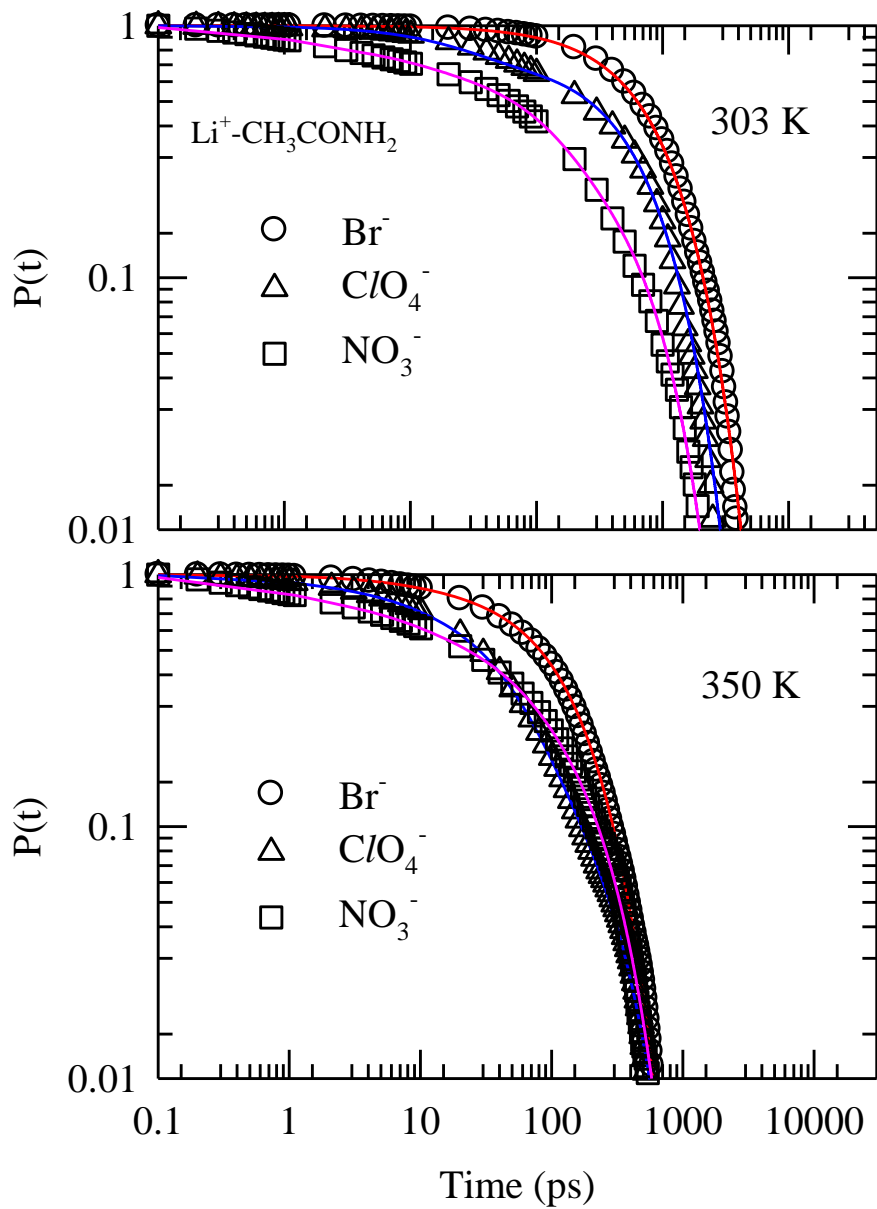


Figure 5.13: Simulated cluster lifetime distribution of $\text{Li}^+ - \text{CH}_3\text{CONH}_2$ for all DESs. The upper panel shows the distribution at 303 K and the lower panel shows the same at 350 K.

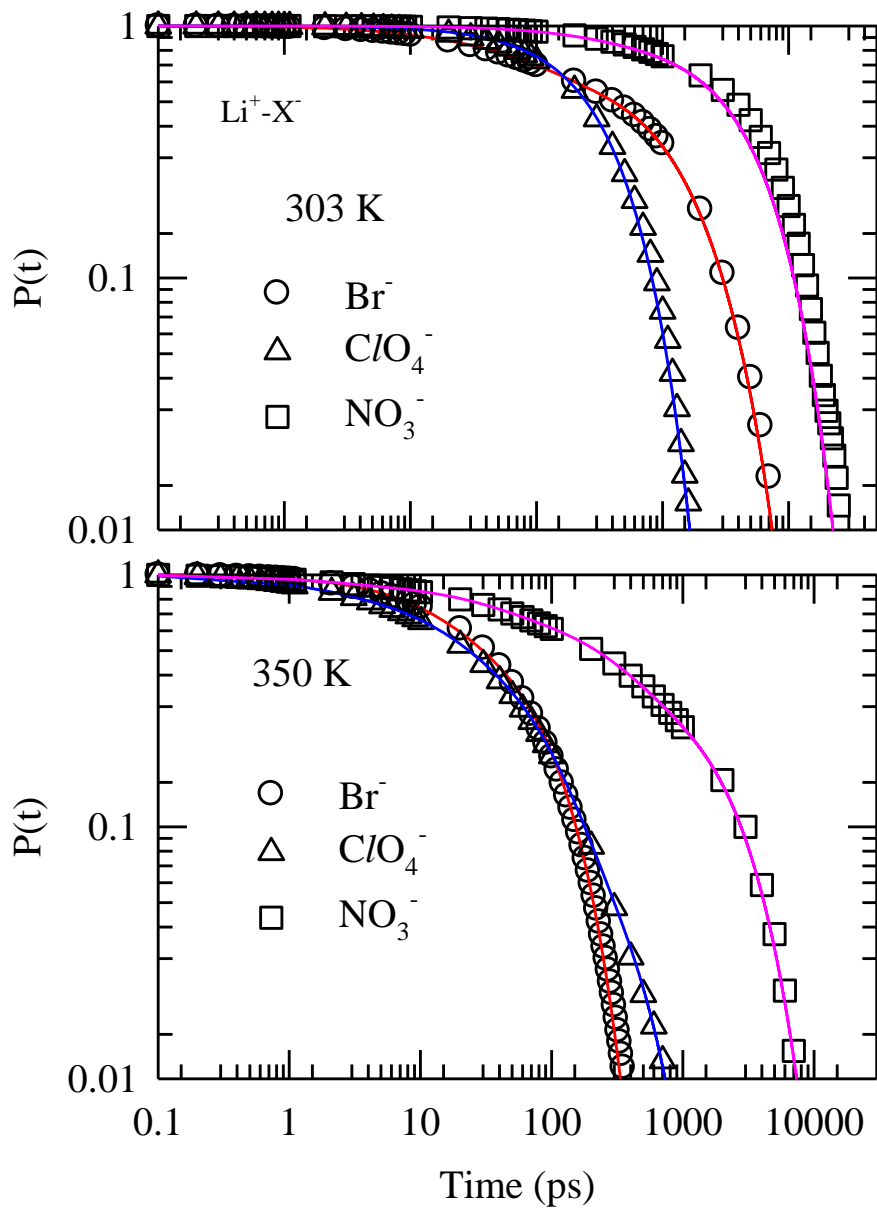


Figure 5.14: Simulated cluster lifetime distribution of $\text{Li}^+ - \text{X}^-$ for all DESs. The upper panel shows the distribution at 303 K and the lower panel shows the same at 350 K.

Table 5.1: Average lifetime obtained from multi-exponential fitting parameters of various life-time distributions.

<i>Anion</i>	<i>Temp(K)</i>	<i>Acet – Acet (ps)</i>	<i>Li⁺ – Acet (ps)</i>	<i>Li⁺ – X⁻ (ps)</i>
<i>Br⁻</i>	303	1595.3	909.1	1067.3
	350	39.8	123.0	58.4
<i>ClO₄⁻</i>	303	106.1	500.0	357.1
	350	30.0	66.4	72.1
<i>NO₃⁻</i>	303	124.0	232.5	4525.0
	350	24.9	76.0	890.7

5.4. Conclusions

Molecular dynamics simulations were performed with DESs consisting of CH_3CONH_2 and lithium salts of Br^- , ClO_4^- and NO_3^- at a fixed mole fraction at 303 K and 350 K. Various structures formed among the interspecies were identified via analysing RDFs. First we have discussed how the amide structure changes in presence of an added electrolyte and also its anion dependence. The planar structure of NO_3^- and its smallest size effect the amide – ion interaction as found from the RDF analysis. $Li^+ - Li^+$ RDF reflects the presence of heterogeneous environment in all the DESs. The observed multiple peaks in the $Li^+ - Li^+$ RDF also suggests that three different kinds of anion conformations are possible for ClO_4^- and NO_3^- . Cluster size and lifetime distributions have also been analysed in order to understand the local microscopic structure. Both size and lifetime distribution have been partitioned into three categories $CH_3CONH_2 - CH_3CONH_2$, $Li^+ - CH_3CONH_2$ and $Li^+ - X^-$. This would give us a better idea about the effect of the electrolyte. Note, while

defining a cluster we have considered only two species. However, in reality all the species, namely, CH_3CONH_2 , Li^+ and X^- can form clusters altogether as shown in Figure 5.15.

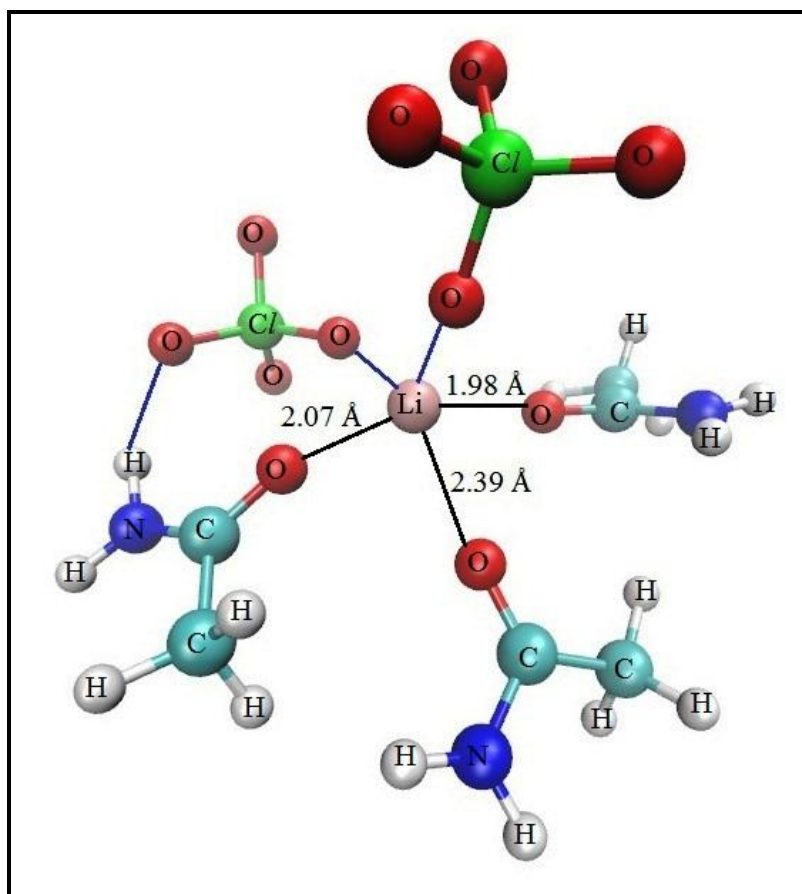


Figure 5.15: A six member cluster comprising three CH_3CONH_2 molecules, one Li^+ and two ClO_4^- ions are shown. These types of clusters involving all the species are formed inside the mixtures. However, these are not analysed here as they do not offer any new qualitative results.

But the statistics of these clusters are very less and would not give us any better qualitative result. Therefore we have restricted us only upto two species. The cluster size distribution of $CH_3CONH_2 - CH_3CONH_2$ and $Li^+ - CH_3CONH_2$ is found to be distinctly different from the $Li^+ - X^-$. The anion dependence of the cluster size is evident only in $Li^+ - CH_3CONH_2$ distribution. As the temperature is increased the distribution becomes narrower but only slightly. Next, we have shown the lifetime distribution following the

protocol of hydrogen bond lifetime. Here the anion dependence is evident from all the cases. $CH_3CONH_2 - CH_3CONH_2$ and $Li^+ - CH_3CONH_2$ clusters have higher lifetime in presence of Br^- . On the other hand, $Li^+ - X^-$ clusters are found to be most stable in presence of NO_3^- .

Similar structural investigation can be extended to other non-ionic DESs,⁸³ binary mixtures⁸⁴⁻⁸⁵ and ionic liquids.⁸⁶ Next it would be interesting to study the dynamic heterogeneity of these systems^{74,87} and its anion dependence. Although, the heterogeneity in these systems have been analysed via time-resolved fluorescence experiments,^{22,25} a detail in depth all-atom simulation study is needed for complete understanding of these complex solvent systems.

References:

1. D. V. Wagle, H. Zhao, and G. A. Baker, *Acc. Chem. Res.* **47**, 2299 (2014).
2. R. D. Rogers and K. R. Seddon, *Ionic liquids: Industrial Application for Green Chemistry*; ACS Symposium Series 818; American Chemical Society: Washington, DC, 2002.
3. P. Wasserscheid and T. Welton, *Ionic Liquids in Synthesis*; Wiley-VCH: New York, **2003**.
4. D. V. Wagle, H. Zhao, and G. A. Baker, *Acc. Chem. Res.* **47**, 2299 (2014).
5. Q. Zhang, K. De Oliveira Vigier, S. Royer, and F. Jerome, *Chem. Soc. Rev.* **41**, 7108 (2012).
6. A. P. Abbott, G. Capper, D. L. Davies, R. K. Rasheed, and V. Tambyrajah, *Chem. Commun.* **1**, 70 (2003).
7. E. L. Smith, A. P. Abbott, and K. S. Ryder, *Chem. Rev.* **114**, 11060 (2014).
8. A. P. Abbott, G. Capper, D. L. Davies, K. J. McKenzie, and S. U. Obi, *J. Chem. Eng. Data.* **51**, 1280 (2006).
9. A. P. Abbott, P. M. Cullis, M. J. Gibson, R. C. Harris, and E. Raven, *Green Chem.* **9**, 868 (2007).
10. A. P. Abbott, T. J. Bell, S. Handa, and B. Stoddart, *Green Chem.* **8**, 784 (2006).
11. H. Zhao and G. A. Baker, *J. Chem. Technol. Biotechnol.* **88**, 3 (2013).
12. P. Wasserscheid and W. Keim, *Angew. Chem., Int. Ed.* **39**, 3772 (2000).
13. J. G. Cordano, N. C. Rubin, and R. W. Bradshaw, *J. Sol. Energy Eng.* **133**, 011014 (2011).
14. A. P. Abbott, G. Capper, D. L. Davies, and R. Rasheed, *Chem. -Eur. J.* **10**, 3769 (2004).
15. A. P. Abbott, G. Capper, D. L. Davies, and R. Rasheed, *Inorg. Chem.* **43**, 3447 (2004).
16. A. P. Abbott, G. Capper, D. L. Davies, H. L. Munro, R. K. Rasheed, and V. Tambyrajah, *Chem. Commun.* **19**, 2010 (2001).
17. M. Sharma, C. Mukesh, D. Mondal, and K. Prasad, *RSC Adv.* **3**, 18149 (2013).
18. Y. Dai, J. van Spronsen, G.-J. Witkamp, R. Verpoorte, and Y. H. Choi, *J. Nat. Prod.* **76**, 2162 (2013).
19. Q. Zeng, Y. Wang, Y. Huang, X. Ding, J. Chen, and K. Xu, *Analyst* **139**, 2565 (2014).
20. G. van der Zwan and J. T. Hynes, *J. Chem. Phys.* **78**, 4174 (1983).

21. G. van der Zwan and J. T. Hynes, *Chem. Phys.* **152**, 169 (1991).
22. T. Pradhan and R. Biswas, *J. Phys. Chem. A* **111**, 11524 (2007).
23. B. Guchhait, S. Das, S. Daschakraborty, and R. Biswas, *J. Chem. Phys.* **140**, 104514 (2014).
24. A. Das, S. Das, and R. Biswas, *Chem. Phys. Lett.* **581**, 47 (2013).
25. B. Guchhait, H. A. R. Gazi, H. K. Kashyap, and R. Biswas, *J. Phys. Chem. B* **114**, 5066 (2010).
26. B. Guchhait, S. Daschakraborty, and R. Biswas, *J. Chem. Phys.* **136**, 174503 (2012).
27. H. A. R. Gazi, B. Guchhait, S. Daschakraborty, and R. Biswas, *Chem. Phys. Lett.* **501**, 358 (2011).
28. A. Das and R. Biswas, *J. Phys. Chem. B* **119**, 10102 (2015).
29. S. N. Tripathy, Z. Wojnarowska, J. Knapik, H. Shirota, R. Biswas, and M. Paluch, *J. Chem. Phys.* **142**, 184504 (2015).
30. K. Mukherjee, A. Das, S. Choudhury, A. Barman, and R. Biswas, *J. Phys. Chem. B* **119**, 8063 (2015).
31. R. Biswas, A. Das, and H. Shirota, *J. Chem. Phys.* **141**, 134506 (2014).
32. T. Pal and R. Biswas, *Chem. Phys. Lett.* **517**, 180 (2011).
33. S. Das, R. Biswas, and B. Mukherjee, *J. Phys. Chem. B* **119**, 274 (2015).
34. S. Das, R. Biswas, and B. Mukherjee, *J. Phys. Chem. B* **119**, 11157 (2015).
35. S. Das, R. Biswas, and B. Mukherjee, *J. Chem. Phys.* (under minor review)
36. A. Manthiram, *J. Phys. Chem. Lett.* **2**, 176 (2011).
37. E. M. Erickson, C. Ghanty, and D. Aurbach, *J. Phys. Chem. Lett.* **5**, 3313 (2014).
38. G. A. Nazri and G. Pistoia, *Lithium Batteries: Science and Technology*; Springer: New York, **2004**.
39. S. S. Zhang, *J. Power Sources* **162**, 1379 (2006).
40. P. H. Figueiredo, L. J. A. Siqueira, and M. C. C. Ribeiro, *J. Phys. Chem. B* **116**, 12319 (2012).
41. Z. Li, G. D. Smith, and D. Bedrov, *J. Phys. Chem. B* **116**, 12801 (2012).
42. O. Borodin and G. D. Smith, *J. Phys. Chem. B* **110**, 4971 (2006).
43. R. Biswas, S. Roy, and B. Bagchi, *Phys. Rev. Lett.* **75**, 1098 (1995).
44. R. Biswas and B. Bagchi, *J. Am. Chem. Soc.* **119**, 5946 (1997).
45. B. Bagchi and R. Biswas, *Acc. Chem. Res.* **31**, 181 (1998).

46. W. Smith and T. R. Forster, *The DL_POLY Molecular Simulation Package*; Daresbury Laboratory: Cheshire, U. K, **1999**.
47. J. A. Mitchell and E. E. Reid, *J. Am. Chem. Soc.* **53**, 1879 (1931).
48. A. D. MacKerell Jr., J. Wiorkiewicz-Kuczera, and M. Karplus, *M. J. Am. Chem. Soc.* **117**, 11946 (1995).
49. K. P. Jensen and W. L. Jorgensen, *J. Chem. Theory Comput.* **2**, 1499 (2006).
50. C. Cadena and E. J. Maginn, *J. Phys. Chem. B* **110**, 18026 (2006).
51. J. N. Canongia Lopes, J. Deschamps, and A. A. H. Padua, *J. Phys. Chem. B* **108**, 2038 (2004).
52. C. W. Yong, DL_FIELD, STFC Daresbury Laboratory: Cheshire, U.K., **2011**.
53. M. P. Allen and D. J. Tildesley, *Computer Simulations of Liquids*; Oxford University Press: New York, **1987**.
54. L. Martinez, R. Andrade, E. G. Birgin, and J. M. Martinez, *J. Comput. Chem.* **30**, 2157 (2009).
55. S. Nose, *J. Chem. Phys.* **81**, 511 (1984).
56. W. G. Hoover, *Phys. Rev. A: At., Mol., Opt. Phys.* **31**, 1695 (1985).
57. W. Humphrey, A. Dalke, and K. Schulten, *J. Mol. Graph.* **14**, 33 (1996).
58. L. T. Costa and M. C. C. Ribeiro, *J. Chem. Phys.* **124**, 184902 (2006).
59. O. Borodin, G. D. Smith, and W. Henderson, *J. Phys. Chem. B* **110**, 16879 (2006).
60. O. Borodin and G. D. Smith, *J. Phys. Chem. B* **110**, 11481 (2006).
61. Z. Li, G. D. Smith, and D. Bedrov, *J. Phys. Chem. B* **116**, 12801 (2012).
62. N. E. Triggs and J. J. Valentini, *J. Phys. Chem.* **96**, 6922 (1992).
63. T. W. Whitfield, G. I. Martyna, S. Allison, S. P. Bates, H. Vass, and J. Crain, *J. Phys. Chem. B* **110**, 3624 (2006).
64. S. S. Kudvua, D. Blaser, R. Boese, and G. R. Desiraju, *J. Org. Chem.* **66**, 1621 (2001).
65. R. Ludwig, *J. Mol. Liq.* **84**, 65 (2000).
66. R. Ludwig, F. Weinhold, and T. C. Farrar, *J. Chem. Phys.* **107**, 499 (1997).
67. M. C. Etter, *Acc. Chem. Res.* **23**, 120 (1990).
68. T. Ottersen, *Acta. Chem. Scand.* **29**, 939 (1975).
69. D. Zobel, P. Luger, W. Dreissig, and T. Koritsanszky, *Acta Crystallogr., Sect. B: Struct. Sci.* **48**, 837 (1992).

70. G. A. Jeffrey, J. R. Ruble, R. K. McMullan, D. J. DeFrees, J. S. Binkley, and J. Pople, *Acta Crystallogr., Sect. B: Struct. Sci.* **36**, 2292 (1980).
71. S. Nasr, M. Ghédira, and R. Cortés, *J. Chem. Phys.* **110**, 10487 (1999).
72. S. Nasr, *J. Chem. Phys.* **115**, 6569 (2001).
73. A. W. Omta, M. F. Kropman, S. Woutersen, and H. J. Bakker, *Science* **301**, 347 (2003).
74. G. V. Bondarenko and Y. E. Gorbaty, *Mol. Phys.* **109**, 783 (2011).
75. T. Pal and R. Biswas, *J. Phys. Chem. B* **119**, 15683 (2015).
76. S. Li, Z. Cao, Y. Peng, L. Liu, Y. Wang, S. Wang, J.-Q. Wang, T. Yan, X.-P. Gao, D.-Y. Song, and P.-W. Shen, *J. Phys. Chem. B* **112**, 6398 (2008).
77. T. Méndez-Morales, J. Carrete, O. Cabeza, O. Russina, A. Triolo, L. J. Gallego, and L. M. Varela, *J. Phys. Chem. B* **118**, 761 (2014).
78. T. Méndez-Morales, J. Carrete, S. Bouzon-Capelo, M. Perez-Rodriguez, O. Cabeza, L. J. Gallego, and L. M. Varela, *J. Phys. Chem. B* **117**, 3207 (2013).
79. L. Dougan, S. P. Bates, R. Hargreaves, J. P. Fox, J. Crain, J. L. Finney, V. Reat, and A. K. Soper, *J. Chem. Phys.* **121**, 6456 (2004).
80. C. G. Hanke and R. M. Lynden-Bell, *J. Phys. Chem. B* **107**, 10873 (2003).
81. D. C. Rapaport, *Mol. Phys.* **50**, 1151 (1983).
82. A. Chandra, *Phys. Rev. Lett.* **85**, 768 (2000).
83. A. Luzar, *J. Chem. Phys.* **113**, 10663 (2000).
84. A. Das, S. Das, and R. Biswas, *J. Chem. Phys.* **142**, 034505 (2015).
85. S. Indra and R. Biswas, *Mol. Simul.* **41**, 471 (2015).
86. S. Indra and R. Biswas, *J. Chem. Phys.* **142**, 204501 (2015).
87. T. Pal and R. Biswas, *Theor. Chem. Acc.* **132**, 1348 (2013).
88. T. Pal and R. Biswas, *J. Chem. Phys.* **141**, 104501 (2014).

Chapter 6

Dynamic Heterogeneity in Acetamide/Electrolyte Deep Eutectic Solvents: Dependence on Temperature and Anion Identity

6.1. Introduction

Dynamic heterogeneity (DH) refers to the spatially varying relaxation rates of particles in a given medium. This micro-heterogeneous relaxation dynamics appears when a liquid is quickly cooled and brought near to the glass transition temperature (T_g), giving rise to micro-domains composed of molecules relaxing at different rates.¹⁻¹⁰ As the system nears the T_g , medium dynamics slows down dramatically. This drastic slowdown of the dynamics is reflected by huge changes in shear viscosity (η), diffusion coefficient (D) and structural relaxation time (τ).¹¹⁻¹² Sometimes the long time dynamics show multi/stretched exponential behaviour, reflecting a distribution of relaxation times.¹³⁻¹⁶ Additionally, particle displacements deviate significantly from the Gaussian distribution for homogeneous systems.¹⁷ As a result, understanding the microscopic dynamics of molecules in strongly cooled systems have remained as one of most desirable events in physical chemistry.¹⁸⁻²⁰ The DH aspect has been studied employing Lennard-Jones binary mixtures at low temperatures.²¹⁻³³ Interestingly, several DH features appear at ambient condition for several amide containing deep eutectic solvents (DESs),³⁴⁻⁴² ionic liquids (ILs)⁴³⁻⁵⁸ and IL mixtures with common molecular solvents.⁵⁹⁻⁶⁶

Advanced experimental techniques including nuclear magnetic resonance,⁶⁷⁻⁶⁹ fluorescence spectroscopy,⁷⁰⁻⁷¹ confocal microscopy⁷²⁻⁷⁴ etc. have been applied to experimentally detect signatures of molecular dynamics in glassy liquids and colloids. These measurements have reported existence of spatial correlations among local particles. After the seminal studies of Kob and Anderson,^{29-30,75} a large number of molecular dynamic simulations also have been performed which have shown the presence of both mobile particles (undergoing large displacements relative to predictions from Gaussian distribution) and immobile particles (undergoing small displacements) within a given time frame.⁷⁶ The immobile particles form a

domain whereas the mobile particles form string-like clusters and execute cooperative movements.⁷⁶ These suggest the presence of more than one length scale that characterise the spatial correlation in local dynamics.¹¹ Estimation of this length scale is possible via four point correlation functions⁷⁷⁻⁸⁰ although this requires certain approximation. An interesting component here is finding out the interconnection between the growing length scale and slowing down of the medium dynamics.^{1,9,11,20} The work presented here focuses on exploring this connection in amide/electrolyte DESs.

DESs are molten mixtures of compounds with melting temperatures lower than the melting temperatures of the individual mixture components.⁸¹⁻⁸⁵ It is believed that the extensive hydrogen bond network among the mixture components along with the enhanced entropy in the liquid phase brings the melting temperature down. DESs have offered various applications in industry primarily as “green solvents”, an alternative to the traditional organic solvents. The easy preparation route coupled with biodegradable nature, cost-effectiveness, easy handling has triggered applications of DESs in pharmaceutical industry, biomass treatment, biocatalysis, electrodeposition and preparation of functional materials.⁸¹⁻⁸⁸ Also, one can tailor the rate of a chemical reaction by designing suitable reaction media by altering the DES components.⁸⁹⁻⁹¹ However, a smarter use of these DESs demands a proper understanding of the medium structure and dynamics.

DESs comprised of acetamide and electrolytes have been studied previously via experiments and computer simulations.^{34-41,92-93} These earlier studies have reported heterogeneity in the solution structure and dynamics. Fluorescence spectroscopic measurements³⁴⁻³⁵ have suggested presence of spatial heterogeneity and shown partial decoupling between relaxation rate and medium viscosity. Dielectric relaxation (DR) measurements of these DESs⁹² in the frequency range $0.2 \leq \nu / GHz \leq 50$ have also shown break-down of hydrodynamics while explaining the relaxation times in terms of single particle rotation. Molecular dynamic simulations of molten acetamide⁹⁴ and acetamide containing DESs⁹³ have suggested the presence of orientational jumps for acetamide molecules. These studies reported power law distributions for jump and waiting time distributions, supporting the inhomogeneity feature of these media. The effect of heterogeneity is also observed from orientational correlation and hydrogen bond dynamics of acetamide in these DESs which showed stretched exponential decay kinetics.⁹⁵ The structural investigation of these DESs has revealed presence of clusters

with varying sizes and lifetimes.⁹⁶ All these strongly indicate presence of both spatial and temporal heterogeneities in these ion-containing dipolar media at ambient condition.

In the present study, we have performed all-atom molecular dynamic simulations of acetamide and lithium salts of bromide, perchlorate and nitrate at 303 K and 350 K to calculate various two point and multi-point correlations. The main aim of the present work is to explore the heterogeneity aspect of the mixture and its anion/temperature dependence. First, we have calculated the mean square displacements (MSDs) of acetamide in these DESs. and monitored the deviation from the Gaussian behaviour of particle displacements. We have also simulated the wavevector dependent acetamide dynamic structure factors in order to find out the relaxation kinetics at the nearest and at the collective length-scales. Additionally, DH has been characterised via the simulated four point dynamic susceptibility and particle overlap function which show significant anion and temperature dependence. Finally, dynamic correlation length has been extracted from the simulated four point correlation function.

6.2. Simulation Details

All-atom simulations were performed at two temperatures 303 K and 350 K using the package DL_POLY version 2.20.⁹⁷ Each system comprised of 512 molecules, of which there were 400 acetamide (CH_3CONH_2) and 56 pairs of Li^+ and X^- where X^- represent Br^- , NO_3^- and ClO_4^- . This provides, as in experiments, a mole ratio of 78:22 between acetamide and electrolyte. The potential function used has the following form:

$$U(R) = \sum_{\text{bonds}} K_r (r - r_{eq})^2 + \sum_{\text{angles}} K_\theta (\theta - \theta_{eq})^2 + \sum_{\text{dihedrals}} K_\phi [1 + \cos(n\phi - \delta)] + \sum_{i < j}^{\text{atoms}} \left(\frac{A_{ij}}{R_{ij}^{12}} - \frac{B_{ij}}{R_{ij}^6} \right) + \sum_{i < j}^{\text{atoms}} \frac{q_i q_j}{4\pi\epsilon_0 R_{ij}}. \quad (6.1)$$

Note this particular form of potential function has been used earlier for modeling DESs.^{35,39-40,93-94} In Eq. 6.1, K_r and K_θ are respectively the bond and angle constants, r_{eq} and θ_{eq} the equilibrium bond length and angle. K_ϕ denotes the dihedral constant, n the periodicity, ϕ the dihedral angle, and δ the phase shift. R_{ij} is the distance between atoms i and j with

partial charges q_i and q_j , respectively. The interaction parameters for the acetamide molecule were taken from the CHARMM⁹⁸ force field. The force field parameters for Li^+ , Br^- , NO_3^- and ClO_4^- were taken from the existing literature.⁹⁹⁻¹⁰⁰ Note these force field parameters, summarized in Appendix A and Appendix B (Table B1-Table B4, Figure B1-Figure B2) were used earlier to simulate acetamide dynamic structure factors,^{35,39} orientational and hydrogen bond dynamics in these DESs.^{93,94} The force field was constructed with DL_FIELD.¹⁰² The short-range van der Waals interaction was represented by the Lennard-Jones (LJ) potential.¹⁰³ The long-range electrostatic potential was treated via Ewald summation technique¹⁰³ using an Ewald parameter of $\alpha = 0.2 \text{ \AA}^{-1}$ and a 6x6x6 k-point grid.

The initial configurations were built using Packmol¹⁰⁴ and equilibrated in the NPT ensemble at 1 atm. pressure for 1 ns. The simulated densities for all the three systems were found to be in good agreement with those from experiments^{35,37} (Appendix D, Table D1). Nose-Hoover thermostat and barostat¹⁰⁵⁻¹⁰⁶ were used to control the temperature and pressure with time constants of 0.4 and 1.0 ps respectively. Subsequently, further equilibration of 5 ns followed by a production run of 100 ns was carried out in the NVT ensemble. Periodic boundary conditions were employed in all three directions, and the equations of motion were integrated using a time step of 2 fs employing the velocity Verlet algorithm.¹⁰³ The SHAKE algorithm was applied to constrain the bonds. The snapshots were saved after every 100 fs for data analysis.

6.3. Results and Discussion

6.3.1. Mean Square Displacement (MSD)

The time dependence of the MSD is defined by

$$\langle r_i^2(t) \rangle = \frac{1}{N} \left\langle \sum_{i=1}^N (\vec{r}_i(t) - \vec{r}_i(0))^2 \right\rangle. \quad (6.2)$$

Here, \vec{r}_i is the position vector of the i -th particle. The angular bracket denotes the averaging over time origins and number of molecules. Figure 6.1 shows the anion dependence of MSDs

of the centre of mass of acetamide in a double logarithmic scale. The upper panel shows the dependence at 303 K and the lower panel shows the same at 350 K. Here, the centre of mass

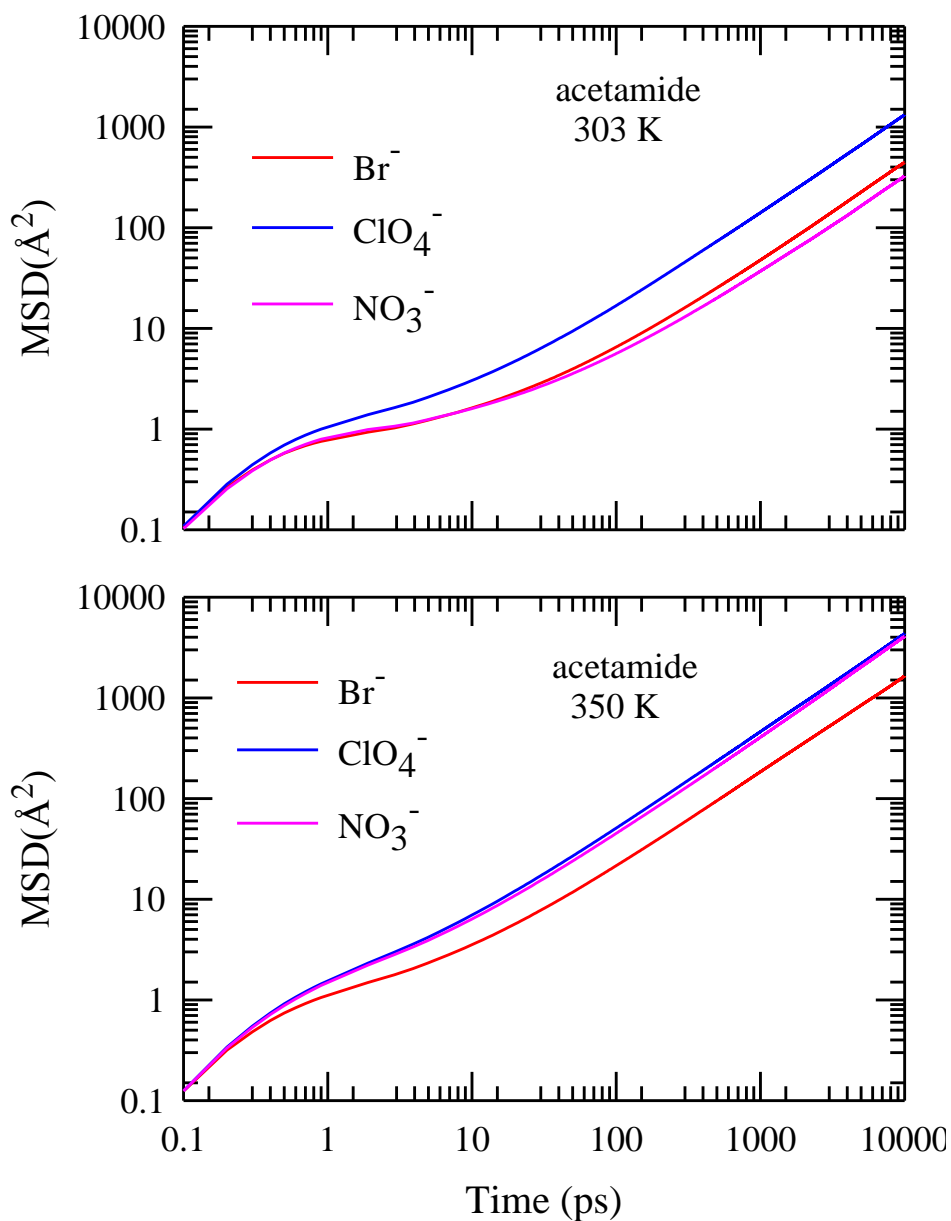


Figure 6.1: Anion dependent translational mean square displacements (MSDs) of acetamide at 303 K (upper panel) and at 350 K (lower panel). The diffusion co-efficients calculated from Einsteins Equation are provided in **Table 6.1**.

of the acetamide molecule is the *C* atom of the $-CONH_2$ group. In a dynamically heterogeneous environment MSD shows three characteristic regimes. At the initial few pico-

seconds the motion of the particle is ballistic such that $\langle r_i^2(t) \rangle \propto t^2$. At sufficiently long time when the motion enters into the diffusive regime, the MSD varies linearly with time, $\langle r_i^2(t) \rangle \propto t$. It is believed that at this time scale the molecule is able to escape the cage formed by its local neighbours. This allowing of the particle by the local neighbours to escape is structural relaxation and intimately connected to the medium viscosity. At the intermediate time a plateau region is obtained where $\langle r_i^2(t) \rangle \propto t^\alpha$, with α significantly less than unity. The plateau in this sub-diffusive regime occurs because of insufficient displacement for the particle for a significant duration of time. This suggests caging of particles by its neighbours and has been observed in super-cooled liquids^{80,110} and ILs.¹¹¹⁻¹¹² A careful examination of Figure 6.1 reveals that the duration of the sub-diffusive regime is the longest in presence of NO_3^- followed by Br^- and ClO_4^- . At higher temperature, the cage relaxes quickly decreasing the duration of sub-diffusive regime.

The self-diffusion co-efficient of acetamide were calculated from the MSDs using the Einstein equation¹⁰³

$$D = \frac{1}{6} \lim_{t \rightarrow \infty} \frac{d}{dt} \left\langle \sum_{i=1}^N (\vec{r}_i(t) - \vec{r}_i(0))^2 \right\rangle \quad (6.3)$$

The calculated values of the self diffusion co-efficient (D) are provided in Table 6.1. As expected, acetamide in presence of ClO_4^- has the highest diffusion co-efficient at both the temperatures studied. Note the fastest dynamics of acetamide in presence of ClO_4^- has been also observed earlier from the analysis of orientational and hydrogen bond dynamics⁹⁵ and dynamic structure factor relaxations.³⁵ At 303 K, the diffusion co-efficient value of acetamide decreases as $\text{ClO}_4^- > \text{Br}^- > \text{NO}_3^-$. However at higher temperature, the trend is different as $\text{ClO}_4^- > \text{NO}_3^- > \text{Br}^-$.

Table 6.1 Comparison of Diffusion Co-efficients of acetamide calculated from the slope of the corresponding MSD

Anion	303 K($10^7 \times \text{cm}^2/\text{sec}$)	350 K($10^6 \times \text{cm}^2/\text{sec}$)
Br^-	7.26 ± 0.04	2.71 ± 0.02
ClO_4^-	20.17 ± 0.01	7.20 ± 0.04
NO_3^-	5.32 ± 0.03	6.84 ± 0.03

6.3.2. Non-Gaussian ($\alpha_2(t)$) and new Non-Gaussian ($\gamma(t)$) Parameter

The overall dynamical heterogeneity of a system can be quantified by the non-Gaussian parameter defined as:^{108,113}

$$\alpha_2(t) = \frac{3 \langle \delta r^4(t) \rangle}{5 \langle \delta r^2(t) \rangle^2} - 1 \quad (6.4)$$

Here $\langle \delta r^4(t) \rangle = \left\langle N^{-1} \sum_{i=1}^N |\Delta r_i(0,t)|^4 \right\rangle$, $\langle \delta r^2(t) \rangle = \left\langle N^{-1} \sum_{i=1}^N |\Delta r_i(0,t)|^2 \right\rangle$ and $\delta r_i(t)$ is the

displacement of i-th particle within time duration t from any arbitrary time origin. Non-Gaussian parameter gives the extent of deviation from the Gaussian distribution of particle motion typical for homogeneous systems and has been routinely calculated for examining the presence of DH.^{66,107-108,113} It is believed that the peak position of $\alpha_2(t)$ provides the timescale for the maximum DH. However, this is only a qualitative estimate as one can get a further slower timescale via the new non-Gaussian (NNG) parameter, $\gamma(t)$. This additional parameter can be calculated from the following equation:^{66,107}

$$\gamma(t) = \frac{1}{3} \langle \delta r^2(t) \rangle \left\langle \frac{1}{\delta r^2(t)} \right\rangle - 1 \quad (6.5)$$

$$\text{Where } \left\langle \frac{1}{\delta r^2(t)} \right\rangle = \left\langle \frac{1}{N} \sum_{i=1}^N \frac{1}{|\Delta r_i(o,t)|^2} \right\rangle$$

Note $\alpha_2(t)$ corresponds to particle displacements which are larger than expected from Gaussian distribution and thus dominated by the ‘mobile’ particles. On the contrary, $\gamma(t)$ is strongly influenced by the displacements which are less than those predicted by the Gaussian distribution. Thus, the additional slower timescale reflects the presence of these slow particles. Hence simultaneous analysis of $\alpha_2(t)$ and $\gamma(t)$ would provide information about different timescales present in a given system. The presence of multiple timescale then would naturally indicate microheterogeneity of that system.

Figure 6.2 gives the anion dependence of $\alpha_2(t)$ and $\gamma(t)$ of acetamide in these DESs at both the temperatures considered. The upper panel presents the dependence at 303 K and the lower panel shows the same at 350 K. Both $\alpha_2(t)$ and $\gamma(t)$ exhibit a non-monotonic time dependence giving a peak in the intermediate time. The peak height of $\alpha_2(t)$ which reflects the extent of DH is maximum in presence of NO_3^- at both the temperatures followed by ClO_4^- and Br^- . Interestingly, even at 350 K, which is 150 K above the T_g of these DESs,³⁴ all the three DESs possess DH as reflected from the plot. For $\gamma(t)$, the peak height is the highest in the presence of NO_3^- followed by ClO_4^- and Br^- at 303 K. This relative ordering changes at higher temperature as the peak height at 350 K is the maximum in the presence of ClO_4^- followed by NO_3^- and Br^- . Table 6.2 summarizes the timescales τ_{NG} and τ_{NNG} corresponding to the peak position of $\alpha_2(t)$ and $\gamma(t)$ at 303 K and 350 K. τ_{NG} at 303 K follows the order: $\text{NO}_3^- > \text{Br}^- > \text{ClO}_4^-$. τ_{NG} peaks at 120 ps for NO_3^- which is ~2.4 times longer than that for Br^- and ~5 times longer than that for ClO_4^- . At 350 K the peak height decreases and τ_{NG} becomes faster. In fact, this shortening of timescale is the most prominent for NO_3^- (~12 times), from 120 ps at 303 K to 10 ps at 350 K. Also noteworthy is the change of relative ordering of τ_{NG} at 350 K as $\text{Br}^- > \text{NO}_3^- > \text{ClO}_4^-$. For all the anions at both the temperatures, the peak position of $\gamma(t)$ occurs at a much slower timescale than that for $\alpha_2(t)$. This signifies that DH survives over a longer period of timescale than predicted by $\alpha_2(t)$ and some acetamide molecules remain immobile for a longer time extended up to τ_{NNG} . Note this lingering of slow timescale strongly depends on the anion identity. It is evident from

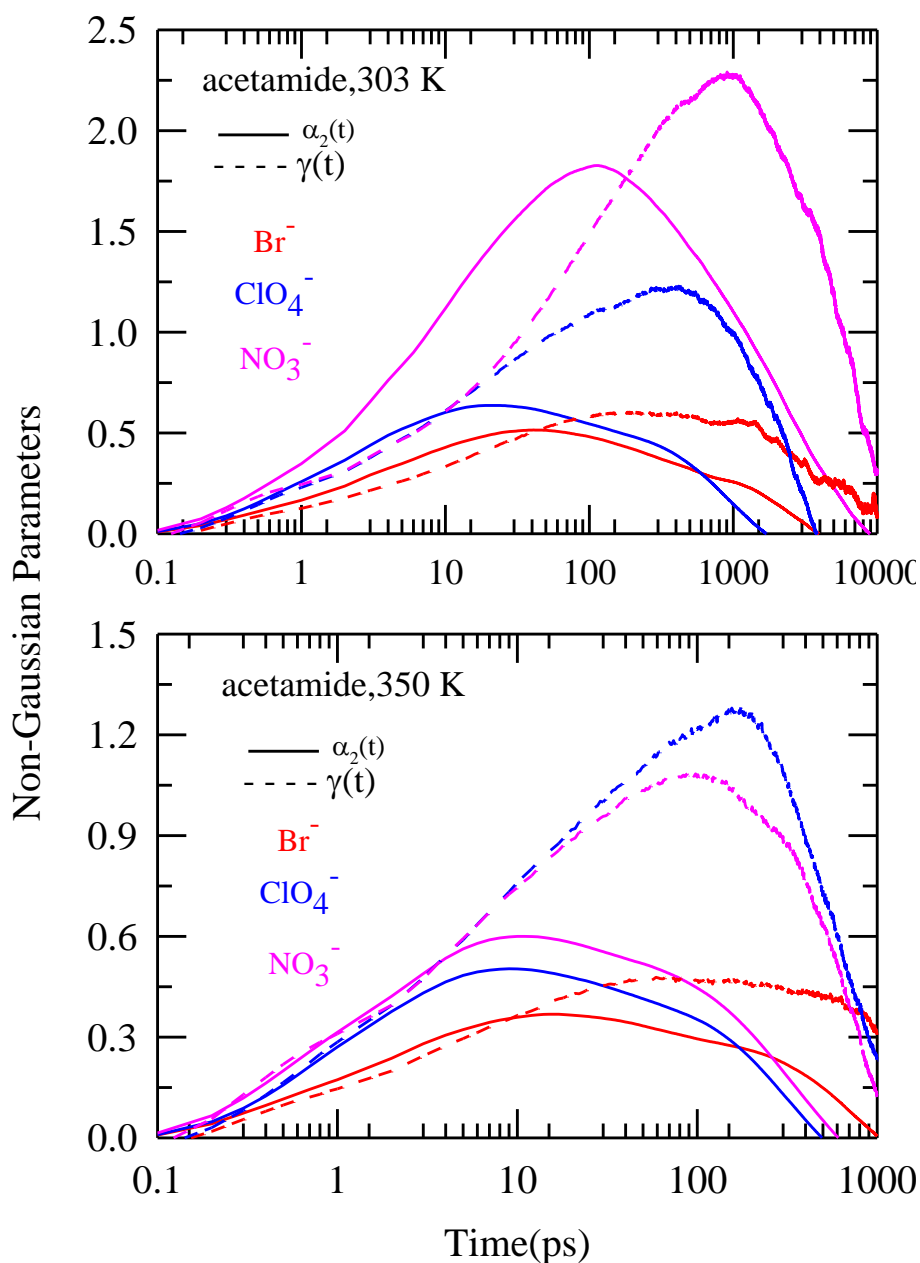


Figure 6.2: Comparison between simulated non-Gaussian and new non-Gaussian parameters, $\alpha_2(t)$ and $\gamma(t)$, respectively at 303 K (upper panel) and at 350 K (lower panel) for acetamide in presence of Br^- , NO_3^- and ClO_4^- . The solid lines denote $\alpha_2(t)$ and dashed lines represent $\gamma(t)$. The peak times of corresponding plots are provided in **Table 6.2**.

Table 6.2 that in presence of ClO_4^- , τ_{NNG} occurs at 420 ps at 303 K which is ~ 17 times longer as compared to τ_{NG} (25 ps). However, for NO_3^- τ_{NNG} (1000 ps) is ~ 8 times to τ_{NG} (120ps) and

for Br^- this slowing down is even less, only about 6 times. The relative ordering of τ_{NNG} is also somewhat different than τ_{NG} . At 303 K, τ_{NNG} follows the order: $NO_3^- > ClO_4^- > Br^-$. However, at 350 K, this relative ordering assumes the sequence: $ClO_4^- > NO_3^- > Br^-$. These results are qualitatively similar to those observed earlier for ILs.^{66,80} Also note that at 350 K, the peak values of $\alpha_2(t)$ and $\gamma(t)$ are substantial which suggests existence of substantial DH even at 350 K which is nearly 150 K above the T_g .

Table 6.2 Comparison of anion dependence of $\alpha_2(t)$ and $\gamma(t)$ of acetamide at 303 K and 350 K for various DESs.

Anion	303 K		350 K	
	τ_{NG} (ps) ^a	τ_{NNG} (ps) ^b	τ_{NG} (ps)	τ_{NNG} (ps)
Br^-	50	300	20	60
ClO_4^-	25	420	8	210
NO_3^-	120	1000	10	100

a) represents the time at which non-Gaussian parameter, $\alpha_2(t)$, attains a peak.

b) represents the time at which new non-Gaussian parameter, $\gamma(t)$, attains a peak.

6.3.3. Self and distinct parts of acetamide dynamic structure factor

Representative relaxation of acetamide dynamic structure factor (both self and distinct parts) is shown in Figure 6.3 which corresponds to acetamide/LiBr DES. While the upper panel shows the wavenumber (k) dependent relaxation of the self part of the dynamic structure factor (or, incoherent scattering function, ISF), the lower panel presents the relaxation of the distinct part (or, coherent scattering function, CSF). The wavenumbers chosen to represent four different length-scales of density fluctuation and correspond to length-scale (i) the

longest (0.18 \AA^{-1}) allowed in the present simulation, (ii) spanning first two solvation shells

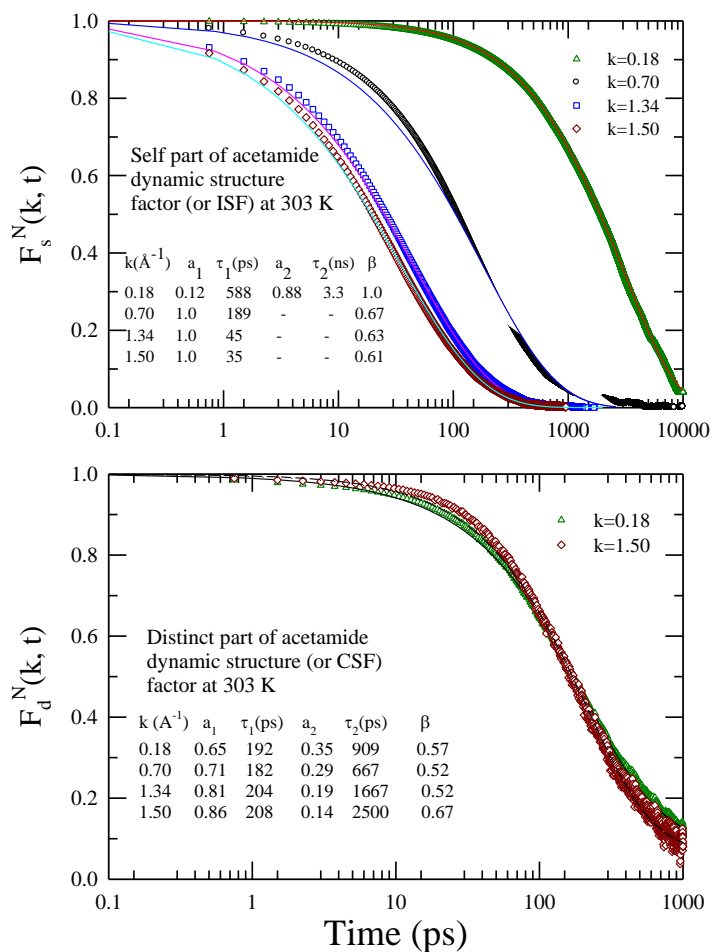


Figure 6.3: Relaxation of simulated incoherent and coherent scattering functions at different wavenumbers (k) for acetamide molecules at 303 K in $[0.78\text{CH}_3\text{CONH}_2 + 0.22\text{LiBr}]$ deep eutectic melt. $F_x^N(k, t) = F_x(k, t)/F_x(k, t=0)$ with $x = s$ or d . Symbols represent simulated data and lines through them the best fits. Fit parameters are also shown in insets. While the wavenumber dependent incoherent scattering function (ISF) has been obtained via Fourier transforming the simulated self part of the van Hove function, $G_s(r, t)$, coherent scattering function (CSF) has been obtained by Fourier transforming the simulated distinct part, $G_d(r, t)$. Representations are color-coded. For the CSF, relaxations at two wavenumbers are shown only to avoid clutter. Simulations are done using a total of 1024 particles and all-atom description for the interacting potentials. Simulations using 512 particles suggest a maximum deviation of $\sim 25\%$ on the fitted time-constants.

determined by the second peak position (0.7 \AA^{-1}) of the simulated acetamide-acetamide radial distribution function (rdf), (iii) involving only the first nearest neighbours determined by the first peak position (1.34 \AA^{-1}), and (iv) even shorter by considering half height position of the first peak after which it reaches the maximum (1.50 \AA^{-1}). Note that except for the relaxation at $k=0.18 \text{ \AA}^{-1}$, the relaxation of ISF at other wavenumbers is not only strongly stretched exponential but also characterized by a single time constant in 30-200 ps range. Interestingly, simulated relaxation of the CSF is also characterized by a dominating component (~60-80%) with a timescale of ~200 ps, followed by a much slower stretched exponential component. These results are important mainly for the following two reasons: (i) the stretched exponential relaxations at various length-scales for both ISF and CSF justifies the explanation of experimentally observed fractional viscosity dependence in terms of temporal heterogeneity and (ii) stronger decoupling and larger λ_{exc} dependence of emission shift for a shorter lifetime probe like DTN.³⁹ The nanosecond component present in the relaxation of CSF at all these wavenumbers and at $k=0.18 \text{ \AA}^{-1}$ for ISF also justifies the sensing of spatio-temporal heterogeneity by a longer lifetime probe like C153 and relatively weaker decoupling from medium viscosity.

6.3.4. Temporal Heterogeneity and Anion Dependence of acetamide dynamic structure factor

The wavevector (k) dependent incoherent scattering function, $F_s^N(k, t) = F_s(k, t)/F_s(k, t=0)$, is obtained via Fourier transforming the simulated self part of the van Hove correlation function,¹¹¹ $G_s(\mathbf{r}, t)$, as follows:

$$F_s(\mathbf{k}, t) = \int d\mathbf{r} \exp[-i\mathbf{k}\cdot\mathbf{r}] G_s(\mathbf{r}, t). \quad (6.6)$$

Figure 6.4 depicts the anion dependence of acetamide self dynamic structure factor relaxation, where the simulated $F_s^N(k, t)$ at the nearest neighbour ($k = 1.33 \text{ \AA}^{-1}$) and the lowest accessible ($k = 0.18 \text{ \AA}^{-1}$) wavevectors for ($\text{CH}_3\text{CONH}_2 + \text{LiNO}_3$), ($\text{CH}_3\text{CONH}_2 + \text{LiBr}$) and ($\text{CH}_3\text{CONH}_2 + \text{LiClO}_4$) DESs at 303 K are presented. The nearest neighbour wavevector corresponds to the first peak of the simulated radial distribution function for carbonyl carbon of acetamide molecules. Solid lines through these simulated data represent best fits. Fit

parameters and the average decay times for $F_S^N(k, t)$ are summarized in Table E1, Appendix E. Note the decay rates at both the wavevectors are different in presence of different anions, reflecting the anion dependence. Importantly, $F_S^N(k, t)$ at the nearest neighbour wavevector exhibits strongly stretched exponential decay in each case, suggesting heterogeneous relaxation dynamics for acetamide in these DESs. Note also that while $F_S^N(k, t)$ in presence of Br^- at $k = 1.33 \text{ \AA}^{-1}$ depicts stretched exponential decay with a single time constant, the corresponding decays in presence of either NO_3^- or ClO_4^- require a sum of a fast exponential and a slow stretched exponential. Eventhough the values for the stretching exponent (β) at $k = 1.33 \text{ \AA}^{-1}$ are not greatly different for these anions, the average relaxation times ($\langle \tau \rangle$) substantially differ. For example, our simulated $\langle \tau \rangle$ is the longest in presence of NO_3^- and the shortest in presence of ClO_4^- . The $\langle \tau \rangle$ value being much faster in presence of ClO_4^- (~ 15 and ~ 3 times faster than those in presence of NO_3^- and Br^- respectively) also provides a justification for the observed relatively less viscosity decoupling (in other words, larger p values) of solute solvation and rotational dynamics in presence of ClO_4^- than in presence of the other two anions in these $(\text{CH}_3\text{CONH}_2 + \text{LiX})$ DESs.³⁵

$F_S^N(k, t)$ decays at $k \sim 0.18 \text{ \AA}^{-1}$, shown in the lower panel of Figure 6.4, describe a much slower relaxation dynamics than those at $k = 1.33 \text{ \AA}^{-1}$ but exhibits the similar anion trend; that is, the decay being the fastest in presence of ClO_4^- and the slowest in presence of NO_3^- with the decay in presence of Br^- in between. The decay rates at both the nearest neighbour and collective wavevectors therefore suggest that dynamics in presence of ClO_4^- should be the fastest and most homogeneous among the three acetamide DESs studied here. In fact, this has indeed been reflected by our dynamic Stokes shift and anisotropy measurements.³⁵

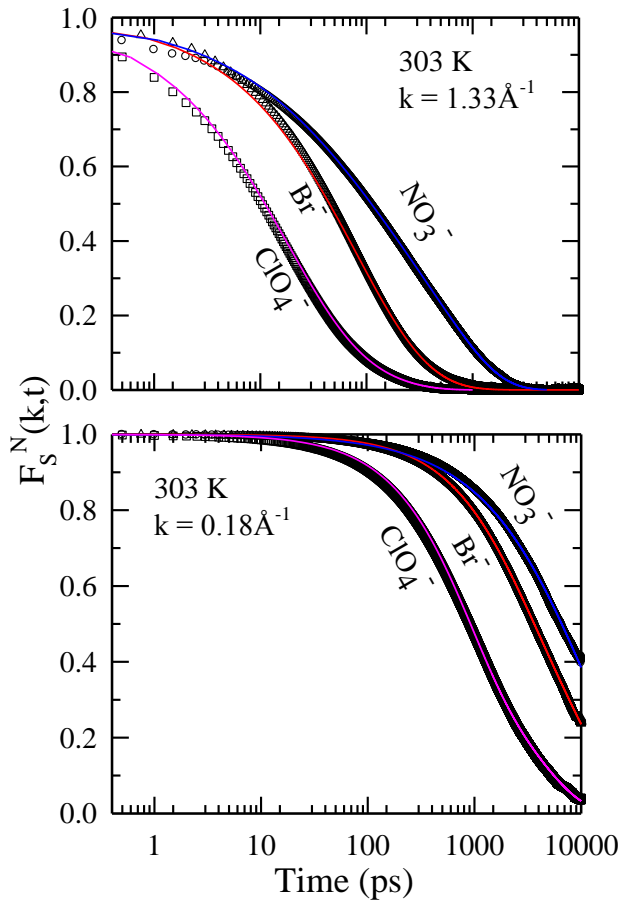


Figure 6.4: Anion dependence of acetamide dynamic structure factor relaxation, $F_s^N(k, t)$, simulated for $(\text{CH}_3\text{CONH}_2 + \text{LiX})$ DESs at 303 K at two wavevectors. While the upper panel presents relaxation at the nearest neighbour wavevector ($k = 1.33 \text{ \AA}^{-1}$), the lower panel shows the data for the lowest accessible wavevector in the present simulations ($k \sim 0.18 \text{ \AA}^{-1}$). Lines going through the simulated data (symbols) are the best fits. Fit parameters are shown in Appendix E, Table E1.

Interestingly, at both these wavevectors, $F_s^N(k, t)$ relaxation rates in presence of Br^- are faster than those in presence of NO_3^- even though experimental viscosity η of $(\text{CH}_3\text{CONH}_2 + \text{LiBr})$ DESs is larger than that of $(\text{CH}_3\text{CONH}_2 + \text{LiNO}_3)$.³⁴ In addition, the diffusive timescales, σ^2/D , for an acetamide molecule in these DESs calculated from Stokes-Einstein relation with slip boundary condition (using $\sigma_{\text{CH}_3\text{CONH}_2} = 4.52 \text{ \AA}$, $\eta = 2.11 \text{ P}$ and 13.12 P respectively for NO_3^- containing and Br^- containing DESs at $\sim 303 \text{ K}$)³⁴ are $\sim 29 \text{ ns}$ and $\sim 182 \text{ ns}$. For

(CH₃CONH₂ + LiClO₄), $\sigma^2/D \approx 20$ ns at the same temperature. These diffusive timescales are obviously much longer than the simulated $\langle \tau \rangle$ values at $k = 0.18 \text{ \AA}^{-1}$. This comparison not only indicates viscosity decoupling of acetamide diffusion in these DESs but suggests also that such decoupling is the most pronounced for (CH₃CONH₂ + LiBr) which is the most viscous among these DESs.

Subsequently, temperature effects on heterogeneous dynamics of acetamide are explored in Figure 6.5 where simulated $F_S^N(k,t)$ corresponding to both the nearest neighbour and collective wavevectors at 303 K and 350 K are compared for (CH₃CONH₂ + LiBr), (CH₃CONH₂ + LiNO₃) and (CH₃CONH₂ + LiClO₄) DESs. While the best fits through the simulated data points are shown by solid lines, fit parameters and average decay times for $F_S^N(k,t)$ have been summarized in Appendix E, Table E2. Clearly, $F_S^N(k,t)$ exhibits heterogeneous dynamics ($\beta \sim 0.6-0.7$) at 350 K which is ~ 150 K above the measured T_g of these deep eutectics. As expected, the acetamide relaxation becomes faster at higher temperature with collective wavevector $\langle \tau \rangle$ at 350 K becoming ~ 3 times shorter for Br⁻ containing and ClO₄⁻ containing DESs, and ~ 11 times shorter for NO₃⁻ containing DES than those at 303 K. For this temperature change, η reduces by a factor of ~ 20 for (CH₃CONH₂ + LiBr), ~ 10 for (CH₃CONH₂ + LiNO₃) and ~ 6 for (CH₃CONH₂ + LiClO₄) DES. This again indicates that among these three anions, Br⁻ induces the most pronounced viscosity decoupling for acetamide relaxation, providing a further support to the conclusion derived from dynamic anisotropy measurements presented earlier.³⁵

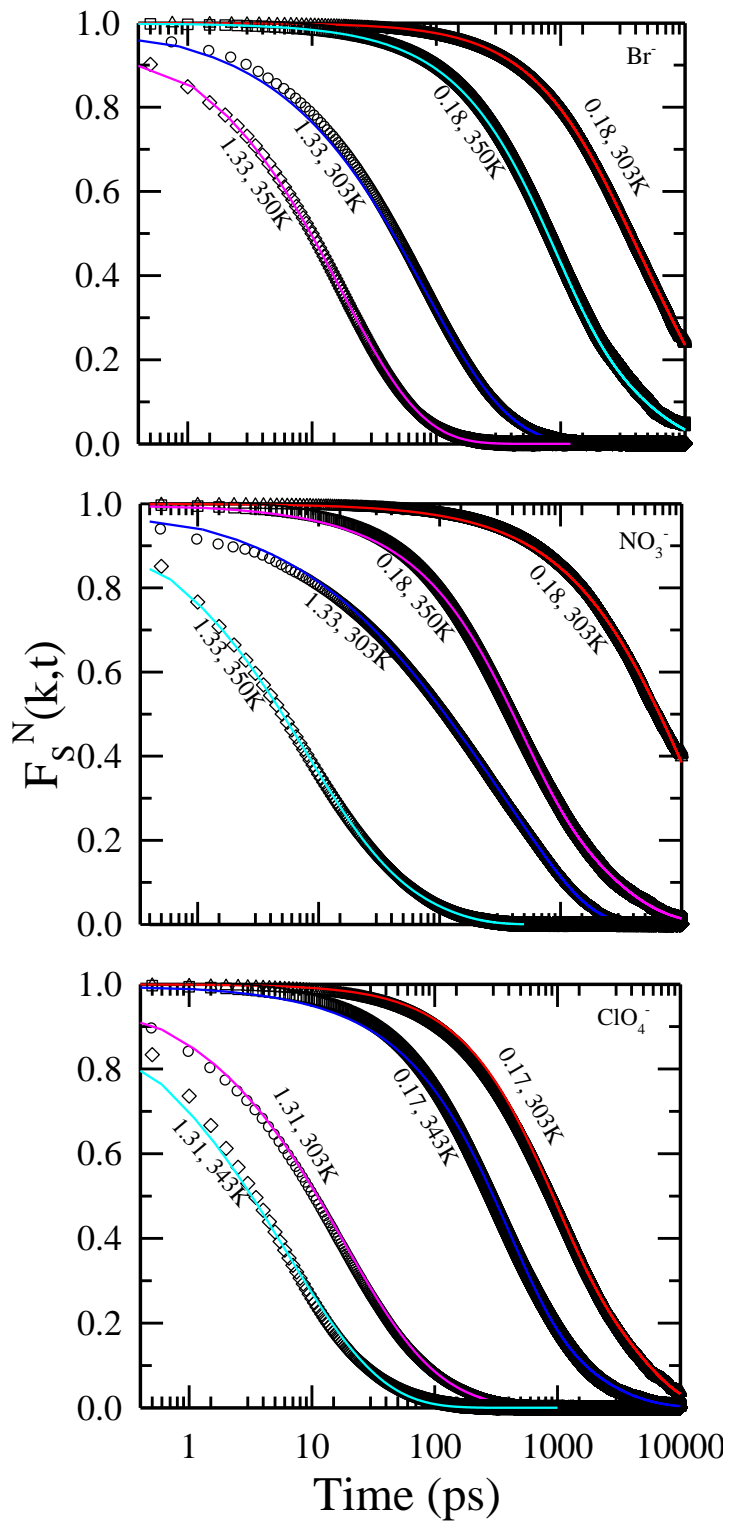


Figure 6.5: Temperature dependence of acetamide dynamic structure factor relaxation, $F_s^N(k,t)$ simulated for $(\text{CH}_3\text{CONH}_2 + \text{LiX})$ DEs at $k = 1.33 \text{ \AA}^{-1}$ and $k \sim 0.18 \text{ \AA}^{-1}$. Simulated relaxations are at 303 K, and 350 K for these two wavevectors. Results for three different

anions are presented in three different panels. Other representations remain the same as in **Figure 6.4**. Fit parameters are shown in Appendix E, Table E2.

6.3.5. Self-part of the van-Hove function($G_s(r,t)$)

Next we present results on $G_s(r,t)$ to further explore the DH in these DESs. $G_s(r,t)$ gives the probability that a particle is at a position r at time t given that it was at the origin at time $t = 0$. It is defined as:¹¹¹

$$G_s(r,t) = \frac{1}{N} \sum_{i=1}^N \langle \delta(r - |\vec{r}_i(t) - \vec{r}_i(0)|) \rangle \quad (6.7)$$

$G_s(r,t)$ is Gaussian at short times because of inertial motion (free particle limit). At long times when MSD is linearly proportional to t , $G_s(r,t)$ also exhibits Gaussian distribution of particle displacements. The Gaussian approximation can be calculated by the following expression:¹¹¹

$$G_0(r,t) = \left[\frac{3}{2\pi} \langle |\Delta r(t)|^2 \rangle \right]^{3/2} \exp \left[-\frac{3r^2}{2 \langle |\Delta r(t)|^2 \rangle} \right] \quad (6.8)$$

But in the intermediate time which corresponds to the sub-diffusive regime of MSD ($\langle \Delta r^2 \rangle \propto t^\alpha$ with $\alpha < 1$), $G_s(r,t)$ deviates significantly from Gaussian distribution. Interestingly, recent studies have shown that $G_s(r,t)$ can remain non-Gaussian even when MSD is linear in t .¹¹⁴ This happens when the dynamics are still in the cross over region between sub-diffusive and diffusive regime and $G_s(r,t)$ takes longer time to reach Gaussian behaviour as compared to MSD to become linear with time.

Figure 6.6 presents the anion dependent $G_s(r,t)$ of acetamide at a time when the respective $\alpha_2(t)$ attains the peak value and compared with the Gaussian distribution. The dotted lines represent the corresponding Gaussian behaviour. The upper panel shows the distribution at 303 K and the lower panel at 350 K. Deviation from the Gaussian behaviour is clear, deviation being more prominent at 303 K than at 350 K. This deviation from the Gaussian distribution reflects DH of the system. At the elevated temperature, the peak height decreases and the distribution gets broader because increased kinetic energy at elevated temperature

allows particles to access larger displacements. A closer observation also suggests that the

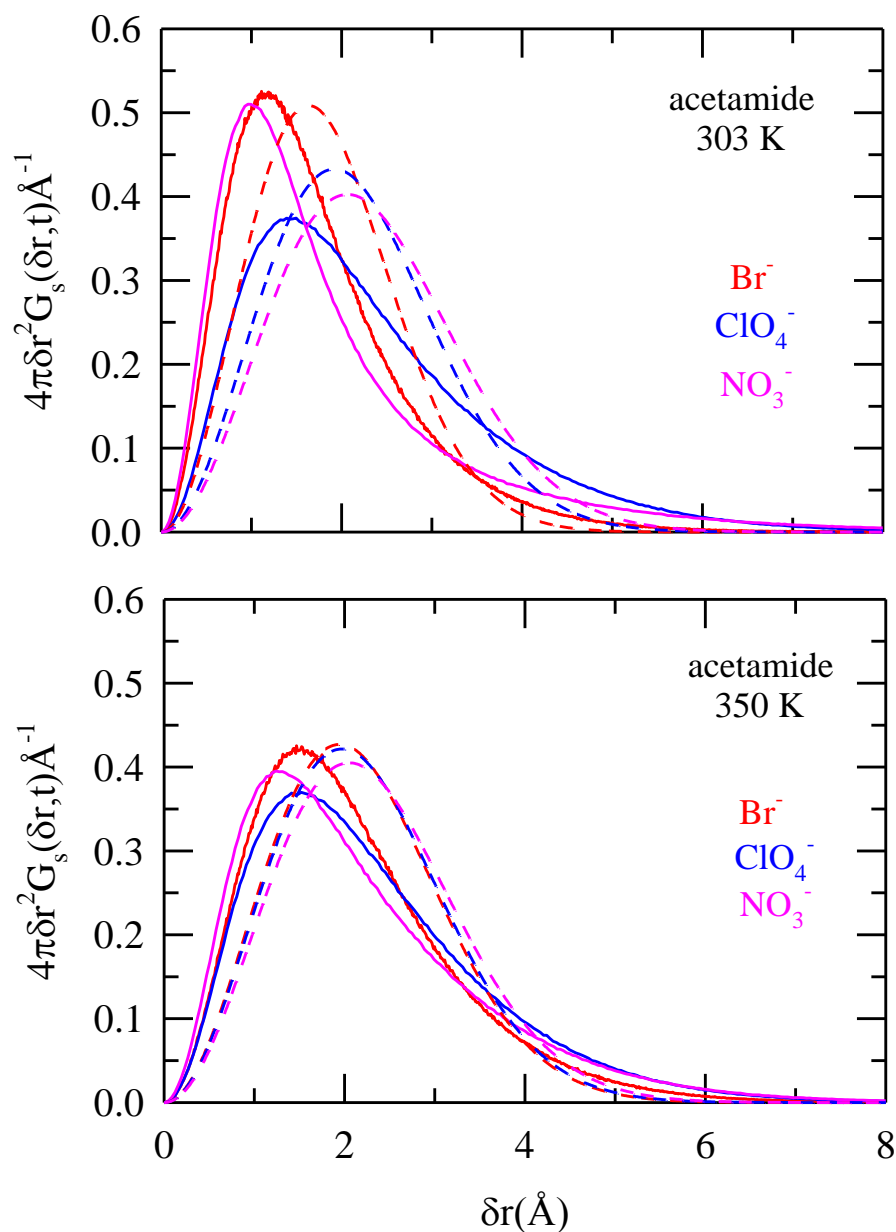


Figure 6.6: Simulated self-part of van Hove correlation function, $G_s(r, t)$ of acetamide and their Gaussian approximation for all the DESs at 303 K (upper panel) and at 350 K (lower panel). The solid lines denote $G_s(r, t)$ and dashed lines represent the approximate Gaussian distribution. Note that both these functions were calculated at time $t = \tau_{NG}$.

deviation is the most prominent in presence of NO_3^- and the minimum in presence of ClO_4^- . It also reflects the fact that acetamide molecules are most efficiently/rigidly trapped in presence

of NO_3^- which decreases the diffusion co-efficient (D) as compared to the other anions. Similar behaviour also has been observed for alkali silicate glasses¹¹⁵ and ILs.¹¹¹

6.3.6. Probability distributions of single particle displacements ($P(\log_{10}(\delta r);t)$)

The probability distributions of particle displacement δr can be derived from the self part of the van Hove correlation function via the following equation:^{110,116}

$$P(\log_{10}(\delta r);t) = \ln(10)4\pi\delta r^3 G_s(\delta r,t) \quad (6.9)$$

If the van Hove function is Gaussian at all the times then the peak height of the probability distribution function attains a peak height of 2.13¹¹⁰ and becomes independent of time. Any deviation from that peak height reflects the deviations from the Gaussian behaviour and attributed to the DH in a given system.

Figure 6.7 depicts anion dependence of $P(\log_{10}(\delta r);t)$ of acetamide at 303 K and 350 K as a function of logarithm of single particle displacements, $\log_{10}(\delta r)$. We have calculated the distribution at the peak value of $\alpha_2(t)$ and compared to the Gaussian distribution. The dotted lines represent the corresponding Gaussian distribution. Interestingly, all of the simulated distributions show peak heights deviated from 2.13. Even at 350 K, marked deviation is observed for all the mixtures indicating substantial presence of DH. Note that we have calculated the distribution function even for time $t > \tau_{\text{NNG}}$ to check whether bimodality develops or not. Bimodality for $P(\log_{10}(\delta r);t)$ for various systems including ILs,⁶⁶⁻⁸⁰ binary mixtures,¹¹⁰ colloid systems¹¹⁷ etc have been observed earlier. The bimodal distribution of $P(\log_{10}(\delta r);t)$ is a characteristic of DH that suggests particles accessing displacements of differing lengthscales. However, we have not observed any such bimodality for acetamide for all the mixtures at 303 K and 350 K. The effect of anion identity is also observed at both the temperatures. The deviation of peak height is maximum for NO_3^- at 303 K followed by Br^- and ClO_4^- . However, this relative ordering changes at the higher temperature as the peak height is the minimum for ClO_4^- . In addition, the peaks of these distributions occurs around 0.3σ which corresponds to a value of $\sim 1.3 \text{ \AA}$ (taking acetamide diameter 4.2 \AA). These suggest that acetamide displacements in these DESs are limited probably because of the strong interaction with Li^+ /anions. However, the long tail of these distributions extends up to

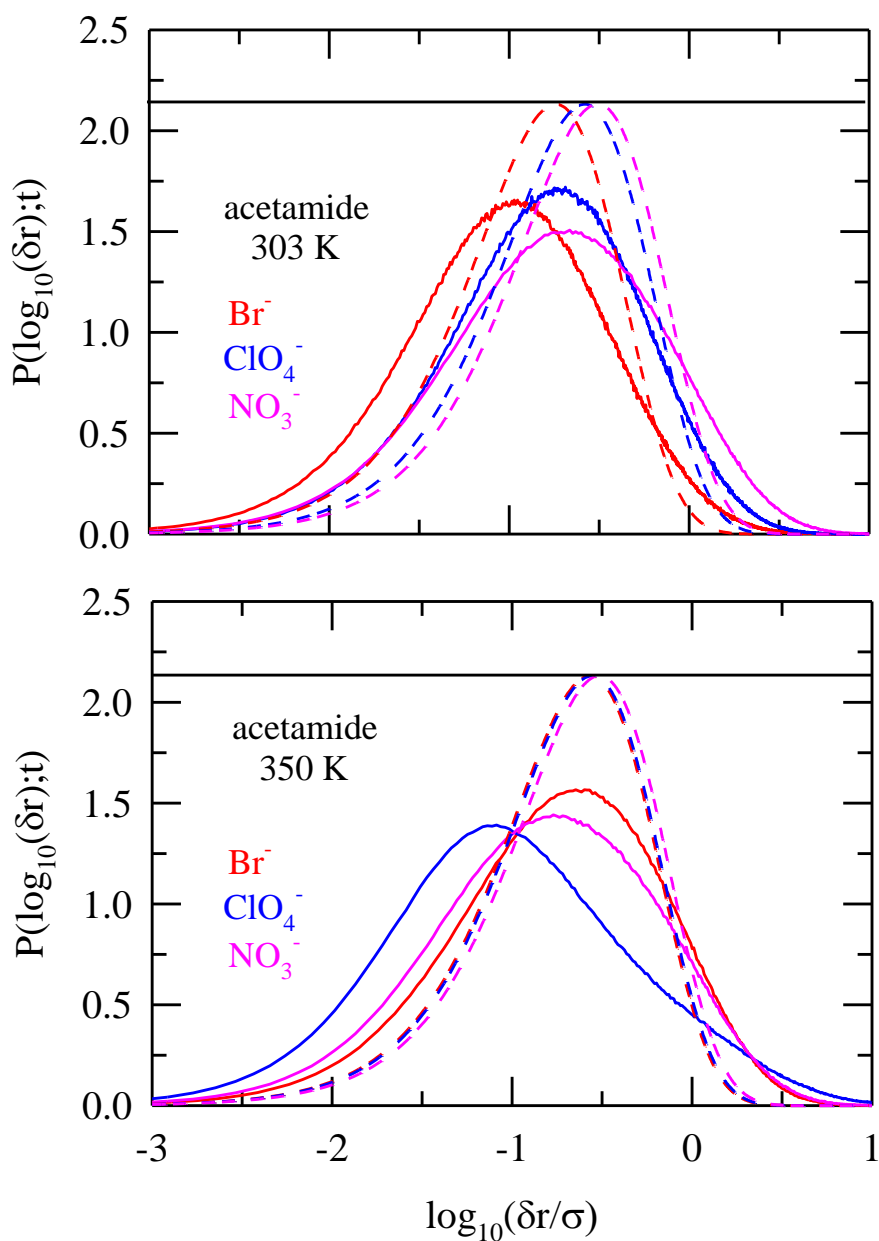


Figure 6.7: Anion dependent single particle displacement distribution, $P(\log_{10}(\delta r); t)$ of acetamide in these DESs at 303 K (upper panel) and at 350 K (lower panel). These distributions were simulated at time $t = \tau_{NG}$. The continuous lines represent the displacement distributions and the dashed line show the corresponding Gaussian approximation. Horizontal continuous line represents the peak height (~ 2.13) for Gaussian distribution of particle distribution.

a length of which is approximately twice of acetamide diameter. Thus the present analysis clearly demonstrates that particle displacement distributions in these DESs deviate considerably from the Gaussian behaviour, a typical characteristics of systems possessing DH.

6.3.7. Four point dynamic susceptibility, overlap function and correlation length

Four point dynamic susceptibility $\chi_4(k,t)$ measures the spatial correlations among particles with similar mobility at two space points over a certain time period.^{77,79,118-120} So it can follow simultaneously the time evolution of particle density and thus can detect the growth of spatially correlated regions giving it an advantage over conventional two point correlation functions. $\chi_4(k,t)$ can be calculated from self part of intermediate scattering function, $F_S(k,t)$ via the following equation:⁶⁶

$$\chi_4(k,t) = N[\langle F_S(k,t)^2 \rangle - \langle F_S(k,t) \rangle^2] \quad (6.10)$$

Where $F_S(k,t) = \frac{1}{N} \sum_{i=1}^N \langle \cos k \cdot [r_i(t) - r_i(0)] \rangle$

Here we have calculated $\chi_4(k,t)$ only for nearest neighbour wavevector i.e for $k\sigma = 2\pi$, σ corresponds to the length scale where the first peak of simulated radial distribution function ($g(r)$) of acetamide ($CH_3CONH_2 - CH_3CONH_2$) molecule appears. A more simplified version of four-point correlation function which has been discussed many times for the studies of DH is the overlap function $Q(t)$. It can be defined as:^{66,80}

$$Q(t) = \sum_{i=1}^N w(|r_i(0) - r_i(t)|) \quad (6.11)$$

Here $r_i(t)$ is the position of i -th particle at time t and N is the number of particles, $w(r) = 1$ if $r \leq a$ and zero otherwise, $a = 0.3\sigma$ with σ is the diameter of the particle of interest. Thus $w(r)$ is chosen in such a way that it neglects the displacements smaller than a , arising from the motion of the particles caged by its nearest neighbours. However precise choice of a is found to be qualitatively unimportant. The timescale associated with $Q(t)$ exhibits a similar behaviour to $F_S(k,t)$ with $k\sigma \rightarrow 2\pi$.

Figure 6.8 shows the anion dependence of four point dynamic susceptibility, $\chi_4(k,t)$ as a function of time for acetamide molecules. The upper panel shows the dependence at 303 K

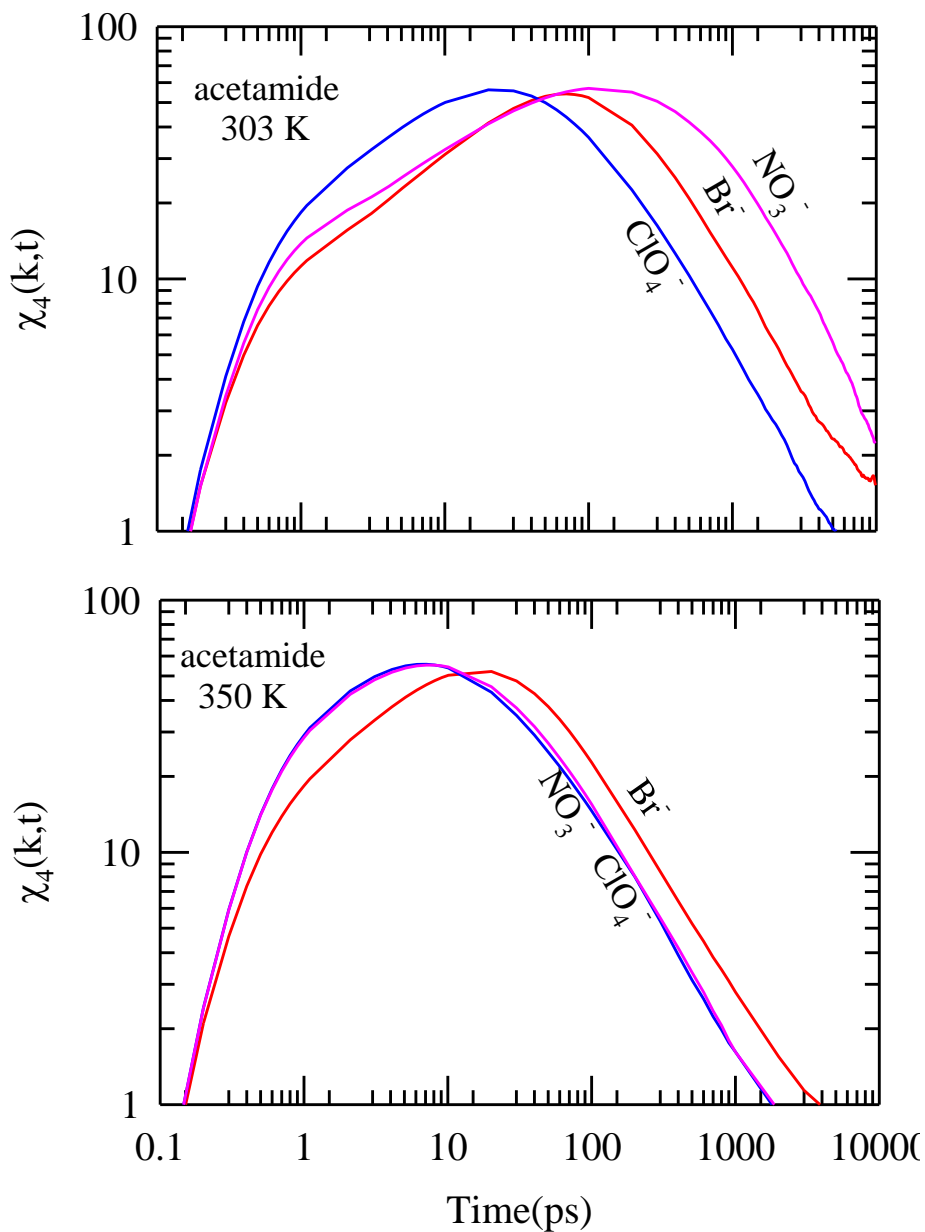


Figure 6.8: Anion dependent simulated four-point dynamic susceptibility, $\chi_4(k,t)$ of acetamide in these DESs at 303 K (upper panel) and at 350 K (lower panel).

and the lower panel gives the same at 350 K. All the plots show non-monotonous time dependence with a peak in the intermediate time (denoted as τ_4^{\max}). Similar behaviour has also been observed for various others systems possessing DH like ILs,⁶⁶⁻⁸⁰ binary mixtures,¹²¹

glass forming liquids,⁸⁰ colloidal gels¹²² and poly-dispersed systems.¹²³ Since $\chi_4(k, t)$ measures the correlation of the fluctuation in $F_S(k, t)$, its non-monotonic behaviour is a reflection of correlation among particles of similar mobility. Hence the correlation grows with time in the beginning and then decays after giving a peak at time τ_4^{\max} . So, one can relate the amplitude of $\chi_4(k, t)$ as the extent of spatial correlation and τ_4^{\max} as the time when this correlation becomes maximum. It is evident from the plot that the extent of spatial correlation is independent of the anion identity and event not affected by the increase in temperature. However τ_4^{\max} shows anion dependence and decreases in general for all the anions with increase in temperature.

Figure 6.9 shows the anion dependence $Q(t)$ relaxation for acetamide in these DESs at 303 K and 350 K. As mentioned before that $Q(t)$ follows the density relaxation at a smaller length-scale (0.3σ) and thus closely related to the nearest-neighbour relaxation of self-part of the intermediate scattering function, $F_S(k\sigma \rightarrow 2\pi, t)$. We observe that density relaxation ordering for $Q(t)$ is similar to $F_S(k\sigma \rightarrow 2\pi, t)$ for both 303 K and 350 K.³⁵ Also the relaxation is found to be stretched exponential in presence of NO_3^- at 303 K. Multi-exponential fitting parameters of $Q(t)$ for all are provided in Appendix E, Table E3.

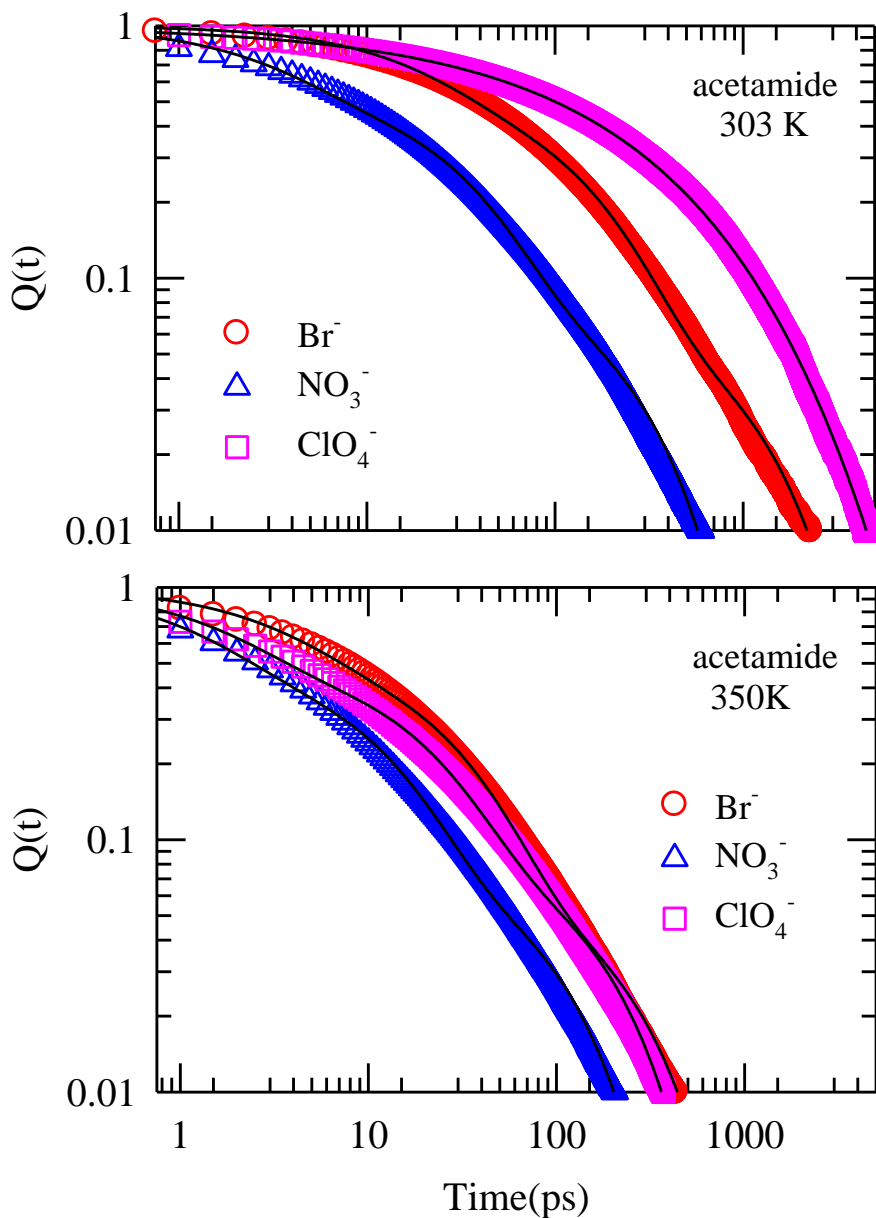


Figure 6.9: Anion dependent simulated overlap function, $Q(t)$ of acetamide in these DESs at 303 K (upper panel) and at 350 K (lower panel).

We have also compared the relaxation of $F_s(k\sigma \rightarrow 2\pi, t)$ and $Q(t)$ as shown in Figure 6.10. Though the relaxation decay for both are similar, the decay of $Q(t)$ is always slower than $F_s(k\sigma \rightarrow 2\pi, t)$ which is characterized by $1/e$ of the decay times. Table 6.3 gives a comparison of the τ_4^{\max} , τ_α and $1/e$ time of the $Q(t)$ relaxation in presence of all the anions at

both the temperature. τ_4^{\max} is highest for NO_3^- and occurs at ~ 100 ps followed by Br^- and ClO_4^- . With increase in temperature τ_4^{\max} shifts to lower values and this shift is ~ 3 - 14 times depending on the anion identity. It is noteworthy that τ_4^{\max} value is qualitatively similar to τ_α and $1/e$ time of the $Q(t)$ relaxation indicating a close relation among them. Also these timescales are close to τ_{NG} but ~ 8 - 20 times slower than the corresponding τ_{NG} supporting the presence of slow acetamide.

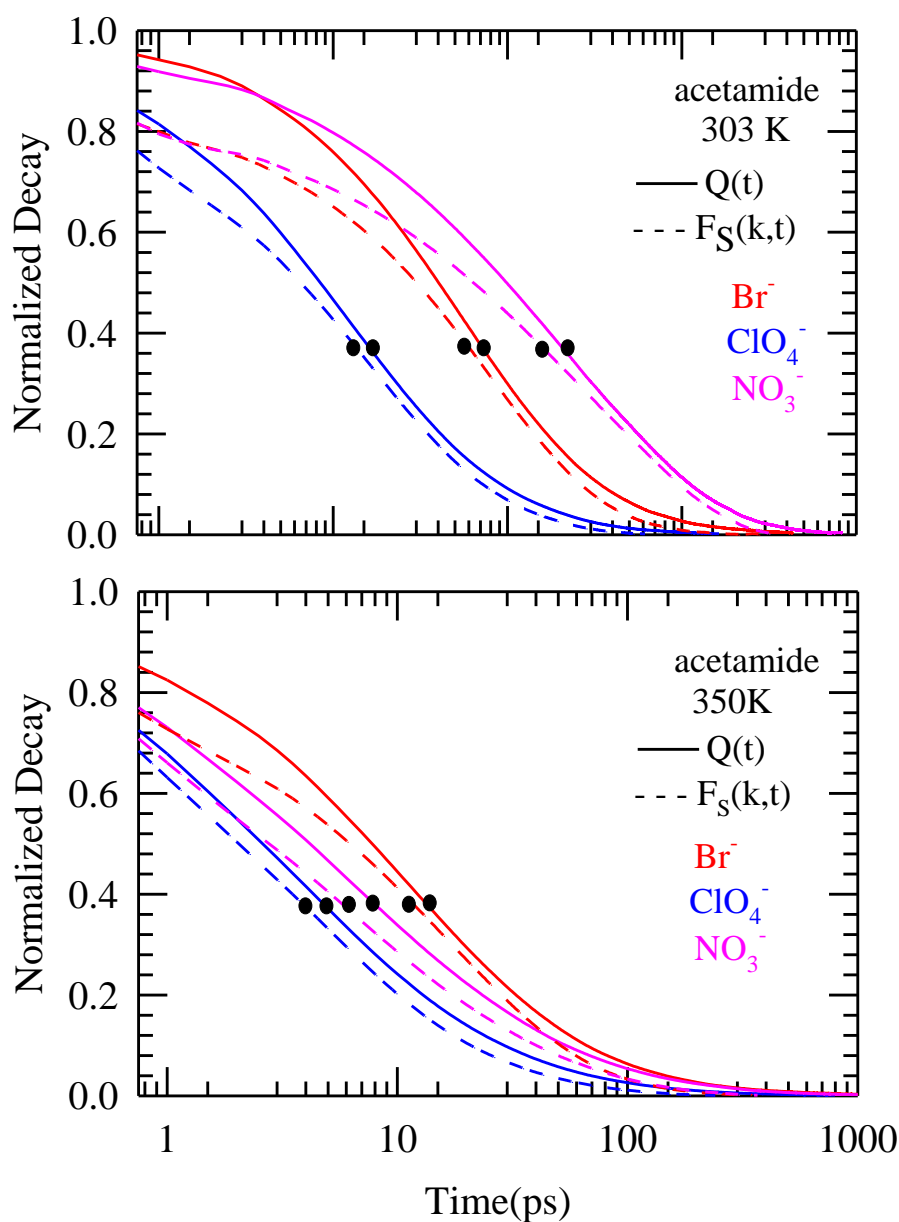


Figure 6.10: Anion dependent simulated overlap function and self-part of intermediate scattering function, $Q(t)$ and $F_S(k\sigma \rightarrow 2\pi, t)$, respectively of acetamide in these DESs at 303

K (upper panel) and at 350 K (lower panel). The data for $F_S(k\sigma \rightarrow 2\pi, t)$ has been reported from earlier work.³⁵ The continuous line represent the relaxation decay of $Q(t)$ and the dashed line show the same for $F_S(k\sigma \rightarrow 2\pi, t)$. Bullets denote the respective $1/e$ decay time of the corresponding relaxation.

Table 6.3 Comparison of anion dependent $1/e$ decay times between $F_S(k\sigma \rightarrow 2\pi, t)$ and $Q(t)$ of acetamide at 303 K and 350 K for various DESs.

Anion	303 K			350 K		
	τ_4 (ps) ^c	τ_α (ps) ^d	$\tau_{1/e}^Q$ (ps) ^e	τ_4 (ps)	τ_α (ps)	$\tau_{1/e}^Q$ (ps)
Br^-	70	61	72	22	12	14
ClO_4^-	25	13	16	6	4	5
NO_3^-	100	162	210	7	6	9

c) represents the time at which the corresponding $\chi_4(k, t)$ attains a peak.

d) τ_α denotes the time at which the corresponding normalized self dynamic structure factor at nearest neighbour wavenumber, $F_S(k\sigma \rightarrow 2\pi, t)$ has relaxaed to a value of $1/e$.

e) $\tau_{1/e}^Q$ denotes the time at which the corresponding overlap function, $Q(t)$, has relaxaed to a value of $1/e$.

The emergence of spatial correlation via four-point correlation also motivates to extract the growing correlation length of DH $\xi(t)$ at τ_4^{\max} . Four-point correlation function $S_4(k, t)$ in the limit of small wave-numbers can be related to $\xi(t)$ via the following Ornstein-Zernike relation:^{77,118,124-125}

$$\frac{S_4(k, t)}{\chi_4(k \rightarrow 0, t)} = \frac{1}{1 + [k \xi(t)]^p} \quad (6.12)$$

Here, we have obtained $S_4(k, t)$ from the corresponding radial distribution function, $g(r)$ as follows:

$$S_4(k, t) = 4\pi\rho[Q(t) / N]^2 \int_0^{\infty} dr r^2 \frac{\sin kr}{kr} g(r) \quad (6.13)$$

Following earlier works,^{66,80} we have taken $p = 2$ for the present study. Note the estimation of $\xi(t)$ from the Ornstein-Zernike equation is strictly valid for at the collective limit ($k \rightarrow 0$).

Figure 6.11 presents the numerical fit as described above and the estimated $\xi(t)$ for acetamide in these DESs at both 303 K and 350 K. The values of $\xi(t)$ as obtained from the fitting of the corresponding four-point correlation functions are summarized in Table 6.4. Interestingly, $\xi(t)$ does not depend on anion identity and also independent of temperature. $\xi(t)$, estimated for acetamide spans about $\sim 7.8 \text{ \AA}$ which is roughly twice of its diameter. Keeping in mind the system size dependence and ensemble sensitivity of $\xi(t)$, it provides a rough estimate of growing correlation length. However these are the indicators of local clusters formation which has been discussed in details earlier.⁹⁶

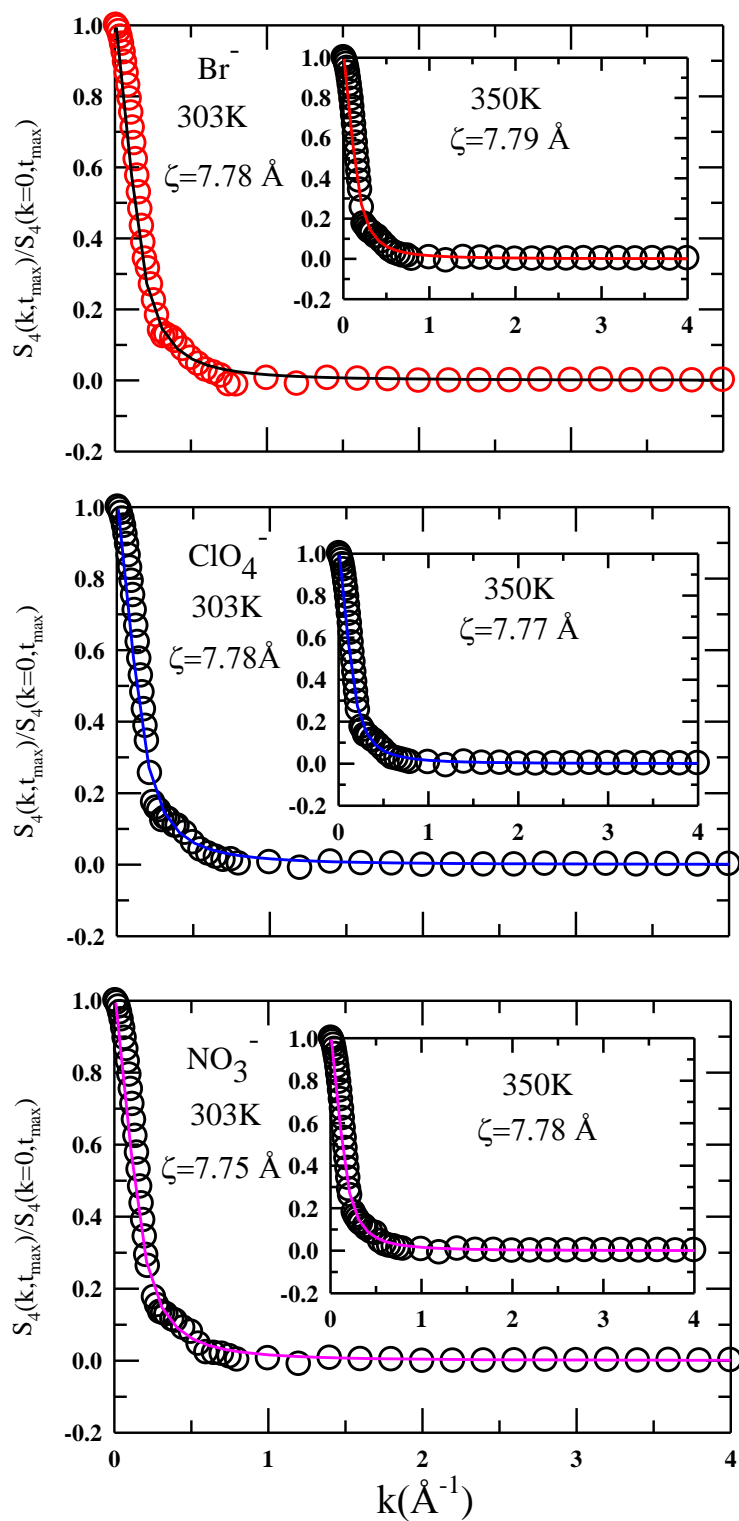


Figure 6.11: Estimated dynamic correlation length, $\xi(t)$ of acetamide in these DESs. The main panels show the result at 303 K and insets represent the same at 350 K. Black bullets represent the simulated data and the continuous lines denote the corresponding fittings of the Orstein-Zernike expression.

Table 6.4 Anion dependence of $\xi(t)$ of acetamide obtained from the fitting of $S_4(k,t)$ at 303 K and 350 K for various DESs.

Anion	303 K	350 K
Br^-	7.78Å	7.79Å
ClO_4^-	7.78Å	7.77Å
NO_3^-	7.75Å	7.78Å

6.4. Concluding Remarks

In summary, we have analysed various parameters including four-point correlation functions systematically to characterize the length scale and time scale of DH associated with acetamide containing DESs. We have also looked into the effect of anion identity and temperature on DH. Though extensive progress have been made to understand the conjecture between length scale and time scale associated with DH in glass former liquids, only a few studies have been performed with DESs which show DH at ambient condition.

We have investigated the timescale associated with DH for these amide DESs at 303 K and 350 K. The analysis $\alpha_2(t)$ suggests that depending on anion identity DH can survive upto a few ns and with increase in temperature this timescale decreases substantially. However this timescale is dominated by fast particles. One can also obtain a slower timescale via $\gamma(t)$ which is influenced by slow particles. This simultaneous presence of fast and slow particle is the main characteristics of DH. The stretched exponential relaxation of wavevector dependent amide dynamic structure factors support the experimentally observed results in terms of temporal heterogeneity. Our simulated van Hove correlation functions show pronounced deviation from Gaussian distribution with deviation being the maximum for NO_3^- . Again anion displacement distributions of acetamide in these DESs also show strong deviation from Gaussian peak height and the hopping length scale (\sim twice of

acetamide diameter) matches qualitatively with dynamic correlation length calculated later. Simulated peak times for four-point dynamic susceptibility also depict anion dependence and the timescale is close to $1/e$ times of overlap function and τ_α suggesting a close relation among them. We have also estimated the growing correlation length of acetamide from numerical fitting of four-point correlation functions. We observe that dynamic correlation length $\xi(t)$ span about twice of acetamide diameter and does not depend either on anion identity or temperature. Similar correlation length has also been found for ILs¹⁰⁷, ILs+water⁶⁶ and other binary mixtures.¹²¹

Finally, it is of fundamental importance to understand various length scales and time scales associated with DH and investigate the connection among them. The present study is an attempt towards this general understanding. Similar investigation can be conducted by varying the chain length of acetamide/cation in these DESs,³⁵ for ILs+nonpolar binary mixtures¹²⁶, biologically relevant moieties¹²⁷⁻¹²⁹ and other solutes.¹³⁰⁻¹³² All these would constitute our future work.

References:

1. M. D. Ediger, *Annu. Rev. Phys. Chem.* **51**, 99 (2000).
2. M. D. Ediger, C. A. Angell, and S. R. Nagel, *J. Phys. Chem. B* **100**, 13200 (1996).
3. R. Richert, *J. Non-Cryst. Solids* **172-174**, 209 (1994).
4. J. Jackle, *Rep. Prog. Phys.* **49**, 171 (1999).
5. K. L. Ngai, *J. Non-Cryst. Solids* **275**, 7 (2000).
6. C. A. Angell, K. L. Ngai, G. B. McKenna, P. F. McMillan, and S. W. Martin, *J. Appl. Phys.* **88**, 3113 (2000).
7. P. G. Debenedetti and F. H. Stillinger, *Nature* **410**, 259 (2001).
8. M. D. Ediger and P. Harrowell, *J. Chem. Phys.* **137**, 080901 (2012).
9. H. J. Sillescu, *J. Non-Cryst. Solids* **243**, 81 (1999).
10. D. Chakrabarti and B. Bagchi, *Phys. Rev. Lett.* **96**, 187801 (2006).
11. S. Karmakar, C. Dasgupta, and S. Sastry, *Annu. Rev. Condens. Matter Phys.* **5**, 255 (2014).
12. C. A. Angell, *J. Phys. Chem. Solids* **49**, 863 (1988).
13. K. Schmidt-Rohr and H. W. Spiess, *Phys. Rev. Lett.* **66**, 3020 (1991).
14. A. Heuer, M. Wilhelm, H. Zimmermann, and H. W. Spiess, *Phys. Rev. Lett.* **75**, 2851 (1995).
15. U. Tracht, M. Wilhelm, A. Heuer, H. Feng, K. Schmidt-Rohr, and H. W. Spiess, *Phys. Rev. Lett.* **81**, 2727 (1998).
16. E. Vidal Russel and N. E. Israeloff, *Nature* **408**, 695 (2000).
17. G. Szamel and E. Flenner, *Europhys. Lett.* **67**, 779 (2004).
18. R. Richert, *J. Phys.: Condens. Matter* **14**, R703 (2002).

19. L. Berthier and G. Biroli, *Rev. Mod. Phys.* **83**, 587 (2011).
20. S. Karmakar, C. Dasgupta, and S. Sastry, *Rep. Prog. Phys.* **79**, 016601 (2016).
21. G. Wahnstrom, *Phys. Rev A* **44**, 3752 (1991).
22. R. D. Mountain, *Growing Length Scales in Supercooled Liquids, Supercooled Liquids: ACS Symposium Series*, **676**, 122 (1997).
23. W. Kob, C. Donati, S. J. Plimpton, P. H. Poole, and S. C. Glotzer, *Phys. Rev.Lett.* **79**, 2827 (1997).
24. C. Donati, J. F. Douglas, W. Kob, S. J. Plimpton, P. H. Poole, and S. C. Glotzer, *Phys. Rev. Lett.* **80**, 2338 (1998).
25. C. Donati, S. C. Glotzer, P. H. Poole, W. Kob, and S. J. Plimpton, *Phys. Rev. E* **60**, 3107 (1999).
26. S. C. Glotzer and C. Donati, *J. Phys.: Condens. Matter* **11**, A285 (1999).
27. C. Donati, S. C. Glotzer, and P. H. Poole, *Phys. Rev. Lett.* **82**, 5064 (1999).
28. S. C. Glotzer, V. N. Novikov, and T. B. Schroder, *J. Chem. Phys.* **112**, 509 (2000).
29. W. Kob and H. C. Andersen, *Phys. Rev. E* **51**, 4626 (1995).
30. W. Kob and H. C. Andersen, *Phys. Rev. E* **52**, 4134 (1995).
31. B. Bernu, Y. Hiwatari, and J. P. Hansen, *J. Phys. C: Solid State Phys.* **18**, L371 (1985).
32. B. Bernu, J. P. Hansen, Y. Hiwatari, and G. Pastore, *Phys Rev A* **36**, 4891 (1987).
33. D. Coslovich and G. Pastore, *J. Phys.: Condens. Matter* **21**, 285107 (2009).
34. B. Guchhait, S. Daschakraborty, and R. Biswas, *J. Chem. Phys.* **136**, 174503 (2012).
35. B. Guchhait, S. Das, S. Daschakraborty, and R. Biswas, *J. Chem. Phys.* **140**, 104514 (2014).
36. S. N. Tripathy, Z. Wojnarowska, J. Knapik, H. Shirota, R. Biswas, and M. Paluch, *J. Chem. Phys.* **142**, 184504 (2015).

37. R. Biswas, A. Das, and H. Shirota, *J. Chem. Phys.* **141**, 134506 (2015).
38. B. Guchhait, H. A. R. Gazi, H. K. Kashyap, and R. Biswas, *J. Phys. Chem. B* **114**, 5066 (2010).
39. A. Das, S. Das, and R. Biswas, *Chem. Phys. Lett.* **581**, 47 (2013).
40. A. Das, S. Das, and R. Biswas, *J. Chem. Phys.* **142**, 034505 (2015).
41. H. A. R. Gazi, B. Guchhait, S. Daschakraborty, and R. Biswas, *Chem. Phys. Lett.* **501**, 358 (2011).
42. A. Das and R. Biswas, *J. Phys. Chem. B* **119**, 10102 (2015).
43. A. Samanta, *J. Phys. Chem. B* **110**, 13704 (2006).
44. A. Samanta, *J. Phys. Chem. Lett.* **1**, 1557 (2010).
45. J. A. Ingram, R. S. Moog, N. Ito, R. Biswas, and M. Maroncelli, *J. Phys. Chem. B* **107**, 5926 (2003).
46. S. Arzhantsev, H. Jin, G. A. Baker, and M. Maroncelli, *J. Phys. Chem. B* **111**, 4978 (2007).
47. X.-X. Zhang, M. Liang, N. P. Ernsting, and M. Maroncelli, *J. Phys. Chem. B* **117**, 4291 (2013).
48. A. Stoppa, J. Hunger, R. Buchner, G. Hefter, A. Thoman, and H. Helm, *J. Phys. Chem. B* **112**, 4854 (2008).
49. J. Hunger, A. Stoppa, S. Schrödle, G. Hefter, and R. Buchner, *ChemPhysChem* **10**, 723 (2009).
50. S. Daschakraborty and R. Biswas, *J. Chem. Phys.* **140**, 014504 (2014).
51. S. Daschakraborty, T. Pal, and R. Biswas, *J. Chem. Phys.* **139**, 164503 (2013).
52. S. Daschakraborty and R. Biswas, *J. Chem. Phys.* **137**, 114501 (2012).
53. H. K. Kashyap and R. Biswas, *J. Phys. Chem. B* **112**, 12431 (2008).
54. H. K. Kashyap and R. Biswas, *J. Phys. Chem. B* **114**, 254 (2010).
55. S. Daschakraborty and R. Biswas, *Chem. Phys. Lett.* **510**, 202 (2011).

56. S. Daschakraborty and R. Biswas, *Chem. Phys. Lett.* **545**, 54 (2012).
57. H. K. Kashyap and R. Biswas, *J. Phys. Chem. B* **114**, 16811 (2010).
58. H. K. Kashyap and R. Biswas, *Indian J. Chem.* **49A**, 685 (2010).
59. X.-X. Zhang, M. Liang, J. Hunger, R. Buchner, and M. Maroncelli, *J. Phys. Chem. B* **117**, 15356 (2013).
60. M. Liang, X.-X. Zhang, A. Kaintz, N. P. Ernsting, and M. Maroncelli, *J. Phys. Chem. B* **118**, 1340 (2014).
61. A. Stoppa, J. Hunger, G. Hefter, and R. Buchner, *J. Phys. Chem. B* **116**, 7509 (2012).
62. D. Chakrabarty, A. Chakraborty, D. Seth, and N. Sarkar, *J. Phys. Chem. A* **109**, 1764 (2005).
63. S. Daschakraborty and R. Biswas, *J. Phys. Chem. B* **115**, 4011 (2011).
64. S. Daschakraborty and R. Biswas, *J. Phys. Chem. B* **118**, 1327 (2014).
65. T. Pal and R. Biswas, *J. Chem. Phys.* **141**, 164502 (2014).
66. T. Pal and R. Biswas, *J. Phys. Chem. B* **119**, 15683 (2015).
67. G. Hinze, *Phys. Rev. E* **57**, 2010 (1998).
68. R. Bohmer, G. Hinze, G. Diezemann, B. Geil, and H. Sillescu, *Europhys. Lett.* **36**, 55 (1996).
69. S. C. Kuebler, A. Heuer, and H. W. Spiess, *Phys. Rev. E* **56**, 741 (1997).
70. D. K. Sasmal, A. K. Mandal, T. Mondal, and K. Bhattacharyya, *J. Phys. Chem. B* **115**, 7781 (2011).
71. S. Patra and A. Samanta, *J. Phys. Chem. B* **116**, 12275 (2012).
72. A. H. Marcus, J. Schofield, and S. A. Rice, *Phys. Rev. E* **60**, 5725 (1999).
73. W. K. Kegel and A. van Blaaderen, *Science* **287**, 290 (2000).
74. Q.-H. Wei, C. Bechinger, and P. Leiderer, *Science* **287**, 625 (2000).

75. W. Kob and H. C. Andersen, *Phys. Rev. Lett.* **73**, 1376 (1994).
76. S. C. Glotzer, *J. Non-Cryst. Solids* **274**, 342 (2000).
77. N. Laceyvic, F. W. Starr, T. B. Schroder, and S. C. Glotzer, *J. Chem. Phys.* **119**, 7372 (2003).
78. N. Laceyvic, F. W. Starr, T. B. Schröder, V. N. Novikov, and S. C. Glotzer, *Phys. Rev. E: Stat. Phys., Plasmas, Fluids, Relat. Interdiscip. Top.* **66**, 030101(R) (2002).
79. K. Kim and S. Saito, *J. Chem. Phys.* **138**, 12A506 (2013).
80. K. Kim and S. Saito, *J. Chem. Phys.* **133**, 044511 (2010).
81. D. V. Wagle, H. Zhao, and G. A. Baker, *Acc. Chem. Res.* **47**, 2299 (2014).
82. Q. Zhang, K. De Oliveira Vigier, S. Royer, and F. Jerome, *Chem. Soc. Rev.* **41**, 7108 (2012).
83. A. P. Abbott, G. Capper, D. L. Davies, R. K. Rasheed, and V. Tambyrajah, *Chem. Commun.* **70** (2003).
84. A. P. Abbott, D. Boothby, G. Capper, D. L. Davies, and R. K. Rasheed, *J. Am. Chem. Soc.* **126**, 9142 (2004).
85. M. Francisco, A. van Den Bruinhorst, M. C. Kroon, *Angew. Chem., Int. Ed.* **52**, 3074 (2013).
86. M. Francisco, A. van den Bruinhorst, M.-C. Kroon, *Green Chem.* **14**, 2153 (2012).
87. H. Zhao and G. A. Baker, *J. Chem. Technol. Biotechnol.* **88**, 3 (2013).
88. D. Carriazo, M. C. Serrano, M. C. Gutierrez, M. L. Ferrer, and F. del Monte, *Chem. Soc. Rev.* **41**, 4996 (2012).
89. G. van der Zwan and J. T. Hynes, *Chem. Phys.* **152**, 169 (1991).
90. G. van der Zwan and J. T. Hynes, *J. Chem. Phys.* **78**, 4174 (1983).
91. T. Pradhan and R. Biswas, *J. Phys. Chem. A* **111**, 11524 (2007).

92. K. Mukherjee, A. Das, S. Choudhury, A. Barman, and R. Biswas, *J. Phys. Chem. B* **119**, 8063 (2015).
93. S. Das, R. Biswas, and B. Mukherjee, *J. Phys. Chem. B* **119**, 11157 (2015).
94. S. Das, R. Biswas, and B. Mukherjee, *J. Phys. Chem. B* **119**, 274 (2015).
95. S. Das, R. Biswas, and B. Mukherjee, *J. Chem. Phys* (under minor review).
96. S. Das, B. Mukherjee, and R. Biswas, *J. Phys. Chem. B* (to be submitted).
97. W. Smith and T. R. Forster, *The DL_POLY Molecular Simulation Package*; Daresbury Laboratory: Cheshire, U. K., **1999**.
98. A. D. MacKerell Jr., J. Wiorkiewicz-Kuczera, and M. Karplus, *J. Am. Chem. Soc.* **117**, 11946 (1995).
99. J. P. Jensen and W. L. Jorgensen, *J. Chem. Theory Comput.* **2**, 1499 (2006).
100. C. Cadena and E. J. Maginn, *J. Phys. Chem. B* **110**, 18026 (2006).
101. J. N. Canongia Lopes, J. Deschamps, A. A. H. Padua, *J. Phys. Chem. B* **108**, 2038 (2004).
102. C. W. Yong, *DL_FIELD STFC Daresbury Laboratory*: Cheshire, U.K., **2011**, http://www.cse.scitech.ac.uk/ccg/software/DL_FIELD.
103. M. P. Allen and D. J. Tildesley, *Computer Simulations of Liquids*; Oxford University Press: New York, **1987**.
104. L. Martinez, R. Andrade, E. G. Birgin, and J. M. Martinez, *J. Comput. Chem.* **30**, 2157 (2009).
105. S. Nose, *J. Chem. Phys.* **81**, 511 (1984).
106. W. G. Hoover, *Phys. Rev. A: At., Mol., Opt. Phys.* **31**, 1695 (1985).
107. T. Pal and R. Biswas, *J. Chem. Phys.* **141**, 104501 (2014).
108. F. Faupel, W. Frank, M. P. Macht, H. Mehrer, V. Naundorf, K. Ratzke, and H. R. Schober, *Rev. Mod. Phys.* **75**, 237 (2003).

109. J. Habasaki and K. L. Ngai, *J. Non-Cryst. Solids* **352**, 5170 (2006).
110. E. Flenner and G. Szamel, *Phys. Rev. E* **72**, 011205 (2005).
111. J. Habasaki and K. L. Ngai, *J. Chem. Phys.* **129**, 194501 (2008).
112. Z. Hu and C. J. Margulis, *Proc. Natl. Acad. Sci. U.S.A.* **103**, 831 (2006).
113. M. S. Shell, P. G. Debenedetti, and F. H. Stillinger, *J. Phys.: Condens. Matter* **17**, S4035 (2005).
114. G. Kwon, B. J. Sung, and A. Yethiraj, *J. Phys. Chem. B* **118**, 8128 (2014).
115. J. Habasaki, K. L. Ngai, and Y. Hiwatari, *J. Chem. Phys.* **120**, 8195 (2004).
116. J.-P. Hansen, *Phys. A* **201**, 138 (1993).
117. D. R. Reichman, E. Rabani, and P. L. Geissler, *J. Phys. Chem. B* **109**, 14654 (2005).
118. S. Franz and G. Parisi, *J. Phys.: Condens. Matter* **12**, 6335 (2000).
119. C. Donati, S. Franz, G. Parisi, and S. C. Glotzer, *J. Non-Cryst. Solids* **307-310**, 215 (2002).
120. C. Toninelli, M. Wyart, L. Berthier, G. Biroli, and J.-P. Bouchaud, *Phys. Rev. E* **71**, 041505 (2005).
121. S. Indra, B. Guchhait, and R. Biswas, *J. Chem. Phys.* **144**, 124506 (2016).
122. T. Kawasaki and H. Tanaka, *J. Phys.: Condens. Matter* **23**, 194121 (2011).
123. T. Abete, A. de Candia, E. Del Gado, A. Fierro, and A. Coniglio, *Phys. Rev. Lett.* **98**, 088301 (2007).
124. L. Berthier, *Phys. Rev. E* **69**, 020201(R) (2004).
125. R. Yamamoto and A. Onuki, *Phys. Rev. E: Stat. Phys., Plasmas, Fluids, Relat. Interdiscip. Top.* **58**, 3515 (1998).
126. M. Deetlefs, C. Hardacre, M. Nieuwenhuyzen, O. Sheppard, and A. K. Soper, *J. Phys. Chem. B* **109**, 1593 (2005).

127. S. Roy and B. Bagchi, *J. Phys. Chem. B* **118**, 5691 (2014).
128. S. Roy and B. Bagchi, *J. Phys. Chem. B* **117**, 4488 (2013).
129. S. Roy, B. Jana, and B. Bagchi, *J. Chem. Phys.* **136**, 115103 (2012).
130. S. Chowdhuri and A. Chandra, *J. Chem. Phys.* **119**, 4360 (2003).
131. M. S. Skaf, *J. Phys. Chem. A* **103**, 10719 (1999).
132. G. M. Sando, K. Dahl, and J. C. Owrutsky, *J. Phys. Chem. B* **111**, 4901 (2007).

Chapter 7

Reorientational Dynamics in 1-butyl-3-methylimidazolium hexafluorophosphate ([BMIM][PF₆]) Ionic Liquid: Are Angular Jumps Predominant?

7.1. Introduction

Ionic liquids (ILs) are defined as molten salts that remain in liquid phase below 100⁰ C.¹ Some of the ILs remain liquid around room temperature and are known as room temperature ionic liquids (RTILs). It is believed that reduced electrostatic interaction among bulky ions along with diffused and asymmetric charge distributions creates a frustration in the lattice arrangements of designated for ionic compounds. This frustration coupled with the entropic gain for being in the molten state then allows these electrolytes to be in the liquid phase near room temperature. ILs have several remarkable properties like low vapour pressure, non-flammability, easy separation route, wide electrochemical window and recyclability. ILs have remained one of the prime subject of intense research in the recent past²⁻⁶ and have seen industrial and technological applications. ILs have been widely used for energy applications such as batteries⁷⁻⁸ and supercapacitors,⁹ fuel cells,¹⁰ solar cells,¹¹ carbon dioxide capturing,¹²⁻¹³ and dissolution of protein¹⁴ and cellulose.¹⁵ However, like deep eutectic solvents,¹⁶⁻¹⁹ ILs have been mainly used as reaction media.²⁰ Several questions are then associated with the use of these ILs as reaction media. For example, how does a given IL control the rate of a chemical reaction?²¹⁻²² What would be the impact of IL structure on the rate of a reaction? Answer to these questions then naturally demands a thorough understanding of structure and dynamics of these Coulomb liquids.

1-butyl-3-methylimidazolium hexafluorophosphate ([BMIM][PF₆]) is one of the most widely studied systems. Several experimental²³⁻²⁴ and theoretical studies²⁵⁻²⁹ have been performed to

explore the interaction and dynamics in this IL. The thermodynamic properties of the system in the glassy and crystalline state have been measured by using wide angle neutron and X-ray diffraction techniques.³⁰ Macroscopic properties like viscosity, melting point etc. have been investigated using classical molecular dynamics simulation technique.³¹ Various structural properties including radial distribution functions, spatial density distributions, and dynamical properties like orientational correlation, electrical conductivity, hydrogen bond (H-bond) dynamics, ion-pair dissociation dynamics have been investigated via molecular dynamic simulations.³² Dynamic heterogeneity aspect of this ILs has been studied by analyzing non-Gaussian parameters, coherent and incoherent scattering functions and mean square displacements over a wide temperature range.³³ The study also showed that the activation energy for diffusion is slightly higher for anion as compared to cation. Though certain aspects of orientational dynamics of various ILs have been investigated by using FTIR,³⁴ dielectric relaxation³⁵ and computer simulations,³⁶ a systematic investigation of orientational dynamics is still unavailable. Here we have mainly focused on the orientational dynamics of the IL and tried to connect it with the H-bond fluctuation dynamics.

Rotational dynamics of 1-ethyl-3-methylimidazolium hexafluorophosphate ([EMIM][PF₆]) IL has been studied via molecular dynamic simulations³⁷ where propensity for large-angle jumps of cations rather than the conventional rotational diffusion has been reported. Further, the orientational dynamics of neat IL³⁸ and IL in presence of polar co-solvent³⁹ has been experimentally measured via optical heterodyne detected optical Kerr effect (OHD-OKE) spectroscopy. A power-law distribution for the dynamics has been suggested by these measurements. Also, the reorientational dynamics of ILs has been investigated by ¹³C NMR technique⁴⁰ and magnetic relaxation study.⁴¹ Recently, the H-bond dynamics of a protic IL, ethylammonium nitrate ([CH₃CH₂NH₃][NO₃]), has been investigated via dielectric relaxation and femtosecond-infrared spectroscopic techniques.⁴² Their investigation has suggested that the rotation of ethylammonium cation ([CH₃CH₂NH₃]⁺) takes place via large angular jumps and the jump angle $\sim 106^\circ$. However, full characterization of angular jumps vis-à-vis role of the counter ions has not been explored yet. This particular study aims at providing a comprehensive picture of orientational dynamics and the mechanism of rotation for both the cation and the anion in

[BMIM][PF₆]. Reorientational jumps of both the ions have been monitored via a method that closely follows the framework developed earlier for studying reorientation dynamics of liquid water⁴³ and employed later to study the orientational dynamics of molten acetamide⁴⁴ and acetamide in presence of various electrolytes.⁴⁵ The dynamics has been explored via simulating jump and waiting time distributions, jump angle distributions, change in radial and angular distances during successful jumps. Further attempts have been made to connect the orientational dynamics with H-bond fluctuation dynamics. Since the cation and anion vary widely in size and shape, the difference in all the calculated properties are expected to be more complex than those predicted from excluded volumes only.

7.2. Simulation Details

All-atom molecular dynamics simulations were performed at 298 K with a total of 1024 pairs of ions that constituted [BMIM][PF₆] by using the package GROMACS version 4.5.4.⁴⁶ A schematic diagram of *BMIM*⁺ and *PF*₆⁻ along with the naming scheme for atoms is provided in Figure 7.1. The interaction among the molecules is represented via the following potential function:

$$\begin{aligned}
 U(R) = & \sum_{bonds} K_r (r - r_{eq})^2 + \sum_{angles} K_\theta (\theta - \theta_{eq})^2 + \sum_{dihedrals} \left[\frac{V_1}{2} (1 + \cos \phi) + \frac{V_2}{2} (1 - \cos 2\phi) + \frac{V_3}{2} (1 + \cos 3\phi) \right] \\
 & + \sum_{i < j}^{atoms} \left(\frac{A_{ij}}{R_{ij}^{12}} - \frac{B_{ij}}{R_{ij}^6} \right) + \sum_{i < j}^{atoms} \frac{q_i q_j}{4\pi\epsilon_0 R_{ij}}
 \end{aligned}
 \tag{7.1}$$

In Eq. 7.1, K_r is the bond constant with the equilibrium bond distance r_{eq} , K_θ is the angle constant with the equilibrium angle θ_{eq} , V_1, V_2 , and V_3 are the co-efficients of the Fourier series and ϕ is the dihedral angle. R_{ij} is the distance between i and j atom with partial charges q_i and q_j , respectively. The short-range van der Waals interaction was represented by the Lennard-Jones (LJ) potential, and the long-range electrostatic potential was treated via particle mesh Ewald summation technique (PME).⁴⁷ The interaction parameters of *BMIM*⁺ and *PF*₆⁻ were taken from the existing literature.⁴⁸⁻⁴⁹ Following earlier works,⁵⁰ the potential parameters including the total

charge of cation and anion as well as some of the Lennard-Jones parameters were modified. These refinements were done previously to accurately obtain the structure and dynamical properties.⁵⁰ All the force field parameters of $BMIM^+$ and PF_6^- are summarized in Appendix F (Table F1-Table F5).

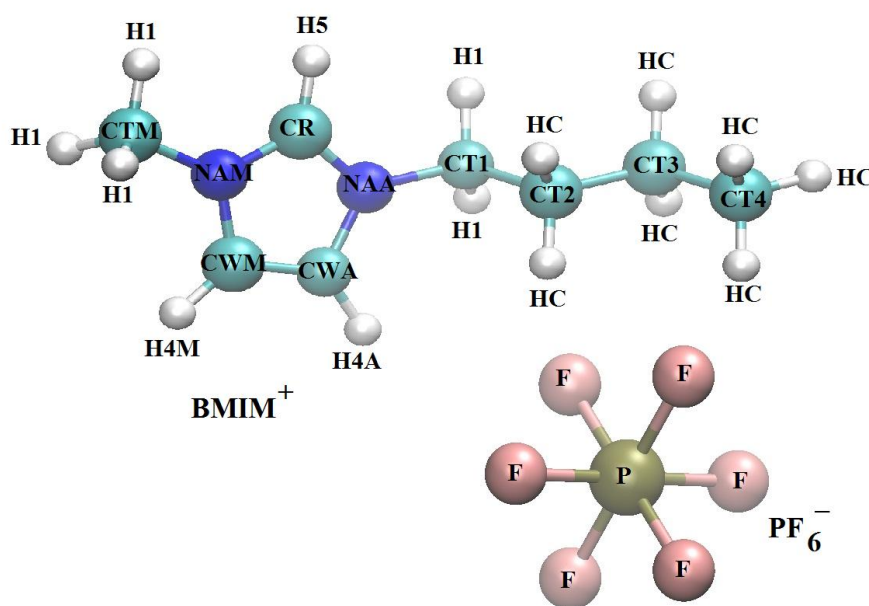


Figure 7.1: Chemical structure of $BMIM^+$ and PF_6^- with force field atom types. Representations shown here are used while discussing various simulated properties.

The geometry of an isolated cation, $[BMIM]^+$ and anion $[PF_6]^-$ were optimized via ab-initio calculations using the HF/6-31 + G(d) basis set with initial charges of +0.8 and -0.8, respectively. The initial configuration was built using Packmol⁵¹ and minimized via steepest decent algorithm in GROMACS. All the bonds were kept constrained by applying the Lincs⁵² algorithm of order 8. First the system was heated at 450 K at 1 atm pressure under NPT ensemble using the velocity rescaling thermostat⁵³ and Berendsen barostat,⁵⁴ with coupling constants of 0.5 ps and 2.0 ps, respectively for 100 ps. Then the temperature was brought down to 298 K via a step-down process (using a 50 K step) with each step continuing for 100 ps in NPT ensemble. This was done to ensure proper equilibration. Subsequently, the system was

equilibrated for 1 ns in NPT followed by further equilibration in NVT for 2 ns using the velocity rescale thermostat.⁵³ The density of the final system was found to be 1.40 gm/cc which was fairly close to the experimental value,⁵⁵ 1.37 gm/cc. Finally, the production run was carried for 10 ns in NVT ensemble. The cut-off radius was set to 35 Å. Periodic boundary conditions were employed in all the three directions, and the equations of motion were integrated using a time step of 2.0 fs employing the leap-frog algorithm.⁵⁶ The trajectories were saved every 0.1 ps for analyzing the jump dynamics. A second simulation run was carried for 100 ns with 128 pairs of ions at 298 K. This separate run was conducted for analyzing the orientational correlation and H-bond dynamics as 10 ns production run was not sufficient for the full decay. The second system was prepared following the exact protocol of the earlier one.

7.3. Analysis Protocol

We first present the evidence of angular jumps in the reorientational dynamics of $BMIM^+$ cation and PF_6^- anion. Figure 7.2 shows the time series of the cosine of the angle made by a chosen vector of each ion with the Z axis of the simulation box. For $BMIM^+$, the selected vector connects CTM of methyl group and CT1 of the butyl group and for PF_6^- , we have randomly selected one of the P-F vectors. The representative pictures are shown in Figure 7.3. It is observed that both the ions execute diffusive Brownian motion with large amplitude jumps in between, as observed previously for molten acetamide⁴⁴ and acetamide in presence of various electrolytes.⁴⁵ Interestingly, the fluctuation of the cosine of the angle is much wider (spanning from -1.0 to +1.0 for anion and from -0.30 to +1.0 for cation) and frequent for PF_6^- as compared to $BMIM^+$ indicating much restricted angular jumps for cation. This qualitative difference in reorientational jump is probably originating from the large differences in size and shape. The result of this difference would be reflected later when we present and discuss various other properties.

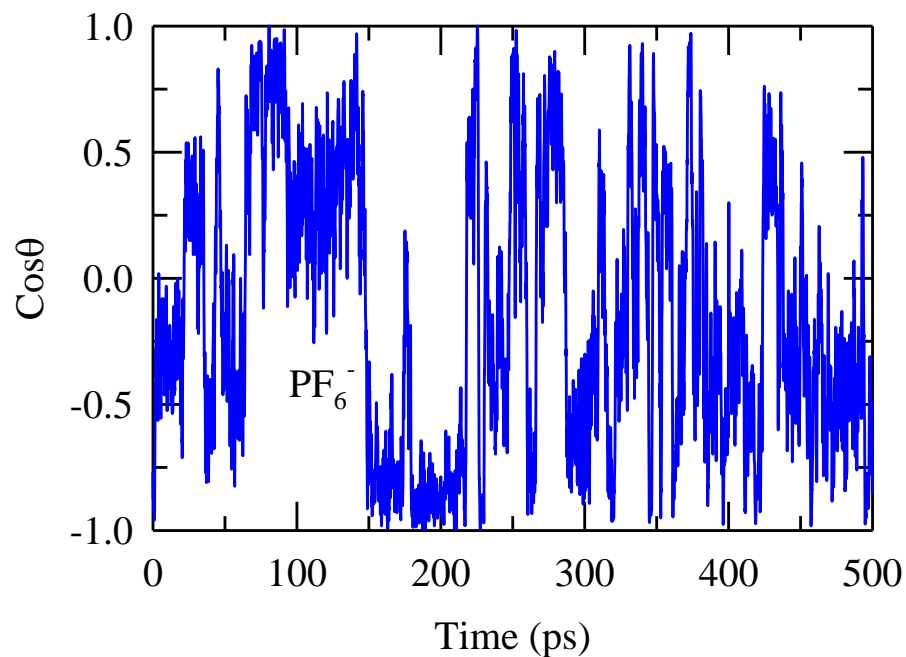
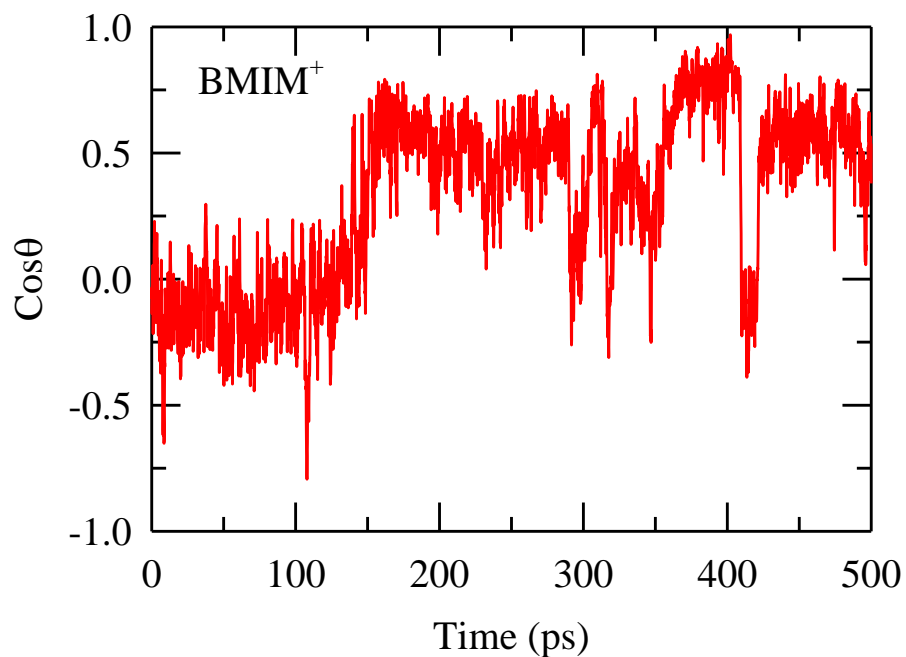
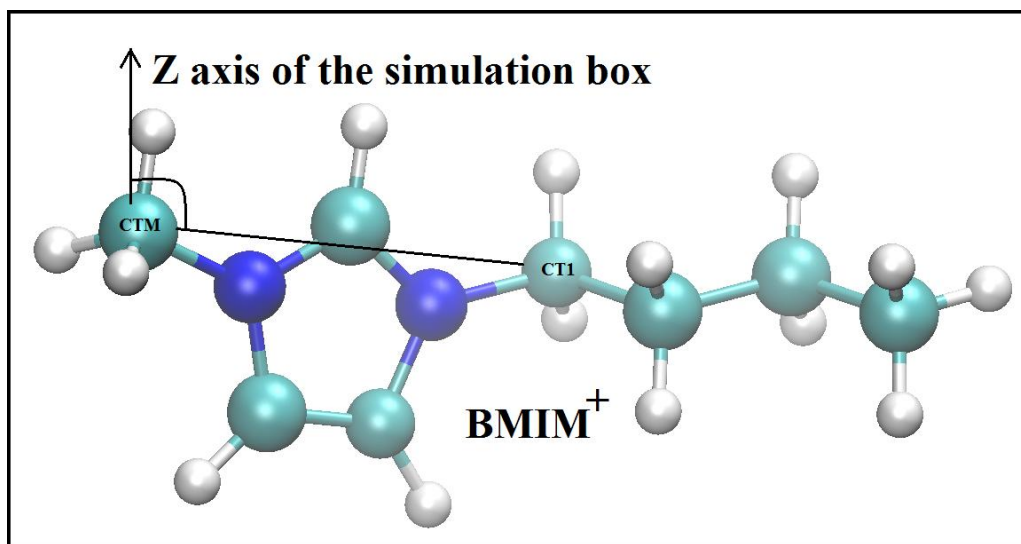


Figure 7.2: Plot shows the time series of the cosine of the angle which the selected vector of a randomly chosen BMIM^+ (shown in the upper panel) and PF_6^- (shown in the lower panel) makes with the Z axis of the simulation box. The reorientational dynamics exhibits diffusive reorientation as well as large amplitude jumps.



Z axis of simulation box

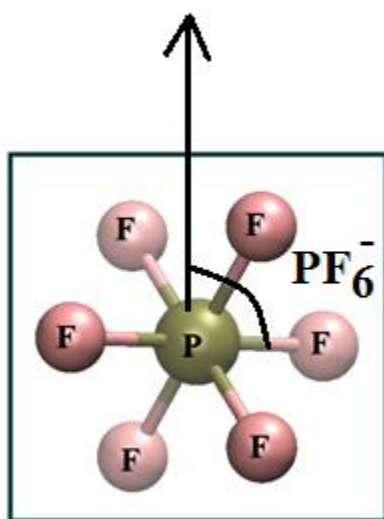


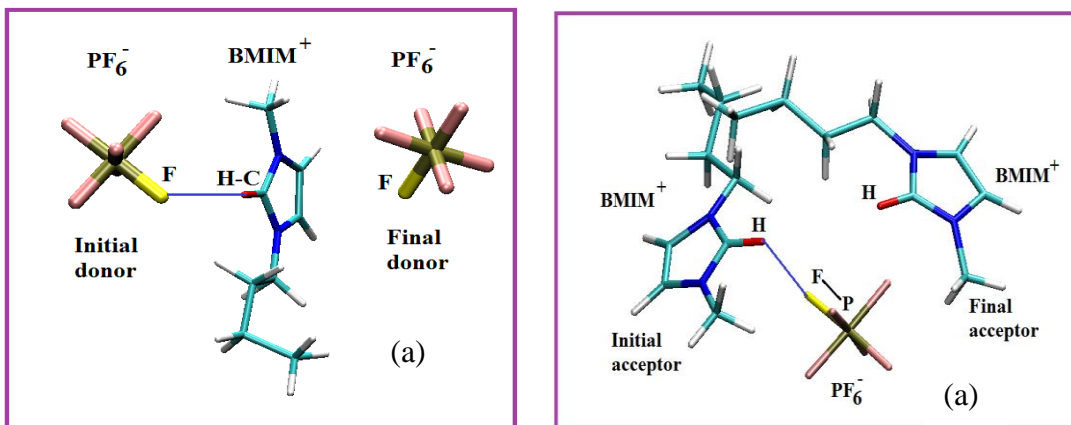
Figure 7.3: The angles formed by the chosen vector for both the ions with the Z axis of the simulation box are shown here. For $BMIM^+$, we have selected the vector that joins CTM and CT1. For PF_6^- , we have chosen one of the P-F vectors.

The analysis mechanism is similar to what we have done previously for molten acetamide⁴⁴ and acetamide in presence of various electrolytes.⁴⁵ Since the orientational jump involves an exchange of H-bond partners, we have to select the H-bonded pairs first. H-bonds can be defined by various ways based on geometric criteria, energy consideration or orbital occupancy.⁵⁷ Here

we have chosen the widely accepted geometric criteria which depends on a distance (R) and an angle (deg). $BMIM^+$ cation contains 15 hydrogen (H) atoms and it is very difficult to monitor the jump dynamics for each of these atoms. However the electrostatic potential map has shown that the H atoms attached with the imidazolium ring (H5, H4A and H4M) of the $BMIM^+$ cation are potential hydrogen donors.³² Hence in this study, we have restricted the jump dynamics concerning to only those 3 H atoms. Specifically, H5 atom is considered to be H-bonded with one of the fluorine (F) atom of PF_6^- if (i) the distance between CR and F atom, R_{CR-F} , is less than a cut-off distance, $R_{cut-off}^1$, (ii) the distance joining H5 and this F atom, R_{H5-F} is less than some specified distance, $R_{cut-off}^2$ and (iii) the angle between the vectors joining CR and H5 atom and the vector joining CR atom of the cation and the selected F atom of the anion, $\theta_{F-CR-H5}$, is less than some cut-off angle, θ_{cut} . The two cut-off distances, $R_{cut-off}^1$ and $R_{cut-off}^2$ have been selected at 4.2 Å and 3.7 Å based on the first minima of the respective radial distribution function, shown in Appendix F (Figure F1 and Figure F2). The cut-off angle, θ_{cut} , has been chosen at 30° after monitoring the corresponding angular distribution function, shown in Appendix F (Figure F3). Following the similar protocol, we have defined the H-bond for H4A and H4M atoms with F atom of the anion. For PF_6^- , we have randomly chosen one of the F atoms out of the available six F atoms which is H-bonded to H5/H4A/H4M atom of the imidazolium ring. Specifically, the selected F atom is considered to be H-bonded to H5 if (i) the distance between H5 and F, R_{H5-F} is less than a cut-off distance, $R_{cut-off}^1$, (ii) the distance between P and H5 is also less than some specified distance, $R_{cut-off}^2$ and (iii) the angle formed by the vector joining P and the selected F atom and the vector joining P and H5 atom, θ_{F-P-H5} is less than a cut-off angle, θ_{cut} . Once again, the cut-off distance is selected at 3.7 Å for $R_{cut-off}^1$ and 5.6 Å for $R_{cut-off}^2$ based on the first minima of the corresponding radial distribution function, shown in Appendix F (Figure F2 and Figure F4). The angle cut-off, θ_{cut} is chosen at 130° after monitoring the angular distribution function provided in Appendix F (Figure F5). The large angular cut-off has been used previously also for simulating H-bond dynamics of ILs.³² Following the same protocol, we have defined the H-bond between the selected F atom and H4A/H4M atom. Thus

we have separately analyzed the jump dynamics for the possible three cases for both cation and anion.

Based on the above definition of H-bond, we have selected pairs of ions which are H-bonded. Now we have devised a unique scheme for the analysis purpose. First we assign a flag value to all the chosen atoms of each ions, like $flag_BMIM_H5(i,t)$ which gives the information whether the H5 atom of $BMIM^+$ with index number i is H-bonded to any of the F atom of PF_6^- at time instant t or not. If it is H-bonded then the value of $flag_BMIM_H5(i,t)$ gives the index of the PF_6^- ion which is H-bonded to the i -th $BMIM^+$ at time instant t . If H5 does not take part in H-bonding at time instant t , then the value of $flag_BMIM_H5(i,t)$ become zero. Similarly, we can assign $flag_BMIM_H4A(i,t)$ and $flag_BMIM_H4M(i,t)$ for monitoring H-bonds with H4A and H4M, respectively. Also, in the same way we can calculate flag values for PF_6^- which are denoted as $flag_PF_6_H5(i,t)$, $flag_PF_6_H4A(i,t)$ and $flag_PF_6_H4M(i,t)$ involving F atom which is H-bonded to H5/H4A/H4M. Figure 7.4 shows a typical microscopic process for the reorientation of $BMIM^+$ (shown in the left panels) and PF_6^- (shown in right hand panels) which has been extracted from the simulated trajectory. The rotating molecule, $BMIM^+$ is initially H-bonded to PF_6^- (represented as initial donor) via H5. Then this H-bond breaks and the rotating $BMIM^+$ undergoes an angular jump and form a new H-bond with another PF_6^- (represented as final donor). Similar mechanism has also been observed for PF_6^- .



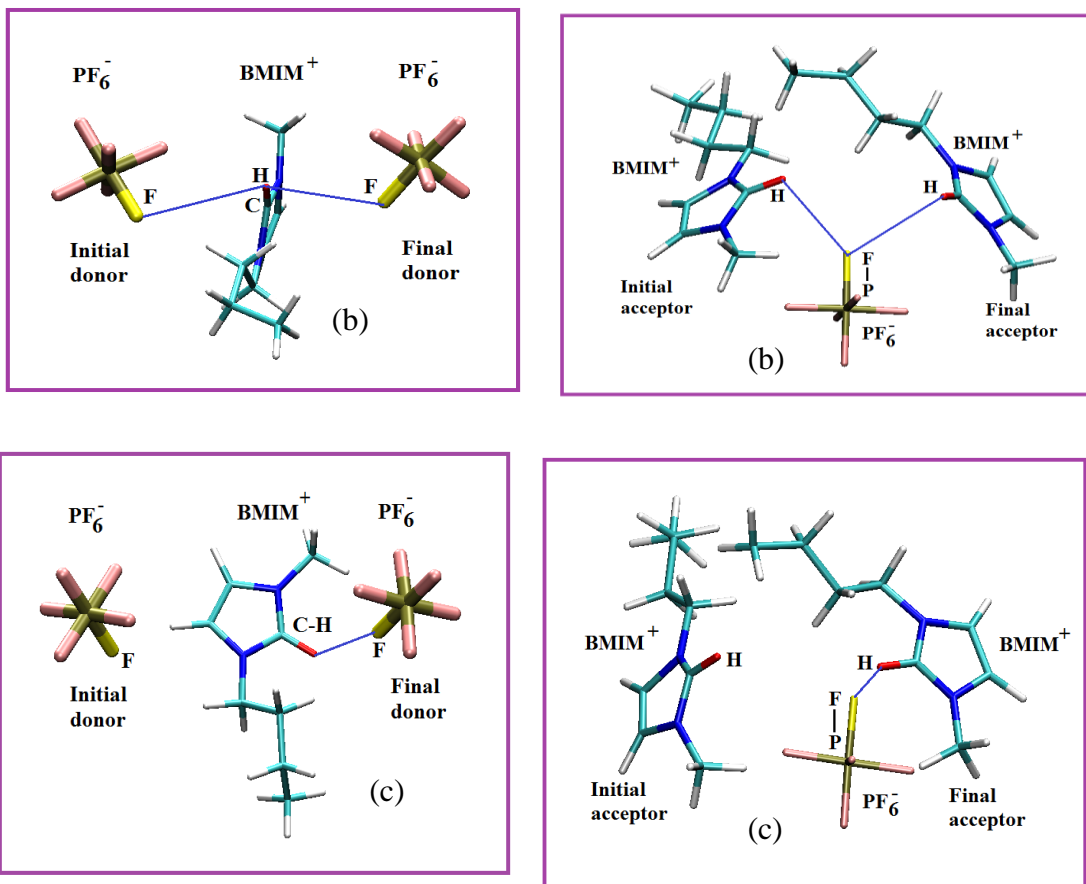


Figure 7.4: Microscopic jump process extracted from the trajectory. The left panels show $BMIM^+$ undergoing a large amplitude angular jump resulting in a change of the identity of its H-bond partners. The right panels show the large amplitude jump of PF_6^- ion.

The process can be also expressed in terms of flag variable as shown in Figure 7.5. Initially for $BMIM^+$, $flag_BMIM_H5(i,t)$ has a nonzero value A which means that the rotating $BMIM^+$ ion is H-bonded via H5 to PF_6^- with index number A. Now because of some thermal fluctuation or previously occurred jumps, this H-bond breaks and the rotating $BMIM^+$ ion with index number i performs an angular jump to find its final partner, another PF_6^- ion with index number B. It should be noted that initially formed H-bond may break temporarily and then reform. But it does not involve any change in H-bonding partner and hence is not associated with large amplitude angular jump. Thus we have not considered those events for the analysis. We are

only interested in the microscopic processes that involve a change in H-bond partner. It is also to be noted that our analysis procedure allows the change of the identity of the partners for $BMIM^+$ but not for PF_6^- during microscopic jump. For example, during the angular jump of $BMIM^+$, both the initial and the final donor can be any one of the six available F atoms of PF_6^- . However, for the angular jump of PF_6^- , if the initial acceptor is H5 atom, then the final acceptor is also H5 atom, that is, the atomic identity of the acceptor is retained.

$flag_BMIM_H5(i,t)$

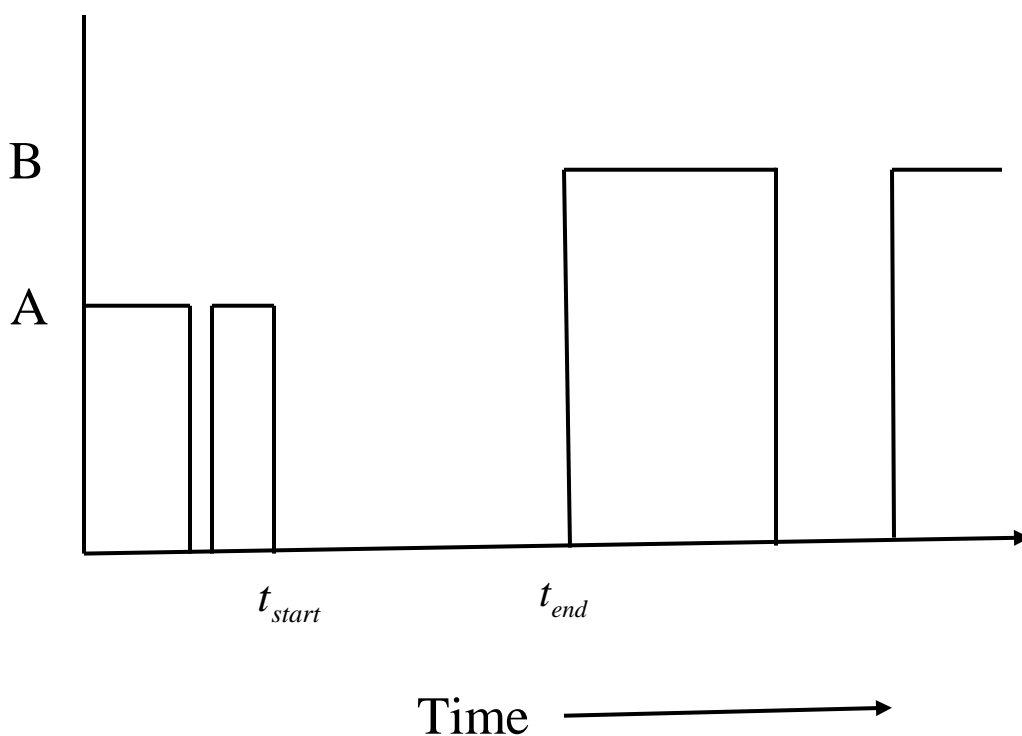


Figure 7.5: Schematic representation of the time series of a typical flag variable associated with a randomly chosen $BMIM^+$ ion. It shows a H-bond switching process which is associated with large amplitude angular jump of the chosen ion. The starting times (t_{start}) and ending times (t_{end}) are also depicted.

Once we know the flag values for both $BMIM^+$ and PF_6^- for all the time frames, we can identify, the starting time (t_{start}) and ending time (t_{end}) for each microscopic process as shown

schematically in Figure 7.5. The starting time (t_{start}) is defined as the last instant when $BMIM^+$ with index number i is H-bonded to its initial donor, PF_6^- with index number A. Similarly, the ending time (t_{end}) is the first instant when $BMIM^+$ with index number i is H-bonded to its final donor, PF_6^- with index number B. Thus from the analysis of the time series of flag values, we can identify all the initial and final donors (PF_6^-), for H-bond switching events of $BMIM^+$ ions via H5 atom and also the starting time (t_{start}) and the ending time (t_{end}) for all microscopic processes. Similarly, from the analysis of the other flag values of $BMIM^+$ ion, $flag_BMIM_H4A(i,t)$ and $flag_BMIM_H4M(i,t)$, we can identify the initial and final donors, starting and ending time of all the microscopic processes that involve the exchange of H4A and H4M atom, respectively. In a similar way, we can also find out initial and final acceptors, and also the starting and ending time for PF_6^- ion involving H5, H4A and H4M atoms from the analysis of $flag_PF_6_H5(i,t)$, $flag_PF_6_H4A(i,t)$ and $flag_PF_6_H4M(i,t)$.

After identifying the starting and ending time of all the successful jumps, we can easily calculate jump time distributions and waiting time distributions for both the ions involving all the possible cases. Suppose we are considering the j -th jump for the i -th ion. Now the difference between $t_{end}(i, j)$ and $t_{start}(i, j)$ will provide the microscopic jump time. On the other hand, microscopic waiting time is the difference between $t_{start}(i, j+1)$ and $t_{end}(i, j)$. It is to be noted that during waiting time, the rotating ion remains H-bonded with its partner. On the contrary, during jump time the initially formed H-bond breaks, the rotating ion performs an angular jump and finally forms a new H-bond with another new partner, thus resulting to an exchange of H-bond partners. We have taken this approach to calculate jump and waiting time distribution for $BMIM^+$. However, we have made certain modifications for calculating the jump and waiting time distributions for PF_6^- . First, we have calculated the H-bond between all the six F atoms of PF_6^- with H5 atom of $BMIM^+$ and have constructed six different series of flag values. Now following the protocol for $BMIM^+$, we have calculated the jump and waiting times for all the time frames for these six different sets of flags. Then we have superimposed these six sets of

jump times and waiting times on each other to finally obtain the jump time and waiting time for the molecular PF_6^- . The superimposing procedure is very simple. We have assigned the values of flag variables as zero in between $t_{start}(i, j)$ and $t_{end}(i, j)$ and values as one for the rest of timeframes for all six sets of flags to construct a final flag series. Thus the flag value zero of this final flag series signifies the flight mode of any of the six F atoms of PF_6^- . Similarly flag value one suggest the waiting mode of one of the F atoms. Now from this series of zero and one flag values for all time frames, one can calculate the jump and waiting time distributions. Following the similar protocol, we have calculated jump and waiting time distributions corresponding to H4A and H4M atoms. In this way one can construct the jump and waiting time distributions of molecular PF_6^- from the jump and waiting times of all the six F atoms.

After the identification of starting time and ending time of all the microscopic processes, we can calculate the transition state of each jump via monitoring the translational and orientational coordinates. Transition state is defined as the time instant, between t_{start} and t_{end} , when the distance between the initial partner and rotating molecule is equal to the distance between the final partner and the rotating molecule. The representative picture is shown in Figure 7.6 where the H5 atom of $BMIM^+$ ion is initially H-bonded to F atom of initial donor (F_A) and after the angular jump it again forms a H-bond with another F atom of final donor (F_B). In order to calculate the transition state we first calculate the difference between R_{CR-FA} and R_{CR-FB} within the time frame t_{start} and t_{end} , and identify the time instant when this difference is zero or minimum within the prescribed numerical precision. The angle formed by F_A of the initial H-bond donor, CR of the rotating molecule and F_B of the final donor at the transition state is the transition angle. In the same way, we can calculate the transition state involving H4A and H4M atom of the rotating $BMIM^+$ ion. For orientations of PF_6^- involving H5 atom, we have monitored the difference of the distances $R_{P-H5(I)}$ and $R_{P-H5(F)}$. Here H5(I) and H5(F) are initial and final acceptors, respectively. The transition angle is formed by P-H5(I) and P-H5(F) vectors at the

transition state. Similarly, we have calculated transition angles of PF_6^- involving H4A and H4M atoms, respectively.

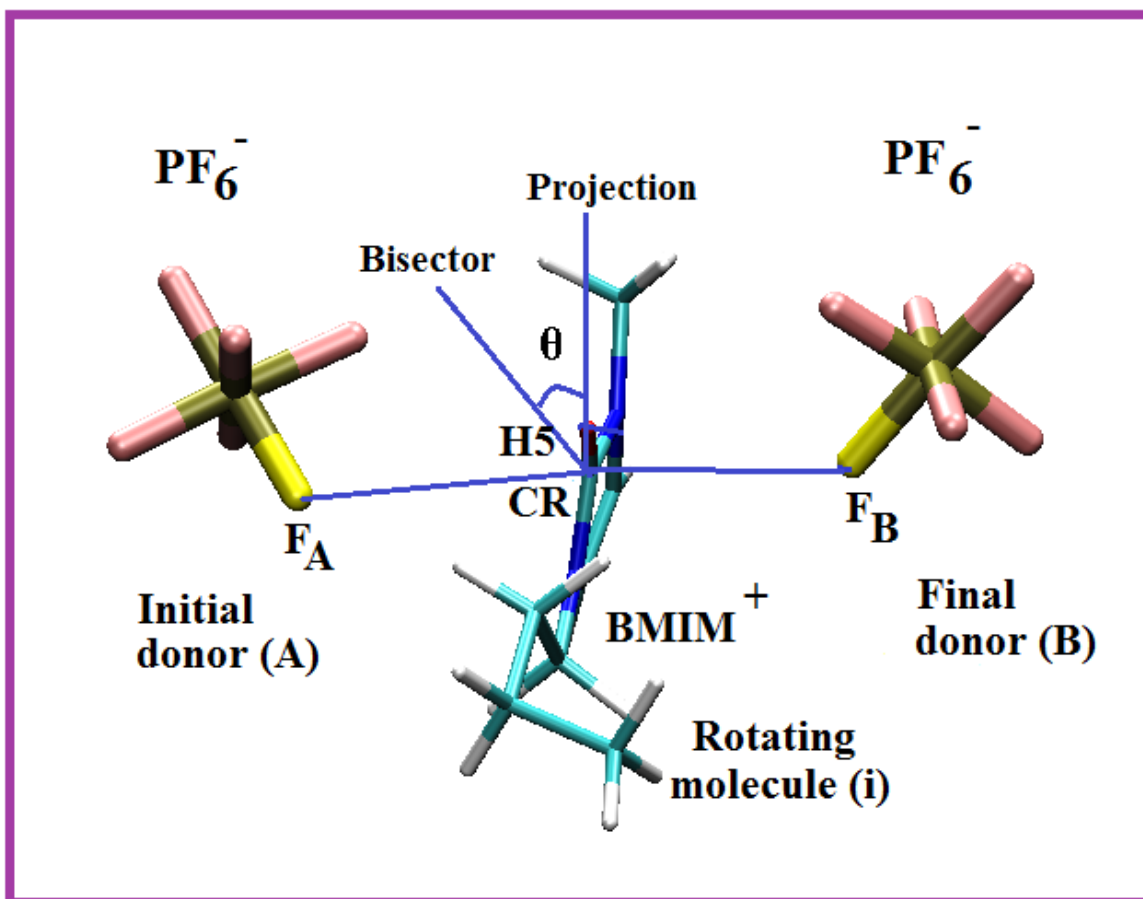


Figure 7.6: Distance and angles that describes a jump process of $BMIM^+$ (molecule i), its initial donor PF_6^- (molecule A) and final donor PF_6^- (molecule B). The distance between the atom CR of $BMIM^+$ and F_A of molecule A, and F_B of molecule B are denoted as R_{CR-FA} and R_{CR-FB} , respectively. The angle between the projection of the CR-H5 vector on the plane $F_A - CR - F_B$ and the bisector of the plane $F_A - CR - F_B$ is also shown.

Once we identify the transition state, we can easily calculate the time evolution of the average trajectory involving H5, H4A, H4M atom of both $BMIM^+$ and PF_6^- . For calculating the average

trajectory involving H5 atom of $BMIM^+$ as the rotating ion, F_A as the initial donor and F_B as the final donor, we calculate R_{CR-FA} , R_{CR-FB} and the angle formed by the projection of the CR-H5 vector on the $F_A - CR - F_B$ plane and the bisector of the angle $F_A - CR - F_B$. Following the same protocol we calculate the average trajectory involving H4A and H4M atom of $BMIM^+$. For calculating the average trajectory of PF_6^- involving H5 atom, we have calculated the distances $R_{P-H5(I)}$ and $R_{P-H5(F)}$, and the angle formed by the projection of the selected P-F vector on the $H5(I) - P - H5(F)$ plane and the bisector of the angle $H5(I) - P - H5(F)$. Likewise, we calculate average trajectories of PF_6^- for H4A and H4M atoms. We have also applied the idea of “coherent averaging” during the calculation of average trajectory. During the “coherent averaging”, the transition state of each microscopic orientational jump is chosen as the origin of time at the centre of the average trajectory with jump starting at -10 ps and ending at +10 ps. In this way, we superimpose all the transition states for all the microscopic trajectories chosen. This will provide us the generic picture of the orientational jump from microscopic trajectories without the loss of any important feature due to inherent thermal fluctuation. The duration of 20 ps time window has been selected after monitoring the distances and angles are reaching their saturation values at the beginning and end of each average trajectory.

7.4. Results and Discussion

Figure 7.7 and Figure 7.8 show the time evolution of average trajectories for successful orientational jumps for $BMIM^+$ and PF_6^- , respectively. The upper panels of Figure 7.7 show the time evolution of the change in distances, defined earlier for reorientation jumps of $BMIM^+$ and the lower panels show the same for the angles. The time evolution of average trajectories corresponding to the successful jump of PF_6^- via H5, H4A and H4M atoms are presented in Figure 7.8. All the trajectories presented here exhibit a symmetric transition state which can be explained in terms of the orientational jump of $BMIM^+$ via H5. At the transition state, the distance between the initial donor and the rotating molecule (R_{CR-FA}) equals the distance between

final donor and the rotating molecule (R_{CR-FB}). Also, the projection of CR-H5 vector on $F_A - CR - F_B$ plane and the bisector of the angle $F_A - CR - F_B$ coincide. This reflects the translational-rotational coupling of the inherent dynamics that we have previously observed for molten acetamide⁴⁴ and acetamide in presence of various electrolytes.⁴⁵

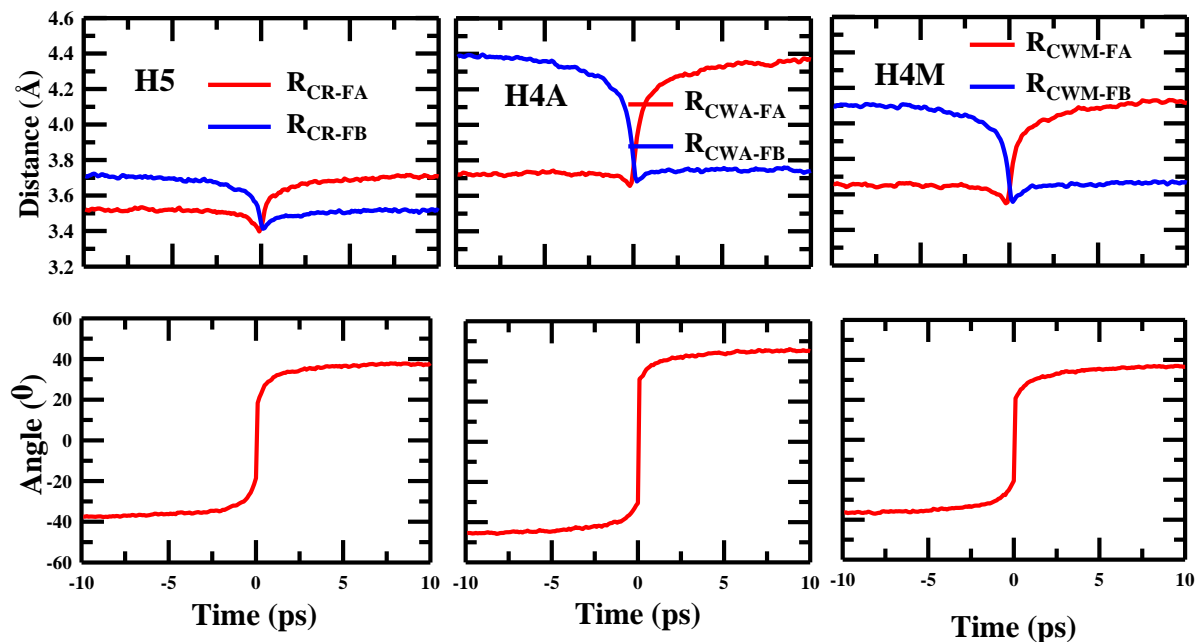


Figure 7.7: Average trajectory in terms of geometrical quantities described in **Figure 7.6**. Columns starting from left show the simulation results for H5, H4A and H4M atom, respectively. The upper panel shows the time evolution of change in distance between the rotating $BMIM^+$ and the initial H-bond donor (red curve) and the final H-bond donor (blue curve). The lower panel shows the time evolution of the angle defined earlier in **Figure 7.6**.

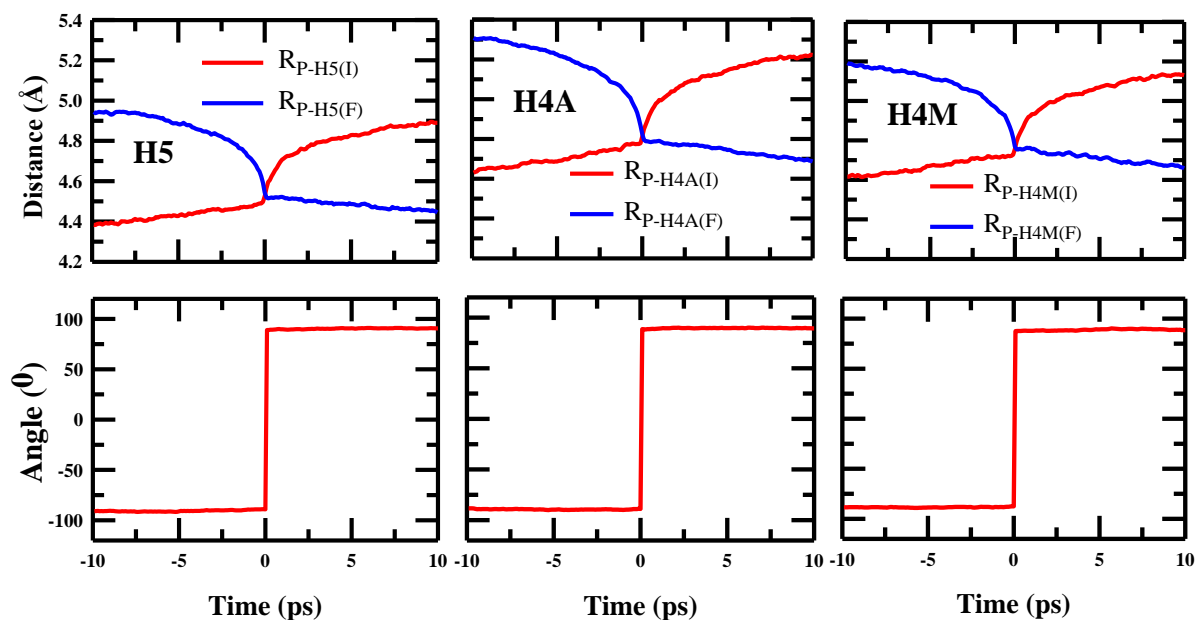


Figure 7.8: Average trajectories calculated for the large amplitude angular jump of a chosen PF_6^- ion.

In order to understand the change in distance and angle during a successful orientational jump, we have calculated mean translational and rotational displacement associated with all the trajectories. Table 7.1 shows both of these displacements for $BMIM^+$ and PF_6^- for the orientational jumps occurring via H5, H4A and H4M atoms. It appears from the table that the change in distance and angle is prominent for both $BMIM^+$ and PF_6^- . Additionally, the change in distance is slightly higher (except H4A) for PF_6^- as compared to $BMIM^+$. However, the change in angle is ~ 2 - 2.5 times higher for PF_6^- with average change in angle close to $\sim 180^\circ$. The smaller extent of translational and rotational displacement for $BMIM^+$ can be related to its bigger size. Now we look at the effects of orientational jump on individual atoms. For both $BMIM^+$ and PF_6^- , maximum translational displacement takes place for H4A (0.7 \AA) followed by H4M and H5. Interestingly, a combination of FTIR and DFT calculations³⁴ on the structure and ion-pair formation of ionic liquids suggest that higher acidity of H5 leads to the strongest H-bond

formation as compared to H4A and H4M atoms. This stronger interaction probably leads to the minimum displacement as we have seen before for orientational jumps of acetamide/electrolyte DESs.⁴⁵

Table 7.1 Change in radial distances and angles for various atom types of both cation and anion during orientation jumps in (BMIM+PF₆) IL.

Ion	Atom Type	Distance ($\Delta R / \text{\AA}$)	Angle (Deg)
<i>BMIM</i> ⁺	H5	0.2	74
	H4A	0.7	90
	H4M	0.4	72
<i>PF</i> ₆ ⁻	H5	0.5	180
	H4A	0.7	180
	H4M	0.6	180

Figure 7.9 and Figure 7.10 gives the simulated jump and waiting time distributions for *BMIM*⁺ and *PF*₆⁻ ions. We have already defined the microscopic jump and waiting time based on the time series of flag values. As mentioned before, we have explicitly calculated both the distributions for *BMIM*⁺ for the orientational jumps via H5, H4A and H4M atoms. However, for *PF*₆⁻ we have adopted the molecular approach which is based on the superimposition of all the six different flag values. The three panel plots of Figure 7.9 and Figure 7.10 show both the distributions for H5, H4A and H4M atom, respectively. The long time distributions are fitted to a power-law distribution of the type, $P(t) \propto A(t/\tau)^{-\beta}$. All the parameters

(τ_{jump} , β_{jump} , $\tau_{waiting}$ and $\beta_{waiting}$) are summarized in the inset of the figures. Such power-law dependence of long-time dynamics reflects the presence of heterogeneous dynamics that we have earlier discovered for acetamide/electrolyte DESs.⁴⁵

Jump and waiting time distributions calculated for $BMIM^+$ and PF_6^- are strikingly different. For $BMIM^+$, τ_{jump} values are in general a factor of 4-5 less than the corresponding $\tau_{waiting}$ value with β_{jump} values slightly greater than the respective $\beta_{waiting}$ values. This is the general case where the $\tau_{waiting}$ values are found to be greater than the corresponding τ_{jump} values and has been observed regularly for the orientational dynamics of liquid water,⁴³ water in presence of anions,⁵⁷ molten acetamide,⁴⁴ acetamide in presence of various electrolytes etc.¹⁹ However, we have observed the opposite trend for PF_6^- . Here, τ_{jump} values are found to be a factor of 2.0-2.5 greater than the corresponding $\tau_{waiting}$ values with $\beta_{waiting}$ greater than β_{jump} except in presence of H5. It can be rationalized by considering the number of H-bonds formed by H5, H4A and H4M atoms respectively. Earlier molecular dynamic simulation study³² has shown that the numbers of H-bonds formed by H5, H4A and H4M (with the available 6 F atoms) are 3.4, 2.9, and 2.6, respectively. This means that approximately half of the F atoms are that are placed inside the first coordination shell remain H-bonded with H5, H4A and H4M. This strong H-bond interaction not only increases $\tau_{waiting}$ for PF_6^- as compared to $BMIM^+$ ($\tau_{waiting}$ for PF_6^- is roughly a factor of ~ 2 greater than $\tau_{waiting}$ of $BMIM^+$) but also increases the search time for appropriate final H-bond partner irrespective of the atom identity. In fact, it appears that the consistent persisting of three H-bonds increases the search time so much that the jump time ultimately exceeds the waiting time. Additionally, we also observe that τ_{jump} , $\tau_{waiting}$, β_{jump} and $\beta_{waiting}$ (represented as τ_j , τ_w , β_j and β_w in Figure 7.9 and Figure 7.10) values does not depend crucially on atom identity for both $BMIM^+$ and PF_6^- .

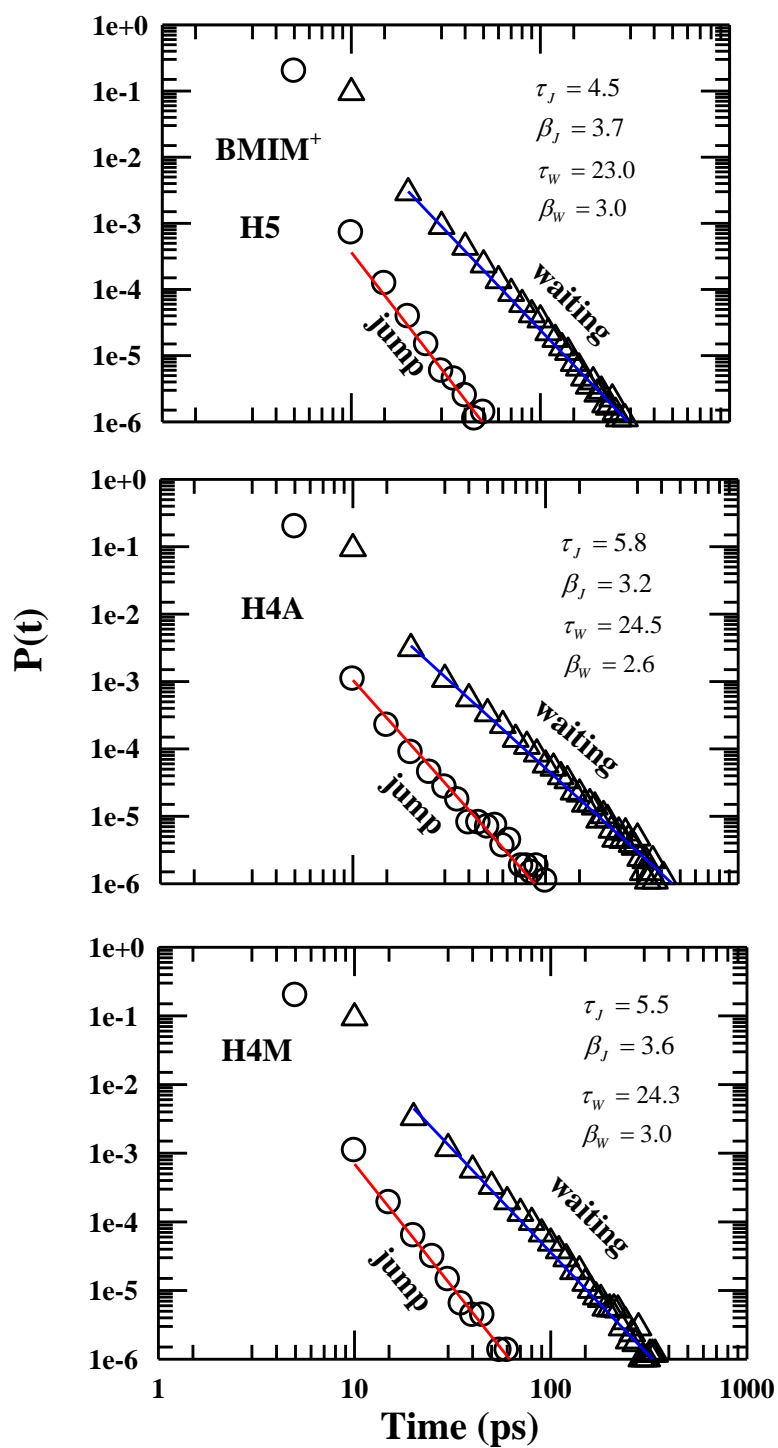


Figure 7.9: Jump and waiting time distribution for $BMIM^+$ for various atom types. Fit parameters that describe the power law dependence of the long time tails of the distributions are provided inside each panel.

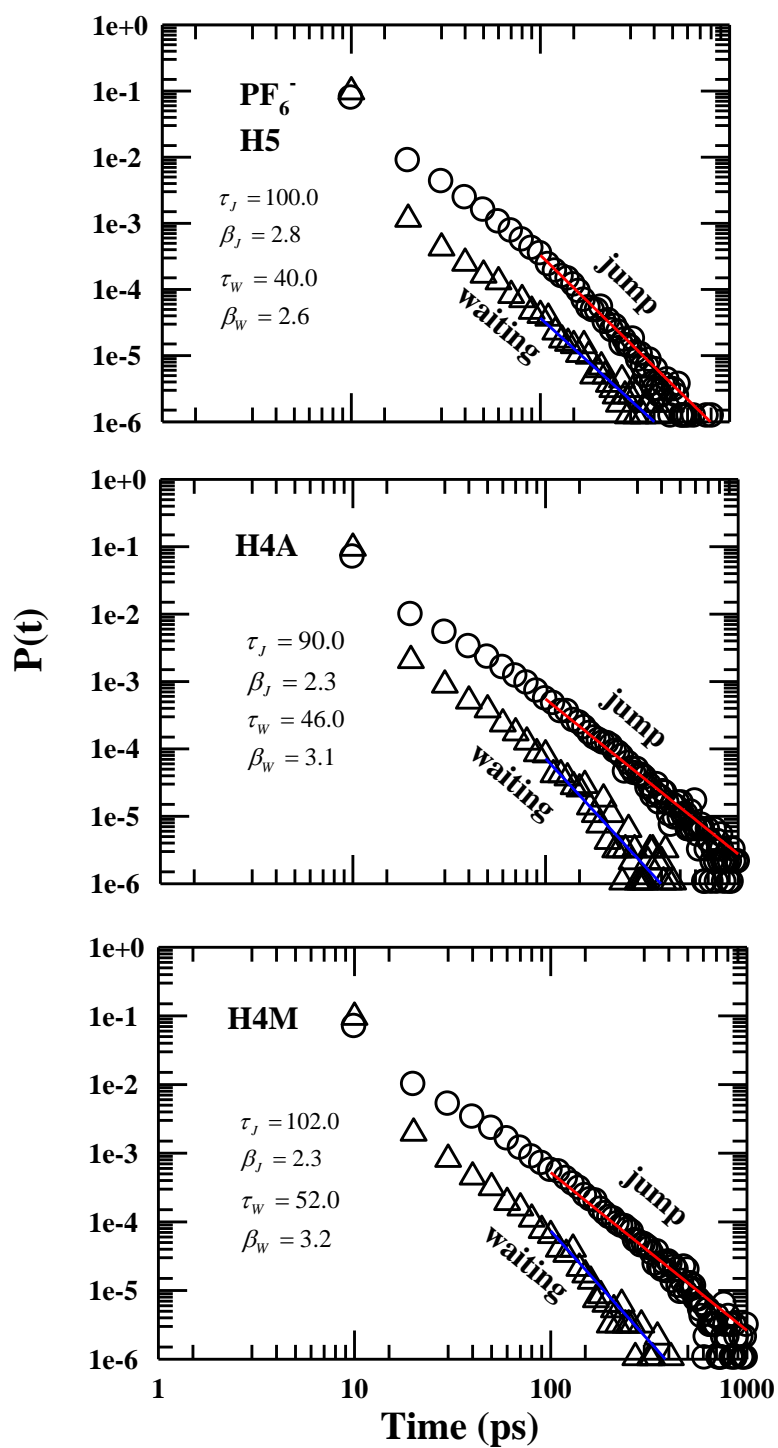


Figure 7.10: Jump and waiting time distribution for PF_6^- for various atom types.

We have also estimated the mean and the root mean squared deviation (RMSD) times of jump and waiting time distributions. This can be especially helpful to understand the intrinsic timescale associated with orientational jumps. The mean time has been calculated numerically from the relation, $\langle \tau \rangle = \int_0^{\infty} d\tau \tau P(\tau)$. Similarly the RMSD of these distributions is obtained from the relation, $\sigma = \left[\int_0^{\infty} d\tau (\tau - \langle \tau \rangle)^2 P(\tau) \right]^{1/2}$. Table 7.2 summarizes the mean and RMSD values of three different atoms for both $BMIM^+$ and PF_6^- . We observe that $\langle \tau_{\text{waiting}} \rangle$ values are very similar for both the ions (~ 1 ps) and do not depend on atom type though σ_{waiting} differs depending on atom type identity. We also observe that $\langle \tau_{\text{jump}} \rangle$ values are similar for various types of atoms for $BMIM^+$ and slightly less than the corresponding $\langle \tau_{\text{waiting}} \rangle$ values. However, for PF_6^- , $\langle \tau_{\text{jump}} \rangle$ values are found to be ~ 1.6 - 2.0 times higher than the corresponding $\langle \tau_{\text{waiting}} \rangle$ values following the earlier trend. Also, one can find that $\langle \tau_{\text{jump}} \rangle$ values are in general ~ 1.8 - 2.5 times higher for PF_6^- than the corresponding $\langle \tau_{\text{jump}} \rangle$ values for $BMIM^+$. Similarly, σ_{jump} values are found to be ~ 7 - 9 times higher for PF_6^- than $BMIM^+$. All these observations also reflect the inherent complexity associated with the reorientational dynamics of such a complex liquid.

Table 7.2: Mean and root mean square deviation times calculated from waiting and jump time distributions for various atom types for both the ions.

Ion	Atom Type	Mean waiting time ($\langle \tau_{waiting} \rangle$) (ps)	Mean jump time ($\langle \tau_{jump} \rangle$) (ps)	Waiting time RMSD ($\sigma_{waiting}$) (ps)	Jump time RMSD (σ_{jump}) (ps)
$BMIM^+$	H5	1.1	1.0	4.0	1.8
	H4A	1.2	1.0	5.0	1.9
	H4M	1.2	1.0	4.5	1.8
PF_6^-	H5	1.1	1.8	4.4	10.0
	H4A	1.2	2.5	5.0	17.3
	H4M	1.1	2.5	4.4	16.9

Figure 7.11 shows the jump angle distributions for $BMIM^+$ and PF_6^- for various types of atoms calculated between t_{start} and t_{end} of the microscopic jump events. The upper panel shows the distributions for $BMIM^+$ and the lower panel shows the same for PF_6^- . It is observed that jump angle distributions for $BMIM^+$ does not depend on the atom type identity. Additionally, the distributions peak around 75° and show a long tail toward larger angles. For PF_6^- , we find that the distributions are broader and the peak is shifted towards larger angle. It is also noted that the distributions are similar for H4A and H4M atoms types with peak value around 95° . However, the distribution becomes slightly narrower for H5 atom and the peak value for jump angle distribution shift to a larger value around 105° . In order to understand what kind of local molecular structure gives rise to these peak values of the respective jump angle distributions, we have constructed two snapshots corresponding to the peak values. Figure 7.12 presents this two geometric snapshots for $BMIM^+$ and PF_6^- . It is observed that the present geometric positions are preferred in order to avail maximum number of H-bonds. For $BMIM^+$, in addition to the H-bonds formed by H5 atom, other H-bonds can be formed by the interactions with the methyl H and alkyl H atoms. Note the earlier simulation studies have already suggested that both methyl H

and alkyl H can form H bond with the anions.⁵⁸ For PF_6^- , it is found that the rotating molecule is somewhat sandwiched in between two $BMIM^+$ and thus give a higher peak value. It has already been suggested from the calculations of spatial distribution function that the most probable position to find an anion is below and above the imidazolium ring which maximizes the possibility of forming H-bonds.³² Thus our results corroborates well with the earlier results.

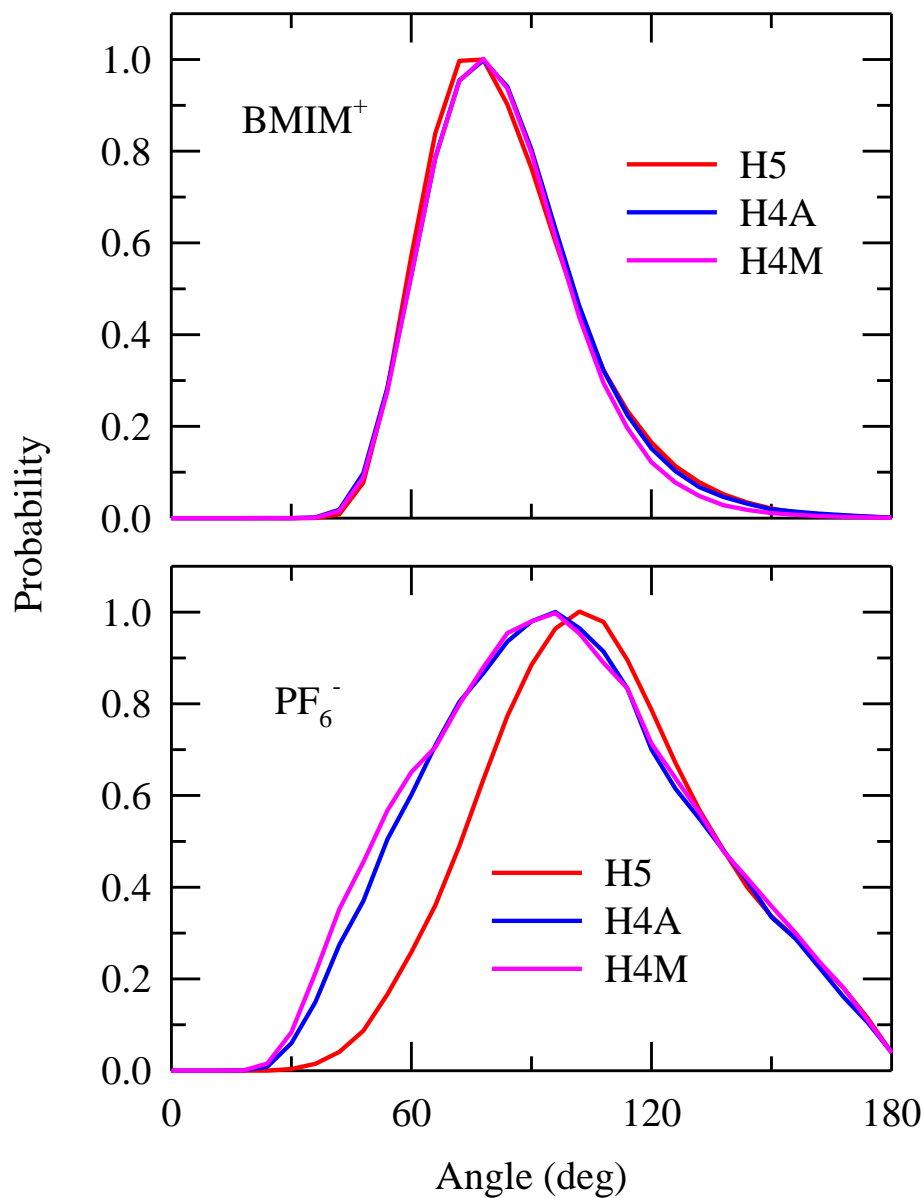
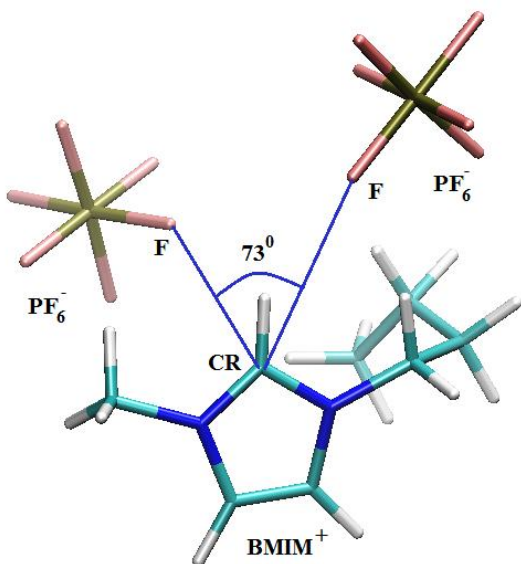
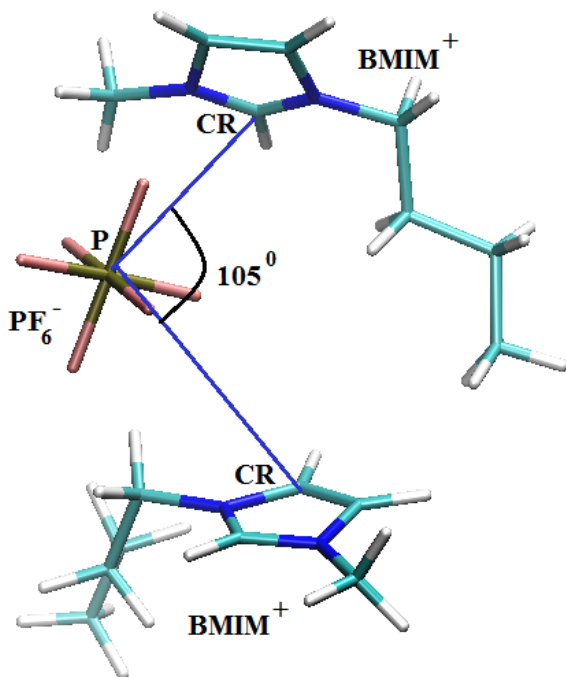


Figure 7.11: Jump angle distributions for $BMIM^+$ (shown in the upper panel) and PF_6^- (shown in the lower panel) for various atom types.



(a)



(b)

Figure 7.12: Transition state configurations corresponding to the peak of the jump angle distribution of $BMIM^+$ and PF_6^- .

It is already shown before that the orientational relaxations of both $BMIM^+$ and PF_6^- take place via large amplitude angular jumps. This should also be reflected from the calculation of orientational relaxation functions. Figure 7.13 demonstrates the orientational correlation function, $C_l(t)$ which can be defined as⁵⁹

$$C_l(t) = \langle P_l |u(0) \cdot u(t)| \rangle / \langle P_l |u(0) \cdot u(0)| \rangle \quad (7.2)$$

Where, P_l denotes the Legendre polynomial of rank l and u is a unit vector. For cation, the unit vector joins CTM and CT1, and for the anion the unit vector is represented by any one the P-F vector out of six available vectors. Following the Debye's model of diffusive reorientation in homogeneous environment,⁶⁰⁻⁶¹ one can fit the correlation function as monoexponential and the corresponding reorientation time τ_l can be expressed as

$$\tau_l = \frac{1}{l(l+1)D_R} \quad (7.3)$$

Where, D_R is the rotational diffusion co-efficient. For a Debye-like behavior, the ratio of $\tau_1 / \tau_2 \approx 3$.⁶⁰⁻⁶¹ However, the ratio can deviate significantly from a value of 3 due to the presence of large amplitude angular jumps⁶¹ as we have noticed previously for water,⁴³ molten acetamide⁴⁴ and acetamide in presence of various electrolytes.⁴⁵ The upper panel of Figure 7.13 shows the normalized $C_l(t)$ decays simulated for $l=1$ (first rank) and $l=2$ (second rank) for $BMIM^+$ and the bottom panel shows the same for PF_6^- . Multi-exponential fit parameters for the decays are summarized in Table 7.3. For $BMIM^+$, the ratio between the longest time constants, $(\tau_{l=1} / \tau_{l=2})^{longest}$ has been found to be ~ 1.5 . For PF_6^- , this ratio is ~ 0.6 . Such strong deviation from a value of three strongly suggests the presence of non-Debye reorientation mechanism which could be large amplitude angular jumps. The stronger deviation for the anion can be understood if we recall Figure 7.2 where we have observed stronger fluctuation for the anion. Also, the average relaxation time for the anion is much shorter than that for the cation. For

example, $\langle \tau_1 \rangle$ for the cation is 3800 ps while the same for the anion is 8.5 ps, a factor of ~ 450 less. This can be rationalized considering the much bigger size and asymmetry for the cation. Previous study of this IL has also found similar timescale for orientational correlation.³²

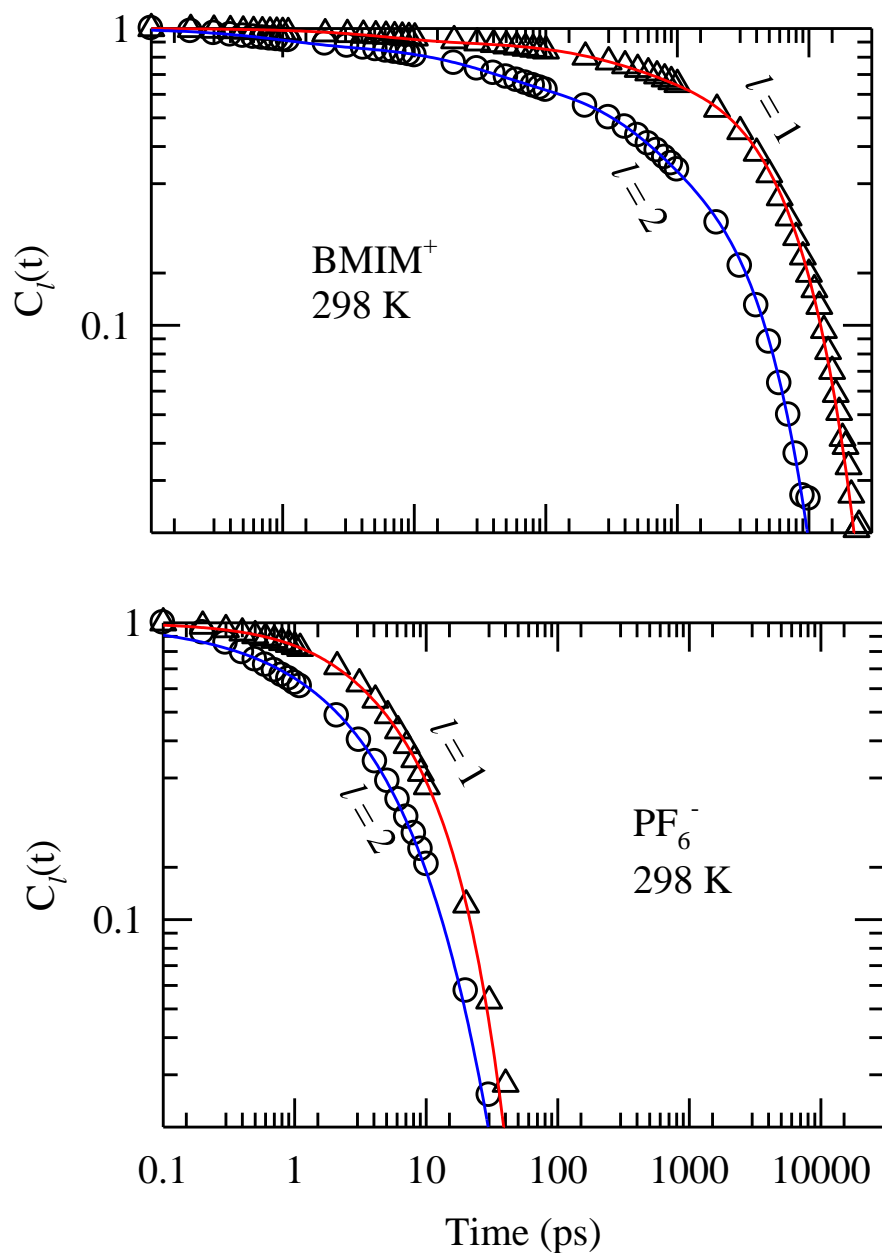


Figure 7.13: Simulated reorientational correlation functions of first ($l = 1$) and second ($l = 2$) ranks for $BMIM^+$ (shown in the upper panel) and PF_6^- (shown in the lower panel). Fit parameters are summarized in **Table 7.3**.

Table 7.3: Multi-exponential fitting parameters for the simulated rank dependent orientational correlation functions of both the ions at 298 K

Ion		a_1	τ_1 (ps)	a_2	τ_2 (ps)	a_3	τ_3 (ps)	a_4	τ_4 (ps)	β	$\langle \tau \rangle$ (ps)
$BMIM^+$	$C_1(t)$	0.10	6.0	0.15	303.0	0.75	5000.0	-	-	1.0	3800.0
	$C_2(t)$	0.11	0.9	0.20	28.4	0.26	400.0	0.43	3333.0	1.0	1543.0
PF_6^-	$C_1(t)$	0.27	2.2	0.73	10.8	-	-	-	-	1.0	8.5
	$C_2(t)$	0.37	0.7	0.49	5.5	0.14	17.0	-	-	1.0	5.3

Finally, we have calculated H-bond dynamics of this IL. It is to be noted that for H-bond calculation we have considered the H-bonds among the six F atoms of anion and three H atoms (H5, H4A and H4M) of the imidazolium ring. There are two different types of H-bond relaxation functions. One measures the timescale that requires the continuous presence of H-bonds and do not allow the breaking due to librations in the intermediate time. This continuous H-bond correlation function, $S_{HB}(t)$ can be defined in the following way:⁶²⁻⁶⁵

$$S_{HB}(t) = \langle h(o)H(t) \rangle / \langle h \rangle \quad (7.4)$$

Here, $h(t')$ is a variable for a pair of molecules and $h(t')=1$, if H-bonded at time t' and zero otherwise. $H(t)$ is a history dependent function of $h(t')$ and it is unity if $h(t')$ is continuously unity between any arbitrary time origin t_0 and later time $t_0 + t$. The angular bracket denotes the averaging over time origins and number of molecules. The average timescale obtained from $S_{HB}(t)$ can be identified as the average lifetime of the H-bond. The other H-bond correlation function $C_{HB}(t)$ gives the structural relaxation timescale due to translational and rotational diffusion and can be defined in the following way.^{62-63,66-67}

$$C_{HB}(t) = \langle h(o)h(t) \rangle / \langle h \rangle \quad (7.5)$$

Here, $h(t')$ is also a variable for a pair a molecule and $h(t')=1$ if H-bonded at time t' . $C_{HB}(t)$ describes the relaxation of a pair which is H-bonded at any arbitrary time origin t_0 and later time $t_0 + t$, with the possibility of breaking and reforming in the intermediate times. The upper panel of Figure 7.14 shows the decay of $S_{HB}(t)$ and the lower panel shows the decay for $C_{HB}(t)$. Multi-exponential fitting parameters of these simulated decays are shown inside each of these panels. It is observed that the average lifetime of H-bond calculated from $S_{HB}(t)$ is 2.4 ps while the average structural relaxation time calculated from $C_{HB}(t)$ is ~ 8.5 ns. The subpicosecond component (0.5 ps with 30% amplitude) of $C_{HB}(t)$ and picosecond component (2.4 ps) of $S_{HB}(t)$ is quantitatively similar to mean jump and waiting time that we have calculated earlier. Also the ~ 20 ps component of $C_{HB}(t)$ is close to $\tau_{waiting}$ and the ~ 700 ps timescale has its origin in the simulated $C_l(t)$ decays. The much slower ~ 26 ns component in structural relaxation decay is probably originating from the ions-pairs. Note the formation of ion-pairs in ILs is already argued previously.^{34,68-69}

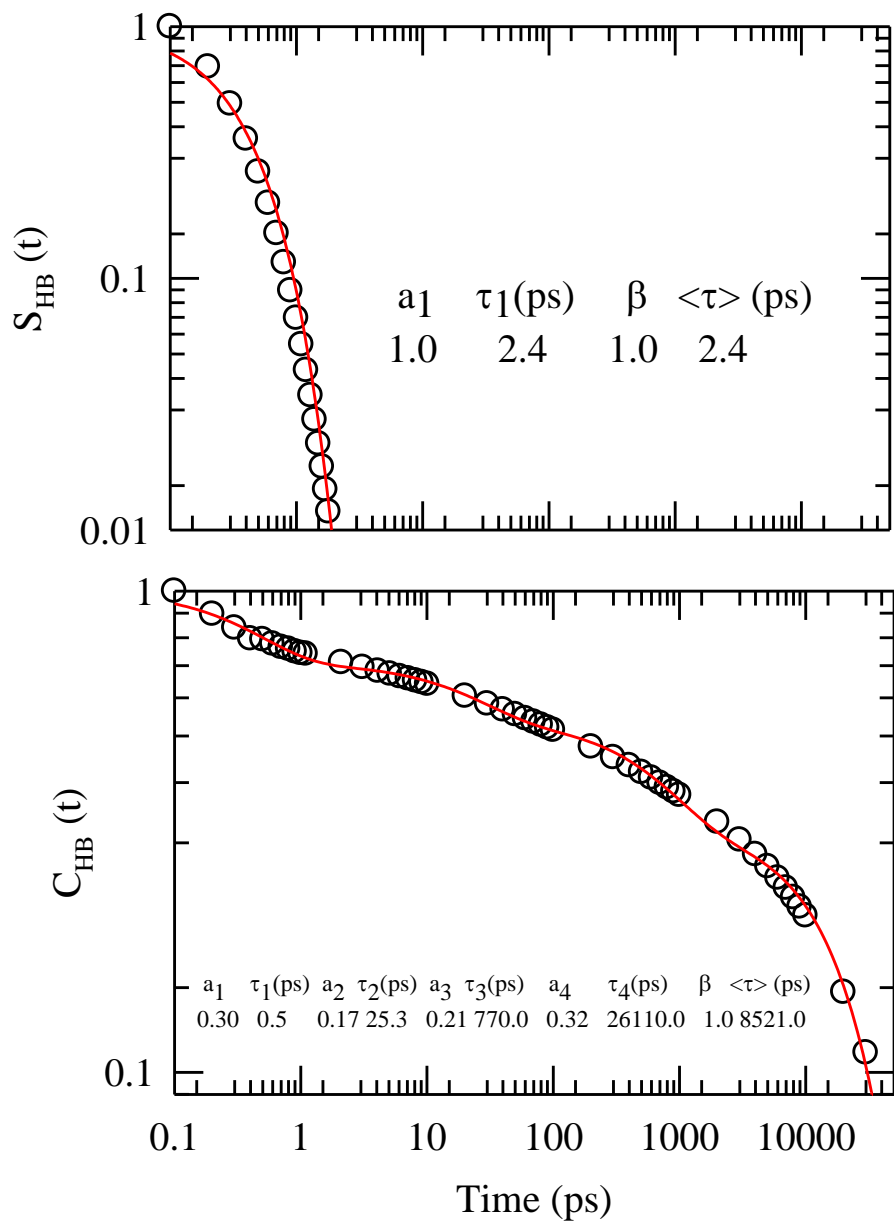


Figure 7.14: Simulated decay of H-bond correlation functions $S_{HB}(t)$ and $C_{HB}(t)$. Multi-exponential fit parameters are shown inside each panel.

7.5. Conclusions

In summary, the present study has revealed the presence of large amplitude orientational jumps for both cation and anion in (BMIM+PF₆) IL. It is also observed that the extent and frequency of large amplitude jumps is higher for the anion as compared to the cation, the bulky size and asymmetry of the cation being the probable reason. Jump angle distributions are found to be broader for the anion and depend weakly on the atom type identity. The long time dynamics of jump and waiting time distributions follow power law distribution which is reminiscent of the presence of heterogeneous dynamics.¹⁹ The ratio of the longest time constants associated with the first and second rank orientational correlation function simulated for *BMIM*⁺ and *PF*₆⁻ deviates significantly from diffusive orientational diffusion suggesting the presence of angular jumps. Also substantial translation-rotation coupling has been observed for the orientation of both the ions. The simulated H-bond dynamics suggest that the lifetime of the H-bond is very fast while the structural relaxation time is very long. The presence of ~26 ns timescale with ~30% amplitude suggests the presence of quite a few number of ions pairs. Also these strong H-bonding present in ILs may significantly dominate its structure and dynamics.

It is to be noted that the present study considers orientational jumps only via three H atoms of imidazolium ring although the methyl H atoms as well as the alkyl H atoms can form the H-bonds. The interconnection between orientational jump and H-bond correlation can be extended to other room temperature ionic liquids (RTILs) and their binary mixtures of polar and non-polar solvents. ILs are industrially relevant and rich in basic scientific aspects. However it requires the proper understanding of the microscopic structure and dynamics in order to fully utilize their potential.⁷⁰

References:

1. R. Hayes, G. G. Warr, and R. Atkin, *Chem. Rev.* **115**, 6357 (2015).
2. J. P. Hallett and T. Welton, *Chem. Rev.* **111**, 3508 (2011).
3. T. Welton, *Chem. Rev.* **99**, 2071 (1999).
4. R. D. Rogers and K. R. Seddon, *Science* **302**, 792 (2003)
5. T. L. Greaves and C. J. Drummond, *Chem. Rev.* **108**, 206 (2008).
6. C. A. Angell, Y. Ansari, and Z. Zhao, *Faraday Discuss.* **154**, 9 (2012).
7. A. Guerfi, M. Dontigny, P. Charest, M. Petitclerc, M. Lagace, A. Vijh, and K. Zaghib, *J. Power Sources* **195**, 845 (2010).
8. A. Lewandowski and A. Swiderska-Mocek, *J. Power Sources* **194**, 601 (2009).
9. C. Arbizzani, *J. Power Sources* **185**, 1575 (2008).
10. T. Yasudaa and M. Watanabe, *MRS Bull.* **38**, 560 (2013).
11. C. Pinilla, M. G. Del Popolo, R. M. Lynden-Bell, and J. Kohanoff, *J. Phys. Chem. B* **109**, 17922 (2005).
12. G. Cevasco and C. Chiappe, *Green Chem.* **16**, 2375 (2014).
13. J. E. Bara, D. E. Camper, D. L. Gin, and R. D. Noble, *Acc. Chem. Res.* **43**, 152 (2010).
14. J. P. Mann, A. McCluskey, and R. Atkin, *Green Chem.* **11**, 785 (2009).
15. R. P. Swatloski, S. K. Spear, J. D. Holbrey, and R. D. Rogers, *J. Am. Chem. Soc.* **124**, 4974 (2002).
16. B. Guchhait, S. Das. S. Daschakraborty, and R. Biswas, *J. Chem. Phys.* **140**, 104514 (2014).
17. A. Das, S. Das, and R. Biswas, *Chem. Phys. Lett.* **581**, 47 (2013).
18. A. Das, S. Das, and R. Biswas, *J. Chem. Phys.* **142**, 034505 (2015).
19. S. Das, R. Biswas, and B. Mukherjee, *J. Chem. Phys.* (under minor review).
20. N. V. Plechkova and K. R. Seddon, *Chem. Soc. Rev.* **37**, 123 (2008).
21. G. van der Zwan and J. T. Hynes, *Chem. Phys.* **152**, 169 (1991).
22. G. van der Zwan and J. T. Hynes, *J. Chem. Phys.* **78**, 4174 (1983).
23. A. Triolo, O. Russina, V. Arrighi, F. Juranyi, S. Janssen, and C. M. Gordon, *J. Chem. Phys.* **119**, 8549 (2003).

24. A. Triolo, O. Russina, C. Hardacre, M. Nieuwenhuyzen, M. A. Gonzalez, and H. Grimm, *J. Phys. Chem. B* **109**, 22061 (2005).
25. T. I. Morrow and E. J. Maginn, *J. Phys. Chem. B* **106**, 12807 (2002).
26. H. K. Kashyap and R. Biswas, *J. Phys. Chem. B* **112**, 12431 (2008).
27. T. Pal and R. Biswas, *Theor. Chem. Acc.* **132**, 1348 (2013).
28. T. Pal and R. Biswas, *J. Phys. Chem. B* **119**, 15683 (2015).
29. T. Pal and R. Biswas, *J. Chem. Phys.* **141**, 164502 (2014).
30. A. Triolo, A. Mandanici, O. Russina, V. Rodriguez-Mora, M. Cutroni, C. Hardacre, M. Nieuwenhuyzen, H.-J. Bleif, L. Keller, and M. A. Ramos, *J. Phys. Chem. B* **110**, 21357 (2006).
31. B. Szefczyk and W. A. Sokalski, *J. Phys. Chem. B* **118**, 2147 (2014).
32. W. Zhao, F. Leroy, B. Heggen, S. Zahn, B. Kirchner, S. Balasubramanian, and F. Muller-Plathe, *J. Am. Chem. Soc.* **131**, 15825 (2009).
33. S. S. Sarangi, W. Zhao, F. Muller-Plathe, and S. Balasubramanian, *ChemPhysChem* **11**, 2001 (2010).
34. T. Koddermann, C. Wertz, A. Heintz, and R. Ludwig, *ChemPhysChem* **7**, 1944 (2006).
35. H. Weingartner, P. Sasisankar, C. Daguinet, P. J. Dyson, I. Krossing, J. M. Slattery, and T. Schubert, *J. Phys. Chem. B* **111**, 4775 (2007).
36. C. Schroder, C. Wakai, H. Weingartner, and O. Steinhauser, *J. Chem. Phys.* **126**, 084511 (2007).
37. Y. Shim and H. J. Kim, *J. Phys. Chem. B* **112**, 11028 (2008).
38. H. Cang, J. Li, and M. D. Fayer, *J. Chem. Phys.* **119**, 13017 (2003).
39. A. L. Sturlaugson, K. S. Fruchey, and M. D. Fayer, *J. Phys. Chem. B* **116**, 1777 (2012).
40. J. H. Antony, D. Mertens, A. Dolle, P. Wasserscheid, and W. R. Carper, *ChemPhysChem* **4**, 588 (2003).
41. A. Wolf, R. Ludwig, P. Sasisanker, and H. Weingartner, *Chem. Phys. Lett.* **439**, 323 (2007).
42. J. Hunger, T. Sonnleitner, L. Liu, R. Buchner, M. Bonn, and H. J. Bakker, *J. Phys. Chem. Lett.* **3**, 3034 (2012).
43. D. Laage and J. T. Hynes, *Science* **311**, 832 (2006).

44. S. Das, R. Biswas, and B. Mukherjee, *J. Phys. Chem. B* **119**, 274 (2015).
45. S. Das, R. Biswas, and B. Mukherjee, *J. Phys. Chem. B* **119**, 11157 (2015).
46. D. van der Spoel, E. Lindahl, B. Hess, A. R. van Buuren, E. Apol, P. J. Meulenhoff, D. P. Tieleman, A. L. T. M. Sijbers, K. A. Feenstra, R. van Drunen, and H. J. C. Berendsen, *Gromacs User Manual version 4.5.4*, www.gromacs.org , **2010**.
47. U. Essmann, L. Perera, M. L. Berkowitz, T. Darden, H. Lee, and L. G. Pedersen, *J. Chem. Phys.* **103**, 8577 (1995).
48. J. N. Canongia Lopes, J. Deschamps, and A. A. H. Padua, *J. Phys. Chem. B* **108**, 2038 (2004).
49. O. Borodin, G. D. Smith, and R. L. Jaffe, *J. Comput. Chem.* **22**, 641 (2001).
50. B. L. Bhargava and S. Balasubramanian, *J. Chem. Phys.* **127**, 114510 (2007).
51. L. Martinez, R. Andrade, E. G. Birgin, and J. M. Martinez, *J. Comput. Chem.* **30**, 2157 (2009).
52. B. Hess, H. Bekker, H. J. C. Berendsen, and J. G. E. M. Fraaije, *J. Comp. Chem.* **18**, 1463 (1997).
53. G. Bussi, D. Donadio, and M. Parrinello, *J. Chem. Phys.* **126**, 014101 (2007).
54. H. J. C. Berendsen, J. P. M. Postma, W. F. van Gunsteren, A. DiNola, and J. R. Haak, *J. Chem. Phys.* **81**, 3684 (1984).
55. H. Tokuda, K. Hayamizu, K. Ishii, A. B. H. Susan, and M. Watanabe, *J. Phys. Chem. B* **108**, 16593 (2004).
56. R. W. Hockney, S. P. Goel, and J. Eastwood, *J. Comp. Phys.* **14**, 148 (1974).
57. D. Laage and J. T. Hynes, *Proc. Natl. Acad. Sci. U.S. A.* **104**, 11167 (2007).
58. P. A. Hunt, R. Matthews, and C. Ashworth, *Chem. Soc. Rev.* **44**, 1257 (2015).
59. J. P. Hansen and I. R. McDonald, *Theory of simple liquids*, 3rd Ed., Academic:San Diego, **2006**.
60. P. Debye, *Polar Molecules*; The Chemical Catalog Company: New York, **1929**.
61. K. Seki, B. Bagchi, and M. Tachiya, *Phys. Rev. E* **77**, 031505 (2008).
62. D. C. Rapaport, *Mol. Phys.* **50**, 1151 (1983).
63. A. Chandra, *Phys. Rev. Lett.* **85**, 768 (2000).

64. A. Luzar, *J. Chem. Phys.* **113**, 10663 (2000).
65. S. Indra and R. Biswas, *Mol. Simul.* **41**, 471 (2015).
66. A. Luzar and D. Chandler, *Nature* **379**, 55 (1996).
67. A. Luzar and D. Chandler, *Phys. Rev. Lett.* **76**, 928 (1996).
68. Y. Zhang and E. J. Maginn, *J. Phys. Chem. Lett.* **6**, 700 (2015).
69. N. T. Scharf, A. Stark, and M. M. Hoffmann, *J. Phys. Chem. B* **116**, 11488 (2012).
70. M. Armand, F. Endres, D. R. MacFarlane, H. Ohno, and B. Scrosati, *Nature Materials* **8**, 621 (2009).

Chapter 8

Concluding Remarks and Future Problems

8.1. Concluding Remarks

To summarize, the present Thesis provides a detailed investigation on interaction and dynamics of liquids possessing both Coulomb and H-bond interactions via all-atom molecular dynamics simulations. The systems considered are deep eutectic solvents and ionic liquids which are both environmental friendly solvents with immense applications in industrial and technological sectors. The medium heterogeneity and its dependence on electrolytes and temperature have been explored employing the methodology followed earlier to understand structure and dynamics of deeply supercooled liquids. Our study has also monitored the impact of H-bond interactions on dynamics. Spatio-temporal heterogeneity has been investigated extensively via multi-point correlations, producing estimates for the correlated domain size and timescale. Mechanism of angular displacements for dipolar species in deep eutectics and ionic liquids has been extensively investigated with a special emphasis on orientational jumps. Jump time and waiting time distributions were found to follow power-law – a feature that strongly indicates presence of dynamic heterogeneity. Signatures for spatial heterogeneity in deep eutectics have been reflected in the cluster size and lifetime distributions. Finally, we have analyzed the orientational dynamics of [BMIM][PF₆] ionic liquid where separate dynamics of cation and anion has been monitored and quantified. Our investigation has generated a molecular level understanding of the relation between heterogeneity and solution dynamics, and guides how deep eutectics could be better used as reaction media. In addition, our study on reorientational dynamics thoroughly examines the generality of jump modes in H-bonded systems for angular diffusion.

Since we have provided conclusions at the end of each of the chapters in this Thesis, we refrain from providing conclusion separately. Instead, we discuss here a few interesting problems which are relevant and can be studied in the near future.

8.2. Future Problems

8.2.1. Alkyl chain length dependence of spatial and temporal heterogeneity in amide/electrolyte deep eutectics

It is expected that as the chain length of the alkyl group increases, the hydrophobic character of the molecule to which such a group is attached increases. Small angle X-ray scattering¹ (SAXS), neutron scattering² (SANS) measurements, neutron-spin echo³⁻⁴ (NSE) studies, molecular dynamics simulations⁵⁻⁶ of ILs have shown that aggregation of alkyl groups increases with increase in alkyl chain length, inducing spatial heterogeneity in the system. Recently, fluorescence anisotropy measurements⁷ using a fluorescent probe in amide/electrolyte DESs have revealed dependence of spatio-temporal heterogeneity on alkyl chain length. However, full characterization of the impact of alkyl chain-length on heterogeneity has not been investigated yet. All-atom molecular dynamic simulations can be performed to quantify the alkyl chain-length dependence of non-Gaussian parameters, particle displacement distributions, and correlated length and timescales.⁸⁻¹⁰ Similar study can be extended to explore the dependence of spatio-temporal heterogeneity on ion identity.

8.2.2. Dielectric relaxation and solvation dynamics in amide/electrolyte deep eutectics

Dielectric relaxation spectroscopy (DRS) measurements have been performed previously¹¹⁻¹² for a few amide/electrolyte DESs within the frequency window $10^{-7} \leq \nu / \text{MHz} \leq 10^2$ which have suggested presence of microheterogeneity in the solution and also reported a colossal static dielectric constant (ϵ_0). Additionally, the relaxation times (spreading from 0.55 second to couple of nano seconds) obtained from the experiments suggest extremely slow relaxation rate which was interpreted in terms of the rotational motion of nano-domains formed via the interaction between amide and electrolyte molecules. However, fast response timescale of DESs has not been measured yet. Existing measurements of dielectric relaxations of acetamide/electrolyte DESs in the frequency window $0.2 \leq \nu / \text{GHz} \leq 50$ report a significant missing of early part.¹³ Simulations of dielectric relaxation of deep eutectics using realistic potentials and long run with

sufficiently large systems will be able to cross-check the validity of the existing dielectric relaxation timescales and their interpretation. Note ionic deep eutectics are conducting solutions, and therefore ion conductivity at the low frequency limit can significantly alter the solution dielectric constant. Full solvation response has not been measured yet for these exotic solvent systems. Simulations can help here in shading light on the interrelationship between solvation and dielectric response in these systems, and stimulate further experimental studies.

8.2.3. Microsecond simulation study of DESs close to glass transition temperature

The glass transition temperature (T_g) of DESs are ~ 190 K.^{7,14} The structure and dynamics of amide containing DESs and also the effect of heterogeneity has been studied at room temperature and above the room temperature.¹⁵⁻¹⁹ Though there are some experimental studies of ILs just below and above the T_g ²⁰⁻²³, there are hardly any simulation studies available near T_g with atomistic details possibly because of the long equilibration and production run. However, with the advancement of the computer cluster architectures, it is now possible to simulate DESs for several microseconds. The studies are mainly interesting from basic scientific point of view as it can address several interesting points like, the relation between dramatic slowdown of dynamics and growing length scales as a function of temperature, how the static structure reorganizes around T_g etc.²² In spite of intense research for decades, a well accepted explanation of the drastic slow down of the dynamics upon approaching the T_g is still missing. It is possible to approach this problem via all-atom simulations.

8.2.4. Effect of medium heterogeneity on the interaction and dynamics of choline chloride/urea deep eutectics

Recent time-resolved fluorescence measurements²³ have shown moderate presence of both spatial and dynamic heterogeneities in (choline chloride+urea) deep eutectics. Molecular dynamic simulations can be performed in order to understand the extent of spatial and dynamical heterogeneity in terms of various two and multi-point correlation functions as already done for amide/electrolyte deep eutectics¹⁷ and also how it affects the medium dynamics. Also one can study the hydrogen bond interactions among various interspecies. For example, urea can form hydrogen bonds with chlorides or choline or with another urea molecule. Various kinds of doubly ionic hydrogen bond interactions are already reported only recently for choline chloride/urea deep eutectic solvents.²⁴ However, the characterization of hydrogen bond timescales is essential to understand the dynamics of the medium.

8.2.5. Effects of non-polar solvents on medium heterogeneity in IL/solvent binary mixtures

The heterogeneity aspect of neat ILs and (ILs+Polar Solvent) binary mixtures has been studied via experiments²⁵ and simulations²⁶ techniques. Recently the time scale and length scale associated with dynamic heterogeneity have been characterized for [OMIM][BF₄]/water binary mixtures.²⁶ However the effect of non-polar solvents like hexane, benzene on the medium dynamics of ILs/DESs has not been investigated yet. This is somewhat surprising given that these solvent systems are one of the most widely studied systems for last two decades. Nevertheless, effect of heterogeneity on the dynamics of (IL+ non polar) solvents can be studied via all-atom molecular dynamic simulations. Following earlier protocols,¹⁰ one can characterize various time and length scales associated with the dynamic heterogeneity of these mixtures. Also one can monitor the effect of solvent on the IL cluster size and lifetime distributions.¹⁸

8.2.6. Effects of heterogeneity on the transport properties of polymer ILs

Extensive research has been carried out for developing polymer electrolytes which are safe, have high storage capability and also non hazardous.²⁷ The unique properties of ILs have made them promising candidates for large scale applications in electrochemical industry²⁸⁻²⁹ and can be a suitable alternative of traditional organic liquid electrolytes. Recently scientists have been able to polymerize ionic liquids by incorporating polymerizable groups such as vinyl groups into the structure of ILs.³⁰⁻³³ These polymer ILs are expected to possess the unique features of ILs and good mechanical strength of polymers. However, poor conductivity still remains the major challenge. Molecular dynamics simulations can be performed to understand the molecular level interactions and dynamics of these polymers in order to tune the properties. And the knowledge gained from the simulation studies can be applied for smarter use of these IL polymers.

8.2.7. Transport in ionic deep eutectics: Validity of the Hole Theory

A comprehensive understanding of transport properties is required for suitable designing of DESs as their utility is often limited by high viscosity and low conductivity values. The Hole theory has been used previously to understand transport data of ionic deep eutectics³⁴ and ionic liquids³⁵⁻³⁶ and found to be helpful for rational designing of solvents with low viscosity. It is argued that the viscosity of the liquids is affected by the large ion:hole-size ratio. The idea is to use ions which are relatively small but the liquids must contain large cavities. However, it has some serious limitations. The theory is purely predictive, and the apparent applicability may arise from cancellation of opposing effects of counter approximations. Simulations can help in detecting presence of voids (or holes) in deep eutectics via Voronoi diagram analyses, and also by examining their sizes and shapes, and their dependence on ion identity.

References:

1. A. Triolo, O. Russina, B. Fazio, R. Triolo, and E. D. Cola, *Chem. Phys. Lett.* **457**, 362 (2008).
2. C. Hardacre, J. D. Holbrey, C. L. Mullan, T. G. A. Youngs, and D. T. Bowron, *J. Chem. Phys.* **133**, 074510 (2010).
3. O. Yamamuro, T. Yamada, M. Kofu, M. Nakakoshi, and M. Nagao, *J. Chem. Phys.* **135**, 054508 (2011).
4. M. Kofu, M. Nagao, T. Ueki, Y. Kitazawa, Y. Kitazawa, Y. Nakamura, S. Sawamura, M. Watanabe, and O. Yamamuro, *J. Phys. Chem. B* **117**, 2773 (2013).
5. H. V. R. Annapureddy, H. K. Kashyap, P. M. De Biase, and C. J. Margulis, *J. Phys. Chem. B* **114**, 16838 (2010).
6. C. S. Santos, H. V. R. Annapureddy, N. S. Murthy, H. K. Kashyap, E. W. Castner Jr., and C. J. Margulis, *J. Chem. Phys.* **134**, 064501 (2011).
7. B. Guchhait, S. Das, S. Daschakraborty, and R. Biswas, *J. Chem. Phys.* **140**, 104514 (2014).
8. K. Kim and S. Saito, *J. Chem. Phys.* **133**, 044511 (2010).
9. E. Flenner and G. Szamel, *Phys. Rev. E* **72**, 011205 (2005).
10. T. Pal and R. Biswas, *J. Chem. Phys.* **141**, 104501 (2014).
11. A. Amico, G. Berchiesi, C. Cametti, and A. Di Biasio, *J. Chem. Soc., Faraday Trans. 2*, **83**, 619 (1987).
12. G. Berchiesi, M. De Angelis, G. Rafaiiani, and G. Vitali, *J. Mol. Liq.* **61**, 11 (1992).
13. K. Mukherjee, A. Das, S. Choudhury, A. Barman, and R. Biswas, *J. Phys. Chem. B* **119**, 8063 (2015).

14. B. Guchhait, S. Daschakraborty, and R. Biswas, *J. Chem. Phys.* **136**, 174503 (2012).
15. S. Das, R. Biswas, and B. Mukherjee, *J. Phys. Chem. B* **119**, 257 (2015).
16. S. Das, R. Biswas, and B. Mukherjee, *J. Phys. Chem. B* **119**, 11157 (2015).
17. S. Das, R. Biswas, and B. Mukherjee, *J. Chem. Phys.* (to be submitted).
18. S. Das, R. Biswas, and B. Mukherjee, *J. Chem. Phys.* (to be submitted).
19. S. Das and R. Biswas, *J. Chem. Phys.* (to be submitted).
20. N. Shamim and G. B. McKenna, *J. Phys. Chem. B* **114**, 15742 (2010).
21. A. Triolo, A. Mandanici, O. Russina, V. Rodriguez-Mora, M. Cutroni, C. Hardacre, M. Nieuwenhuyzen, H. J. Bleif, L. Keller, and M. A. Ramos, *J. Phys. Chem. B* **110**, 21357 (2010).
22. S. Karmakar, C. Dasgupta, and S. Sastry, *Proc. Natl. Acad. Sci. U. S. A.* **106**, 3675 (2009).
23. A. Das and R. Biswas, *J. Phys. Chem. B* **119**, 10102 (2015).
24. C. R. Ashworth, R. P. Matthews, T. Welton, and P. A. Hunt, *Phys. Chem. Chem. Phys.* **18**, 18145 (2016).
25. H. Jin, X. Li, and M. Maroncelli, *J. Phys. Chem. B* **111**, 13473 (2007).
26. T. Pal and R. Biswas, *J. Phys. Chem. B* **119**, 15683 (2015).
27. P. Wright, *MRS Bull.* **27**, 597 (2002).
28. R. D. Rogers and K. R. Seddon, *Science* **302**, 792 (2003).
29. D. R. Macfarlane, M. Forsyth, P. C. Howlett, J. M. Pringle, J. Sun, G. Annat, W. Neil, and I. E. Izgorodina, *Acc. Chem. Rev.* **40**, 1165 (2007).
30. D. Mecerreyes, *Prog. Polym. Sci.* **36**, 1629 (2011).

31. U. H. Choi, M. Lee, S. R. Wang, W. J. Liu, K. I. Winey, H. W. Gibson, and R. H. Colby, *Macromolecules* **45**, 3974 (2012).
32. A. S. Shaplov, R. Marcilla, and D. Mecerreyes, *Electrochim. Acta* **175**, 18 (2015).
33. F. Fan, W. Wang, A. P. Holt, H. Feng, D. Uhrig, X. Lu, T. Hong, Y. Wang, N. G. Kang, J. Mays, and A. P. Sokolov, *Macromolecules* **49**, 4557 (2016).
34. A. P. Abbott, R. C. Harris, and K. S. Ryder, *J. Phys. Chem. B* **111**, 4910 (2007).
35. A. P. Abbott, D. Boothby, G. Capper, D. L. Davies, and R. K. Rasheed, *J. Am. Chem. Soc.* **126**, 9142 (2004).
36. A. P. Abbott, *ChemPhysChem* **5**, 1242 (2004).

Appendix A

Table A1: Lennard-Jones Parameters for Acetamide

Atom Type	ϵ_i (Kcalmol ⁻¹)	σ_i (Å)
C3	0.08	3.67
H1	0.022	2.35
C6	0.07	3.57
OC2	0.12	3.03
N1	0.20	3.30
HO	0.046	0.40

Table A2: Partial charges on each atom

Atom type	q_i (e)
C3	-0.27
H1	0.09
C6	0.55
OC2	-0.55
N1	-0.64
HO	0.32

Table A3: Bond force constant for Acetamide

Bonds	r_o (Å)	K_b (Kcalmol ⁻¹ Å ⁻²)
C3-H1	1.11	322
C3-C6	1.52	200
C6-OC2	1.23	650
C6-N1	1.36	430
N1-HO	1.00	480

Table A4: Angle force constant for Acetamide

Angles	θ_0 (deg)	K_θ (Kcalmol ⁻¹ rad ⁻²)
H1-C3-H1	108.4	35.5
H1-C3-C6	109.5	33.0
C3-C6-OC2	121.0	15.0
C3-C6-N1	116.5	50.0
OC2-C6-N1	122.5	75.0
C6-N1-HO	120.0	50.0
HO-N1-HO	120.0	23.0

Table A5: Dihedral force constant for Acetamide

Dihedral	K_χ (Kcalmol ⁻¹)	n	δ (deg)
H1-C3-C6-OC2	0.05	6	180.0
H1-C3-C6-N1	0.05	6	180.0
C3-C6-N1-HO	1.4	2	180.0
OC2-C6-N1-HO	1.4	2	180.0

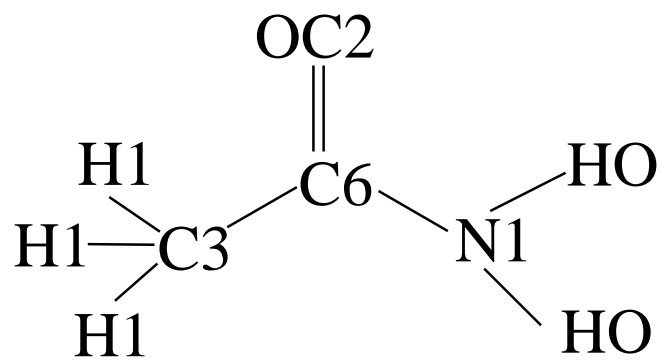


Figure A1: CHARMM representation of acetamide, CH₃CONH₂.

Appendix B

Table B1: Partial Atomic Charges and Lennard-Jones Parameters.

Atom Type	q_i (e)	ε_i (Kcalmol ⁻¹)	σ_i (Å)
NO	0.95	0.0807	3.060
O1,2,3	-0.65	0.1457	2.770
Cl	1.342	0.1481	3.770
OO1,2,3,4	-0.5855	0.1457	2.771

Table B2: Bond force constant parameters.

Bonds	r_o (Å)	K_b (KCalmol ⁻¹ Å ⁻²)
NO-O1/O2/O3	1.2599	525.00
Cl-OO1/OO2/OO3/OO4	1.5006	365.00

Table B3: Angle force constant parameters.

Angles	θ_0 (deg)	K_θ (Kcalmol ⁻¹ rad ⁻²)
O-NO-O	120.00	120.00
OO-Cl-OO	109.47	125.00

Table B4: Partial Atomic Charges and Lennard-Jones Parameters.

Atom Type	q_i (e)	ε_i (Kcalmol ⁻¹)	σ_i (Å)
Li ⁺	1.00	0.0005	2.87
Br ⁻	-1.00	0.7100	4.28

Table B5: Density comparison between simulations and experiments.

Mixtures	Experimental Density (gm/cc); ~313 K	Simulated Density (gm/cc); 303 K	% Deviation
CH ₃ CONH ₂ +LiBr	1.237	1.34	7.68
CH ₃ CONH ₂ +LiNO ₃	1.17	1.30	10
CH ₃ CONH ₂ +LiClO ₄	1.23	1.30	5.4

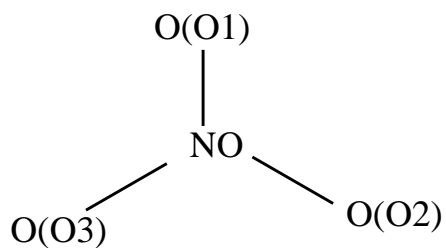


Figure B1: Representation of Nitrate ion.

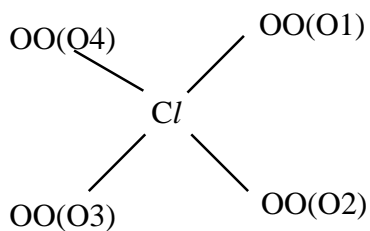


Figure B2: Representation of perchlorate ion.

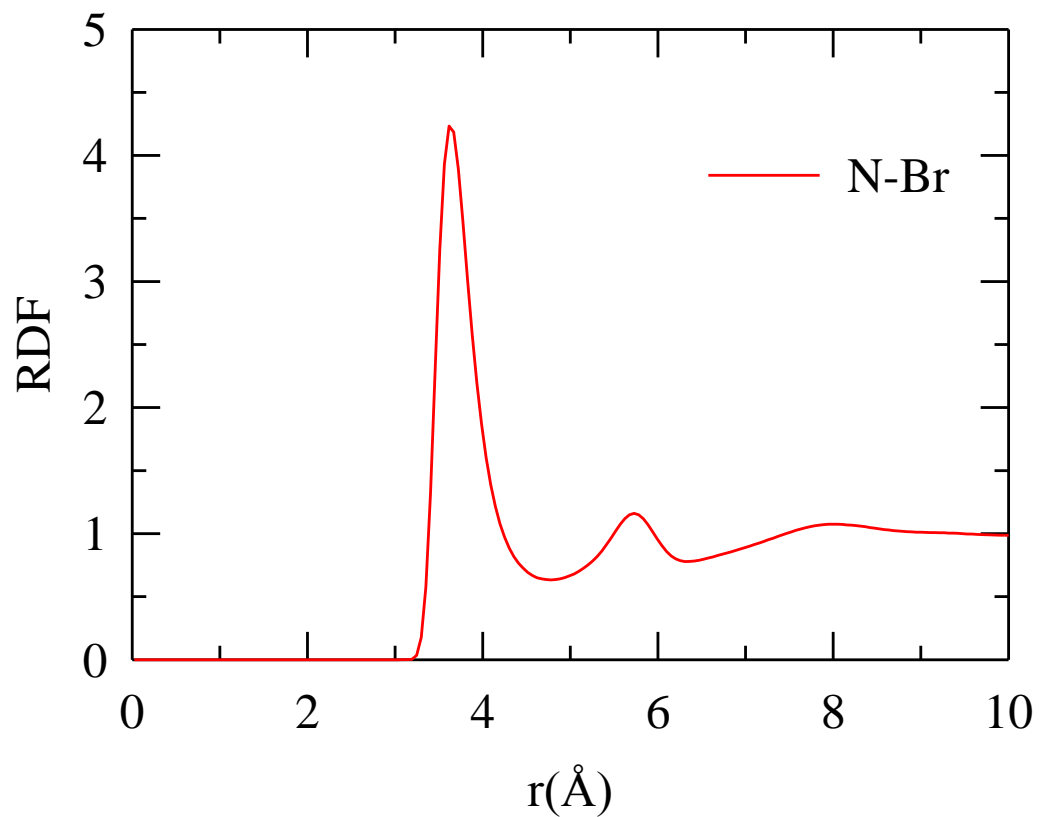


Figure B3: Simulated radial distribution function (RDF) between the nitrogen atom of acetamide and bromide ion for (acetamide + LiBr) DES at 303 K.

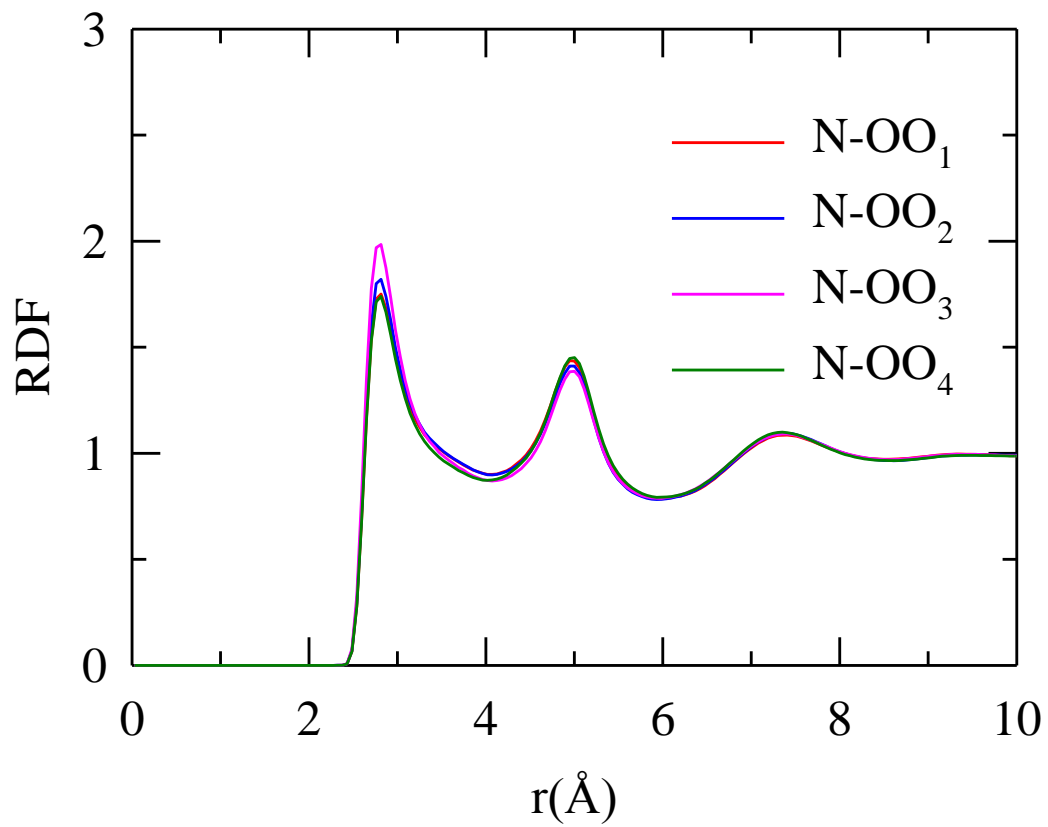


Figure B4: Simulated radial distribution functions (RDFs) between the nitrogen atom of acetamide and oxygen atoms of perchlorate ion for (acetamide + LiClO₄) DES at 303 K .

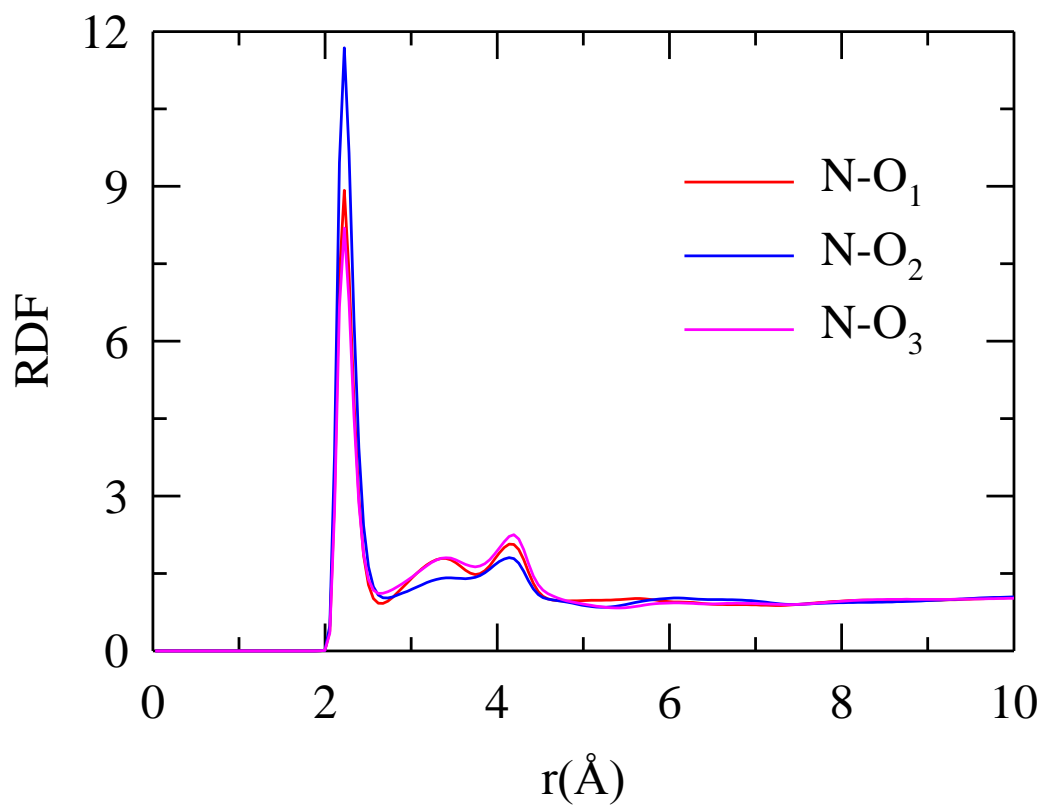


Figure B5: Simulated radial distribution functions (RDFs) between nitrogen atom of acetamide and oxygen atoms of nitrate ion for (acetamide + LiNO₃) DES at 303 K.

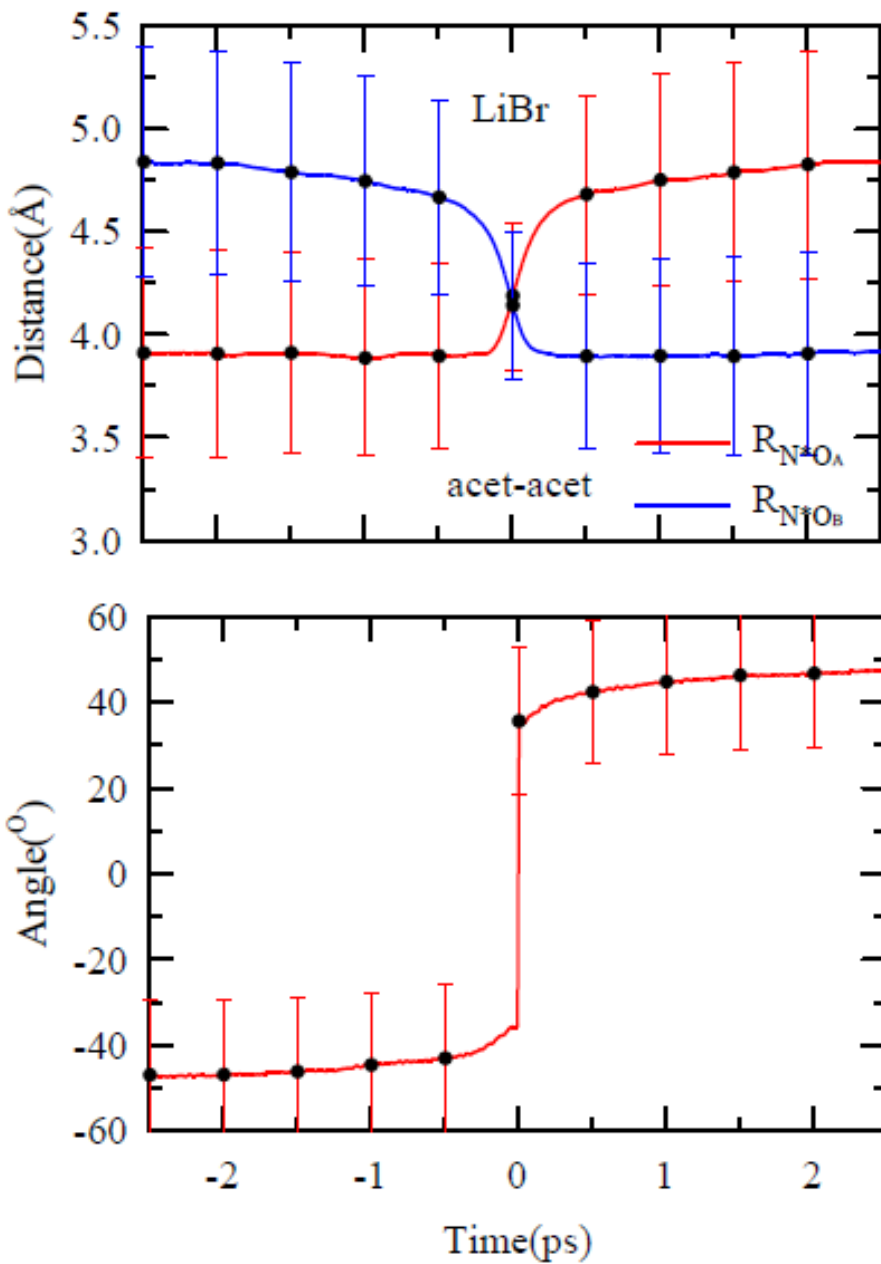


Figure B6: Average trajectories with error bars for acetamide-acetamide pair obtained for (acetamide + LiBr) deep eutectics at 303 K. For details, see **Figures 3.5 & 3.6** of Chapter 3 of the Thesis.

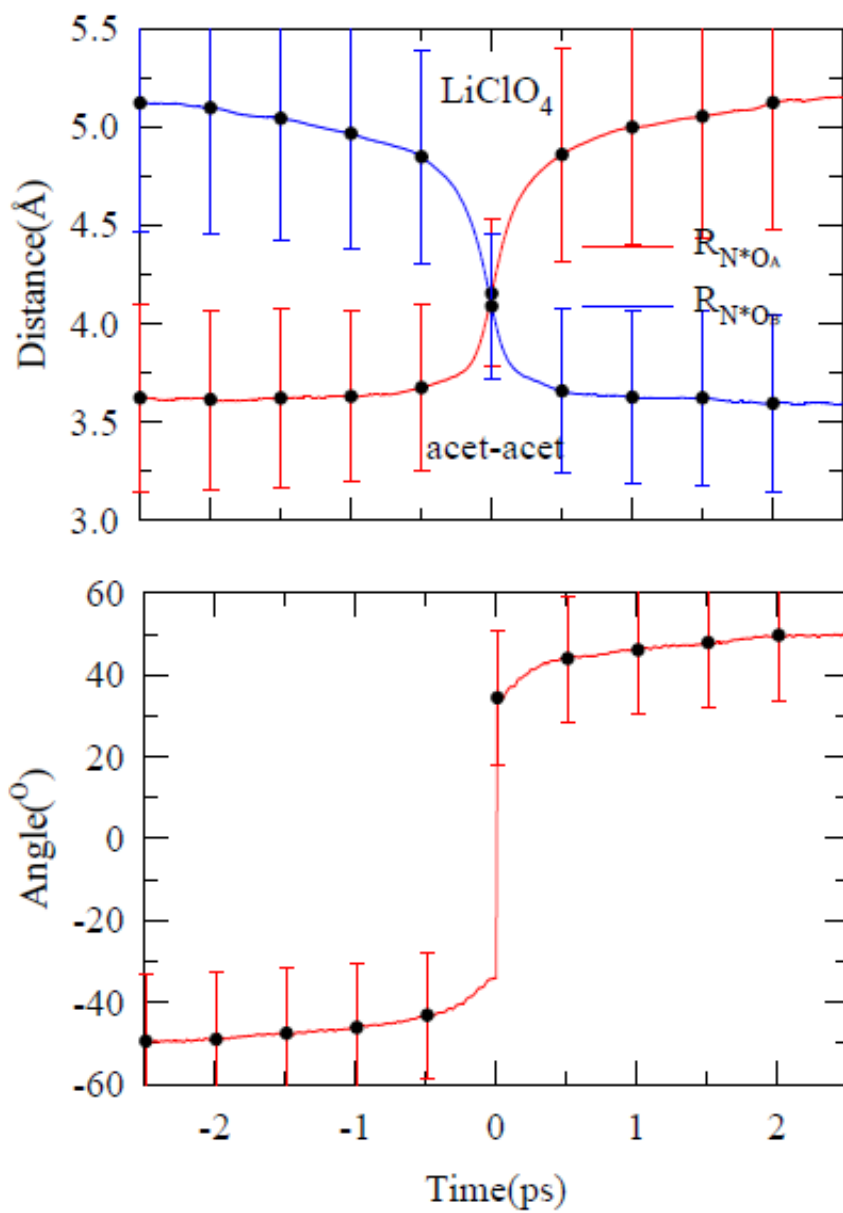


Figure B7: Average trajectories with error bars for acetamide-acetamide pair obtained for (acetamide + LiClO₄) deep eutectics at 303 K. For details, see **Figures 3.5 & 3.6** of Chapter 3 of the Thesis.

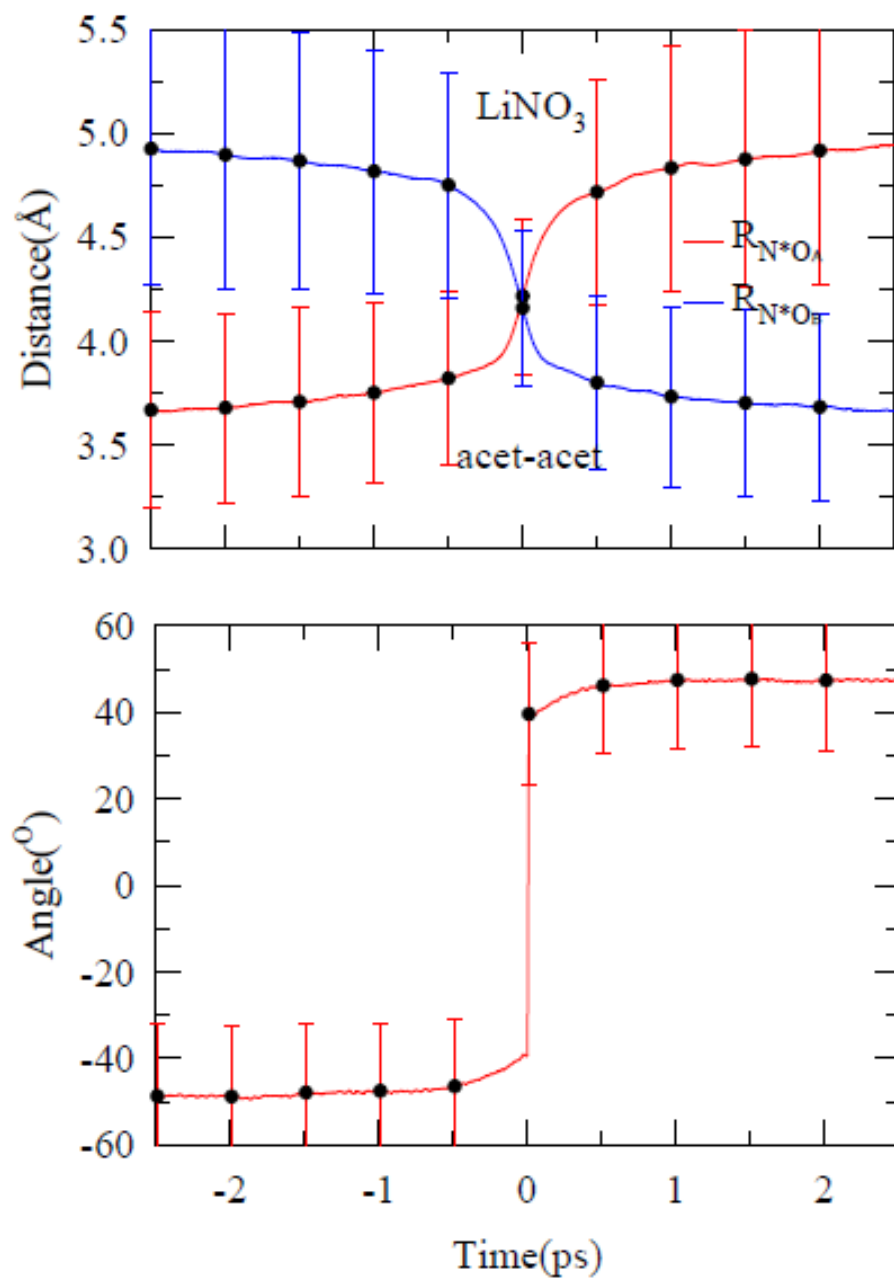


Figure B8: Average trajectories with error bars for acetamide-acetamide pair obtained for (acetamide + LiNO₃) deep eutectics at 303 K. For details, see **Figures 3.5 & 3.6** of Chapter 3 of the Thesis.

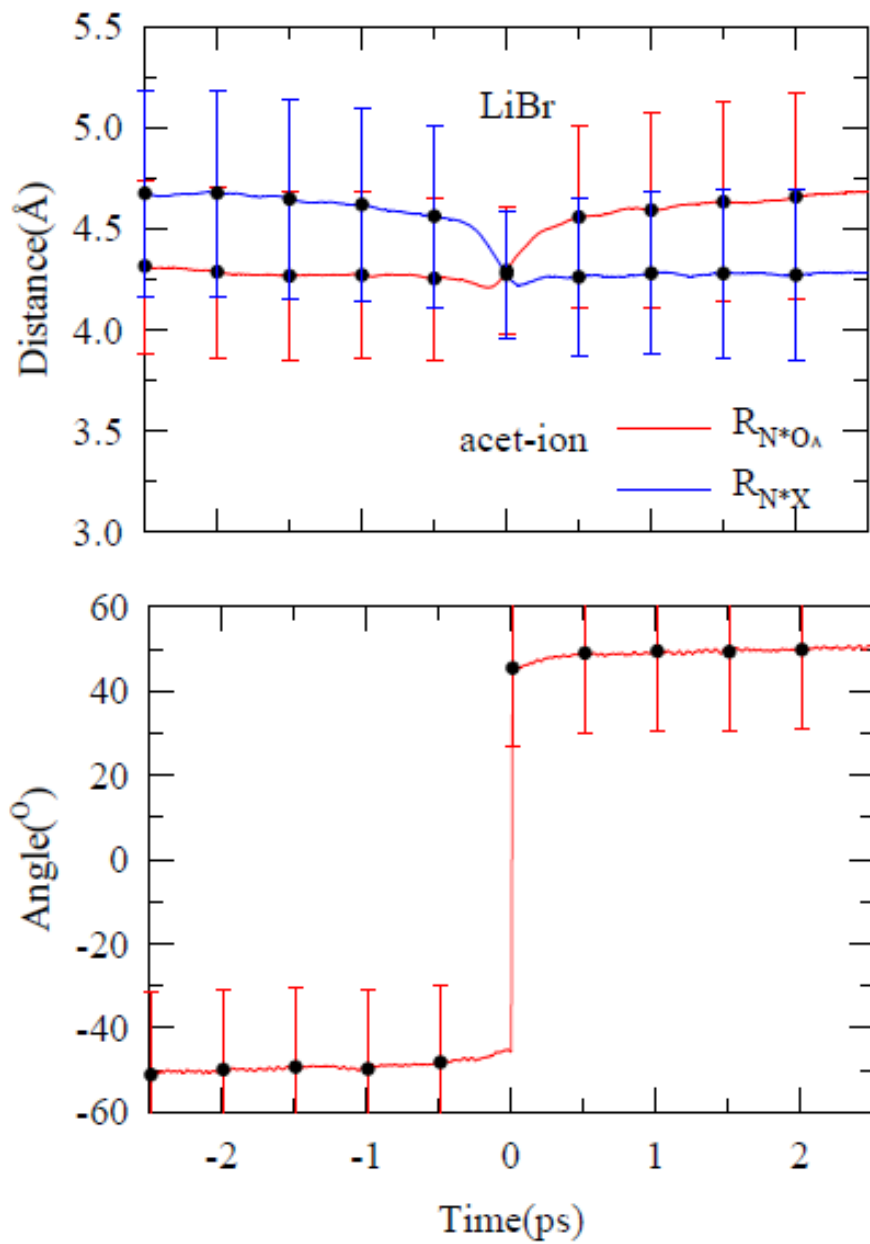


Figure B9: Average trajectories with error bars for acetamide-ion pair obtained for (acetamide + LiBr) deep eutectics at 303 K. For details, see **Figures 3.5 & 3.7** of Chapter 3 of the Thesis.

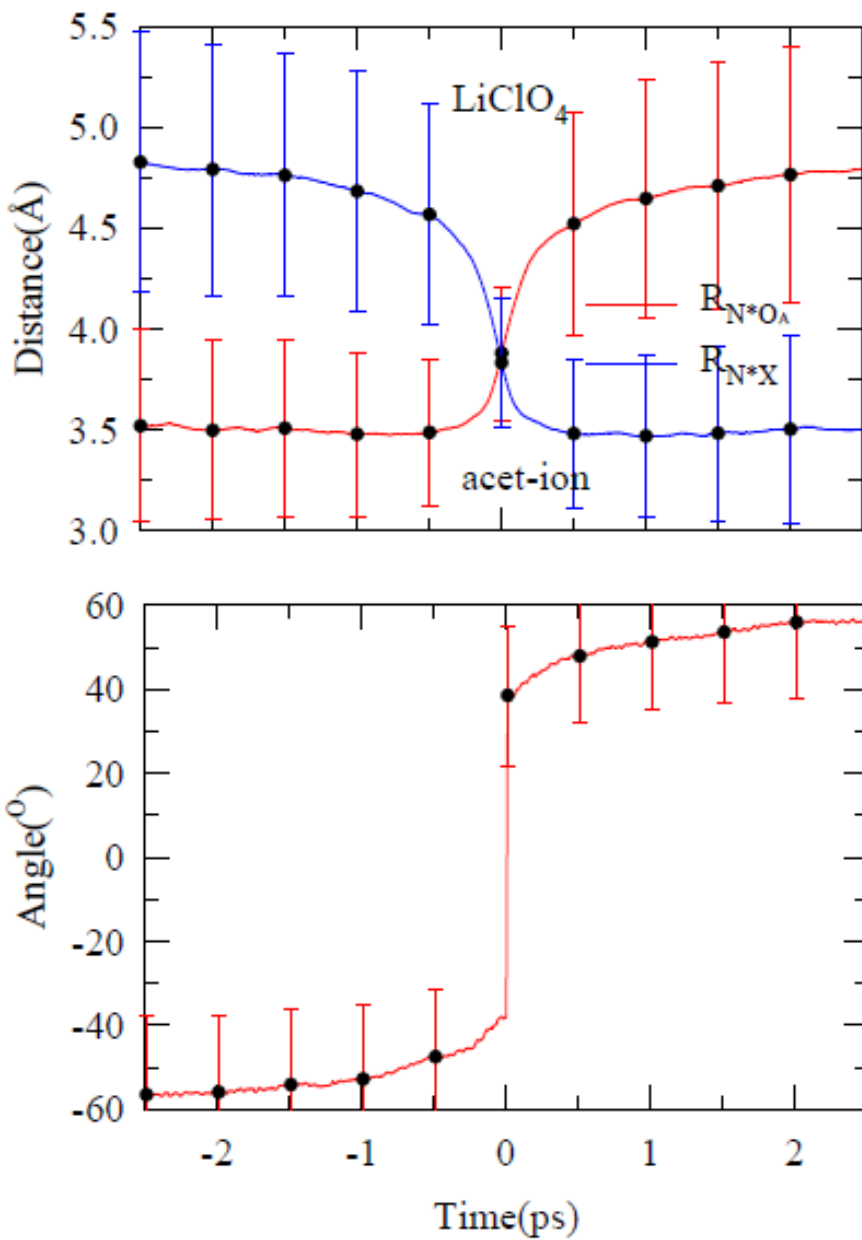


Figure B10: Average trajectories with error bars for acetamide-ion pair obtained for (acetamide + LiClO₄) deep eutectics at 303 K. For details, see **Figures 3.5 & 3.7** of Chapter 3 of the Thesis.

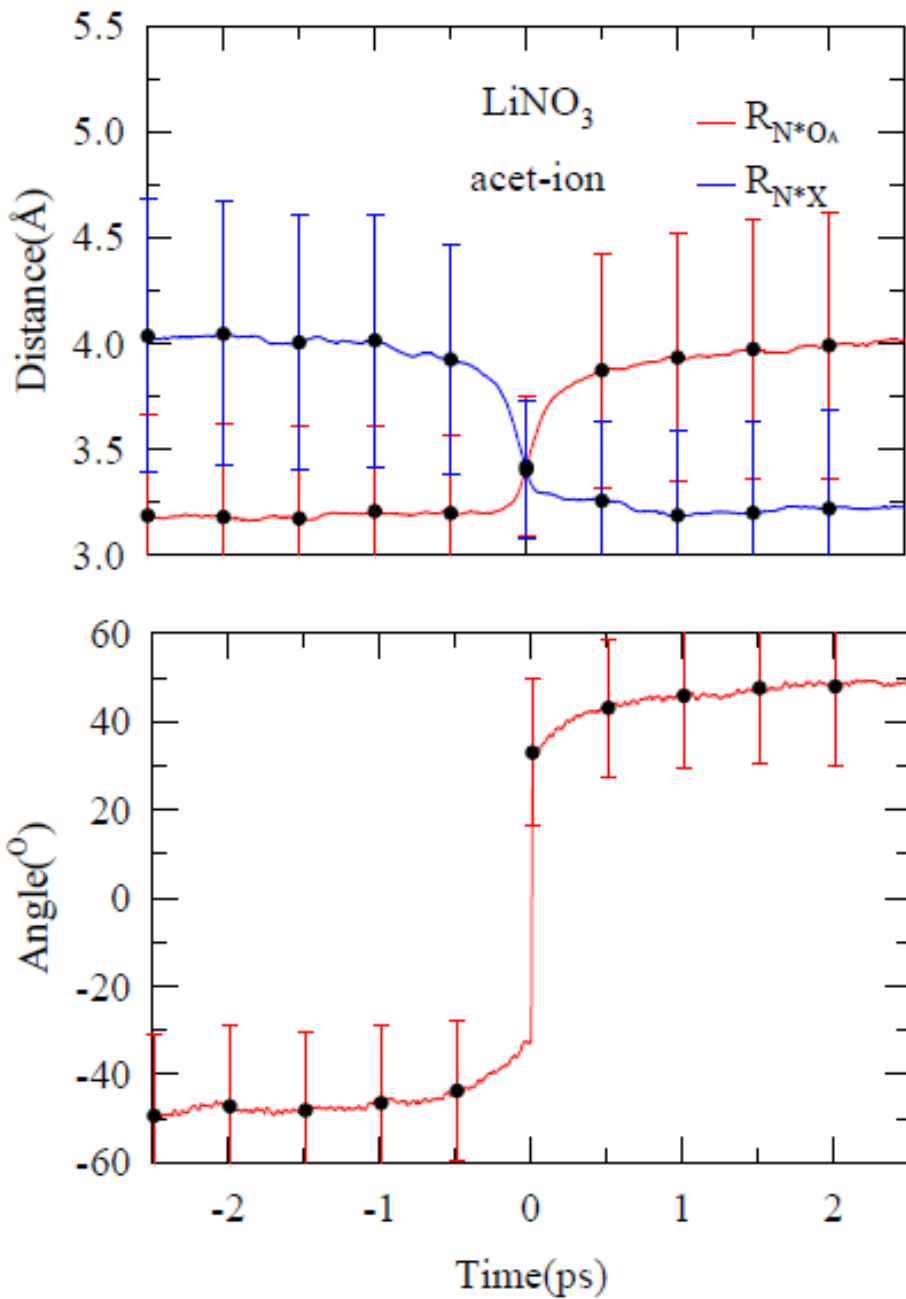


Figure B11: Average trajectories with error bars for acetamide-ion pair obtained for (acetamide + LiNO₃) deep eutectics at 303 K. For details, see **Figures 3.5 & 3.7** of Chapter 3 of the Thesis.

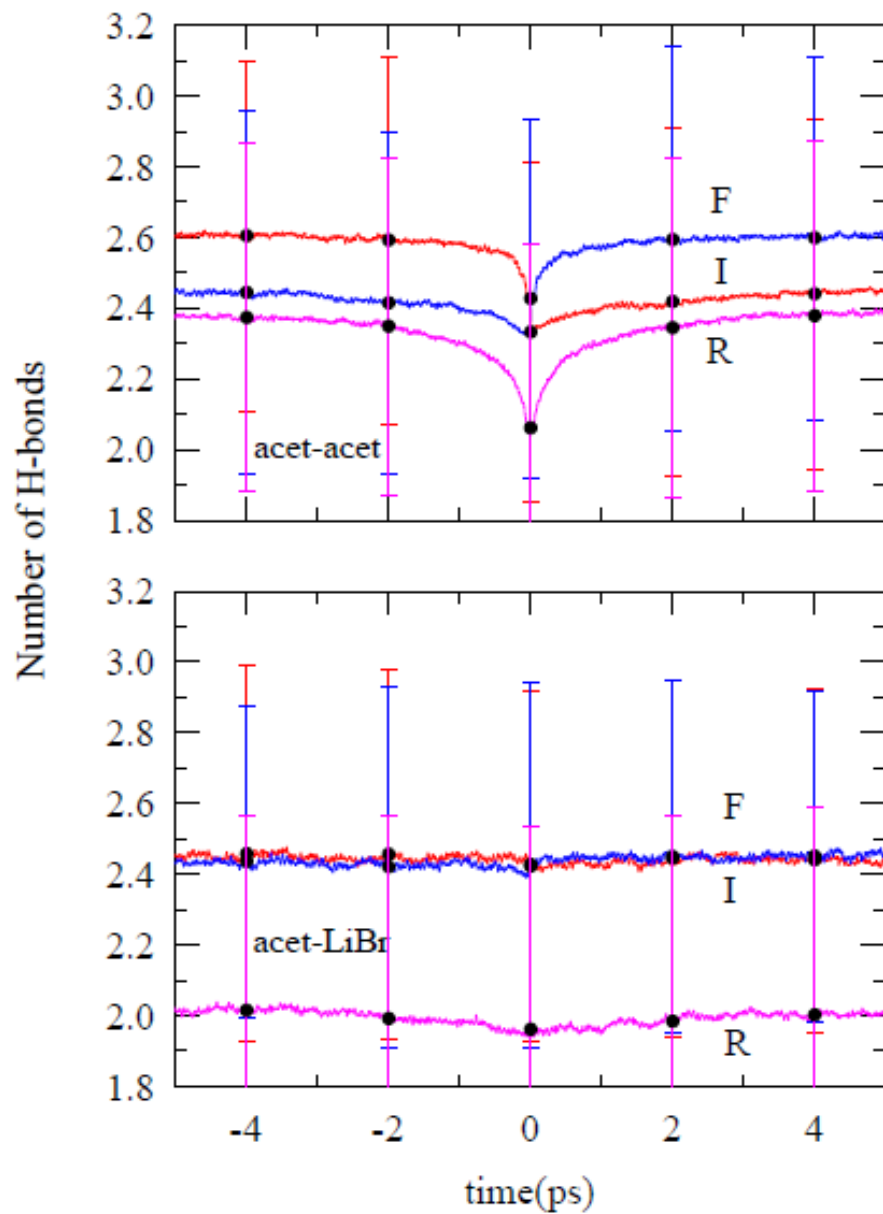


Figure B12: Trajectories with error bars showing time-evolution of the H-bond coordination number at 303 K for (acetamide + LiBr) deep eutectics. For details, see **Figure 3.8** of Chapter 3 of the Thesis.

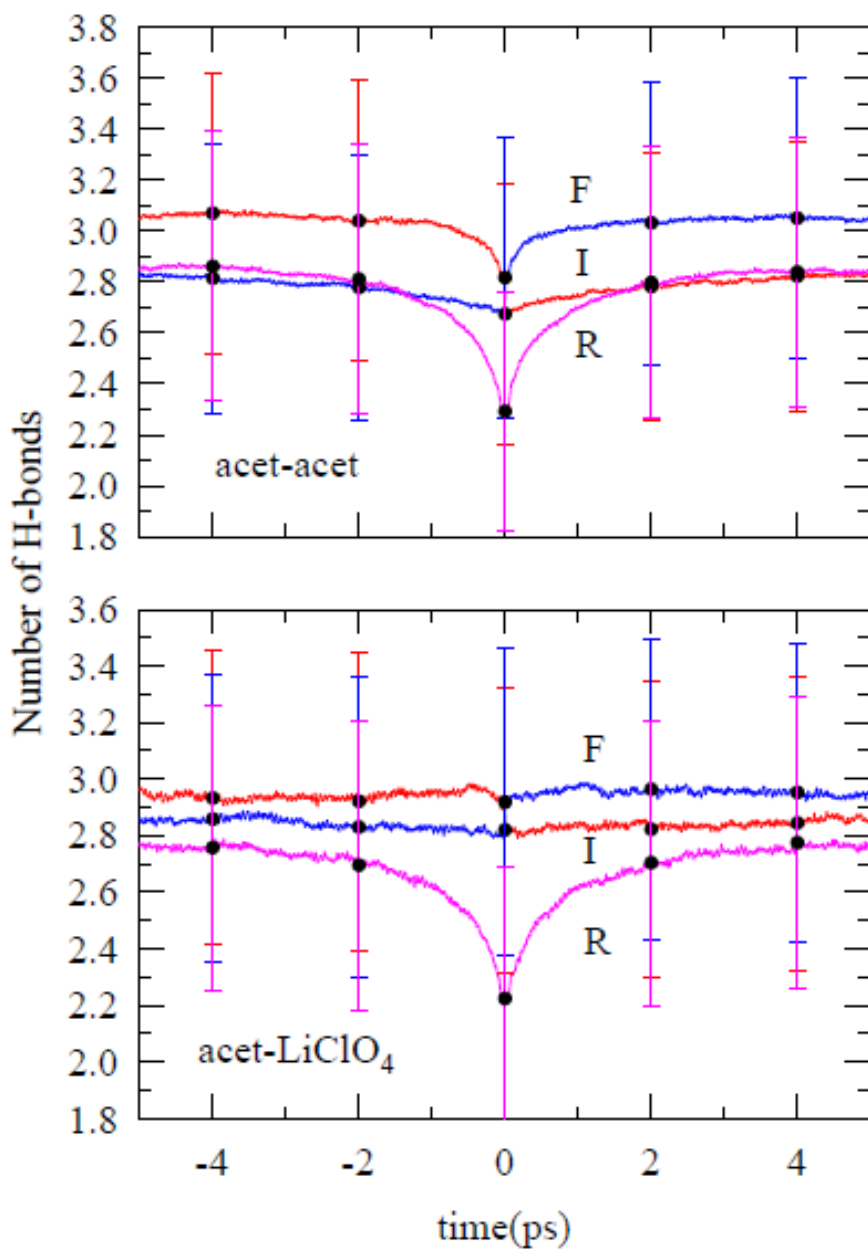


Figure B13: Trajectories with error bars showing time-evolution of the H-bond coordination number at 303 K for (acetamide + LiClO₄) deep eutectics. For details, see **Figure 3.8** of Chapter 3 of the Thesis.

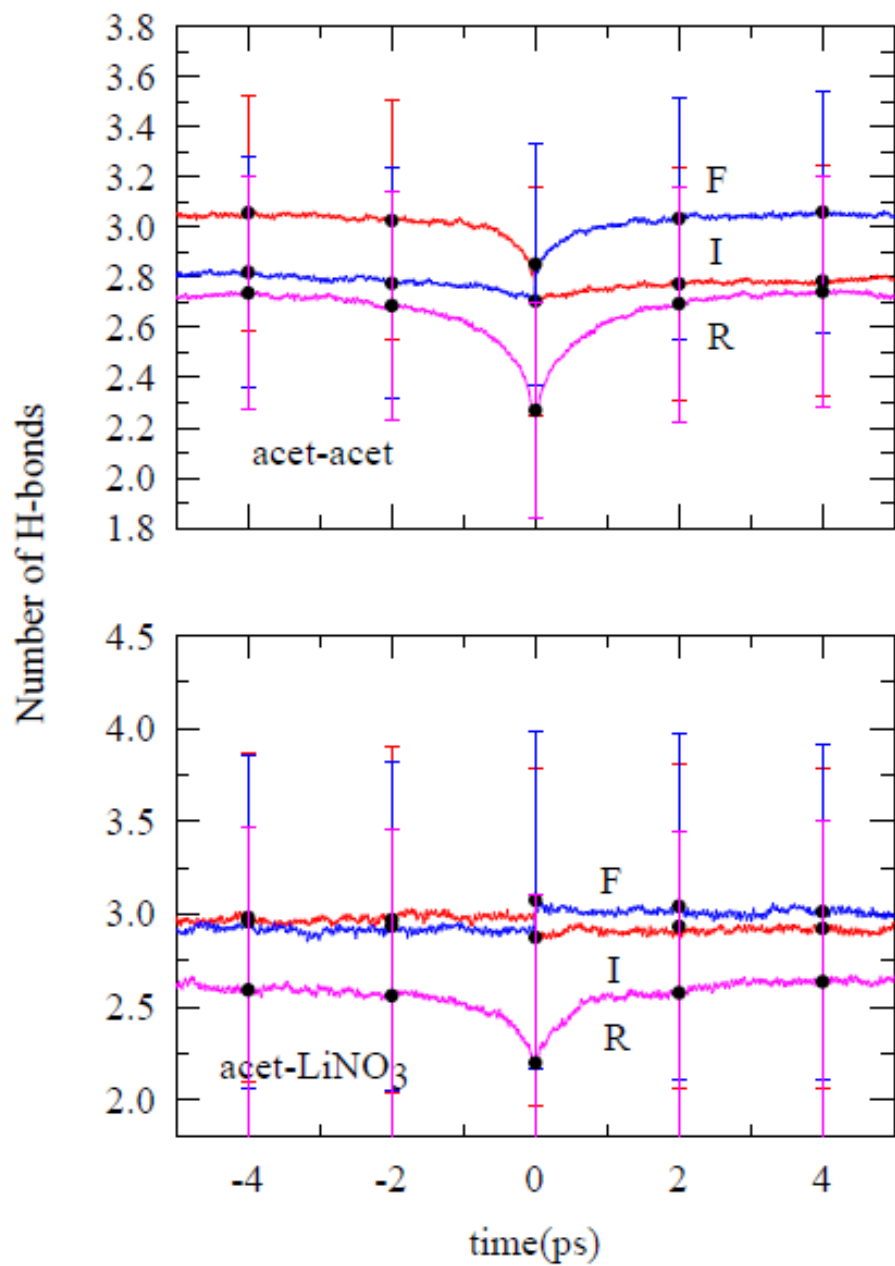


Figure B14: Trajectories with error bars showing time-evolution of the H-bond coordination number at 303 K for (acetamide + LiNO₃) deep eutectics. For details, see **Figure 3.8** of Chapter 3 of the Thesis.

Appendix C

Table C1: Multi-exponential fit parameters of $S_{\text{cont}}^{\text{complex}}(t)$ between lithium (Li^+) and oxygen atom of acetamide for all three DESs at 303 K.

DES	a_1	τ_1 (ps)	a_2	τ_2 (ps)	a_3	τ_3 (ps)	a_4	τ_4 (ps)	β	$\langle \tau \rangle$ (ps)
Br^-	0.05	5.9	0.44	45.7	0.51	130.0	-	-	1.0	86.7
ClO_4^-	0.20	4.3	0.58	17.5	0.22	56.8	-	-	1.0	23.5
NO_3^-	0.14	1.4	0.31	7.3	0.37	29.1	0.18	103.1	1.0	31.8

Table C2: Multi-exponential fit parameters of $C_{\text{str.}}^{\text{complex}}(t)$ between lithium (Li^+) and oxygen atom of acetamide for all three DESs at 303 K.

DES	a_1	τ_1 (ps)	a_2	τ_2 (ps)	a_3	τ_3 (ps)	a_4	τ_4 (ps)	β	$\langle \tau \rangle$ (ps)
Br^-	0.35	1111.0	0.65	17425.0	-	-	-	-	1.0	11715.0
ClO_4^-	0.01	1.4	0.11	256.4	0.71	1429.0	0.17	10000.0	1.0	2743.0
NO_3^-	0.03	0.8	0.11	333.3	0.55	3333.0	0.31	12063.0	1.0	5609.0

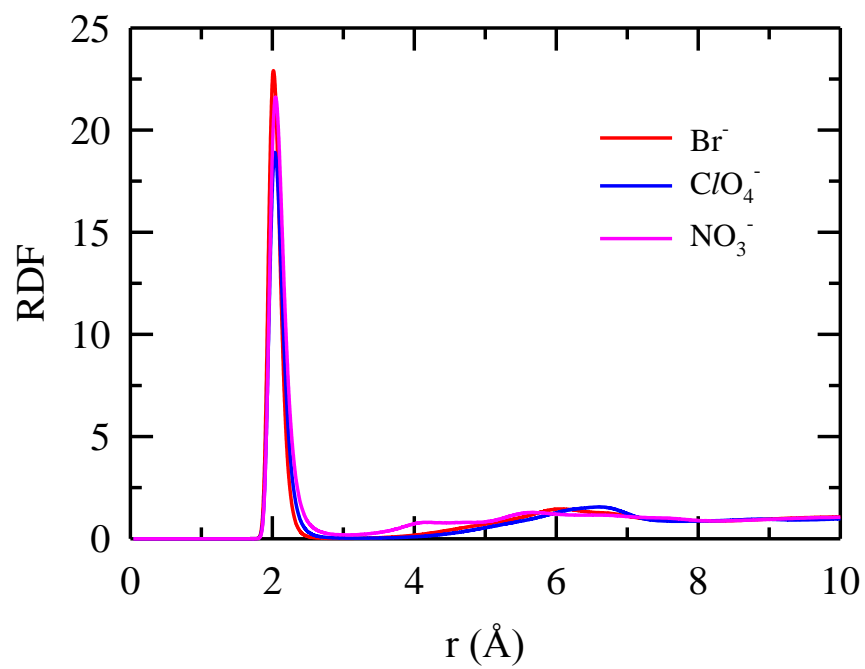


Figure C1: Simulated radial distribution function (RDF) between the lithium (Li^+) and oxygen atom of acetamide for all three DESs at 303 K.

Appendix D

Table D1: Density comparison between simulations and experiments.

Mixtures	Experimental Density (gm/cc); ~313 K	Simulated Density (gm/cc); 303 K	% Deviation	Experimental Density (gm/cc); ~343 K	Simulated Density (gm/cc); 350 K	% Deviation
CH ₃ CONH ₂ +LiBr	1.237	1.34	7.68	-	1.30	-
CH ₃ CONH ₂ +LiNO ₃	1.17	1.30	10	-	1.17	-
CH ₃ CONH ₂ +LiClO ₄	1.23	1.30	5.4	1.20	1.22	1.6

Table D2: Multi-exponential fitting parameters for various cluster lifetime distributions of all the DESs at both the temperatures.

	<i>Temp</i> (K)		a_1	τ_1 (ps)	a_2	τ_2 (ps)	a_3	τ_3 (ps)	a_4	τ_4 (ps)	β	$\langle \tau \rangle$ (ps)
Br^-	303	<i>Acet – Acet</i>	0.19	1.2	0.26	19.0	0.45	140.8	0.10	15267.8	1.0	1595.3
		<i>Li – Acet</i>	1.0	909.1	-	-	-	-	-	-	1.0	909.1
		<i>Li – Br</i>	0.07	10.4	0.26	81.3	0.27	909.1	0.40	2000.0	1.0	1067.3
	350	<i>Acet – Acet</i>	0.18	1.0	0.20	7.2	0.59	36.4	0.03	555.5	1.0	39.8
		<i>Li – Acet</i>	0.07	8.0	0.93	131.6	-	-	-	-	1.0	123.0
		<i>Li – Br</i>	0.30	11.1	0.70	78.7	-	-	-	-	1.0	58.4
ClO_4^-	303	<i>Acet – Acet</i>	0.19	1.0	0.27	10.0	0.41	53.7	0.13	625.0	1.0	106.1
		<i>Li – Acet</i>	0.26	24.5	0.74	666.7	-	-	-	-	1.0	500.0
		<i>Li – ClO₄</i>	1.0	357.1	-	-	-	-	-	-	1.0	357.1
	350	<i>Acet – Acet</i>	0.19	1.0	0.22	6.8	0.49	29.9	0.10	137.0	1.0	30.0

		<i>Li – Acet</i>	0.05	0.9	0.11	5.5	0.60	39.4	0.24	175.4	1.0	66.4
		<i>Li – ClO₄</i>	0.11	1.4	0.26	11.5	0.50	63.7	0.13	285.7	1.0	72.1
<i>NO₃⁻</i>	303	<i>Acet – Acet</i>	0.23	1.2	0.40	16.2	0.28	97.1	0.09	1000.0	1.0	124.0
		<i>Li – Acet</i>	0.15	1.0	0.15	9.3	0.35	104.1	0.35	555.6	1.0	232.5
		<i>Li – NO₃</i>	0.10	250.0	0.90	5000.0	-	-	-	-	1.0	4525.0
	350	<i>Acet – Acet</i>	0.21	1.0	0.26	7.1	0.46	27.6	0.07	145.0	1.0	24.9
		<i>Li – Acet</i>	0.17	0.7	0.17	6.1	0.23	37.9	0.43	153.8	1.0	76.0
		<i>Li – NO₃</i>	0.07	1.7	0.19	29.3	0.34	250.0	0.40	2000.0	1.0	890.7

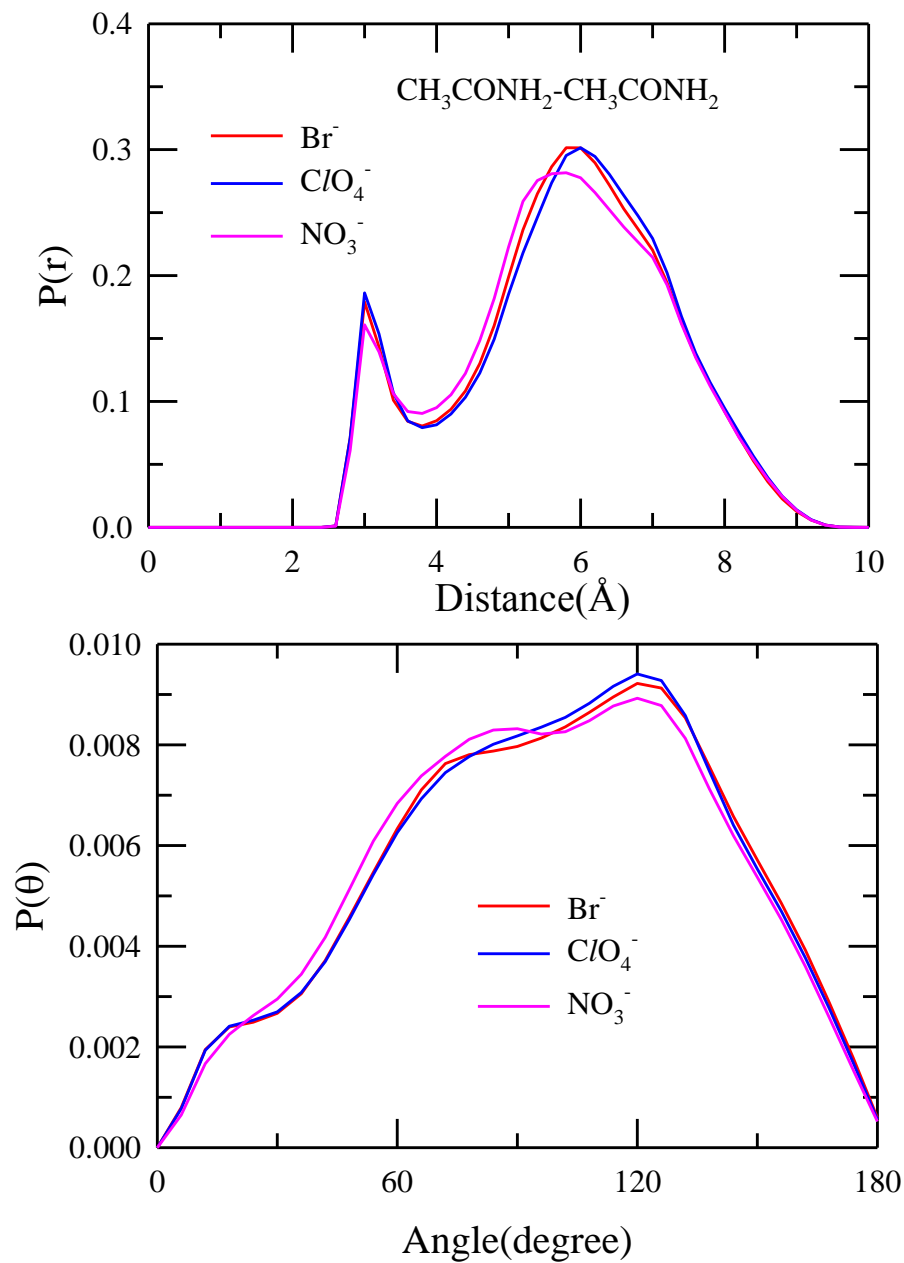


Figure D1: The upper panel shows the distance distribution between the oxygen and nitrogen atom belonging to different pair of acetamide molecules whose centre of mass distance lies within 7 \AA . The lower panel shows the angle (θ_{ONH}) distribution for same. Both the distribution are calculated for all DESs at 303 K.

Appendix E

Table E1: Fit parameters for the simulated anion dependent incoherent scattering function, $F_S^N(k, t)$, for acetamide molecule **(a)** at the nearest neighbour wavevector (shown in the upper panel of **Figure 6.4**) and **(b)** at the lowest accessible wavevector (shown in the lower panel of **Figure 6.4**). $\langle \tau \rangle$ represent average decay times obtained analytically from the fit parameters.

(a)

ion	k (\AA^{-1})	a_1	τ_1 (ns)	a_2	τ_2 (ns)	β	$\langle \tau \rangle$ (ns)
Br^-	1.33	1.0	0.08	-	-	0.63	0.1
NO_3^-	1.33	0.6	0.07	0.4	0.8	0.55	0.6
ClO_4^-	1.31	0.9	0.02	0.1	0.2	0.63	0.04

(b)

ion	k (\AA^{-1})	a_1	τ_1 (ns)	a_2	τ_2 (ns)	β	$\langle \tau \rangle$ (ns)
Br^-	0.18	0.4	2.0	0.6	10.0	1.00	7.0
NO_3^-	0.18	1.0	10.6	-	-	0.76	12.5
ClO_4^-	0.17	0.6	0.77	0.4	4.0	1.00	2.1

Table E2: Fit parameters for the simulated temperature dependent incoherent scattering function, $F_S^N(k, t)$, for acetamide molecule at the nearest neighbour wavevector and collective wavevector shown in **Figure 6.5**. $\langle \tau \rangle$ represent average decay times obtained analytically from the fit parameters. Three tables denotes temperature dependence in presence of **(a)** Br^- ion, **(b)** NO_3^- ion and **(c)** ClO_4^- ion

(a)

T (K)	k (\AA^{-1})	a ₁	τ_1 (ns)	a ₂	τ_2 (ns)	β	$\langle \tau \rangle$ (ns)
303	0.18	0.4	2.0	0.6	10.0	1.00	7.0
350	0.18	0.5	1.0	0.5	3.0	0.71	2.3
303	1.33	1.0	0.08	-	-	0.63	0.11
350	1.33	1.0	0.06	-	-	0.73	0.08

(b)

T (K)	k (\AA^{-1})	a ₁	τ_1 (ns)	a ₂	τ_2 (ns)	β	$\langle \tau \rangle$ (ns)
303	0.18	1.0	10.6	-	-	0.76	12.50
350	0.18	0.4	0.4	0.6	1.1	0.61	1.15
303	1.33	0.6	0.07	0.4	0.8	0.55	0.56
350	1.33	0.9	0.01	0.1	0.1	0.60	0.02

(c)

T (K)	k (\AA^{-1})	a_1	τ_1 (ns)	a_2	τ_2 (ns)	β	$\langle \tau \rangle$ (ns)
303	0.17	0.6	0.77	0.4	4.0	1.00	2.06
350	0.17	0.5	0.37	0.5	0.7	0.61	0.70
303	1.31	0.9	0.02	0.1	0.2	0.63	0.03
350	1.31	1.0	0.01	-	-	0.56	0.01

Table E3: Multi-exponential fitting parameter of $Q(t)$ for various DESs at 303 K and 350 K:A. $CH_3CONH_2 + LiBr$

$T(K)$	$k (\text{\AA}^{-1})$	a_1	$\tau_1(ps)$	a_2	$\tau_2(ps)$	a_3	$\tau_3(ps)$	β	$\langle\tau\rangle(ps)$
303	1.33	0.45	19.5	0.48	140.8	0.07	1111.1	1.0	154.1
350	1.33	0.44	3.6	0.48	27.3	0.08	222.2	1.0	32.5

B. $CH_3CONH_2 + LiNO_3$

$T(K)$	$k (\text{\AA}^{-1})$	a_1	$\tau_1(ps)$	a_2	$\tau_2(ps)$	a_3	$\tau_3(ps)$	β	$\langle\tau\rangle(ps)$
303	1.33	1.0	208.3	-	-	-	-	0.5 0	416.6
350	1.33	0.49	1.8	0.42	19.5	0.09	161.3	1.0	23.6

C. $CH_3CONH_2 + LiClO_4$

$T(K)$	$k (\text{\AA}^{-1})$	a_1	$\tau_1(ps)$	a_2	$\tau_2(ps)$	a_3	$\tau_3(ps)$	β	$\langle\tau\rangle(ps)$
303	1.33	0.44	3.3	0.45	31.2	0.11	250.0	1.0	43.0
350	1.33	0.49	1.3	0.42	11.4	0.09	95.2	1.0	14.0

Appendix F

Table F1: Lennard-Jones Parameters of $BMIM^+$ and PF_6^-

Atom	ϵ_{ij} (KJ/mol)	σ_{ij} (Å)
CR	0.292	3.55
NA(NAA,NAM)	0.711	3.25
CW(CWA,CWM)	0.292	3.55
H4(H4A,H4M)	0.125	1.72
H5	0.125	1.72
CT(CTM,CT1,CT2,CT3,CT4)	0.276	3.50
H1	0.125	1.92
HC	0.125	2.50
P	0.836	3.94
F	0.255	3.118

Table F2: Partial Charges on each atom of $BMIM^+$ and PF_6^-

Atom	$q_i(e)$
CR	0.060
NA(NAA,NAM)	0.052
CW(CWA,CWM)	-0.020
H4(H4A,H4M)	0.096
H5	0.096
CTM,CT1	-0.089
CT2,CT3	-0.038
CT4	-0.065
H1	0.105
HC	0.026
P	0.580
F	-0.230

Table F3: Bond force constant for $BMIM^+$ and PF_6^-

Bonds	r_0 (Å)	K_b (KJmol ⁻¹ Å ²)
CR/CW-H5/H4	1.08	constrained
CT-H1/HC	1.09	constrained
CR-NA	1.315	1996
CW-NA	1.378	1787
CW-CW	1.341	2176
NA-CTM/CT1	1.466	1410
CT-CT	1.529	1121
P-F	1.6	1673

Table F4: Angle force constant for $BMIM^+$ and PF_6^-

Angles	θ_0 (deg)	K_θ (KJmol ⁻¹ rad ²)
CW-NA-CR	108.0	292.6
CW-NA-CTM/CT1	125.6	292.6
CR-NA-CTM/CT1	126.4	292.6
NA-CR-H4/H5	125.1	146.3
NA-CR-NA	109.8	292.6
NA-CW-CW	107.1	292.6
NA-CW-H5/H4	122.0	146.3
CW-CW-H4/H5	130.9	146.3
NA/CT-CT-H1/HC	110.7	156.6
NA/CT-CT-CT	112.7	418.4
H1/HC-CT-H1/HC	107.8	138.1
F-P-F	90.0	836.8

Table F5: Dihedral force constant for $BMIM^+$ and PF_6^-

Dihedrals	V_1 (KJ/mol)	V_2 (KJ/mol)	V_3 (KJ/mol)
X ^a -NA-CR-X	0	19.46	0
X-CW-CW-X	0	44.98	0
X-NA-CW-X	0	12.55	0
CW-NA-CTM/CT1-H1	0	0	0.519
CR-NA-CTM/CT1-H1	0	0	0
CW-NA-CTM/CT1-C2	-7.154	4.43	0.877
CR-NA-CTM/CT1-C2	-5.269	0	0
NA-CTM/CT1-CT2- CT3/CT4	-7.480	-0.681	1.02
NA-CTM/CT1-CT2- HC	0	0	0
CT-CT-CT-H1/HC	0	0	1.531
H1/HC-CT-CT-H1/HC	0	0	1.331
CT-CT-CT-CT	7.28	-0.657	1.167
X-NA-X-X	0	8.37	0
X-CR/CW-X-X	0	9.2	0

^aX represents improper dihedral

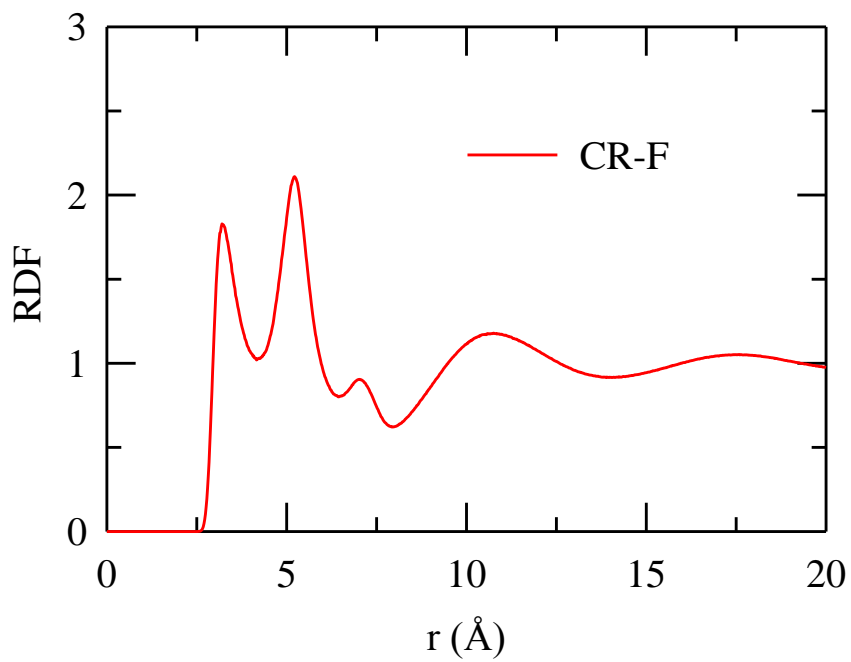


Figure F1: Radial distribution function calculated between CR of $BMIM^+$ and F of PF_6^- . The cut-off distance has been selected at the first minima to define H-bond.

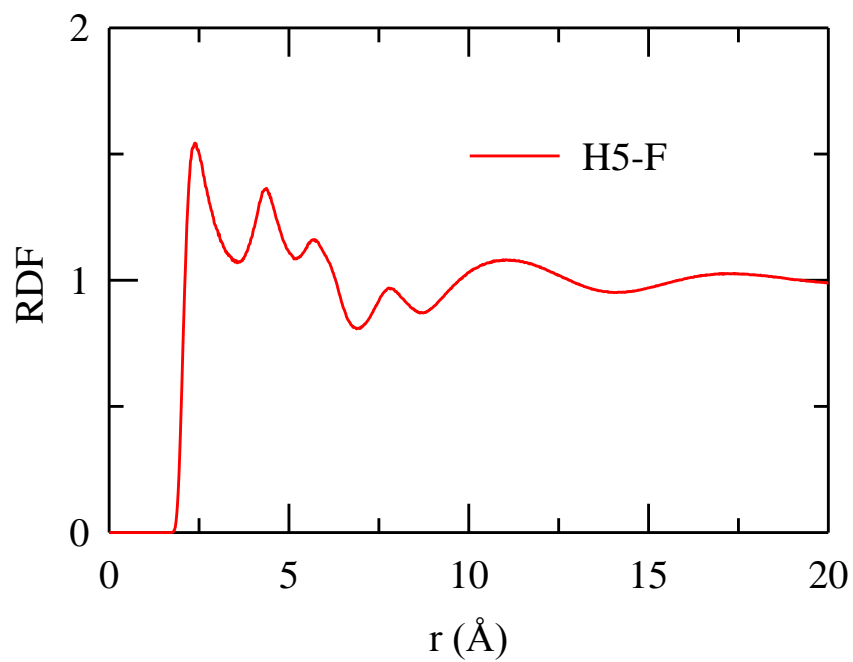


Figure F2: Radial distribution function calculated between H5 of $BMIM^+$ and F of PF_6^- . The cut-off distance has been selected at the first minima to define H-bond.

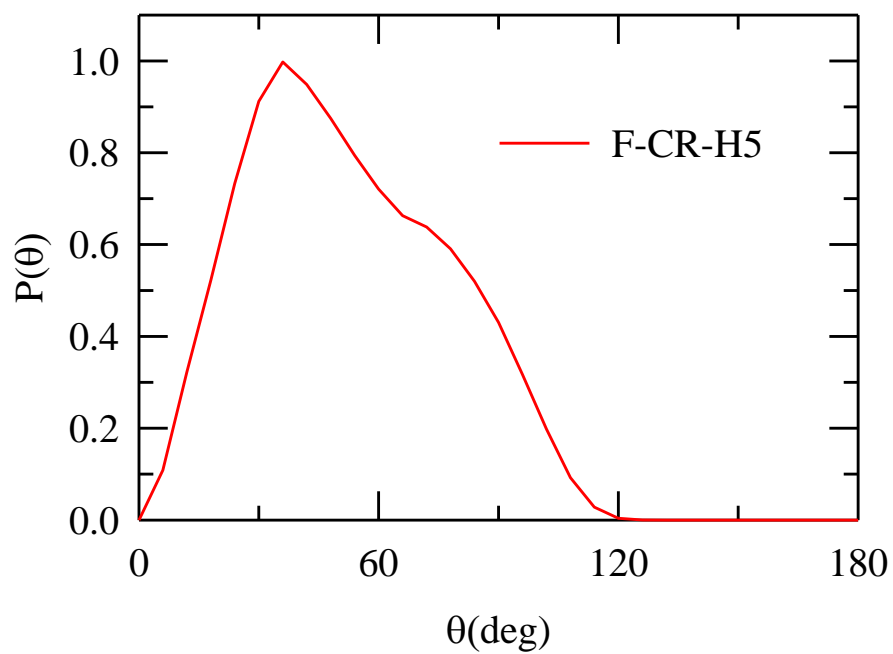


Figure F3: Normalized angular distribution for the angle F-CR-H5 constructed from the vectors joining CR and F, and joining CR and H5 atoms. The angle has been calculated when the corresponding distances (CR-F and CR-H5) are within the cut-off limit as defined by the respective radial distribution functions.

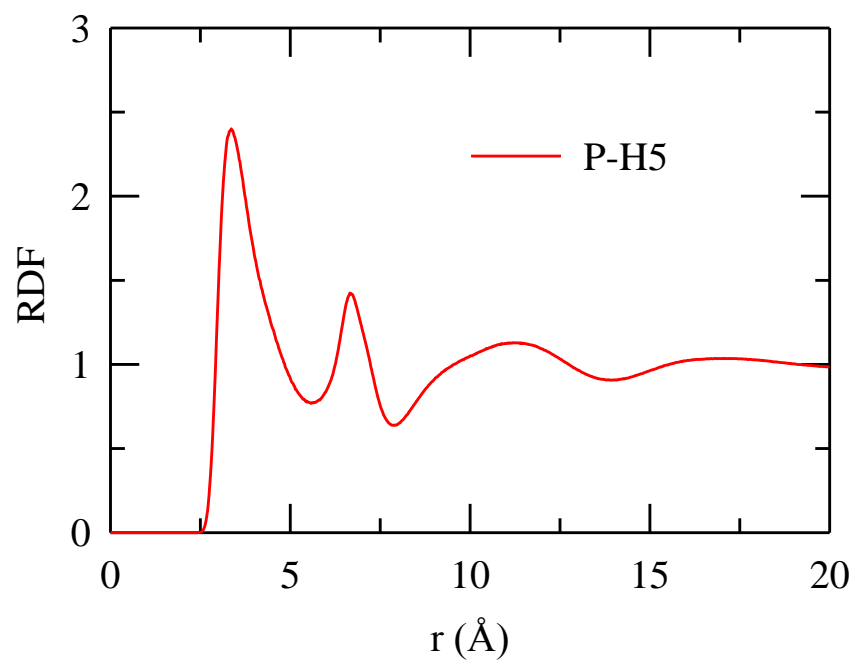


Figure F4: Radial distribution function calculated between P of PF_6^- and H5 of $BMIM^+$. The cut-off distance has been selected at the first minima to define H-bond.

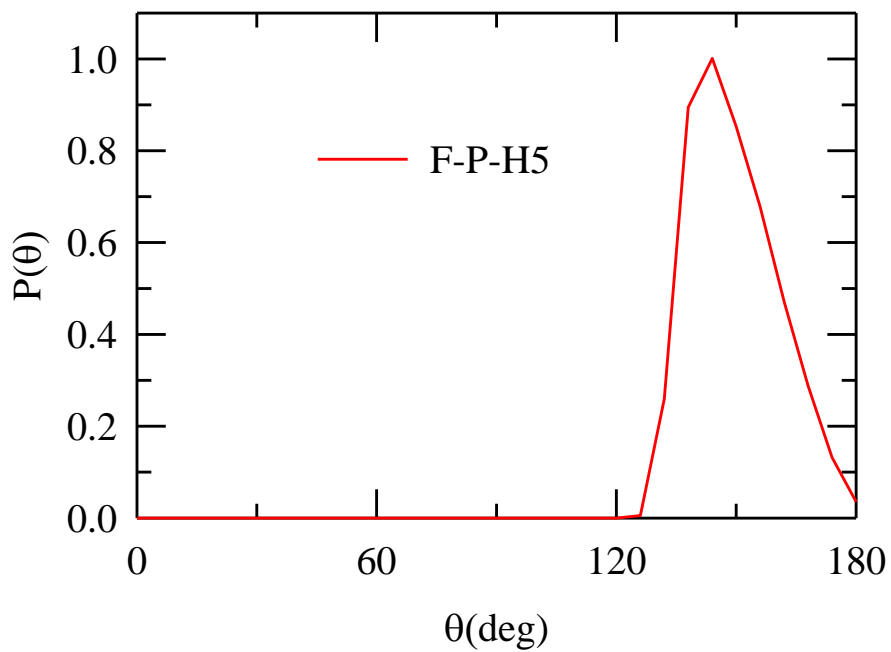


Figure F5: Normalized angular distribution for the angle F-P-H5 constructed from the vectors joining P and F, and joining P and H5 atoms. The angle has been calculated when the corresponding distances (P-F and P-H5) are within the cut-off limit as defined by the respective radial distribution functions.

Addendum I

Urea Induced ‘Homogenization’ of Amide/Electrolyte Deep Eutectics: Initial Simulation Results

Ad. 1.1. Introduction

Here we present initial simulation results on the effects due to addition of urea in acetamide/electrolyte deep eutectic solvents (DESs). We have considered lithium bromide ($LiBr$) and lithium nitrate ($LiNO_3$) as electrolytes here. It has already been stressed that DESs of amide and electrolytes are industrially relevant because of easy preparation route, economic viability, low moisture sensitivity and biodegradable nature.¹⁻⁵ Applications of DESs can be found in electrodeposition, thermal salt cells, electricity production, synthesis of nanomaterials, semi-conductors, and other functional materials etc.¹⁻⁷ Acetamide has been chosen because of its exquisite solvent properties,⁸⁻¹⁰ presence of several functional groups, high dielectric constant ($\epsilon_0 \approx 60$)¹¹ and quite large dipole moment ($3.7 D$).¹¹ Urea is a well-known protein denaturant¹²⁻¹³ with the ability of forming extensive hydrogen bonds.¹⁴ Previously we have observed that acetamide/urea DESs produces a homogeneous melt mixture.¹⁵ On the other hand, acetamide/electrolytes DESs show pronounced signature of spatio-temporal heterogeneity.¹⁶⁻¹⁸ Therefore, a natural curiosity drives us to investigate whether urea affects the heterogeneity aspect of acetamide/electrolyte DESs. We have calculated mean-squared displacements (MSD), non-Gaussian parameters (α_2 and γ), and acetamide dynamic structure factor ($F_s(k,t)$) to investigate this question.

Ad. 1.2. Simulation Details

All-atom molecular dynamics simulations were performed with a total of 512 number of particles for $0.10LiX + 0.90[f(CO(NH_2)_2) + (1-f)CH_3CONH_2]$ DESs with $X^- = Br^-$ and NO_3^- at $f = 0.4$ mole fraction at 338 K with GROMACS version 4.5.4,¹⁹ where the molecules interacted via the following potential function:

$$U(R) = \sum_{bonds} K_r (r - r_{eq})^2 + \sum_{angles} K_\theta (\theta - \theta_{eq})^2 + \sum_{dihedrals} K_\phi (1 + \cos(n\phi - \delta)) + \sum_{i < j}^{atoms} \left(\frac{A_{ij}}{R_{ij}^{12}} - \frac{B_{ij}}{R_{ij}^6} \right) + \sum_{i < j}^{atoms} \frac{q_i q_j}{4\pi\epsilon_0 R_{ij}}. \quad (\text{Ad. 1.1})$$

Note this particular potential function form has been used frequently for simulating structure and dynamics of various amide DESs and ionic liquids.^{16,18,20-28} In Eq. Ad.1.1, K_r is the bond constant with the equilibrium bond distance r_{eq} , K_θ is the angle constant with the equilibrium angle θ_{eq} , K_ϕ is the dihedral constant with periodicity n , dihedral angle ϕ and phase shift δ . R_{ij} is the distance between i and j atom with partial charges q_i and q_j , respectively. CHARMM²⁹ force field parameters were used for acetamide and GROMOS96 force field parameters were taken for urea.³⁰ The force field parameters for Li^+ , Br^- and NO_3^- were taken from the existing literature.³¹⁻³² All these potential parameters were used earlier for simulating various structural and dynamical properties of acetamide/electrolyte¹⁶ and acetamide/urea DESs.¹⁵ The short-range van der Waals interaction was represented by the Lennard-Jones (LJ) potential, and the long-range electrostatic potential was treated via particle mesh Ewald summation technique (PME).³³

The initial configuration was built using Packmol³⁴ and minimized via steepest decent algorithm in GROMACS. The H-bonds of acetamide and urea molecules were kept constraint by applying the shake³⁵ algorithm with tolerance value of 10^{-4} . Then each system was heated slowly from 100 K to 200 K and finally to 338 K with each step continuing for 100 ps in NVT. The final configuration was equilibrated in NPT ensemble at 1 atm pressure using Berendsen temperature

and pressure coupling³⁶ with relaxation time of 0.5 ps and 2.0 ps, respectively for 1 ns. Experimental density was reached after such an equilibration. The simulated density was found to be 1.17 gm/cc and 1.16 gm/cc for Br^- and NO_3^- containing DESs, respectively which match closely with the corresponding experimental values.³⁷ Subsequently, further equilibration of 2 ns followed by a production run of 20 ns was carried out in NVT ensemble using Nose-Hoover thermostat.³⁸⁻³⁹ Periodic boundary conditions were employed in all three directions, and the equations of motion were integrated using a time step of 0.5 fs employing the leap-frog algorithm.⁴⁰ The trajectories were saved every 0.1 ps for data analyses and simulation results.

Ad. 1.3. Results and Discussion

Ad. 1.3.1. Mean-squared displacements (MSD)

MSD provides the simplest evidence for the presence of heterogeneity via a weaker time dependence of MSD ($\propto t^\alpha$, $\alpha < 1$) than the predicted linear dependence after the initial ballistic regime. This t^α dependence is a signature of the rattling in a cage motion⁴¹ and has been routinely found for supercooled liquids⁴² and room temperature ionic liquids.⁴³ Figure Ad. 1.1 shows the simulated MSD curves for acetamide/LiBr/urea and acetamide/LiNO₃/urea. Note in this figure there is no indication of t^α dependence apart from the expected t^2 dependence at the initial regime and t^1 dependence at long time. This indicates the spatially homogeneous dynamics

of these DESs. Translational diffusion coefficients ($D_T = \left[\frac{\langle |\Delta r(t)|^2 \rangle}{6t} \right]_{t \rightarrow \infty}$) of acetamide and urea

have been obtained from MSD plots and summarized in Table Ad. 1.1. It is observed that the diffusion coefficient of acetamide is higher in presence of NO_3^- . However, for urea, the diffusion co-efficient is found to be insensitive to the electrolyte.

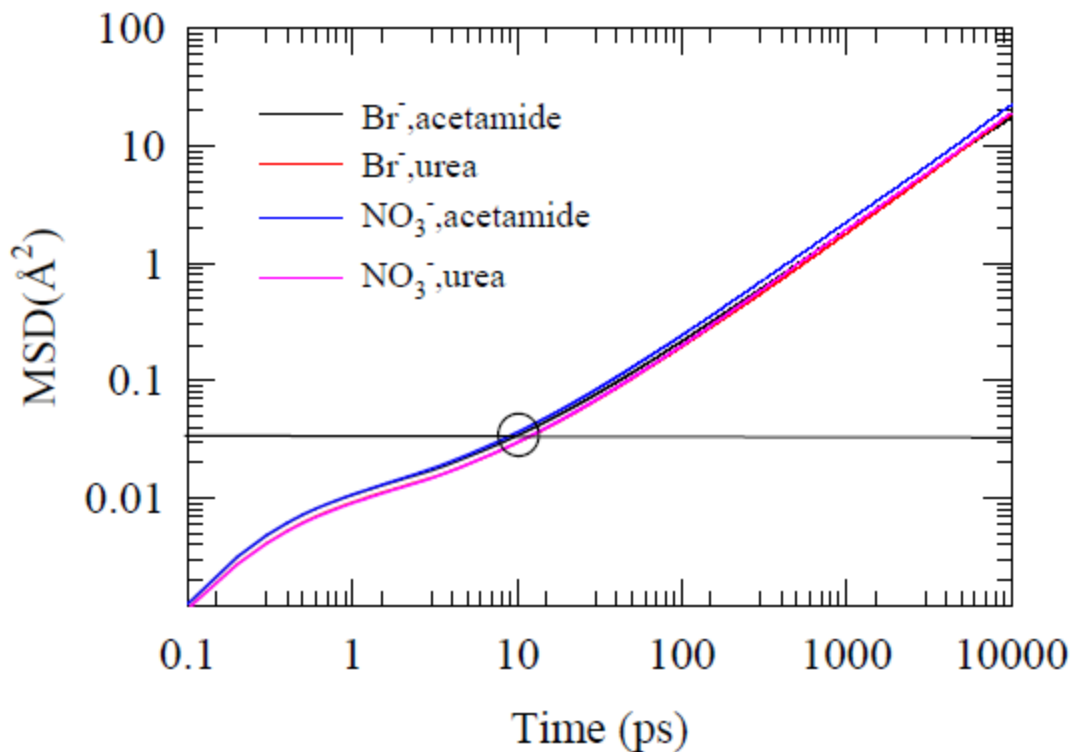


Figure Ad. 1.1: Anion dependence of simulated MSDs for acetamide and urea in $0.10LiX + 0.90[f(CO(NH_2)_2) + (1-f)CH_3CONH_2]$ deep eutectics at 338 K. Circle on MSD curves denote the simulated MSD values at 10 ps. Representations are color coded.

Table Ad. 1.1: Translational diffusion coefficients for acetamide and urea obtained from respective MSD plots at 338 K.

Anion	Diffusion Coefficients for acetamide ($\times 10^6 cm^2 / sec$)	Diffusion Coefficients for urea ($\times 10^6 cm^2 / sec$)
Br^-	2.8 ± 0.01	3.0 ± 0.05
NO_3^-	3.7 ± 0.02	3.1 ± 0.01

Ad. 1.3.2. Non-Gaussian and new non-Gaussian parameters

A routine check for dynamic heterogeneity can be performed via the calculations of the non-Gaussian (α_2) and the new non-Gaussian parameters (γ), defined earlier in Chapter 6 of this Thesis. Note both these parameters provide estimates of the heterogeneity timescales and associated with particle displacement distributions. α_2 is related to the particles which move more than the predicted Gaussian distribution and γ is strongly influenced by the particles which move less than the predicted Gaussian distribution. For a system which does not show any signature of dynamic heterogeneity, both these parameters are expected to overlap significantly and also the peak times are close to each other.¹⁵ Figure Ad. 1.2 shows a comparison of these two parameters in presence of Br^- and NO_3^- . As discussed before, both the curves overlap significantly with similar peak heights (~0.25-0.30) and also similar peak times (~20-30 ps). This provides us another evidence of the homogeneous environment of the medium.

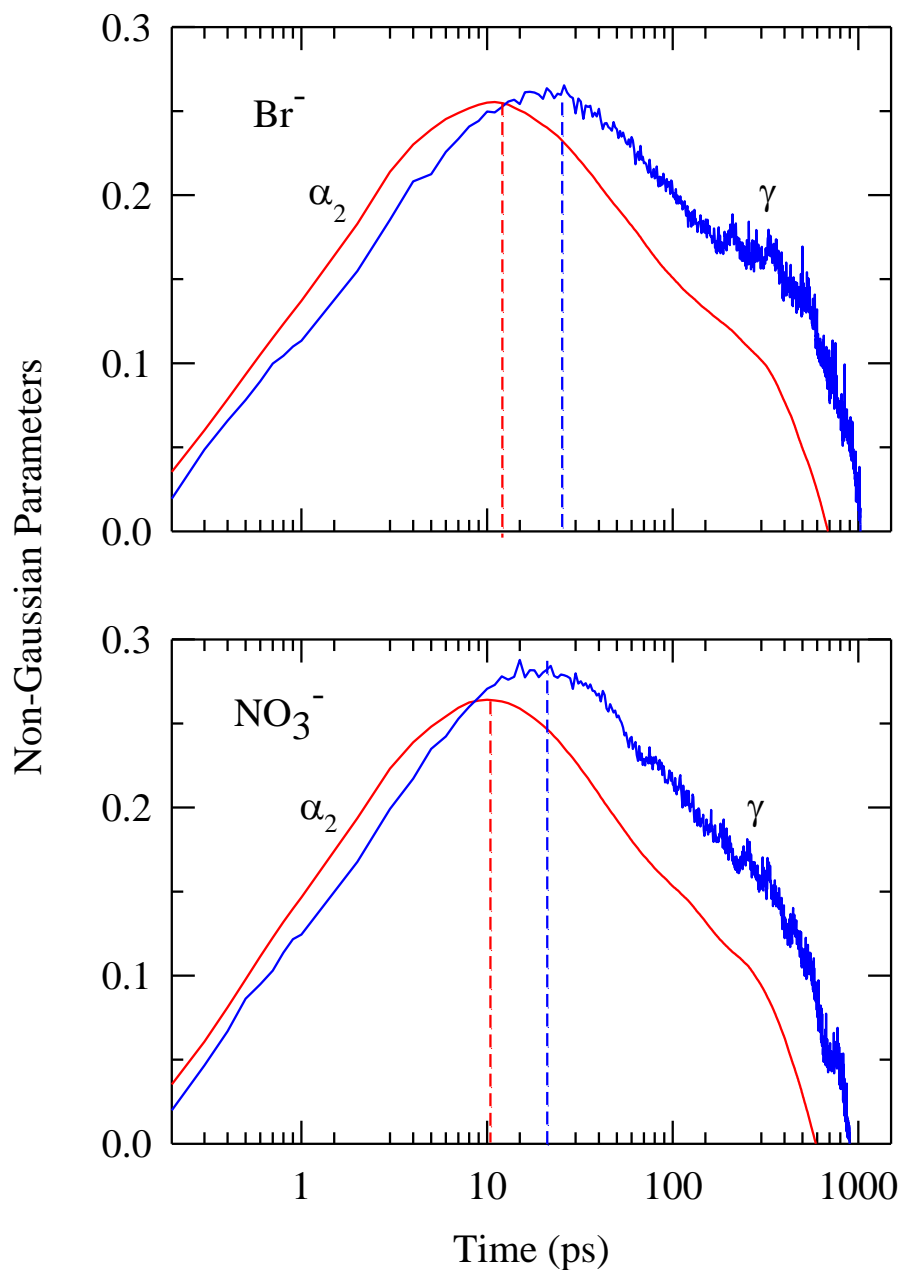


Figure Ad. 1.2: Anion dependence of simulated non-Gaussian (α_2) and new non-Gaussian parameters (γ) for acetamide in $0.10\text{LiX} + 0.90[f(\text{CO}(\text{NH}_2)_2) + (1-f)\text{CH}_3\text{CONH}_2]$ deep eutectics at 338 K. Vertical lines indicate the peak times (approximate) for the respective plot. Representations are color coded.

Ad. 1.3.3. Acetamide dynamic structure factor: Density relaxation profile and timescale

Next, we discuss the density relaxation profile, $F_s(k,t)$ of acetamide in presence of both the electrolytes. The importance of the dynamic structure factor stems from the fact that the stretched exponential relaxation of the corresponding density relaxation function is often considered as a signature of the presence of dynamic heterogeneity.⁴⁴ Figure Ad. 1.3 presents the decay of the normalized self part of the dynamic structure factor at two different wave vectors, lowest wavevector accessible to the present simulation ($k = 0.23 \text{ \AA}^{-1}$) and to the nearest neighbour wavevector ($k = 1.34 \text{ \AA}^{-1}$). The upper panel shows the decay in presence of Br^- and the lower panel shows the same for NO_3^- . Multi-exponential fit parameters for all the decays are provided in Table Ad. 1.2. The absence of any stretched exponential decay corroborates well with the homogeneous dynamics of these DESs. Also, the relaxations corresponding to the nearest neighbour wavenumber possess a significant sub-picosecond component with average relaxation time ~ 15 ps. Such a faster nearest neighbour density relaxation implies that one would not be able to observe excitation wavelength dependence of emission even with a shorter lifetime probe as seen earlier with acetamide/urea DESs.¹⁵

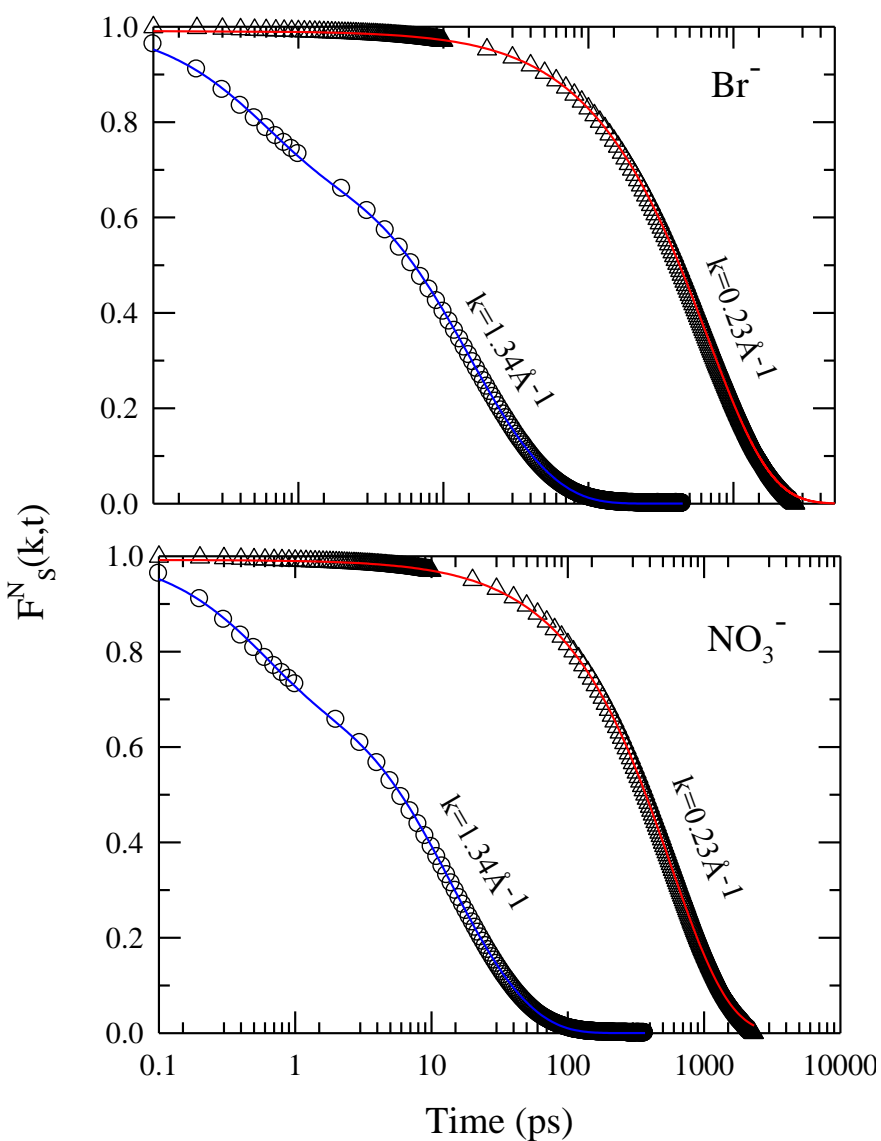


Figure Ad. 1.3: Anion dependence of simulated wavenumber dependent relaxation of the normalized self part of the acetamide dynamic structure factor, $F_s^N(k,t)$, for $0.10\text{LiX} + 0.90[f(\text{CO}(\text{NH}_2)_2) + (1-f)\text{CH}_3\text{CONH}_2]$ deep eutectics at 338 K. Multi-exponential fits through the simulated data are shown by the solid lines.

Table Ad. 1.2: Multi-exponential fit parameters for simulated wavenumber dependent $F_S^N(k,t)$ for acetamide in presence of various electrolytes at 338 K.

Anion	k (\AA^{-1})	a_1	τ_1 (ps)	a_2	τ_2 (ps)	a_3	τ_3 (ps)	β	$\langle\tau\rangle$ (ps)
Br^-	0.23	0.05	86.2	0.95	666.7	-	-	1.0	637.6
	1.34	0.27	0.5	0.35	10.1	0.38	30.0	1.0	15.1
NO_3^-	0.23	0.02	34.6	0.98	555.6	-	-	1.0	545.2
	1.34	0.27	0.5	0.35	10.0	0.38	27.0	1.0	14.0

References

1. D. V. Wagle, H. Zhao, and G. A. Baker, *Acc. Chem. Res.* **47**, 2299 (2014).
2. Q. Zhang, K. De Oliveira Vigier, S. Royer, and F. Jérôme, *Chem. Soc. Rev.* **41**, 7108 (2012).
3. A. P. Abbott, G. Capper, D. L. Davies, R. K. Rasheed, and V. Tambyrajah, *Chem. Commun.* **70** (2003).
4. A. P. Abbott, D. Boothby, G. Capper, D. L. Davies, and R. K. Rasheed, *J. Am. Chem. Soc.* **126**, 9142 (2004).
5. M. Francisco, A. van den Bruinhorst, and M. C. Kroon, *Angew. Chem. Int. Ed.* **52**, 3074 (2013).
6. N. S. V. Narayanan, B. V. Ashokraj, and S. Sampath, *J. Colloid Interf Sci* **342**, 505 (2010).
7. R. Wallace and P. Bruins, *J. Electrochem. Soc.* **114**, 212 (1967).
8. O. F. Stafford, *J. Am. Chem. Soc.* **55**, 3987 (1933).
9. R. A. Wallace, *Inorg. Chem.* **11**, 414 (1972).
10. R. A. Wallace, *J. Phys. Chem.* **75**, 2687 (1971).
11. D. H. Kerridge, *Chem. Soc. Rev.* **17**, 181 (1988).
12. A. Wallqvist, D. Covell and D. Thirumalai, *J. Am. Chem. Soc.* **120**, 427 (1998).
13. B. J. Bennion and V. Daggett, *Proc. Natl. Acad. Sci. U.S.A.* **100**, 5142 (2003).
14. L. B. Sagle, Y. Zhang, V. A. Litosh, X. Chen, Y. Cho, and P. S. Cremer, *J. Am. Chem. Soc.* **131**, 9304 (2009).
15. A. Das, S. Das, and R. Biswas, *J. Chem. Phys.* **142**, 034505 (2015).

16. B. Guchhait, S. Das, S. Daschakraborty, and R. Biswas, *J. Chem. Phys.* **140**, 104514 (2014).
17. K. Mukherjee, A. Das, S. Choudhury, A. Barman, and R. Biswas, *J. Phys. Chem. B* **119**, 8063 (2015).
18. S. Das, R. Biswas, and B. Mukherjee, *J. Phys. Chem. B* **119**, 11157 (2015).
19. D. van der Spoel, E. Lindahl, B. Hess, A. R. van Buuren, E. Apol, P. J. Meulenhoff, D. P. Tieleman, A. L. T. M. Sijbers, K. A. Feenstra, R. van Drunen, and H. J. C. Berendsen, *Gromacs User Manual version 4.5.4*, www.gromacs.org (2010).
20. J. Habasaki and K. Nagi, *J. Chem. Phys.* **129**, 194501 (2008).
21. T. Pal and R. Biswas, *Theor. Chem. Acc.* **132**, 1348 (2013).
22. M. G. Del Popolo and G. A. Voth, *J. Phys. Chem. B* **108**, 1744 (2004).
23. T. I. Morrow and E. J. Maginn, *J. Phys. Chem. B* **106**, 12807 (2002).
24. T. Pal and R. Biswas, *J. Phys. Chem. B* **119**, 15683 (2015).
25. C. G. Hanke, S. L. Price, and R. M. Lynden-Bell, *Mol. Phys.* **99**, 801 (2001).
26. C. J. Margulis, *Mol. Phys.* **102**, 829 (2004).
27. A. Das, S. Das, and R. Biswas, *Chem. Phys. Lett.* **581**, 47 (2013).
28. S. Das, R. Biswas, and B. Mukherjee, *J. Phys. Chem. B* **119**, 274 (2015).
29. A. D. MacKerell Jr., J. Wiorcikiewicz-Kuczera, and M. Karplus, *J. Am. Chem. Soc.* **117**, 11946 (1995).
30. L. J. Smith, H. J. C. Berendsen, and W. F. van Gunsteren, *J. Phys. Chem. B* **108**, 1065 (2004).
31. K. P. Jensen and W. L. Jorgensen, *J. Chem. Theory Comput.* **2**, 1499 (2006).
32. J. N. Canongia Lopes, J. Deschamps, A. A. H. Padua, *J. Phys. Chem. B* **108**, 2038 (2004).
33. U. Essmann, L. Perera, M. L. Berkowitz, T. Darden, H. Lee, and L. G. Pedersen, *J. Chem. Phys.* **103**, 8577 (1995).

34. L. Martinez, R. Andrade, E. G. Birgin, and J. M. Martinez, *J. Comput. Chem.* **30**, 2157 (2009).
35. J. P. Ryckaert, G. Ciccotti, and H. J. C. Berendsen, *J. Comput. Phys.* **23**, 327 (1977).
36. H. J. C. Berendsen, J. P. M. Postma, W. F. van Gunsteren, A. DiNola, and J. R. Haak, *J. Chem. Phys.* **81**, 3684 (1984).
37. S. Nose, *Mol. Phys.* **52**, 255 (1984).
38. A. Das, S. Das, and R. Biswas, *J. Chem. Phys.* (to be submitted)
39. W. G. Hoover, *Phys. Rev. A* **31**, 1695, (1985).
40. R. W. Hockney, S. P. Goel, and J. Eastwood, *J. Comp. Phys.* **14**, 148 (1974).
41. J. P. Hansen and I. R. McDonald, *Theory of Simple Liquids*, 3rd Ed. (Academic, San Diego, **2006**).
42. F. Faupel, W. Frank, M.-P. Macht, H. Mehrer, V. Naundorf, K. Ratzke, and H. R. Schober, *Rev. Mod. Phys.* **75**, 237 (2003).
43. D. Roy, N. Patel, S. Conte, and M. Maroncelli, *J. Phys. Chem. B* **114**, 8410 (**2010**).
44. C. A. Angell, K. L. Ngai, G. B. McKenna, P. F. McMillan, and S. W. Martin, *J. Appl. Phys.* **88**, 3113 (2000).

Addendum II

Hydrogen Bond Dynamics and Viscosity Calculation of Molten Urea and Acetamide/Urea Deep Eutectic Solvent: Initial Simulation Results

Ad. 2.1. Introduction

Here we present initial results from our simulation study of the hydrogen bond (H-bond) fluctuation dynamics of molten urea at 406 K and acetamide/urea deep eutectic solvent (DES) simulated at 335 K. These two temperatures are selected because these systems become molten at these temperatures. DESs are rapidly emerging as solvents for large scale industrial and technological applications because of their exquisite solvent properties, easy preparation route, bio-degradable nature and economical viability.¹⁻⁷ Though DESs have huge potential for large scale applications as reaction media, the static and dynamic aspects of these systems have remained still largely unexplored. Recent time-resolved fluorescence measurements coupled with all-atom molecular dynamic simulation have shown that acetamide/urea DESs are homogeneous media and density relaxation does not bear any signature of distributed kinetics.⁸ We have conducted a detailed analysis here to explore the H-bond dynamics of molten urea and also acetamide/urea DES. For acetamide/urea DES, we have divided the total contribution of H-bond into three parts: (a) acetamide-acetamide, (b) acetamide-urea and (c) urea-urea. This would provide a better understanding of molecular interactions and individual contributions. Also we have simulated the viscosity of both the media. Note viscosity of molten urea (~406 K) is not experimentally available and therefore the present simulations provide a guiding result here.

Ad. 2.2. Simulation Details

All-atom molecular dynamics simulation was performed with 512 numbers of particles for acetamide/urea DES at 335 K at 0.6 mole fraction of acetamide. Additionally, 256 number of urea molecules were simulated at 406 K. All simulations were carried with GROMACS version 4.5.4,⁹ where the molecules interacted via the following potential:

$$U(R) = \sum_{bonds} K_r (r - r_{eq})^2 + \sum_{angles} K_\theta (\theta - \theta_{eq})^2 + \sum_{dihedrals} K_\phi (1 + \cos(n\phi - \delta)) + \sum_{i < j}^{atoms} \left(\frac{A_{ij}}{R_{ij}^{12}} - \frac{B_{ij}}{R_{ij}^6} \right) + \sum_{i < j}^{atoms} \frac{q_i q_j}{4\pi\epsilon_0 R_{ij}}. \quad (\text{Ad. 2.1})$$

This particular form of the potential function has been used frequently for simulating liquid structure and dynamics of ionic liquids and DESs.¹⁰⁻¹⁹ In Eq. Ad 2.1, K_r denotes the bond constant with the equilibrium bond distance r_{eq} , K_θ the angle constant with the equilibrium angle θ_{eq} , K_ϕ the dihedral constant with periodicity n , dihedral angle ϕ and phase shift δ . R_{ij} is the distance between i and j atoms with partial charges q_i and q_j , respectively. CHARMM²⁰ force field parameters were used for acetamide and GROMOS96 force field parameters were taken for urea for the simulation.²¹ These force field parameters were used earlier to simulate various dynamical properties for acetamide/electrolyte DESs²² and acetamide/urea DES⁸ that were in reasonable agreement with experiments. The short-range van der Waals interaction was represented by the Lennard-Jones (LJ) potential, and the long-range electrostatic potential was treated via particle mesh Ewald summation technique (PME).²³

The initial configuration was built using Packmol²⁴ and minimized via steepest decent algorithm in GROMACS. Then each system was heated slowly from 100 K to the final temperature via a step-up process of step 100 K with each step continuing for 100 ps in NVT ensemble. The final configuration was equilibrated in NPT ensemble at 1 atm pressure using V-rescale thermostat²⁵ and Berendsen pressure coupling²⁶ with relaxation time of 0.5 ps and 2.0 ps respectively for 1 ns. Subsequently, further equilibration of 2 ns followed by a production run of 10 ns was carried out

in NPT ensemble using V-rescale thermostat²⁵ and Parrinello-Rahman barostat²⁷⁻²⁸ with relaxation time of 0.5 ps and 2.0 ps respectively. Density for the acetamide/urea DES was found to be 1.14 gm/cc at 335 K and for urea 1.29 gm/cc at 406 K. Simulated density of acetamide/urea DES agrees well with the respective experimental density.⁸ Unfortunately experimental density of molten urea at 406 K is not available in literature. Periodic boundary conditions were employed in all three directions, and the equations of motion were integrated using a time step of 0.5 fs employing the leap-frog algorithm.²⁹ Simulated trajectories were saved every 10 fs for data analyses and simulation results. Separate production runs in NPT ensemble were carried out for each system for 10 ns for the viscosity calculation. The pressure tensor values were saved for 10 fs for the viscosity calculation.

Ad. 2.3. Simulation Results

We have simulated various timescales associated with the H-bond relaxations in molten urea and acetamide/urea DES. Before going to the details, we first define H-bond and H-bond correlation functions. Note, both acetamide and urea molecules are capable of forming inter- and intra-species H-bonds. Hence for a better understanding, we have trisected the total contribution of the H-bond in acetamide/urea DES into three categories (a) acetamide-acetamide (acet-acet) H-bond, (b) acetamide-urea (acet-urea) H-bond, and (c) urea-urea H-bond. This separate analysis would help understanding the origin of different timescales reported by experiments. We have defined H-bond between various pairs based on widely accepted geometric criteria^{50,73,98} which considers distance (R) and angle (θ). Specifically, two urea molecules are considered to be H-bonded if, (i) the distance between the oxygen and nitrogen atoms of two different $CO(NH_2)_2$ molecules, R_{ON} , is less than a cut-off distance, $R_{cut-off}$ and (ii) the angle between the vector joining this nitrogen and one of the hydrogens of one $CO(NH_2)_2$ molecule and the vector joining this nitrogen and an oxygen atom belonging to another urea molecule, θ_{ONH} , is less than 30° . The cut-off distance, $R_{cut-off}$ is selected based on the first minima of the corresponding radial distribution function (RDF). Here, we have taken $R_{cut-off} = 4.2 \text{ \AA}$ by looking at the

$O(CONH_2)_2 - N(CONH_2)_2$ RDF for urea at 406 K as shown in Figure Ad. 2.1 (upper panel). Following the similar protocol, we have defined H-bond among acetamide-urea and acetamide-acetamide pairs. $R_{cut-off}$ is selected as 4.5 Å for both acetamide-urea and acetamide-acetamide H-bond. The corresponding RDFs are provided in Figure Ad. 2.1 (lower panel). For all the pairs, the angle cut-off is chosen as 30° .

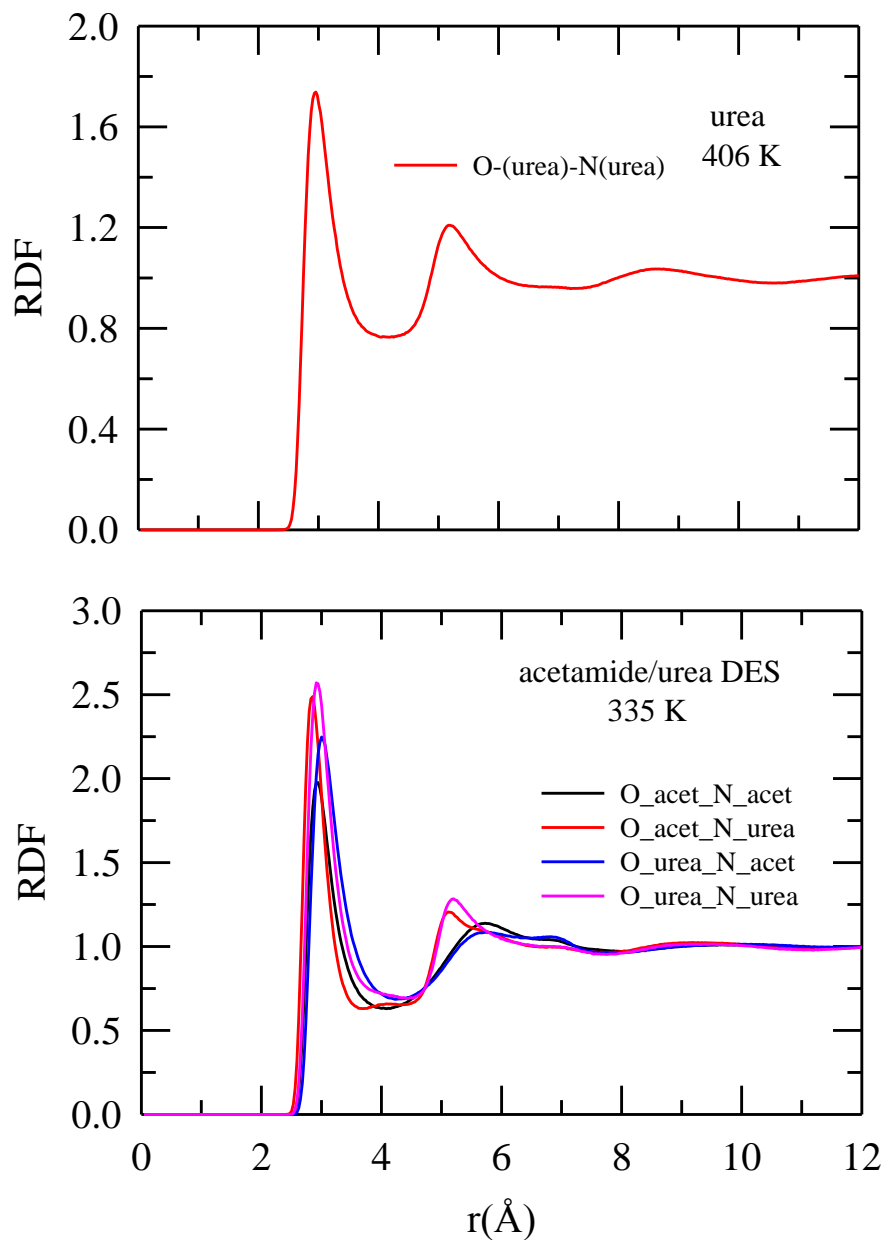


Figure Ad. 2.1: Radial distribution function (RDF), between oxygen and nitrogen atoms belonging to different urea molecules simulated at 406 K (upper panel). In the lower panel various RDFs are shown to define three different types of H-bond of acetamide/urea deep eutectic at 335 K. The cutoff distance for H-bond definition is selected as the first minima of the corresponding RDF.

Based on the above set of criteria, we have selected pair of molecules which are H-bonded and then calculated two well-known H-bond correlation functions, $C_{HB}(t)$ and $S_{HB}(t)$, respectively. $C_{HB}(t)$ is related to the structural relaxation of the molecules due to translational and rotational diffusion. It can be defined in the following way:³²⁻³⁶

$$C_{HB}(t) = \langle h(0)h(t) \rangle / \langle h \rangle \quad (\text{Ad. 2.2})$$

Here $h(t')$ is a variable for a pair of molecules and $h(t') = 1$ if the pair is H-bonded at time t and zero otherwise. The angular bracket denotes the averaging over time origins and number of molecules. $C_{HB}(t)$ is essentially related to a relaxation process where a pair of molecules is H-bonded at time $t = 0$ and also at a later time t allowing possible breaking and reforming in the intermediate time. Hence it relates to the timescale coming from the structural relaxation.³⁷ On the contrary, $S_{HB}(t)$ requires the continuous presence of a H-bond without breaking in the intermediate time. It can be defined in the following way:³²⁻³⁴

$$S_{HB}(t) = \langle h(0)H(t) \rangle / \langle h \rangle \quad (\text{Ad. 2.3})$$

Here $h(t')$ is a time variable for a pair of molecules and $h(t') = 1$ if the pair is H-bonded at time t and zero otherwise. $H(t)$ is a history dependent variable of $h(t')$ and $H(t) = 1$ if the pair remain continuously H-bonded between any arbitrary time origin t_0 and later time $t_0 + t$. Therefore, $S_{HB}(t)$ represents the lifetime of H-bond. The average timescale associated with $S_{HB}(t)$ is generally faster than $C_{HB}(t)$ by an order of magnitude.

Figure Ad. 2.2 shows the relaxation of H-bonds of molten urea at 406 K. The upper panel shows the decay of $S_{HB}(t)$ and the lower panel shows the same for $C_{HB}(t)$. Multi-exponential fitting parameters for $S_{HB}(t)$ and $C_{HB}(t)$ are shown in the inset of each panel. The average time calculated from $S_{HB}(t)$ is 0.20 ps and from $C_{HB}(t)$ is ~ 37 ps. Other than the sub-picosecond component (0.1ps), the three time components obtained from the fitting of $C_{HB}(t)$ matches pretty well with time constants obtained from dielectric relaxation³⁸ (DR) experiments. Figure Ad. 2.3 presents the relaxations of various types of H-bonds of acetamide/urea DES at 335K. The upper panel shows the decay of $S_{HB}(t)$ and the lower panel shows the same for $C_{HB}(t)$. Multi-exponential fitting parameters for all the relaxations are provided in Table Ad. 2.1. The average lifetime, as calculated from $S_{HB}(t)$, of urea-urea H-bond (0.40 ps) is almost equal to that of acetamide-urea H-bond and slightly shorter than acetamide-acetamide H-bond (0.33 ps). However, for $C_{HB}(t)$, the average time constant for urea-urea H-bond (~ 122 ps) is ~ 2 times higher than that of acetamide-urea H-bond (~ 67 ps) and ~ 3 times than acetamide-acetamide H-bond (~ 39 ps). Like molten urea, the simulated time constants for the structural relaxation of the H-bonds in acetamide/urea system match quite well with the DR time scales.³⁸

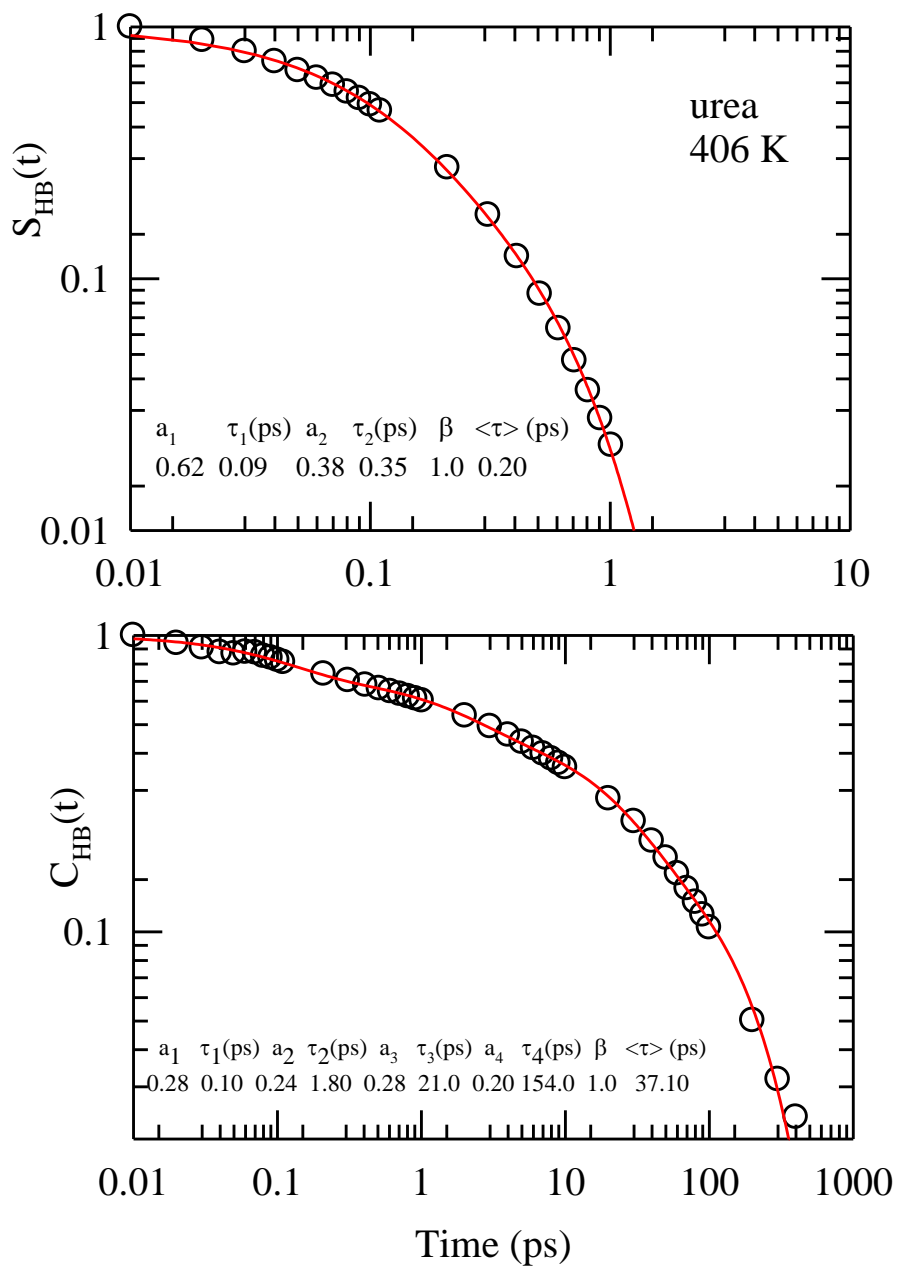


Figure Ad. 2.2: Simulated decay of the H-bond correlation functions among urea molecules at 406 K, $S_{HB}(t)$ and $C_{HB}(t)$. Multi-exponential fitting parameters are provided inside the panels.

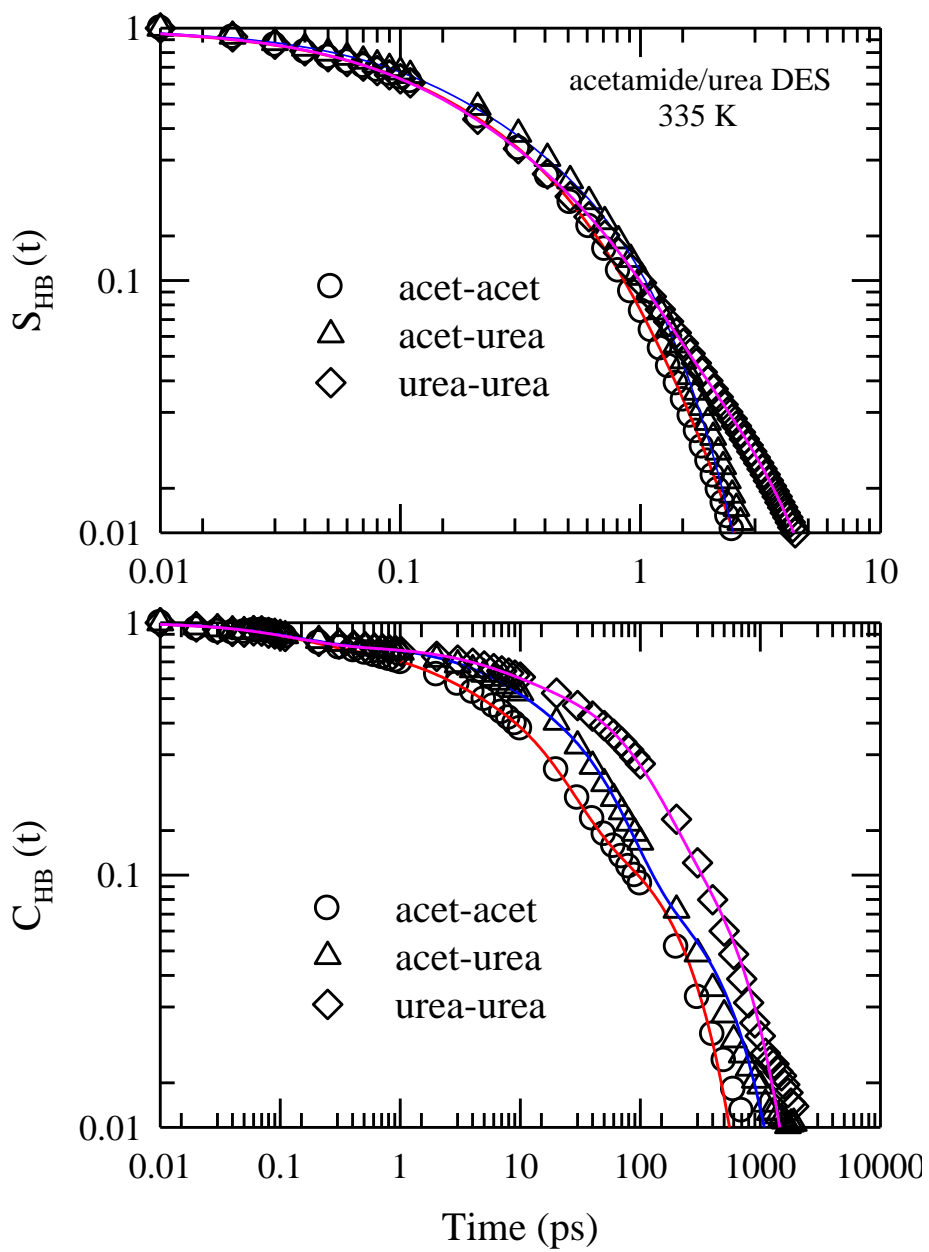


Figure Ad. 2.3: Simulated decay of the H-bond correlation functions among various pairs of acetamide/urea deep eutectic at 335 K, $S_{HB}(t)$ and $C_{HB}(t)$.

Table Ad. 2.1: Multi-exponential fitting parameters for $S_{HB}(t)$ and $C_{HB}(t)$ among various types of H-bond pairs for acetamide/urea DES at 335 K.

$S_{HB}(t)$	Type	a_1	τ_1 (ps)	a_2	τ_2 (ps)	a_3	τ_3 (ps)	a_4	τ_4 (ps)	β	$\langle\tau\rangle$ (ps)
	acet-acet	0.27	0.08	0.57	0.30	0.16	0.90	-	-	1.0	0.33
	acet-urea	0.43	0.12	0.57	0.60	-	-	-	-	1.0	0.40
	urea-urea	0.42	0.10	0.49	0.41	0.09	2.0	-	-	1.0	0.42
$C_{HB}(t)$	acet-acet	0.19	0.13	0.20	1.80	0.45	15.0	0.16	200.0	1.0	39.1
	acet-urea	0.19	0.12	0.23	5.60	0.48	41.3	0.10	454.5	1.0	66.6
	urea-urea	0.20	0.12	0.19	6.10	0.44	80.0	0.17	500.0	1.0	121.4

We have also simulated the shear viscosity co-efficients (η) for molten urea at 406 K and for acetamide/urea DES at 335 K. The viscosity co-efficients has been calculated from the simulated pressure autocorrelation function (PACF), $\langle P_{\alpha\beta}(t)P_{\alpha\beta}(0) \rangle$, which is given by the following Green-Kubo relation,³⁹

$$\eta = \frac{V}{k_B T} \int_0^{\infty} \langle P_{\alpha\beta}(t)P_{\alpha\beta}(0) \rangle dt \quad (\text{Ad. 2.4})$$

Here $\alpha, \beta = x, y, z$ and $P_{\alpha\beta}$ denotes the off-diagonal term of the pressure tensor. The pressure tensor can be calculated from the following relation:

$$P_{\alpha\beta} = \frac{1}{V} \left(\sum_i \frac{P_{i\alpha} P_{i\beta}}{m_i} + \sum_i \sum_{j>i} r_{ij} f_{ij\beta} \right) \quad (\text{Ad. 2.5})$$

Here $f_{ij\beta}$ is the simulated force and m_i is the mass for the i -th particle.⁴⁰

Simulated viscosity coefficient are found to be 0.7 ± 0.2 cP for molten urea at 406 K and 10.0 ± 2.0 cP for acetamide/urea DES at 335 K. Note the experimental viscosity of the acetamide/urea DES at 333 K is 9.87 cP and which is in well agreement with the simulated viscosity. The simulated decays of PACF for both the systems are provided in Figure Ad. 2.4 and Figure Ad. 2.5. The time convergence of the simulated viscosity coefficients are also provided for both the systems in Figure Ad. 2.6.

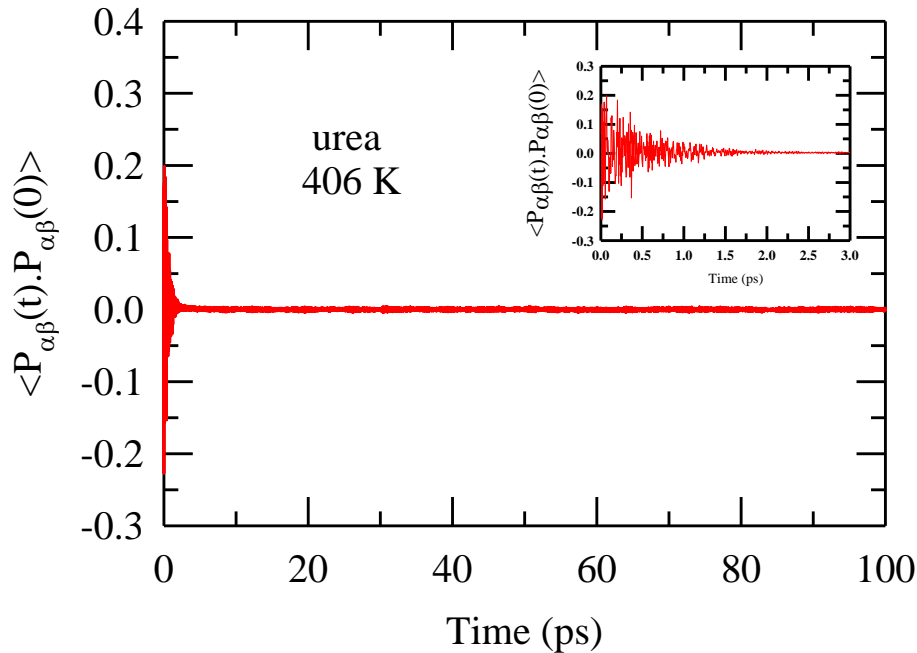


Figure Ad. 2.4: The decay of the pressure autocorrelation function for molten urea at 406 K. Strong fluctuations of pressure autocorrelation function at short times is shown in the inset.

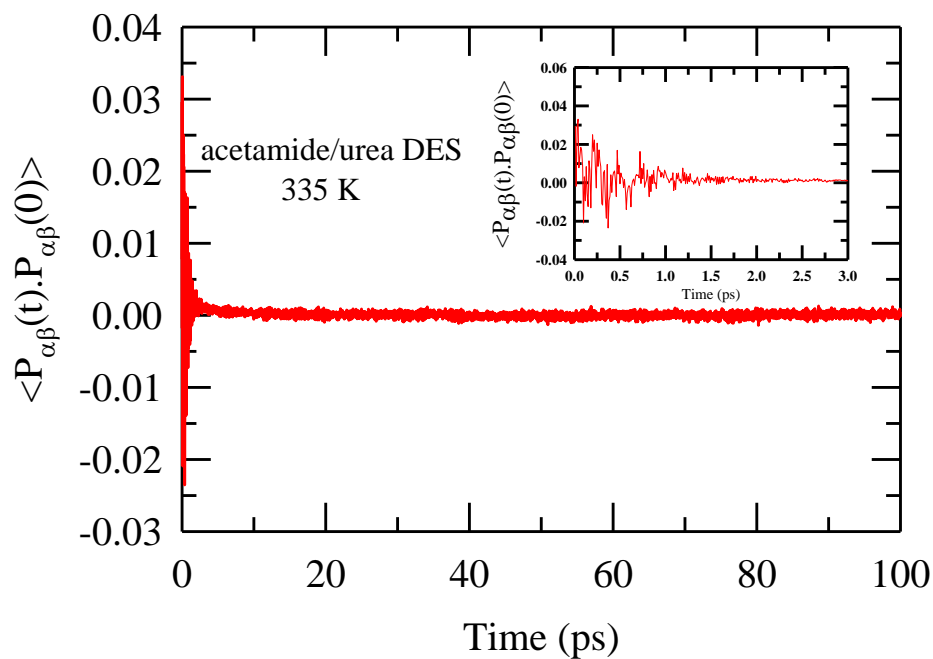


Figure Ad. 2.5: The decay of the pressure autocorrelation function for acetamide/urea deep eutectic at 335 K. Strong fluctuations of pressure autocorrelation function at short times is shown in the inset.

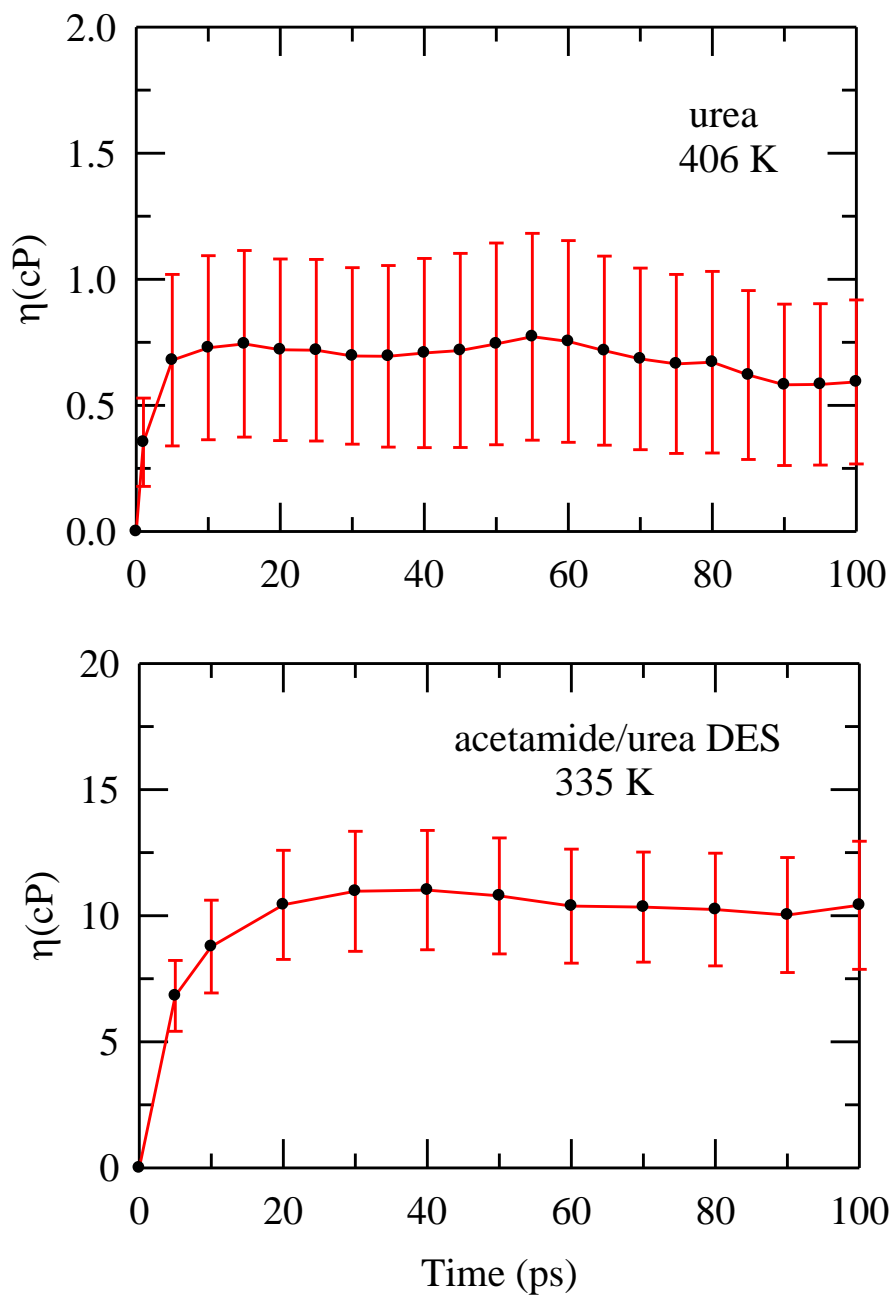


Figure Ad. 2.6: The computed viscosity (η) from the integration of pressure autocorrelation function along with the error bars are shown for molten urea at 406 K (upper panel) and for acetamide/urea deep eutectic (lower panel) at 335 K.

References

1. D. V. Wagle, H. Zhao, and G. A. Baker, *Acc. Chem. Res.* **47**, 2299 (2014).
2. Q. Zhang, K. V. De Oliveira, S. Royer, and F. Jerome, *Chem. Soc. Rev.* **41**, 7108 (2012).
3. A. P. Abbott, G. Capper, D. L. Davies, R. K. Rasheed, and V. Tambyrajah, *Chem. Commun.* **70** (2003).
4. A. P. Abbott, D. Boothby, G. Capper, D. L. Davies, and R. K. Rasheed, *J. Am. Chem. Soc.* **126**, 9142 (2004).
5. M. Francisco, A. van den Bruinhorst, and M. C. Kroon, *Angew. Chem. Int. Ed.* **52**, 3074 (2013).
6. P. Liu, W. J. Hao, P. L. Mo, and H. Z. Zhang, *RSC Adv.* **5**, 48675 (2015).
7. G. Garcia, S. Aparicio, R. Ullah, and M. Atilhan, *Applications. Energy Fuels.* **29**, 2616 (2015).
8. A. Das, S. Das, and R. Biswas, *J. Chem. Phys.* **142**, 034505 (2015).
9. D. van der Spoel, E. Lindahl, B. Hess, A. R. van Buuren, E. Apol, P. J. Meulenhoff, D. P. Tieleman, A. L. T. M. Sijbers, K. A. Feenstra, R. van Drunen, and H. J. C. Berendsen, *Gromacs User Manual version 4.5.4*, www.gromacs.org (2010).
10. J. Habasaki and K. L. Nagi, *J. Chem. Phys.* **129**, 194501 (2008).
11. T. Pal and R. Biswas, *Theor. Chem. Acc.* **132**, 1348 (2013).
12. M. G. Del Popolo and G. A. Voth, *J. Phys. Chem. B* **108**, 1744 (2004).
13. T. I. Morrow and E. J. Maginn, *J. Phys. Chem. B* **106**, 12807 (2002).
14. J. N. Canongia Lopes, J. Deschamps, and A. A. H. Padua, *J. Phys. Chem. B* **108**, 2038 (2004).
15. C. G. Hanke, S. L. Price, and R. M. Lynden-Bell, *Mol. Phys.* **99**, 801 (2001).
16. C. J. Margulis, *Mol. Phys.* **102**, 829 (2004).
17. A. Das, S. Das, R. Biswas, *Chem. Phys. Lett.* **581**, 47 (2013).

18. S. Das, R. Biswas, and B. Mukherjee, *J. Phys. Chem. B* **119**, 274 (2015).
19. S. Das, R. Biswas, and B. Mukherjee, *J. Phys. Chem. B* **119**, 11157 (2015).
20. A. D. MacKerell Jr., J. Wiorkiewicz-Kuczera, and M. Karplus, *J. Am. Chem. Soc.* **117**, 11946 (1995).
21. L. J. Smith, H. J. C. Berendsen, and W. F. van Gunsteren, *J. Phys. Chem. B* **108**, 1065 (2004).
22. B. Guchhait, S. Das, S. Daschakraborty, and R. Biswas, *J. Chem. Phys.* **140**, 104514 (2014).
23. U. Essmann, L. Perera, M. L. Berkowitz, T. Darden, H. Lee, and L. G. Pedersen, *J. Chem. Phys.* **103**, 8577 (1995).
24. L. Martinez, R. Andrade, E. G. Birgin, and J. M. Martinez, *J. Comput. Chem.* **30**, 2157 (2009).
25. G. Bussi, D. Donadio, and M. Parrinello, *J. Chem. Phys.* **126**, 014101 (2007).
26. H. J. C. Berendsen, J. P. M. Postma, W. F. van Gunsteren, A. DiNola, and J. R. Haak, *J. Chem. Phys.* **81**, 3684 (1984).
27. M. Parrinello and A. Rahman, *J. Appl. Phys.* **52**, 7182 (1981).
28. S. Nose and M. L. Klein, *Mol. Phys.* **50**, 1055 (1983).
29. R. W. Hockney, S. P. Goel, and J. Eastwood, *J. Comp. Phys.* **14**, 148 (1974).
30. M. C. Stumpe and H. Grubmuller, *J. Phys. Chem. B* **111**, 6220 (2007).
31. A. S. Mahadevi, Y. I. Neela, and G. N. Sastry, *Phys. Chem. Chem. Phys.* **13**, 15211 (2011).
32. D. C. Rapaport, *Mol. Phys.* **50**, 1151 (1983).
33. A. Chandra, *Phys. Rev. Lett.* **85**, 768 (2000).
34. A. Luzar, *J. Chem. Phys.* **113**, 10663 (2000).
35. A. Luzar and D. Chandler, *Nature*, **379**, 55 (1996).

36. A. Luzar and D. Chandler, *Phys. Rev. Lett.* **76**, 928 (1996).
37. S. Indra and R. Biswas, *Mol. Simul.* **41**, 471 (2015).
38. K. Mukherjee, S. Das, A. Barman, and R. Biswas, *J. Phys. Chem. B* (under review).
39. J. P. Hansen and I. R. McDonald, *Theory of Simple Liquids*, 3rd Ed., Academic: San Diego, 2006.
40. T. Pal and R. Biswas, *Theor. Chem. Acc.* **132**, 1348 (2013).

Addendum III

Heterogeneous Dynamics in Acetamide/NaClO₄/LiBF₄ Ionic Deep Eutectics: An Insight from Molecular Dynamics Simulation

Ad. 3.1. Introduction

The long quest for a “greener” solvent has led to the development of deep eutectic solvents (DESs) as an alternative to common organic solvents.¹⁻⁵ DESs have been used as a solvent for many chemical reactions and in separation technology, as catalysts for biochemical reactions, extraction of proteins, in synthesis of nanoparticles.⁵⁻¹¹ The unique properties of DESs like biodegradable nature, easy preparation route, cheap materials etc. have made it attractive for large scale applications.¹¹⁻²³ Amide/electrolyte DESs have been studied previously using fluorescence spectroscopic techniques²⁴⁻²⁶, dielectric relaxation experiments²⁷ and molecular dynamic simulations.^{24-25,28} The experimental studies^{25,29} have reported strong excitation wavelength dependence of steady state fluorescence, fractional viscosity dependence of both average solvation and rotation rates, and decoupling of translational and rotational motions. Simulation studies²⁵ also have revealed stretched exponential relaxation of amides in these DESs. All these indicate the presence of inherent spatio-temporal heterogeneity in these mixtures. Characterization of this heterogeneity aspect is important not only from basic scientific point of view but also from technological/industrial perspective. Here we have carried out molecular dynamic simulations with Acetamide+NaClO₄/LiBF₄ DESs to analyze the heterogeneity aspect.

Ad. 3.2. Simulation Details

All-atom molecular dynamics simulations were performed at a temperature 303 K with GROMACS version 4.5.4.³⁰ Each mixture comprised of 512 molecules, of which there are 400 acetamide molecules and 56 pairs of Li^+ and X^- ($X^- = BF_4^-, ClO_4^-$). This provides a mole ratio of 78:22 between acetamide and electrolyte. The potential function used has the following form:

$$U(R) = \sum_{bonds} K_r (r - r_{eq})^2 + \sum_{angles} K_\theta (\theta - \theta_{eq})^2 + \sum_{dihedrals} K_\phi (1 + \cos(n\phi - \delta)) + \sum_{i < j}^{atoms} \left(\frac{A_{ij}}{R_{ij}^{12}} - \frac{B_{ij}}{R_{ij}^6} \right) + \sum_{i < j}^{atoms} \frac{q_i q_j}{4\pi\epsilon_0 R_{ij}}. \quad (\text{Ad. 3.1})$$

This particular form of the potential function has been used frequently for simulating liquid structure and dynamics of ionic liquids³¹⁻³² and DESs.^{24-25,28} In Eq. Ad. 3.1, K_r denotes the bond constant with the equilibrium bond distance r_{eq} , K_θ the angle constant with the equilibrium angle θ_{eq} , K_ϕ the dihedral constant with periodicity n , dihedral angle ϕ and phase shift δ . R_{ij} is the distance between i and j atoms with partial charges q_i and q_j , respectively. CHARMM³³ force field parameters were used for acetamide and force field parameters of cations and anions were taken from the existing literature.³⁴⁻³⁶ The short-range van der Waals interaction was represented by the Lennard-Jones (LJ) potential, and the long-range electrostatic potential was treated via particle mesh Ewald summation technique (PME).³⁷

The initial configuration was built using Packmol³⁸ and minimized via steepest decent algorithm in GROMACS. Then each system was heated slowly from 100 K to the final temperature via a step-up process of step 100 K with each step continuing for 100 ps in NVT ensemble. The final configuration was equilibrated in NPT ensemble at 1 atm pressure using V-rescale thermostat³⁹ and Berendsen pressure coupling⁴⁰ with relaxation time of 0.5 ps and 2.0 ps respectively for 1 ns. Subsequently, further equilibration of 2 ns followed by a production run of 20 ns was carried out in NPT ensemble using V-rescale thermostat³⁹ and Parrinello-Rahman

barostat⁴¹⁻⁴² with relaxation time of 0.5 ps and 2.0 ps respectively. Periodic boundary conditions were employed in all three directions, and the equations of motion were integrated using a time step of 0.5 fs employing the leap-frog algorithm.⁴⁴ Simulated trajectories were saved every 10 fs for data analyses and simulation results.

Ad. 3.3. Simulation Results

Ad. 3.3.1. Non-Gaussian and new Non-Gaussian parameters

We follow our earlier protocol⁴⁵ to study dynamic heterogeneity of acetamide+NaClO₄/LiBF₄ DESs via calculating non-Gaussian (NG) and new non-Gaussian parameters (NNG) defined by α_2 and γ . All the necessary expressions to calculate those parameters are already presented in Chapter 6 of this Thesis. The timescales associated with the peak times for α_2 and γ are denoted by τ_{NG} and τ_{NNG} . α_2 is dominated by the particles which move more than the Gaussian distribution. On the other hand, γ is strongly dominated by the particles which move less than the expected Gaussian distribution and therefore is associated with the presence of slow particles. Thus simultaneous calculation of both these parameters would indicate the presence of particles with different mobility reflecting the presence of dynamic heterogeneity. Figure Ad. 3.1 presents a comparison of these two parameters for both the DESs. It is evident from both the panels that dynamics heterogeneity survives almost for one ns. Interestingly for both the electrolytes, α_2 peaks around ~30 ps and γ develops a peak at a later time ~100 ps. The difference between these two signifies the simultaneous presence of fast and slow timescales in these systems.

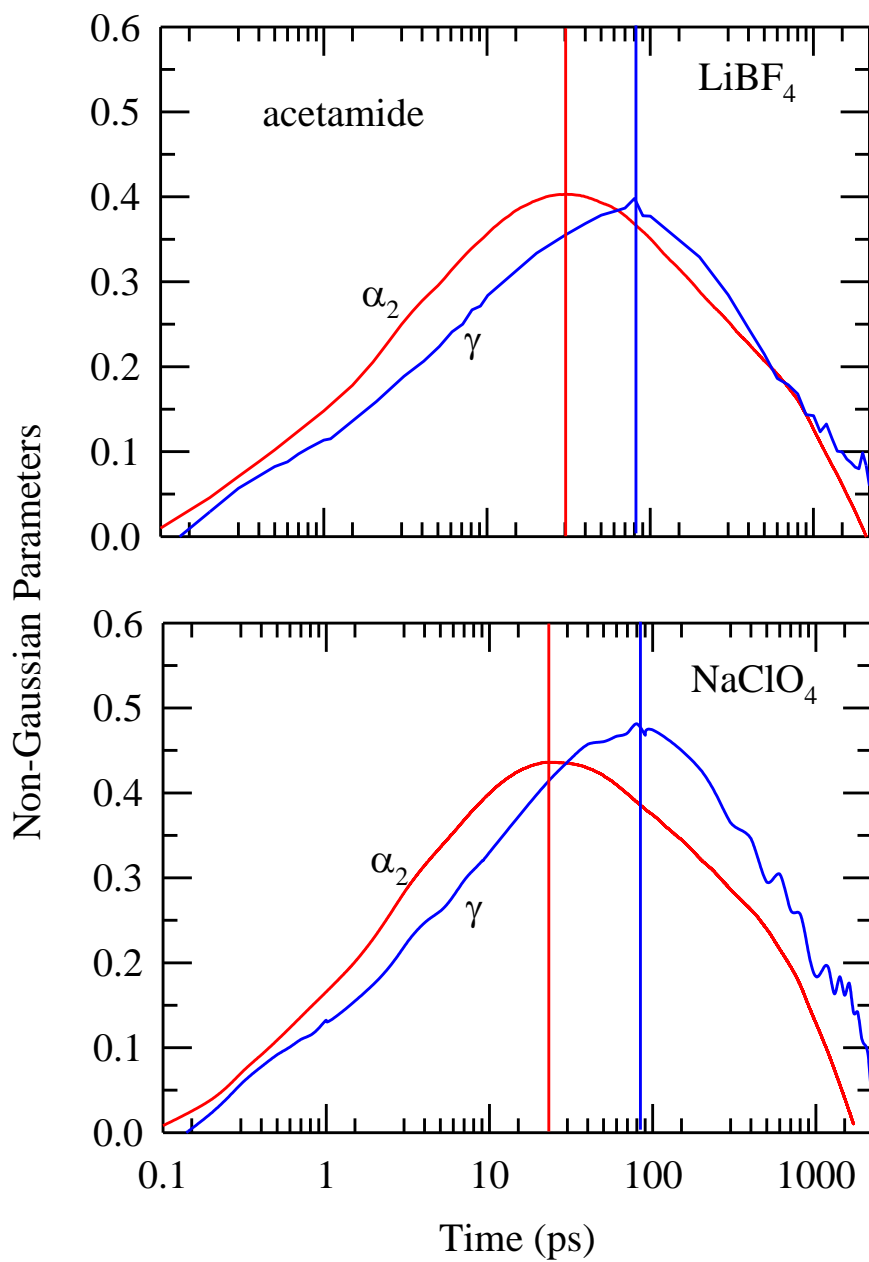


Figure Ad. 3.1: Electrolyte dependence of simulated non-Gaussian (α_2) and new non-Gaussian parameters (γ) for acetamide in these deep eutectics at 303 K. Vertical lines indicate the peak times (approximate) for the respective plot. Representations are color coded.

Ad. 3.3.2. Acetamide dynamic structure factor: Density relaxation profile and timescales

Next we present the density relaxation dynamics via simulating the self-part of the acetamide dynamic structure factors, $F_s(k,t) = \langle \delta\rho_s(k,t)\delta\rho_s(-k,t) \rangle$, where $\delta\rho_s(k,t)$ denotes the wavenumber (k) and time dependent self part of the fluctuating acetamide density. Figure Ad. 3.2 presents the decay of normalized self-dynamic structure factor, $F_s^N(k,t) = F_s(k,t) / F_s(k,t=0)$ for acetamide in presence of two different electrolytes along with the fits. The calculation was done at two wavevectors, $k = 1.36 \text{ \AA}^{-1}$ corresponding to the nearest neighbour wavevector and $k = 0.25 \text{ \AA}^{-1}$ corresponding to the lowest wavevector accessible. The nearest neighbour wavevector corresponds to the first peak of the simulated radial distribution function of the carbonyl carbon of the acetamide molecules. Multi-exponential fit parameters of all the decays are summarized in Table Ad. 3.1. It is observed that the decay rate at both the wavevectors is slightly slower in presence of LiBF_4 electrolyte. Therefore it is expected that the dynamics should be slower in presence of LiBF_4 .

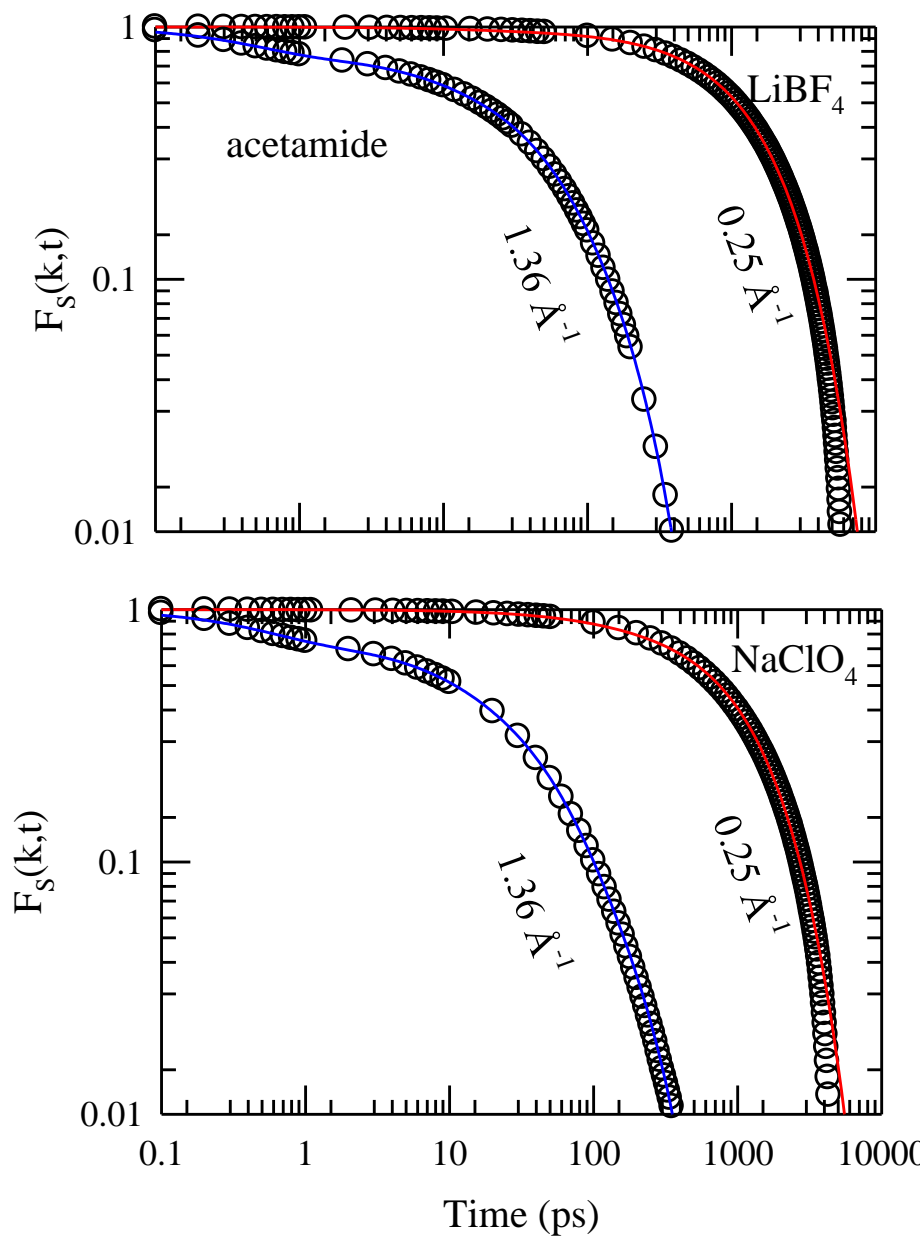


Figure Ad. 3.2: Electrolyte dependence of simulated wavenumber dependent relaxation of the normalized self part of the acetamide dynamic structure factor, $F_S^N(k,t)$, in these deep eutectics at 303 K. Multi-exponential fits through the simulated data are shown by the solid lines.

Table Ad. 3.1: Multi-exponential fit parameters for simulated wavevector dependent $F_S^N(k,t)$ for acetamide in presence of various electrolytes at 303 K.

Electrolyte	k (\AA^{-1})	a_1	τ_1 (ps)	a_2	τ_2 (ps)	a_3	τ_3 (ps)	a_4	τ_4 (ps)	β	$\langle\tau\rangle$ (ps)
<i>LiBF₄</i>	0.25	0.03	13.6	0.97	1667.0	-	-	-	-	1.0	1617.4
	1.36	0.22	0.4	0.11	7.2	0.35	39.4	0.32	111.1	1.0	50.2
<i>NaClO₄</i>	0.25	0.08	91.7	0.92	1250.0	-	-	-	-	1.0	1157.3
	1.36	0.25	0.5	0.17	7.9	0.41	36.1	0.17	126.6	1.0	37.8

References:

1. D. V. Wagle, H. Zhao, and G. A. Baker, *Acc. Chem. Res.* **47**, 2299 (2014).
2. Q. Zhang, K. De Oliveira Vigier, S. Royer, and F. Jérôme, *Chem. Soc. Rev.* **41**, 7108 (2012).
3. A. P. Abbott, G. Capper, D. L. Davies, R. K. Rasheed, and V. Tambyrajah, *Chem. Commun.* **70** (2003).
4. A. P. Abbott, D. Boothby, G. Capper, D. L. Davies, and R. K. Rasheed, *J. Am. Chem. Soc.* **126**, 9142 (2004).
5. M. Francisco, A. van den Bruinhorst, M. C. Kroon, *Angew. Chem. Int. Ed.* **52**, 3074 (2013).
6. N. S. V. Narayanan, B. V. Ashokraj, and S. Sampath, *J. Colloid Interf Sci* **342**, 505 (2010).
7. R. Wallace and P. Bruins, *J. Electrochem. Soc.* **114**, 212 (1967).
8. E. L. Smith, A. P. Abbott, and K. S. Ryder, *Chem. Rev.* **114**, 11060 (2014).
9. N Azizi and E. Batebi, *Catalysis Science & Technology* **2(12)**, 2445 (2012).
10. K. Shahbaz, F. S. Mjalli, M. A. Hashim, and I. M. AlNashef, *Energy & Fuels* **25**, 2671 (2011).
11. B. Singh, H. Lobo, and G. Shankarling, *Catalysis Letters* **141**, 178 (2011).
12. P. A. More, B. L. Gadilohar, and G. S. Shankarling, *Catalysis Letters* **144(8)**, 1393 (2014).
13. M. J. Rodriguez-Alvarez, C. Vidal, J. Diez, and J. Garcia-Alvarez, *Chem. Commun.* **50**, 12927 (2014).
14. Q. Zeng, Y. Wang, Y. Huang, X. Ding, J. Chen, and K. Xu, *Analyst* **139**, 2565 (2014).
15. A. P. Abbott, K. E. Ttaib, G. Frisch, K. S. Ryder, and D. Weston, *Phys. Chem. Chem. Phys.* **14**, 2443 (2012).
16. E. L. Smith, J. C. Barron, A. P. Abbott, and K. S. Ryder, *Analytical Chemistry* **81**, 8466 (2009).

17. A. P. Abbott, M. Azam, K. S. Ryder, and S. Saleem *Analytical Chemistry* **85**, 6653 (2013).
18. A. P. Abbott, R. C. Harris, Y. T. Hsieh, K. S. Ryder, and I. W. Sun, *Phys. Chem. Chem. Phys.* **16**, 14675 (2014).
19. A. P. Abbott, K. E. Ttaib, G. Frisch, K. J. McKenzie, and K. S. Ryder, *Phys. Chem. Chem. Phys.* **11**, 4269 (2009).
20. H.-G. Liao, Y.-X. Jiang, Z.-Y. Zhou, S.-P. Chen, and S.-G. Sun, *Angew. Chem. Int. Ed.* **120**, 9240 (2008).
21. J. A. Hammons, T. Muselle, J. Ustarroz, M. Tzedaki, M. Rats, A. Hubin, and H. Terryn, *J. Phys. Chem. C* **117**, 14381 (2013).
22. L. Wei, Z. Y. Zhou, S. P. Chen, C. D. Xu, D. S. Su, M. E. Schuster, and S. G. Sun, *Chem. Commun.* **49**, 11152 (2013).
23. F. Chen, S. Xie, J. Zhang, and R. Liu, *Mater. Lett.* **112**, 177 (2013).
24. A. Das, S. Das, and R. Biswas, *J. Chem. Phys.* **142**, 034505 (2015).
25. B. Guchhait, S. Das, S. Daschakraborty, and R. Biswas, *J. Chem. Phys.* **140**, 104514 (2014).
26. A. Das, S. Das, and R. Biswas, *Chem. Phys. Lett.* **47**, 581 (2013).
27. K. Mukherjee, A. Das, S. Choudhury, A. Barman, and R. Biswas, *J. Phys. Chem. B* **119**, 8063 (2015).
28. S. Das, R. Biswas, and B. Mukherjee, *J. Phys. Chem. B* **119**, 11157 (2015).
29. B. Guchhait, S. Daschakraborty, and R. Biswas, *J. Chem. Phys.* **136**, 174503 (2012).
30. D. van der Spoel, E. Lindahl, B. Hess, A. R. van Buuren, E. Apol, P. J. Meulenhoff, D. P. Tieleman, A. L. T. M. Sijbers, K. A. Feenstra, R. van Drunen, and H. J. C. Berendsen, *Gromacs User Manual version 4.5.4*, www.gromacs.org (2010).
31. J. Habasaki and K. Nagi, *J. Chem. Phys.* **129**, 194501 (2008).
32. T. Pal and R. Biswas, *Theor. Chem. Acc.* **132**, 1348 (2013).
33. A. D. MacKerell Jr., J. Wiorcikiewicz-Kuczera, and M. Karplus, *J. Am. Chem. Soc.* **117**, 11946 (1995).

34. J. N. Canongia Lopes and A. A. H. Padua, *J. Phys. Chem. B* **110**, 19586 (2006).
35. M. B. Gee, N. R. Cox, Y. Jiao, N. Benteinis, S. Weerasinghe, and P. E. Smith, *J. Chem. Theory Comput.* **7**, 1369 (2011).
36. C. Cadena and E. J. Maginn, *J. Phys. Chem. B* **110**, 18026 (2006).
37. U. Essmann, L. Perera, M. L. Berkowitz, T. Darden, H. Lee, and L. G. Pedersen, *J. Chem. Phys.* **103**, 8577 (1995).
38. L. Martinez, R. Andrade, E. G. Birgin, and J. M. Martinez, *J. Comput. Chem.* **30**, 2157 (2009).
39. G. Bussi, D. Donadio, and M. Parrinello, *J. Chem. Phys.* **126**, 014101 (2007).
40. H. J. C. Berendsen, J. P. M. Postma, W. F. van Gunsteren, A. DiNola, and J. R. Haak, *J. Chem. Phys.* **81**, 3684 (1984).
41. M. Parrinello and A. Rahman, *J. Appl. Phys.* **52**, 7182 (1981).
42. S. Nose and M. L. Klein, *Mol. Phys.* **50**, 1055 (1983).
43. B. Guchhait, S. Das, and R. Biswas, *J. Chem. Phys.* (to be submitted).
44. R. W. Hockney, S. P. Goel, and J. Eastwood, *J. Comp. Phys.* **14**, 148 (1974).
45. S. Das and R. Biswas, *J. Chem. Phys.* (to be submitted).